JOURNAL OF RESEARCH

OF THE U.S. GEOLOGICAL SURVEY

MAY–JUNE 1974
VOLUME 2, NUMBER 3

Scientific notes and summaries of investigations in geology, hydrology, and related fields

U.S. DEPARTMENT OF THE INTERIOR

UNITED STATES DEPARTMENT OF THE INTERIOR
ROGERS C. B. MORTON, Secretary
GEOLOGICAL SURVEY
V. E. McKelvey, Director

For sale by the Superintendent of Documents, U.S. Government Printing Office, Washington, DC 20402. Order by SD Catalog No. JRGS. Annual subscription rate $15.50 (plus $3.75 for foreign mailing). Single copy $2.75. Make checks or money orders payable to the Superintendent of Documents.

Send all subscription inquiries and address changes to the Superintendent of Documents at the above address.

Purchase orders should not be sent to the U.S. Geological Survey library.

Library of Congress Catalog-card No. 72-600241.

The Journal of Research is published every 2 months in Washington, D.C., by the U.S. Geological Survey. It contains papers by members of the Geological Survey and their professional colleagues on geologic, hydrologic, topographic, and other scientific and technical subjects.

Correspondence and inquiries concerning the Journal (other than subscription inquiries and address changes) should be directed to the Journal of Research, Publications Division, U.S. Geological Survey, National Center, Reston, VA 22092.

Papers for the Journal should be submitted through regular Division publication channels.

The Secretary of the Interior has determined that the publication of this periodical is necessary in the transaction of the public business required by law of this Department. Use of funds for printing this periodical has been approved by the Director of the Office of Management and Budget through February 11, 1975.

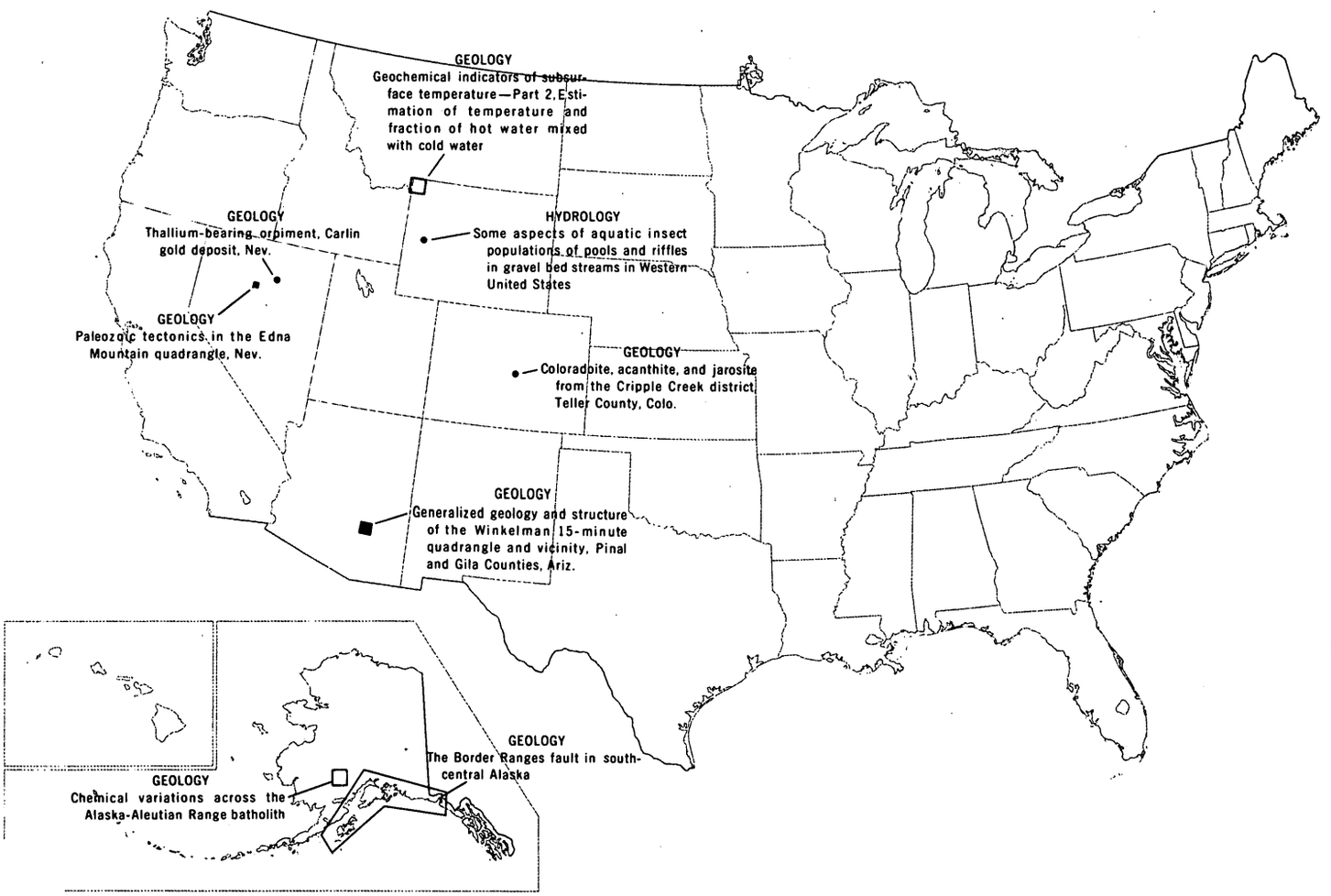

GEOGRAPHIC INDEX TO ARTICLES

See "Contents" for articles concerning areas outside the United States and articles without geographic orientation.

JOURNAL OF RESEARCH

of the

U.S. Geological Survey

Vol. 2 No. 3 May-June 1974

CONTENTS

Abbreviations II

GEOLOGIC STUDIES

Geochemical indicators of subsurface temperature—Part 1, Basic assumptions ..... *R. O. Fournier, D. E. White, and A. H. Truesdell* 259

Geochemical indicators of subsurface temperature—Part 2, Estimation of temperature and fraction of hot water mixed with cold water ..... *R. O. Fournier and A. H. Truesdell* 263

The calculation of aquifer chemistry in hot-water geothermal systems ... *A. H. Truesdell and Wendy Singers* 271

Some morphometric properties of experimentally cratered surfaces ..... *H. J. Moore, R. V. Lugn, and E. B. Newman* 279

Tectonic transition zone in the northeastern Caribbean ..... *M. S. Marlow, L. E. Garrison, R. C. Martin, J. V. A. Trumbull, and A. K. Cooper* 289

Silicoflagellate zonation of Upper Cretaceous to lower Miocene deep-sea sediment ..... *David Bukry and J. H. Foster* 303

Generalized geology and structure of the Winkelman 15-minute quadrangle and vicinity, Pinal and Gila Counties, Ariz. ..... *M. H. Krieger* 311

The Border Ranges fault in south-central Alaska ..... *E. M. MacKevett, Jr., and George Plafker* 323

Paleozoic tectonics in the Edna Mountain quadrangle, Nev. ..... *R. L. Erickson and S. P. Marsh* 331

Coloradoite, acanthite, and jarosite from the Cripple Creek district, Teller County, Colo. ..... *F. A. Hildebrand and G. B. Gott* 339

Thallium-bearing orpiment, Carlin gold deposit, Nev. ..... *A. S. Radtke, C. M. Taylor, F. W. Dickson, and Chris Heropoulos* 341

Chemical variations across the Alaska-Aleutian Range batholith ..... *B. L. Reed and M. A. Lanphere* 343

Spectrophotometric determination of niobium in rocks ..... *L. P. Greenland and E. Y. Campbell* 353

Spectrophotometric determination of silica at high concentrations using fluoride as a depolymerizer ..... *Leonard Shapiro* 357

HYDROLOGIC STUDIES

Occurrence of dissolved organic carbon in selected ground-water samples in the United States ..... *J. A. Leenheer, R. L. Malcolm, P. W. McKinley, and L. A. Eccles* 361

The soil creep—curved tree fallacy ..... *R. L. Phipps* 371

Some aspects of aquatic insect populations of pools and riffles in gravel bed streams in Western United States ..... *B. W. Lium* 379

Recent publications of the U.S. Geological Survey ..... Inside of back cover

ABBREVIATIONS

A	ampere
Å	angstrom
abs	absolute
ADP	ammonium dihydrogen phosphate
atm	atmosphere
BOD	biochemical oxygen demand
Btu	British thermal unit
b.y.	billion years
°C	degree Celsius
cal	calorie
C.I.	color index
CIPW	Cross, Iddings, Pirsson, and Washington
cm	centimeter
cm^3	cubic centimeter
d	day
diam	diameter
DSDP	Deep Sea Drilling Project
emf	electromotive force
eu	entropy unit
F.D.&C.	Food, Drug, and Cosmetic [dye]
ft	foot
ft^2	square foot
ft^3	cubic foot
g	gram
γ	activity coefficient
gal	gallon
h	hour
ID	inside diameter
IDOE	International Decade of Ocean Exploration
in.	inch
J	joule
K	kelvin
kg	kilogram
km	kilometer
km^2	square kilometer
km^3	cubic kilometer
kV	kilovolt
l	liter
lb	pound
ln	logarithm (natural)
log	logarithm (common)
m	meter
m^2	square meter
m^3	cubic meter
M	molarity; molar (concentration)
m	molality; molal (concentration)
MA	megampere
mA	milliampere
mg	milligram
mGal	milligal
mi	mile
mi^2	square mile
min	minute
ml	milliliter
mm	millimeter
mmol	millimole
mo	month
mol	mole
mV	millivolt
m.y.	million years
μg	microgram
μm	micrometer
N	normality
nm	nanometer
OD	outside diameter
PDB	Peedee belemnite
pH	measure of hydrogen ion activity
p/m	part per million
s	second
SMOW	standard mean ocean water
V	volt
W	watt
wt	weight
yd^3	cubic yard
yr	year

Jour. Research U.S. Geol. Survey
Vol. 2, No. 3, May-June 1974, p. 259—262

GEOCHEMICAL INDICATORS OF SUBSURFACE TEMPERATURE—PART 1, BASIC ASSUMPTIONS

By R. O. FOURNIER, D. E. WHITE, and A. H. TRUESDELL,
Menlo Park, Calif.

Abstract.—The chemical and isotopic compositions of hot-spring water and gas are used to estimate subsurface temperatures. The basic assumptions inherent in the methods are seldom stipulated. These assumptions include (1) a temperature-dependent reaction at depth, (2) a supply of the solid phase involved in the reaction to permit saturation of the constituent used for geothermometry, (3) water-rock equilibrium at depth, (4) negligible re-equilibration as the water flows to the surface, and (5) no dilution or mixing of hot and cold water. The first three assumptions are probably good for a few reactions that occur in many places. The last two assumptions probably are not valid for many hot-spring systems; information obtained is therefore for the shallower parts of those systems, or a limiting temperature (generally a minimum) is indicated.

The recent increased interest in geothermal energy has prompted widespread exploration for this resource. As expected, the areas initially receiving the most attention are those in which fumaroles and hot springs of high temperature are found. Thermal springs are numerous in the western United States. Their temperatures range from a few degrees above mean annual temperature to boiling. In general, their relative abundance decreases with increasing temperature. From an exploration point of view, the critical question is, how did a given spring attain its observed temperature? Did the warm temperature result from water circulating deeply in a region of normal or slightly above normal geothermal gradient; that is, does the temperature of the spring represent the highest subsurface temperature deep in the system? Or, did the water come from a very high temperature environment at depth and cool on the way back to the surface? We would like to use the chemical composition of the water to answer these questions. In practice, we have found that springs with high rates of discharge are most suitable for hydrogeochemical prospecting, whereas compositions of springs with low rates of discharge are very difficult to interpret.

BASIC ASSUMPTIONS

There are many basic assumptions inherent in using geochemical indicators to estimate subsurface temperatures (White, 1974). Although these assumptions may be valid in many places, it is unlikely that they will be fulfilled everywhere. The usual assumptions are:

1. Temperature-dependent reactions occur at depth.
2. All constituents involved in a temperature-dependent reaction are sufficiently abundant (that is, supply is not a limiting factor).
3. Water-rock equilibration occurs at the reservoir temperature.
4. Little or no re-equilibration or change in composition occurs at lower temperatures as the water flows from the reservoir to the surface.
5. The hot water coming from deep in the system does not mix with cooler shallow ground water.

A schematic model of a hot-spring system (fig. 1) is useful in assessing these assumptions. Critical elements of the model include a heat source of unspecified nature at the base of the system and interconnected permeability that permits convection to occur. In response to heating, water deep in the system decreases in density and is forced up and out of the system, as at A, by pressure exerted by cold, dense water. The cold water moves down and into the system at the margins along permeable structures, possibly faults or joints such as B—B′. There are many alternative possibilities, including models in which some or all of the ascending water and gas is connate, metamorphic, or even juvenile in origin. In some places the salinity of the deep water may be high enough to counteract the effects of temperature on density. Although connate and metamorphic water is probably dominant in some hot springs (White and others, 1973), isotope data indicate that most hot-spring water is predominantly meteoric in origin.

If the maximum temperature attained by the water at depth is higher than the boiling temperature appropriate for atmospheric conditions, the water will cool by boiling (adiabatically), by conduction, or by a combination of these processes as it moves toward the surface. If, on the other hand, the maximum temperature at depth is less than the boiling temperature at atmospheric conditions, the emerging water, such as at A (fig. 1) may have approximately the maximum temperature at depth or a lower temperature, depending on whether the rate of upflow of water is very fast or slow.

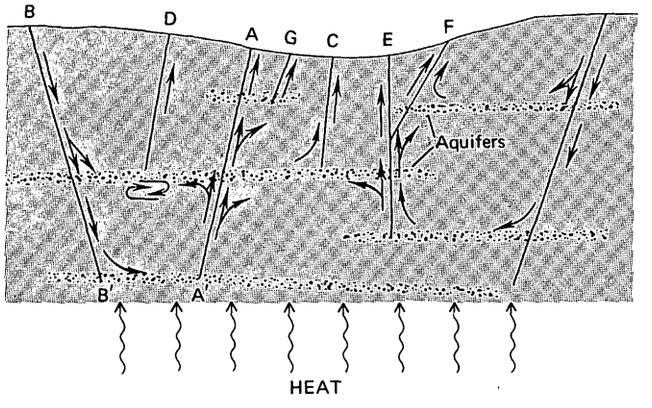

Figure 1.–Schematic model of a hot-spring system having a heat source of unspecified nature and interconnected permeability.

Solubilities

Solubilities of minerals generally change as functions of temperature and water pressure. Therefore, under some circumstances absolute quantities of dissolved constituents are useful indicators of subsurface temperature. However, the dissolving solid phase must be specified and its presence must be assumed at depth. An example is the silica geothermometer, which depends on the solubility of quartz controlling aqueous silica (Fournier and Rowe, 1966; Mahon, 1966).

In general, the solubilities of the common silicates increase with increasing temperature and pressure. As cold subsurface water is heated, it dissolves more and more silicate constituents, reaching a maximum at the hottest (and generally deepest) part of the system. Deposition of silicates may then occur as the water moves back toward the surface and cools, particularly if the cooling is adiabatic. This may result in the self-sealing of the geothermal system, as discussed by Bodvarsson (1964), Facca and Tonani (1967), and White, Muffler, and Truesdell (1971).

The common carbonates have retrograde solubilities (Holland, 1967). Other things being constant, minimum solubilities are attained at the hottest and deepest parts of the system. Generally "other things" are not constant, however. Carbonate solubilities are greatly affected by variations in pH and partial pressure of CO_2. Unfortunately, subsurface pH and P_{CO_2} are not easily estimated from the composition of hot-spring water and gas collected at the surface.

The common sulfates also have retrograde solubilities. Like the carbonates, their usefulness in geothermometry is restricted to systems in which the solid phase is present at depth. One cannot safely assume this unless sulfates have been found in cuttings or cores from holes drilled at the locality in question. In other words, there may be an inadequate supply of the "indicator" constituent in the reservoir, so that the solution at depth is unsaturated with respect to a particular phase; for example, $CaSO_4$ or $BaSO_4$.

Exchange reactions

Equilibrium constants for exchange and alteration reactions also are temperature dependent. In such reactions the ratios of dissolved constituents change with changing temperature of equilibration. Both chemical and isotopic reactions come under this category. Examples are Na:K ratios of chloride solutions equilibrated with alkali feldspars (Orville, 1963; Hemley, 1967), Na:K ratios in natural waters (Ellis, 1970; White, 1965), and Na-K-Ca relations in natural waters (Fournier and Truesdell, 1973). Again, as in the solubility method of geothermometry, the identity of the reactants and products in the high-temperature environment at depth must be assumed. If the assumed phases are not present, the geothermometer yields anomalous results (Fournier and Truesdell, 1970, 1973).

Equilibration at depth

In order to use a geochemical method of estimating subsurface temperature, one must assume equilibrium or at least an approach to equilibrium at depth for a specific "indicator" reaction. At low temperatures, this is a tenuous assumption. Metastable conditions also are likely to occur. However, the assumption of attainment of equilibrium in a high-temperature environment at depth is probably good for many reactions. This assumption is particularly good where the residence time for water in a reservoir at a relatively uniform temperature is long and there is effective mixing or homogenization of introduced water with stored water.

When an increment of water, chemically equilibrated at depth, finally does enter a channel that allows direct movement back to the surface, such as A–A′ in figure 1, the time of upward travel may be very short (minutes or hours) compared with the residence time in the reservoir. Consequently, even though the temperature of the water may decrease markedly, little chemical reaction may occur during upward flow, and the composition of the emerging water may reflect the conditions present in the deep reservoir. However, reservoirs at different depths and temperatures may be present within a given geothermal system. Hot springs located at C, E, and G in figure 1 show various possibilities for water re-equilibrating in shallow reservoirs, so that some or all of the chemical geothermometers will yield estimated subsurface temperatures lower than the maximum temperature deep in the system.

A re-equilibrated water, such as that emerging at G (fig. 1), may give a good indication of the salinity of the deep water. More commonly, deep water entering shallow reservoirs will mix with relatively dilute, shallow water, so that neither the temperature nor salinity of the deepest reservoir is indicated by the spring water that eventually emerges at the surface, as at D and F. If the residence times of both the hot- and cold-water components are long in the shallow aquifer and mixing is thorough, the composition of emerging spring water

as at D, may be indicative of the temperature of that shallow reservoir. In contrast, if the residence time in the shallow reservoir of one or both of the mixing waters is short, the composition of the emerging water (spring F) may give little or no information about that shallow reservoir. Under special circumstances, however, it may be possible to estimate the temperature and proportion of the hot-water component of a mixed water such as that emerging at F. This is discussed elsewhere (Fournier and Truesdell, 1974).

In the discussion to this point, we have assumed essentially no chemical reaction in the channels connecting different reservoirs or reservoirs with springs. Advantageous conditions that minimize reactions within channels are rapid rates of upflow, low temperature, and nonreactive wallrock. Where continued chemical reactions do occur in the channelways leading to the surface, different geochemical indicators yield different apparent temperatures, reflecting varying amounts of re-equilibration at intermediate temperatures.

Enrichment of volatiles

Tonani (1970) emphasizes the relative enrichments in spring waters and fumaroles of comparatively volatile components, particularly NH_3, B, Hg, CO_2, and sulfur compounds, that may indicate subsurface boiling. He generally assumes that steam separates from deep boiling water and that it carries other volatile constituents toward the surface. At shallow depth the steam condenses and mixes with the local ground water. Springs fed by this water are enriched in volatiles relative to chloride.

Tonani's model probably works very well for vapor-dominated systems, as described by White, Muffler, and Truesdell (1971). It has yet to be demonstrated that volatile constituents are enriched relative to chloride in neutral to alkaline hot springs above hot-water-dominated systems, even where boiling temperatures are attained at depth. Enrichment of volatile constituents in spring water may result from processes other than high-temperature boiling. Gases such as CO_2 and CH_4, if sufficiently abundant, may separate from relatively cold water deep underground and escape to the surface. If this gas later encounters shallow ground water, that ground water may become enriched in volatile constituents.

RECOMMENDED PROCEDURE

For estimating subsurface temperatures we set forth the following guidelines despite misgivings that they will be interpreted as hard-and-fast rules for always reflecting subsurface conditions. The intent is simply to suggest starting assumptions where little information is available about hydrologic conditions. As more information is obtained for a specific area, other assumptions may become more reasonable.

The recommended procedures are based upon the temperature and rate of flow of the spring water, as outlined below:

1. Boiling spring:
   (a) Small rate of flow: Assume mostly conductive cooling. Apply chemical indicators assuming little or no steam loss.
   (b) Large rate of flow: Assume adiabatic cooling. Apply chemical indicators assuming maximum steam loss.
2. Spring below boiling:
   (a) Small rate of flow: Likely to have no clear-cut interpretation. May be a water that has never been very hot, a mixed water from sources of different temperatures, or a hot water cooled entirely by conduction. Try geothermometers that assume conductive cooling; indicated temperatures are likely to be minima.
   (b) Large rate of flow: Assume no conductive cooling. Test to see if geothermometers (particularly the Na-K-Ca geothermometers (Fournier and Truesdell, 1973)) suggest chemical equilibration at the temperature (±25°C) of the water. If a higher temperature is indicated, treat as a mixed water according to the method of Fournier and Truesdell (1974).

We have not specified what large and small rates of flow are. Our intent is to distinguish between waters that cool by conduction during their ascent and those that either cool mainly by boiling or do not cool at all. This depends in part on the rate of upflow, the depth of the aquifer supplying the water, and whether a spring is isolated or is part of a larger upflowing system. For preliminary evaluation, an arbitrary cutoff at 200 l/min is suggested for a single isolated spring, and 20 l/min for single springs of larger groups.

CONCLUSIONS

Chemical analyses of hot-spring water and gas may be of great use in an exploration program for geothermal energy. Like all exploration methods, a great many assumptions must be made in order to interpret the data. We urge that these assumptions be kept in mind during the evaluation processes.

REFERENCES CITED

Bodvarsson, Gunnar, 1964, Utilization of geothermal energy for heating purposes and combining schemes involving power generation, heating, and/or by-products, *in* Geothermal Energy II: United Nations Conf., New Sources Energy, Rome 1961, Proc., v. 3, p. 429–436.

Ellis, A. J., 1970, Quantitative interpretation of chemical characteristics of hydrothermal systems, *in* United Nation Symposium on Development and Utilization of Geothermal Resources, Pisa 1970, v. 2, pt, 1: Geothermics, Spec. Issue 2, p. 516–528.

Facca, Giancarlo, and Tonani, Franco, 1967, The self-sealing geothermal field: Bull. Volcanologique, v. 30, p. 271–273.

Fournier, R. O., and Rowe, J. J., 1966, Estimation of underground temperatures from the silica content of water from hot springs and wet-steam wells: Am. Jour. Sci., v. 264, p. 685–597.

Fournier, R. O., and Truesdell, A. H., 1970, Chemical indicators of subsurface temperature applied to hot spring waters of Yellowstone

National Park, Wyoming, U.S.A., *in* United Nations Symposium on Development and Utilization of Geothermal Resources, Pisa 1970, v. 2, pt. 1: Geothermics, Spec. Issue 2, p. 529-535.

——1973, An empirical Na-K-Ca geothermometer for natural waters: Geochim. et Cosmochim Acta., v. 37, p. 1255–1276.

——1974, Geochemical indicators of subsurface temperature–Part 2, Estimation of temperature and fraction of hot water mixed with cold water: U.S. Geol.Survey Jour. Research, v. 2, no. 3, p. 263–270.

Hemley, J. J., 1967, Aqueous Na/K ratios in the system K_2O-Na_2O-Al_2O_3 SiO_2-H_2O [abs.]: Geol. Soc. America, New Orleans 1967, Ann. Mtgs., Programs with Abstracts, p. 94–95.

Holland, H. D., 1967, Gangue minerals in hydrothermal deposits, *in* Barnes, H. L., ed., Geochemistry of hydrothermal ore deposits, New York, Holt, Rinehart, and Winston, p. 382–436.

Mahon, W. A. J., 1966, Silica in hot water discharged from drill holes at Wairakei, New Zealand: New Zealand Jour. Sci., v. 9, p. 135–144.

Orville, P. M., 1963, Alkali ion exchange between vapor and feldspar phases: Am. Jour. Sci., v. 261, p. 201–237.

Tonani, F., 1970, Geochemical methods of exploration for geothermal energy, *in* United Nations Symposium on Development and Utilization of Geothermal Resources, Pisa 1970, v. 2, pt. 1: Geothermics, Spec. Issue 2, p. 492–515.

White, D. E., 1965, Saline waters of sedimentary rocks, *in* Fluids in subsurface environments–A symposium: Am. Assoc. Petroleum Geologists Mem. 4, p. 342–366.

——1974, Geochemistry applied to the discovery, evaluation, and exploitation of geothermal energy resources, *in* United Nations Symposium on Development and Utilization of Geothermal Resources, Pisa 1970: Geothermics, Spec. Issue 2. (In press.)

White, D. E., Barnes, Ivan, and O'Neil, James, 1973 Thermal and mineral waters of nonmeteoric origin, California Coast Ranges: Geol. Soc. America Bull., v. 84, no. 2, p. 547–560.

White, D. E., Muffler, L. J. P., and Truesdell, A. H., 1971, Vapor-dominated hydrothermal systems compared with hot-water systems: Econ. Geology, v. 66, p. 75–97.

Jour. Research U.S. Geol. Survey
Vol. 2, No. 3, May-June 1974, p. 263–270

GEOCHEMICAL INDICATORS OF SUBSURFACE TEMPERATURE—PART 2, ESTIMATION OF TEMPERATURE AND FRACTION OF HOT WATER MIXED WITH COLD WATER

By R. O. FOURNIER and A. H. TRUESDELL, Menlo Park, Calif.

Abstract.—The water in many warm springs with large rates of flow consists of mixtures of hot water that has come from depth and of shallow cold water. Under favorable conditions the original temperature of the hot water and the fraction of the cold water in the mixture can be estimated by using the measured temperature and silica content of the warm spring water and the temperature and silica content of nonthermal water in the region. The method has been applied with apparent success at Yellowstone National Park.

Warm (<80°C) springs with large rates of discharge occur in many places throughout the world. Some of these warm springs originate through deep circulation of meteoric water that is heated mainly by conductive heat transfer from the rock to the water. Other warm springs originate through mixing of high-temperature (>100°C) water with cold meteoric water.

As discussed in part 1 by Fournier, White, and Truesdell (companion article on p. 259 of this issue), water discharged from springs with rates of flow greater than about 100–200 l/min can be assumed to have lost little heat to the wallrock per unit mass of water during the upward movement. For nonboiling springs, if mixing has not occurred, the temperature of the spring is close to the highest temperature attained by that water. If mixing has occurred, however, water of very high temperature may be present at comparatively shallow depth. These possible differences in subsurface conditions may be differentiated in many places on chemical grounds. Specifically, the chemical composition of a water heated only to its eventual discharge temperature is likely to reflect water-rock equilibration at about that temperature, whereas the composition of a mixed water is likely to indicate marked nonequilibration between the water and rock at the spring temperature.

If the composition suggests that the warm spring water is produced by the mixing of cold meteoric water with high-temperature water, it is possible under certain conditions to calculate the temperature and fraction of the hot-water component.

TEST FOR A MIXED WATER

If several springs are present, variations in the temperature or in content of chloride, boron, or other relatively nonreactive constituents may indicate mixed water. Such water is particularly indicated where there is a regular variation in water temperature and chlorinity.

Another approach is to test whether or not the composition of a large flowing spring indicates chemical equilibration at a temperature within about ±25°C of the spring water. Marked nonequilibration suggests a mixed water.

The Na-K-Ca geothermometer (Fournier and Truesdell, 1973) appears to work well for testing chemical equilibration. Water composition, in molality, is related to temperature by the empirically derived equation

$$\log (\mathrm{Na/K}) + \beta \log (\sqrt{\mathrm{Ca/Na}}) = \frac{1647}{273 + t_{°\mathrm{C}}} - 2.24 \qquad (1)$$

in which β=1/3 for water equilibrated above 100°C, and β=4/3 for water equilibrated below 100°C. First, test to see if β=4/3 yields a temperature below 100°C; if it does not, use β=1/3 to estimate the equilibration temperature.

A more sophisticated approach is to perform a complete chemical analysis of the water and then use a computer and appropriate program (Kharaka and Barnes, 1974; Truesdell and Jones, 1973) to test various possible equilibria at the temperature of the spring and selected higher temperatures.

The silica geothermometer (Fournier and Rowe, 1966) has been the most reliable single chemical indicator of reservoir temperature in spring systems that are high in silica and are characterized by sinter deposits and boiling waters. There is an ambiguity, however, in using the silica content of a warm spring to test for water-rock equilibration at the spring temperature: a high silica content in the spring water may be due to either solution of quartz at a much higher temperature (with or without subsequent mixing of hot and cold waters) or solution of cristobalite or amorphous silica at the spring temperature. Therefore, the silica geothermometer (Fournier and Rowe, 1966) should be used with great caution to test for water-rock equilibration at the spring temperature. Although supersaturated silica solutions may occur in nature over a wide range in temperatures, they are not likely to persist for long

periods of time above about 150°C (Fournier, 1973). This is critical for the models that we present in this paper.

MIXING MODELS

Two mixing models that allow calculation of the temperature and fraction of the hot water component are shown schematically in figure 1. In model 1, figure 1*A*, hot water ascends from depth along a permeable channel, possibly a fault or joint. Depending on the initial temperature, the water may boil (cool adiabatically) as it rises. In this event, the water and newly forming steam rise together. At some point, M in figure 1*A*, the hot water encounters cold water from a permeable stratum. At the depth of mixing the weight of a column of cold water extending up to the surface is greater than the weight of the warm mixed water. Thus, the pressure relations are such that cold water enters the hot-water channel and the mixture flows to the surface and is discharged as a warm spring. Depending on the proportion of hot to cold water and the initial enthalpies of each, the spring may have a temperature ranging from very low to boiling.

In model 2, figure 1*B* we assume that boiling occurs in the rising hot water and that some or all of the resulting steam escapes from that water (point S) before the hot water mixes with cold water. We show a fumarole where the steam emerges and a warm spring where the hot water mixed with cold water emerges. Alternatively, the separated steam might possibly condense and combine with shallow ground water and give rise to other warm springs that are not amenable to the methods suggested in this report.

If the channel above S is filled with steam, boiling at S will be at atmospheric pressure, provided there are few constrictions in the channel or impediments to the escape of steam (no throttling occurs). If throttling of the steam occurs, or if the channel is partly or completely filled with water, boiling and escape of steam at S will be at greater than atmospheric pressure.

In both models of figure 1 the calculations depend upon ones knowing the temperatures and silica content of the cold water before mixing[1] and those of the warm spring water after mixing. In addition, it must be assumed that the initial silica content of the deep hot water is controlled by the solubility of quartz and that no further solution or deposition of silica occurs before or after mixing. Numerous observations have shown that natural water deep in hot-spring systems generally is just saturated with quartz (Mahon, 1966; Fournier and Truesdell, 1970; Ellis, 1970; Fournier, 1973). Furthermore,

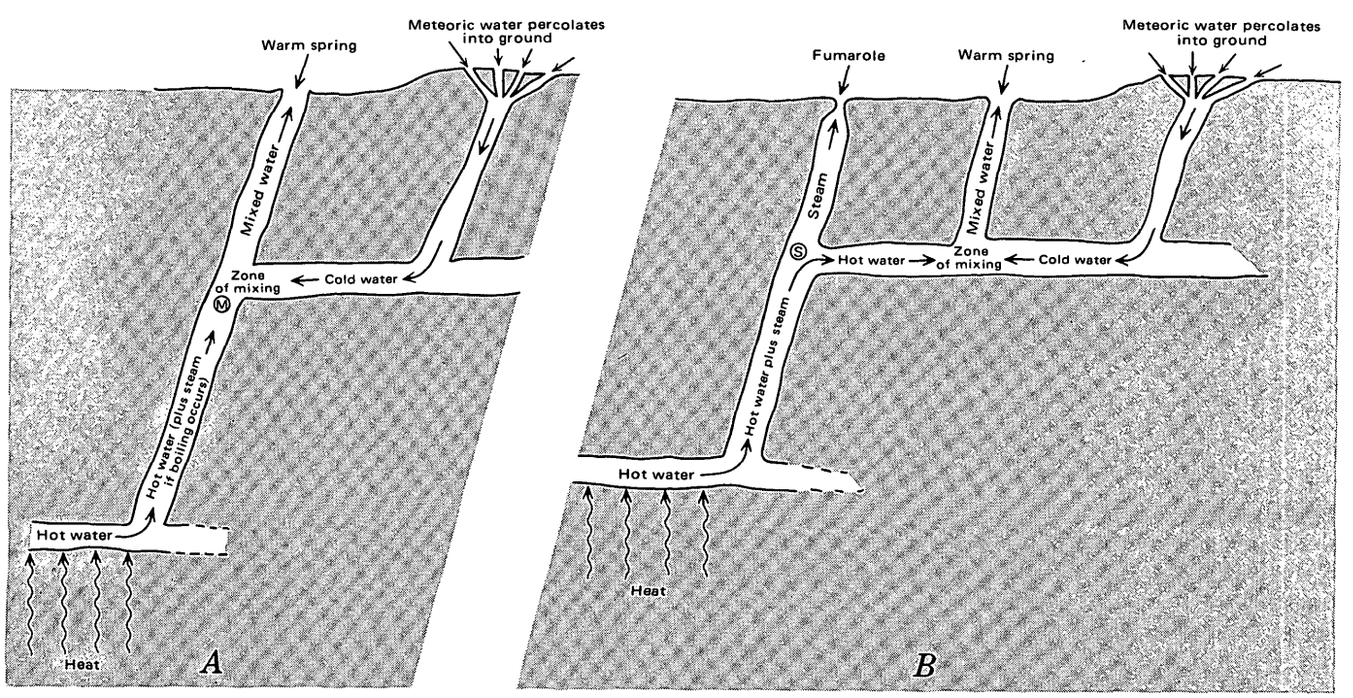

Figure 1.—Schematic model (*A*) for obtaining a mixed-water warm spring in which both the enthalpy and silica content of the hot-water content are the same as in the original deep water (model 1) and schematic model (*B*) in which the hot-water component has lost steam before mixing with cold water (model 2). (See text for discussion.)

[1] If the average temperature and silica content of nonthermal ground water in the region are not known, we suggest estimating the mean annual temperature and using 25 mg/l of silica as a first approximation.

our observations in Yellowstone National Park (Fournier and Truesdell, 1970) and elsewhere (White, 1974) suggest that ascending boiling water generally does not dissolve or precipitate silica if the rate of upflow is fast.

In the calculations that follow, model 1 gives a probable maximum subsurface temperature attained by the hot-water component, and model 2, a probable minimum subsurface temperature. On the basis of the total chemical and physical character of the warm spring, its relation to other hot springs and fumaroles, and its geologic environment, it may be possible to choose the temperature that is more likely to be correct. Even where this is not possible, information on the range of possible subsurface temperatures will be of great interest.

CALCULATIONS

Model 1

In this model the enthalpy of the hot water plus steam that heats the cold water is the same as the initial enthalpy of the deep hot water. Two equations can be written to solve for the two unknowns—the temperature of the hot water and the proportions of the hot and cold water—because the silica content and temperature of the warm spring are different functions of the original temperature of the hot-water component. The first equation relates the heat contents or enthalpies of the hot water, H_{hot}; cold water, H_{cold}; and spring water, H_{spg}; and the fractions of cold water, X, and of hot water, $1-X$, as follows:

$$(H_{cold})(X) + (H_{hot})(1-X) = H_{spg}. \quad (2)$$

Below 100°C the enthalpy of liquid water coexisting with steam (saturated water) in calories per gram is essentially equivalent in magnitude to the temperature of the water in degrees Celsius. Above 100°C the relation of temperature and enthalpy of saturated water can be found in steam tables (Keenan and Keyes, 1936; Keenan and others, 1969). Selected values are given in table 1.

Table 1.—*Enthalpies of liquid water and quartz solubilities at selected temperatures and pressures appropriate for coexistent steam and liquid water*

[Enthalpies from Keenan and others (1969). Quartz solubilities at and below 225°C from Morey and others (1962); above 225°C from unpublished data of R. O. Fournier]

Temperature (°C)	Enthalpy (cal/g)	Silica (mg/l)	Temperature (°C)	Enthalpy (cal/g)	Silica (mg/l)
50	50.0	13.5	200	203.6	265
75	75.0	26.6	225	230.9	365
100	100.1	48	250	259.2	486
125	125.4	80	275	289.0	614
150	151.0	125	300	321.0	692
175	177.0	185			

In a similar manner the second equation relates the silica contents of hot water, Si_{hot}; cold water, Si_{cold}; and spring water, Si_{spg}:

$$(Si_{cold})(X) + (Si_{hot})(1-X) = Si_{spg}. \quad (3)$$

The relation of dissolved silica to the temperature of the aquifer supplying the hot-water component is given by the solubility of quartz at the vapor pressure of the solution (Morey and others, 1962; Fournier, unpub. data, 1974). Selected values are given in table 1.

We use a computer program (Truesdell and others, 1973) to solve equations 2 and 3 and obtain the temperature of the hot water and the fraction of cold water in the mixture, using measurements of the spring temperature and silica content, measurements or estimates of the lowest temperature and average silica content of cold springs in the area, and tabular values of heat content of liquid water and quartz solubilities. Alternatively, a graphical solution can be obtained as follows:

1. Assume a series of values of enthalpy of hot water for the temperatures listed in table 1 and calculate X_t for each, as follows:

$$X_t = \frac{\text{(Enthalpy of hot water)} - \text{(Temperature of warm spring)}}{\text{(Enthalpy of hot water)} - \text{(Temperature of cold spring)}}.$$

2. Plot the calculated values of X_t in relation to the temperatures from which the assumed hot-water enthalpy values were derived (see fig. 2, curve A).

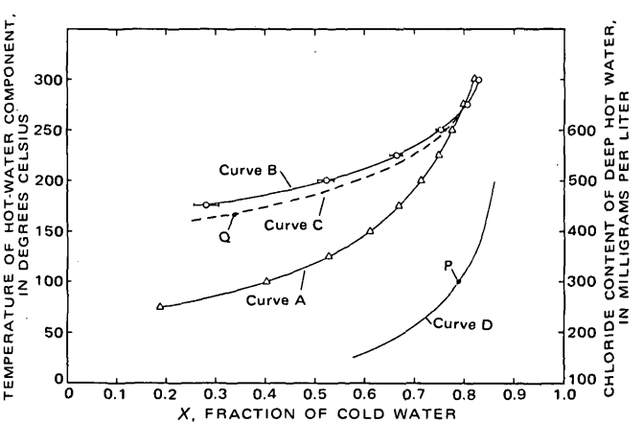

Figure 2.—Fraction of cold water relative to temperature and chloride content of hot-water component in Terrace Spring. Triangles, X_t values listed in table 2; circles, X_{Si} values. The horizontal bars show the possible error due to uncertainty in the silica analysis of the spring water. Points P and Q discussed in text. Curve A, Fraction of cold water based on model 1 enthalpy considerations. Curve B, Fraction of cold water based on model 1 silica considerations. Curve C, Fraction of cold water based on model 2 silica considerations. Curve D, Required chloride contents of deep water.

3. Assume a series of silica contents of hot water appropriate for the temperature listed in table 1 and evaluate X_{Si} for each silica content, as follows:

$$X_{Si} = \frac{\text{(Silica in hot water)} - \text{(Silica in warm spring)}}{\text{(Silica in hot water)} - \text{(Silica in cold spring)}}.$$

4. On the graph previously used, plot the calculated values of X_{Si} in relation to the temperatures for which the silica contents were obtained (see fig. 2, curve B).
5. The point of intersection gives the estimated temperature of the hot-water component and the fraction of cold water.

The two curves possibly may not intersect (fig. 3) or they may intersect at an unreasonably high temperature. These situations would arise if the ascending hot water lost steam or heat before mixing with the cold water (model 2) or if the mixed water dissolved additional silica owing to contact with amorphous silica or rock containing glass. Therefore, we recommend that the mixing model described above be used with extreme caution for warm spring water that has silica contents about equal to the solubility of amorphous silica at the temperature of the spring. For temperatures below 200°C, the approximate solubility of amorphous silica can be calculated from the equation

$$-\log C = \frac{731}{T} - 4.52 \qquad (6)$$

where C is silica solubility in milligrams per liter and T is absolute temperature.

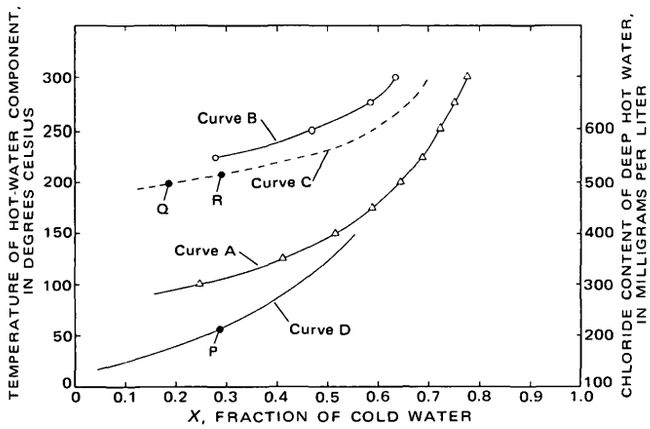

Figure 3.–Fraction of cold water relative to temperature and chloride content of hot-water component in Interchange Spring. Points P, Q, and R discussed in text. See figure 2 for explanation of symbols and curves.

The actual temperature and silica content of the "cold" component at the point of mixing can seldom if ever be known with certainty. If either the temperature or silica content of the cold water were higher than the assumed value, the resulting estimated temperature of the hot-water component would be too high.

Model 2

The enthalpy of the hot water in the zone of mixing is less than the enthalpy of the hot water at depth owing to escape of steam during ascent. The silica content of the hot-water component, however, is fixed by quartz solubility at depth and subsequent enrichment in the liquid water fraction as steam separates. At the point where steam escapes from the ascending hot water and steam mixture, S in figure 1*B*, the residual silica concentration in the hot water increases and is given by the equation

$$\text{Residual silica} = \frac{\text{Original silica}}{1-y} \qquad (7)$$

where y is the fraction of steam formed during movement of water from depth to S.

If one assumes a temperature, t_s, at which steam escapes, it is possible to calculate the residual silica for that condition and, using that information, estimate the original hot-water temperature before steam separates. In general, we set t_s equal to the boiling temperature imposed by local atmospheric conditions. This requires that escape of steam at point S of figure 1*B* occurs at atmospheric pressure, and our calculation yields a minimum probable temperature for the hot-water aquifer. The calculation is carried out as follows:

1. Use the atmospheric boiling temperature for the value of H_{hot} in equation 2 and calculate the corresponding value of X.
2. Use that value of X in equation 3 to estimate the residual silica content of the hot water at t_s.
3. Use the calculated residual silica content and curve A of Fournier and Rowe (1966, fig. 5) to estimate the original subsurface temperature before separation of steam. Curve A of Fournier and Rowe is roughly approximated by the equation

$$-\log C = \frac{1522}{t°C + 273} - 5.75. \qquad (8)$$

If superheated steam emerges from nearby fumaroles or if there are other reasons for believing that steam escapes at greater than atmospheric pressure, an alternate procedure should be used:

1. Assume a value of t_s appropriate for the pressure at which steam is thought to escape at point S of figure 1*B*.
2. Use steam tables (or table 1) to determine the heat content of liquid water in calories per gram at t_s and substitute

that value in equation 2 to estimate a corresponding value of X.

3. Use that value of X in equation 3 to estimate the residual silica content of the hot water at t_s.
4. Estimate the silica content, C, that would have been present in the hot-water component if steam had escaped at atmospheric pressure using the relation

$$C = \frac{\text{Residual silica}}{1 - \frac{x}{1-y}} \quad (9)$$

where X is the fraction of steam that would be formed in going from t_s to the boiling temperature at atmospheric pressure (see fig. 4) and y is the fraction of steam formed in going from the original temperature to t_s. Both y and C are unknown in equation 8. However, the value of y will generally range from 0 to about 0.3, and as a first approximation it can be set equal to 0.1.

5. Use the value of C and Curve A of Fournier and Rowe (1966, fig. 5) or equation 8 to estimate the original subsurface temperature before separation of steam.

A more precise estimate is possible if an iterative process is used in which the value of y is adjusted to reflect successive estimates of the original temperature. In general, we do not believe that the overall accuracy of the method warrants this additional effort.

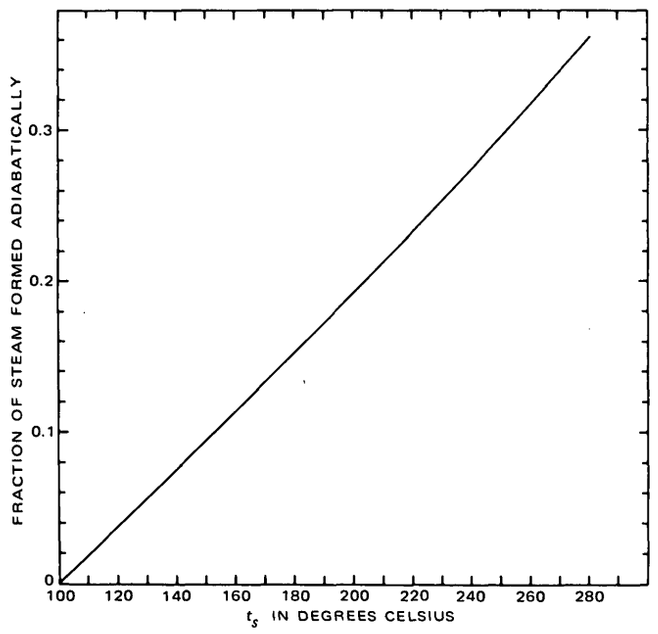

Figure 4.—Fraction of steam that would form by adiabatic cooling from t_s to 100°C.

EXAMPLES OF APPLICATION

These mixing models proposed have been applied to a few large-flowing warm springs in Yellowstone National Park. The results are geologically reasonable but have been substantiated by shallow drilling in the proximity of only one (Interchange Spring) of the springs in question.

The average silica content of the nonthermal ground water in the park was found to be 25±2 mg/l and the temperature of the coldest spring was 5°C, in good agreement with the mean annual temperature of 4°C.

Terrace Spring near Madison Junction flows at about 5,500 l/min, the water temperature is 62°C, and silica content is 140 mg/l (Allen and Day, 1935, p. 353–354). The sodium, potassium, and calcium contents of the water yield an estimated aquifer temperature of 200°C, using the method of Fournier and Truesdell (1973). As this temperature is far greater than the spring temperature of 62°C, the spring is assumed to be a mixed-water type.

Calculated fractions of cold water, assuming various temperatures of hot water and using model 1 and equations 4 and 5, are listed in table 2, column 1, and are plotted in figure 2, curves A and B. The curves intersect at 265°C and a cold water fraction of 0.79. This is a very high estimated aquifer temperature and can be thought of as the maximum probable temperature of the hot-water component.

Although there are no nearby fumaroles, boiling pools, or other physical evidence that points to model 2 as a reasonable possibility, we have applied that model to Terrace Spring in order to establish a lower limit to the probable maximum subsurface temperature at that locality.

Curve C of figure 2 was generated by assuming various values of t_s and using equations 7 and 9 and other relations as discussed in the section on calculations. If steam escaped at atmospheric pressure from an ascending boiling water, the hot-water component would have been at about 92°C at the time of mixing with cold water, and the original temperature of that hot water would have been 165°C (point Q, fig. 2). This is the minimum probable temperature of the aquifer supplying the hot-water component. If higher pressures are assumed for escape of steam, larger fractions of cold water are required and higher estimated aquifer temperatures result, as shown by curve C, figure 2. Again, the probable upper temperature limit is about 265°C where curves A, B, and C intersect at a common point.

For Terrace Spring the aquifer supplying the hot water is probably closer to 265° than 165°C. The spring is located between Lower Geyser Basin (9 km to the south) and Norris Geyser Basin (14.5 km to the northeast) at a relatively low topographic position along the bounding fault of a large caldera (Keefer, 1971; Christiansen and Blank, 1972). Recent drilling by the U.S. Geological Survey has shown that subsurface temperatures beneath parts of Lower Geyser Basin exceed 205°C; those beneath Norris Geyser Basin exceed 240°C (White and others, 1968). Silica and Na-K-Ca geo-

Table 2.–*Values of* X_t *and* X_{Si} *at different assumed temperatures of the hot-water component for warm springs in Yellowstone National Park*
[See text for details]

Temperature (assumed) of hot water (°C)	1		2		3		4	
	X_t (t=62°C)	X_{Si} (SiO_2=140 mg/l)	X_t (t=49°C)	X_{Si} (SiO_2=100 mg/l)	X_t (t=61°C)	X_{Si} (SiO_2=122 mg/l)	X_t (t=76°C)	X_{Si} (SiO_2=270 mg/l)
50	.....	.....	0.022	.....	.....	.....	.....	.....
75	0.186	.....	.371	.....	0.200	.....	.....	.....
100	.401	.....	.537	.....	.410	.....	0.253	.....
125	.527	.....	.635	.....	.534	.....	.410	.....
150	.610	.....	.699	0.250	.616	0.030	.514	.....
175	.669	0.280	.744	.531	.674	.394	.587	.....
200	.713	.521	.778	.688	.718	.596	.642	.....
225	.748	.662	.805	.779	.792	.715	.686	0.279
250	.776	.751	.827	.837	.780	.790	.721	.469
275	.799	.805	.845	.873	.803	.835	.750	.584
300	.820	.828	.861	.888	.823	.855	.775	.633

1. Terrace Spring near Madison Junction. Flow approximately 5,550 l/min. Data from Allen and Day (1935).
2. Spring 1.4 km N. of Biscuite Basin, about 8 m E. of road. Flow about 190 l/min.
3. Spring 2.25 km N. of Biscuite Basin, about 60 m E. of road. Flow about 100 l/min.
4. Interchange Spring, Black Sand Basin. Flow about 2,300 l/min.

thermometers applied to boiling hot-spring water at Norris suggest subsurface temperatures of 250° to 270°C.

The chloride content of Terrace Spring, 64 mg/l is consistent with the higher aquifer temperature and correspondingly large calculated fraction of cold water. Given the chloride concentration in the spring and the average chloride in nonthermal water in the region (<1 mg/l), the chloride content of the deep hot water can be calculated, assuming any given proportion of hot and cold water. Curve D, figure 2, shows the results of that calculation. For a cold-water fraction of 0.79, the chloride content of the hot-water fraction would be about 300 mg/l (point P, fig. 2). This is close to the chloride content of thermal water (before steam loss) found at Lower Geyser Basin.

The second example is one in which mixing model 1 fails, but model 2 gives excellent results. Interchange Spring in Black Sand Basin came into being as a result of an excavation for a highway interchange for diverting traffic around the Old Faithful area. The spring had a temperature of 76°C, a silica content of 270 mg/l, and a flow rate of about 2,000 l/min. The Na-K-Ca content suggests a temperature of 205°C. The calculated fractions of cold water at given temperatures of the hot-water component are listed in table 2, column 4, and plotted in figure 3.

The most notable feature of figure 3 is that curve A, based on enthalpy considerations, and curve B, based on model 1 silica considerations, do not intersect. Evidently either steam escaped from the hot-water component before mixing or the warm spring water dissolved extra silica after mixing occurred. The warm water may be picking up extra silica, for it emerges from sands and gravels composed mostly of fresh obsidian. The obsidian glass could dissolve and raise aqueous silica to saturation with respect to amorphous silica. At 76°C the solubility of amorphous silica is 266 mg/l, which is within the analytical error of the 270 mg/l silica found in the spring water.

We favor the first alternative because the large rate of flow makes equilibration with amorphous silica unlikely and because model 2 gives results in close agreement with what is known about subsurface temperatures near Interchange Spring.

The variation of original hot water temperature relative to the fraction of cold water in the warm spring, curve C, figure 3, is based on model 2 silica considerations. If steam escaped at atmospheric pressure before mixing of hot and cold water, the remaining hot water would have been at 92°C (boiling temperature at the altitude of the spring) and its original temperature would have been about 200°C (point Q, fig. 3).

About the same temperature is estimated from chloride considerations. The chloride content of Interchange Spring is 224 mg/l, the calculated chloride contents of the hot-water component, assuming various fractions of mixed cold water, are shown by curve D, figure 3. The highest concentration of chloride found in discharging boiling springs and geysers in Black Sand Basin was 315 mg/l. Presumably this is the residual chloride concentration attained after maximum separation of steam owing to adiabatic cooling of the ascending water. Therefore, the maximum chloride content of the hot-water component in Interchange Spring is likely to have been 315 mg/l; the corresponding maximum fraction of cold water, 0.285 (point P, fig. 3). This requires that the hot-water component have a temperature of 110°C or less at the time of mixing. For a cold water fraction of 0.285, curve C of figure 3 shows an original hot-water temperature of about 208°C (point R).

The silica contents of boiling springs and geysers in the vicinity of Interchange Spring indicate an aquifer temperature of 190° to 205°C. In addition, two shallow holes drilled near-

by indicate subsurface temperatures exceeding 170° to 180°C. Both holes were terminated before a maximum or leveling-off temperature was attained. One hole is about 900 m to the southeast and had a bottom-hole temperature of 180°C (Fenner, 1936). The other is about 600 m to the west and had a bottom-hole temperature of 170°C (White and others, 1968; Honda and Muffler, 1970).

Apparently the hydrologic system supplying water to Interchange Spring is very similar to model 2. We suggest that the hot-water fraction of the mixed water in Interchange Spring comes from an aquifer at 200° to 208°C. That water cools adiabatically, forming steam as it rises toward the surface. At a shallow level, but before mixing with cold water occurs, the high-enthalpy steam fraction escapes from the remaining lower enthalpy liquid water. This low-enthalpy water at 92° to 110°C then encounters cold ground water and a mixed water at 76°C results. The separated steam fraction probably emerges 350 m northwest of Interchange Spring at the Pine Springs group, where violently boiling springs occur with little or no discharge.

Ideally, large-flow warm springs in a given locality with different temperatures and different compositions should give the same estimated hot-water temperature. Such is found for two large-flow unnamed springs located between Biscuit Basin and Midway Geyer Basin in Yellowstone National Park. The springs have temperatures of 49° and 61°C and silica contents of 100 and 122 mg/l respectively, (table 2, cols. 2 and 3). Applying model 1, the intersection of curves A and B, figure 5, indicates a cold-water fraction of 0.82 for the 49°C spring and 243°C as the maximum probable temperature of the hot-water component. The intersection of curves C and D, figure 5, gives exactly the same temperature, 243°C, for the high-temperature component of the 61°C water. As expected, the fraction of cold water, 0.77, is less in the 61°C water than in the 49°C water. Applying model 2, and assuming t_s = 100°C, a minimum probable temperature of 166°C is obtained for the original temperature of the hot-water component in each spring, which indicates clearly that two waters are mixing in different proportions. Unfortunately, additional data is insufficient to indicate whether the higher or lower estimated temperature of hot-water component is more nearly correct.

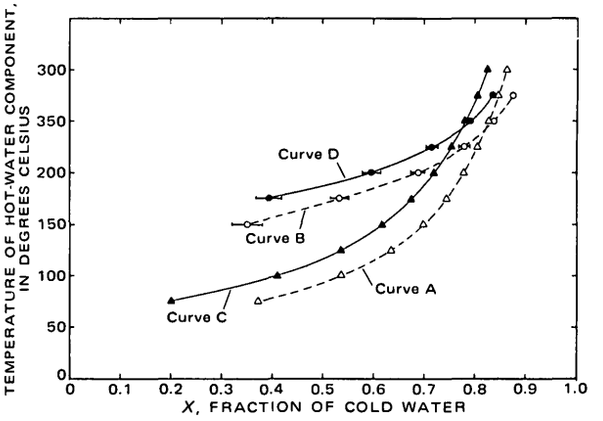

Figure 5.—Fraction of cold water relative to temperature of hot-water component in two springs located between Biscuit and Midway Basins. See figure 2 for explanation of curves and symbols; open symbols refer to the 49°C water and solid symbols to the 61°C water.

CONCLUSIONS

The water in both boiling and nonboiling springs may be a mixture of hot water coming from depth and of cold, near-surface meteoric water. Under favorable conditions nonboiling thermal springs with large rates of flow may yield information about the temperature or range in probable temperatures of the hot-water component and the fraction of cold water in the mixture.

The assumptions necessary for using the mixing models described in this paper probably will not be met in most places. However, even a 10-percent success rate would make them valuable adjuncts of other methods for evaluating the geothermal potential of an area.

REFERENCES CITED

Allen, E. T., and Day, A. L., 1935, Hot springs of the Yellowstone National Park: Carnegie Inst. Washington Pub. 466, 525 p.

Christiansen, R. L., and Blank, H. R., Jr., 1972, Volcanic stratigraphy of the Quaternary rhyolite plateau in Yellowstone National Park: U.S. Geol. Survey Prof. Paper 729-B, 18 p.

Ellis, A. J., 1970, Quantitative interpretation of chemical characteristics of hydrothermal systems, *in* United Nations Symposium on the Development and Utilization of Geothermal Resources, Pisa 1970, v. 2, pt. 1: Geothermics, Spec. Issue 2, p. 516–528.

Fenner, C. N., 1936, Bore-hole investigations in Yellowstone Park: Jour. Geology, v. 44, p. 225–315.

Fournier, R. O., 1973, Silica in thermal waters: Laboratory and field investigations, *in* Proceedings of International Symposium on Hydrogeochemistry and Biogeochemistry, Japan 1970, Volume I, Hydrochemistry: Washington, D.C., J. W. Clark, p. 122–139.

Fournier, R. O., and Rowe, J. J., 1966, Estimation of underground temperatures from the silica content of water from hot springs and wet-steam wells: Am. Jour. Sci., v. 264, p. 685–697.

Fournier, R. O., and Truesdell, A. H., 1970, Chemical indicators of subsurface temperature applied to hot spring waters of Yellowstone National Park, Wyoming U.S.A., *in* United Nations Symposium on Development and Utilization of Geothermal Resources, Pisa 1970, Proc., v. 2, pt. 1: Geothermics, Spec. Issue 2, p. 529–535.

Fournier, R. O., and Truesdell, A. H., 1973, An empirical Na-K-Ca geothermometer for natural waters: Geochim. et Cosmochim. Acta, v. 37, p. 1255–1275.

Fournier, R. O., White, D. E., and Truesdell, A. H., 1974, Geochemical indicators of subsurface temperature—Part 1, Basic assumptions: U.S. Geol. Survey Jour. Research, v. 2, no. 3, p. 259–262.

Honda, S., and Muffler, L. J. P., 1970, Hydrothermal alteration in core from research drill hole Y-1, Upper Geyser Basin, Yellowstone National Park, Wyoming: Am. Mineralogist, v. 55, p. 1714–1737.

Keefer, W. R., 1971, The geologic story of Yellowstone National Park: U.S. Geol. Survey Bull. 1347, 92 p., 1 plate.

Keenan, J. H., and Keyes, F. G., 1936, Thermodynamic properties of steam: New York, John Wiley, 89 p.

Keenan, J. H., Keyes, F. G., and Moore, J. G., 1969, Steam tables. Thermodynamic properties of water, including vapour, liquid, and solid phases: New York, John Wiley, 162 p.

Kharaka, Y. K., and Barnes, Ivan, 1974, SOLMNEQ: Solution mineral equilibrium computations: U.S. Dept. Commerce, Natl. Tech. Inf. Service, PB-215 899, 82 p.

Mahon, W. A. J., 1966, Silica in hot water discharged from drillholes at Wairakei, New Zealand: New Zealand Jour. Sci, v. 9, p. 135–144.

Morey, G. W., Fournier, R. O., and Rowe, J. J., 1962, The solubility of quartz in water in the temperature interval from 29° to 300°C: Geochim. et Cosmochim. Acta, v. 26, p. 1029–1043.

Truesdell, A. H., Fournier, R. O., and Thompson, J. M., 1973, Mixture, a computer program for the calculation of hot water temperature and mixing fractions of large volume warm springs of mixed water origin: U.S. Dept. Commerce, Natl. Tech. Inf. Service, PB-220 732, 12 p.

Truesdell, A. H., and Jones, B. F., 1973, WATEQ, a computer program for calculating chemical equilibria in natural waters: U.S. Dept. Commerce, Natl. Tech. Inf. Service, PB-220 464, 77 p.

White, D. E., Muffler, L. J. P., Truesdell, A. H., and Fournier, R. O., 1968, Preliminary results of research drilling in Yellowstone thermal areas [abs.]: Am. Geophys. Union Trans., v. 49, p. 358.

White, D. E., 1974, Geochemistry applied to the discovery, evaluation, and exploitation of geothermal energy resources, *in* United Nations Symposium on Development and Utilization of Geothermal Resources, Pisa 1970, v. 1, pt. 2: Geothermics, Spec. Issue 2 (In press.)

Jour. Research U.S. Geol. Survey
Vol. 2, No. 3, May-June 1974, p. 271—278

THE CALCULATION OF AQUIFER CHEMISTRY IN HOT-WATER GEOTHERMAL SYSTEMS

By ALFRED H. TRUESDELL and WENDY SINGERS,
Menlo Park, Calif., Chemistry Division, D.S.I.R., New Zealand

Abstract.—The temperature and chemical conditions (pH, gas pressure, and ion activities) in a geothermal aquifer supplying a producing bore can be calculated from the enthalpy of the total fluid (liquid + vapor) produced and chemical analyses of water and steam separated and collected at known pressures. Alternatively, if a single water phase exists in the aquifer, the complete analysis (including gases) of a sample collected from the aquifer by a downhole sampler is sufficient to determine the aquifer chemistry without a measured value of the enthalpy. The assumptions made are that the fluid is produced from a single aquifer and is homogeneous in enthalpy and chemical composition. These calculations of aquifer chemistry involving large amounts of ancillary information and many iterations require computer methods. A computer program in PL-1 to perform these calculations is available from the National Technical Information Service as document PB-219 376.

In active hydrothermal systems that have been drilled, mineral alteration and deposition can be related to observed temperatures and fluid compositions. Chemical analyses of water and steam produced from many types of geothermal systems are now available. However, analyses of fluids collected at the surface do not describe the chemistry of fluids as they occur at depth. The chemical differences between the fluids at the surface and in the deep aquifer are due to the decrease of pressure and temperature during production. Adiabatic expansion during passage up the drill hole may result in steam separation, cooling, and an increase in the concentration of the solutes in the water phase. Loss of dissolved CO_2 and H_2S from the water to the vapor increases the pH value of the water. The increase in pH and solute concentration and the decrease in temperature may cause the water to become supersaturated with calcite or silica minerals and may result in scaling of well casings. The continued production of a geothermal system is likely to decrease the reservoir pressures enough to form steam in the aquifer (Mahon, 1970). The resulting decrease in gas pressures, increase in aquifer pH, and temperature lowering may cause increased calcite deposition in the casing and possibly in the aquifer. Potential mineral deposition may be calculated if the chemistry of aquifer fluids is known.

Underground water temperatures may be calculated from known mineral solubility or ion exchange reactions that control water compositions; for example, quartz solubility (Fournier and Rowe, 1966; Mahon, 1966), Na:K ratios (White, 1965; Ellis, 1970), or Na:K:Ca ratios (Fournier and Truesdell, 1973). The assumptions underlying these calculations have been discussed by White (1970).

Thus, for practical reasons as well as to increase our knowledge of natural systems, it is of interest to calculate the chemical properties of geothermal fluids before they are changed during production. This is the purpose of the computer program described here.

ACKNOWLEDGMENTS

The computer program is a further development of the method of Ellis (1967, 1970) and was partly written in the laboratories of the Chemistry Division, Department of Scientific and Industrial Research (D.S.I.R.), New Zealand, while the author was on a training grant from the U.S. Geological Survey. The calculations have been discussed with A. J. Ellis, W. A. J. Mahon, Werner Giggenbach, and R. B. Glover of the D.S.I.R., New Zealand, and Ivan Barnes, L. J. P. Muffler, R. O. Fournier, and D. E. White of the U.S. Geological Survey. The program was initially written in Elliot-Algol.

ASSUMPTIONS

These calculations assume that fluid from a geothermal well (1) is produced from a single aquifer, (2) does not gain or lose significant heat or matter during passage up the well and through surface pipes to sampling points, and (3) maintains chemical equilibrium at each point of steam-water separation.

The first assumption that the fluid is produced from a single aquifer must be judged in each situation. In general, wells in which discharge enthalpy and silica contents indicate the same aquifer temperature are most probably from a single aquifer and existed in that aquifer as a single liquid phase. Two or more aquifers may, however, contribute fluids to a producing bore. This circumstance can be deduced from the drilling log, the ratios of gaseous components in the steam (Glover, 1970), or a comparison of the water composition with that of other wells in the field (Mahon, 1970).

The second assumption is most probably true for the well-studied and long-producing Wairakei, New Zealand, geothermal system in which the composition of produced fluids has been nearly constant over a decade of observation and in

which the mass of scale deposited is negligible (Mahon, 1970; Grindley, 1965, p. 58). Here also the conductive heat flow is small compared with the heat delivered to the surface in the fluid (Dawson and Dickinson, 1970; Grindley, 1965). This assumption is probably true also for many but not all other hot-water geothermal systems.

The assumption of chemical equilibrium is more difficult to justify. It has been observed that, in the aquifer, saturation with quartz is exactly maintained (Mahon, 1970), and most equilibria involving species dissolved in the aquifer water phase should be more rapid than saturation equilibria with a solid phase. However, during passage up the well and through the separator, CO_2 may not maintain an equilibrium distribution between the steam and water, as shown by Glover (1970), who found at Wairakei that the distribution coefficient for CO_2 between vapor and liquid water was about 70 rather than the equilibrium value of 460 (Ellis and Golding, 1963). The calculated total CO_2 based on analyses of the separated steam may be low by 2 percent or less. This would not significantly change the calculated CO_2 pressures or aquifer pH.

The difference between the actual total pressure in the aquifer and the saturated water-vapor pressure at the aquifer temperature is assumed to have a negligible effect on the equilibrium constants. The constants used in the program all refer to saturated water-vapor pressure conditions.

CHEMICAL AND PHYSICAL CHANGES ON PRODUCTION

The calculations performed in the program can be best illustrated by following the chemical and physical changes in the fluid produced from a representative aquifer. Analyses of water and gas samples from well 20 of the Wairakei, New Zealand, geothermal field are used as an example. The changes are discussed in the order that they occur; that is, from inaccessible conditions to the separated water and steam as analyzed. The program works backwards along the line of these changes and reconstructs the inaccessible states.

The calculated conditions prior to entering the bore are given in table 1. Note that the pH of 6.34 is nearly the neutral pH at the temperature 246°C and that virtually all boric and silicic acids and nearly all carbonic acid and hydrogen sulfide are undissociated. A substantial proportion of total sulfate exists as bisulfate ion, fluoride as neutral hydrogen fluoride, and ammonia as ammonium ion. Ion pairs such as NaCl, KCl, $NaSO_4$ and $CaSO_4$ are more stable than at low temperatures (see tables 4 and 5) and are present in moderate amounts. The enthalpy (enthalpy refers to specific enthalpy throughout) of the fluid is slightly less than that of water in equilibrium with steam (table 1), and a gas phase is probably not present.

The aquifer fluid flows toward and into the well along a gradient of decreasing pressure resulting from the lower density of the two-phase steam-water mixture in the well. The decrease in pressure causes steam separation and a decrease in temperature. These processes continue in the well and in the steam-water separator, which was operated at a pressure of 16.3 bars absolute and a temperature of 202°C. With the decrease of pressure and temperature, the fluid separates into 10.1 percent steam with an enthalpy of 667.4 cal/g and 89.9 percent water with an enthalpy of 206.1 cal/g. (1 cal=4.184 abs J.) The total enthalpy remains 252.8 cal/g (0.101×667.4+0.899×206.1) because no significant amount of heat has been lost in the passage up the well. The gases originally dissolved in the water have largely exsolved into the gas phase (experimental distribution coefficients for CO_2 and H_2S, tables 4 and 5, greatly favor the gas phase, particularly near 200°C). From the separator, the steam is collected and analyzed for CO_2 and H_2S. Collection and analysis methods

Table 1.—*Aquifer fluid adjacent to hole 20, Wairakei, New Zealand*
[1 cal = 4.184 abs J]

Temperature	°C	246
Pressure	bars abs	37.6
Enthalpy[1]	cal/g	252.8
pH[2]		6.34
CO_2 partial pressure	bars	0.79
H_2S partial pressure	do	0.0093

Dissolved constituents	*Concentrations in mmol/1,000 g H_2O*
Li^+	1.5
Na^+	38.3
K^+	4.1
Rb^+	.025
Cs^+	.014
Ca^{+2}	.43
Mg^{+2}	.0
F^-	.29
Cl^-	42.9
Br^-	.05
I^-	.002
SO_4^{-2}	.079
H_3BO_3	1.74
$H_2BO_3^-$	.002
$H_2CO_3^\circ + CO_{2aq}$	7.89
HCO_3^-	.35
CO_3^{-2}	.00001
$H_4SiO_4^\circ$	7.85
$H_3SiO_4^-$	.006
$H_2SiO_4^{-2}$	.00001
NH_4^+	.002
NH_{3aq}	.011
H_2S_{aq}	.25
HS^-	.022
HF°	.050
HSO_4^-	.0023
HCl°	.00006
$NaCl^\circ$	1.27
KCl°	.097
$MgSO_4^\circ$	.0
$CaSO_4^\circ$	.025
KSO_4^-	.015
$NaSO_4^-$	.15
$CaCO_3^\circ$	.0002
$MgOH^+$	.0

[1]Saturated-water enthalpy is 254.6 cal/g.
[2]Neutral pH is 5.6 at 246°C.

Table 2.—*Analysis as reported on water and steam from well 20, Wairakei, New Zealand*

Temperature of steam separation	°C.	202
Temperature of water separation	°C.	99 and 202
CO_2 in high pressure steam	mmol/100 mol H_2O	142
H_2S in high pressure steam	mmol/100mol H_2O	4.5
Water pH measured at 20°C		8.0

Dissolved constituents	*Concentrations in water as analyzed at 20° C in mg/kg*	*Dissolved constituents*	*Concentrations in water as analyzed at 20° C in mg/kg*
Li	14.8	Br	5.4
Na	1,260	I	.4
K	228	SO_4	35
Rb	3.0	B	26
Cs	2.5	HCO_3	7.7
Ca	25	CO_3	0
Mg	0	SiO_2	650
F	8.8	NH_3	.3
Cl	2,164	H_2S	0

for steam and water are given in Ellis, Mahon, and Ritchie (1968). The gas analysis is given in table 2. The steam and water leave the separator in separate lines, and the water enters a silencer, which discharges to the atmosphere. In the silencer an additonal 20 percent of the original water is flashed to steam, and the remaining water flows out the weir box where it is sampled. The proportions of steam and water at each separation point are calculated from an enthalpy balance with the assumption of constant enthalpy. The water sample in a capped polyethylene bottle is cooled and taken to the laboratory where it is analyzed and the pH is measured. The amount of CO_2 and H_2S dissolved in the water after separation is negligible relative to that which partitions into the gas phase and is not analyzed. The enthalpy of the whole fluid is calculated from measurements of the flows of steam and water under controlled conditions.

The properties of the water as analyzed are given in table 2. The steam and water analyses were made by the staff of the Chemistry Division, D.S.I.R., New Zealand. The water analysis has been recalculated in table 3 to show what species were present in the analyzed solution at 20°C. The water composition differs substantially from the composition of the aquifer fluid. The separation of steam has increased the concentration of mineral constituents that are insoluble in steam (compare Li^+ in the tables). The separation of CO_2 and H_2S into the steam phase has increased the pH by 1.7 units.

The pH increase and temperature decrease have increased the ionization of weak acids, particularly boric acid, silicic acid, and carbonic acid. Ion pairs are generally less stable at lower temperatures (tables 4 and 5) and are thus less in evidence. The most important change is the partition of acid gases (CO_2, H_2S) into the steam with the resultant increase in pH. The aquifer pH, the activity coefficient of H^+, and the potassium contents can be combined to calculate a K:H concentration ratio of $10^{3.83}$ which is similar to the extrapolated, pressure-corrected experimental value of $10^{3.92}$ for water in equilibrium with K-mica, K-feldspar, and quartz near 250°C (Hemley, 1959; R. O. Fournier, oral. commun., 1972; Ellis and McFadden, 1972). This similarity suggests that mineralogical buffer systems are the major control on the pH of this aquifer fluid.

Table 3.—*Calculated composition at 20°C of separated well water from well 20, Wairakei, New Zealand*

[Water pH measured at 20° C is 8.0]

Dissolved constituents	*Concentrations in mmol/1,000 g H_2O*	*Dissolved constituents*	*Concentrations in mmol/1,000 g H_2O*
Li^+	2.1	$H_3SiO_4^-$	.25
Na^+	54.9	$H_2SiO_4^{-2}$	.00009
K^+	5.85	NH_4^+	.017
Rb^+	.035	NH_3°	.0006
Cs^+	.019	H_2S	.0
Ca^{+2}	.62	HS^-	.0
Mg^{+2}	.0	HF°	<.000005
F^-	.47	HSO_4^-	<.000005
Cl^-	61.3	HCl°	<.000005
Br^-	.068	$NaCl^\circ$	.05
I^-	.003	KCl°	.005
SO_4^{-2}	.315	$MgSO_4^\circ$	.0
H_3BO^3	2.26	$CaSO_4^\circ$	.007
$H_2BO_3^-$	.15	KSO_4^-	.005
$H_2CO_3^\circ + CO_{2\,aq}$	.003	$NaSO_4^-$	.04
HCO_3^-	.126	$CaCO_3^\circ$	.0002
CO_3^{-2}	.001	$MgOH^+$	.0
$H_4SiO_4^\circ$	10.6		

DATA REQUIRED

Data necessary to the calculation of aquifer chemistry consist of (1) a chemical analysis of the water separated from the water-steam mixture produced from the well, (2) the content of carbon dioxide and hydrogen sulfide in the separated steam, (3) the pressures of water and steam separation and the atmospheric pressure, and (4) the enthalpy of the whole fluid. The water analysis must include the pH, the temperature of pH measurement, and concentrations of all major dissolved constituents, particularly those that form weak acids or bases at low or high temperatures (HCO_3^-, SO_4^{-2}, BO_2^-, F^-, SiO_2, and so forth. A silica analysis is essential because the temperature of the aquifer is calculated by assuming that the aquifer water phase is saturated with quartz (Mahon, 1966).

The CO_2 and H_2S contents of separated steam must be known because both of these gases dissolve in water to form weak acids and their separation from water raises the pH. The pressure of steam separation is introduced because the separation and collection of steam for gas analysis is most efficiently done at high pressure (to achieve a maximum gas to H_2O ratio) and the collection of water is usually from the silencer at atmospheric pressure (Ellis, Mahon and Ritchie, 1968). If the sample is from a downhole sampler, the water analysis and the CO_2 and H_2S contents are sufficient to

calculate the aquifer chemistry, provided that the fluid sampled was a single liquid phase.

AQUIFER TEMPERATURE CALCULATION

The temperature of an aquifer feeding a geothermal well is measured infrequently, and the measurements when made are uncertain. It has been shown (Fournier and Rowe, 1966; Mahon, 1966, 1970) to be preferable to calculate the aquifer temperature from the silica content of the discharge, assuming equilibrium with quartz in the aquifer, rather than to measure the temperature directly. The original silica content in the deep water must be calculated from analytical data allowing for concentration from steam separation and for the presence of steam in the aquifer. The calculation of the aquifer temperature requires enthalpy values of saturated steam and water at that temperature, and therefore an iteration procedure is necessary.

If the pH of the aquifer fluid is greater than about 7, some silica is present as silicate ions, and the indicated temperature from total silica will be too high. In this instance, concentrations of ionic silica species are calculated and subtracted from total silica concentrations because the silica concentration used for the temperature estimate is specifically $SiO_2(aq)$.

CALCULATION OF THE EFFECTS OF STEAM SEPARATION AND EXCESS ENTHALPY

The enthalpies of the total fluid and of water and steam at the pressure and temperature of the aquifer and at each point of separation are necessary for calculating the proportion of water and steam separated and the degree of concentration of the dissolved mineral constituents in the water and of the dissolved gases in the stream. For these calculations, the program uses thermodynamic data for pure water from Keenan, Keyes, Hill, and Moore (1969). The effect of the low mineral contents (<0.3 wt percent NaCl) of most geothermal waters on the thermodynamic properties of water is negligible (J. L. Hass, written commun., 1971). The content of dissolved gases in steam from most geothermal discharges is low (<2 wt percent), and their effect on the thermodynamic properties has been neglected.

With the assumption of constant total enthalpy, the fraction of water or steam in the fluid can be calculated for any temperature (t) from the equations,

$$\text{fraction water} = \frac{\text{enthalpy of steam at } t - \text{fluid enthalpy}}{\text{enthalpy of vaporization at } t}$$

and

$$\text{fraction steam} = \frac{\text{fluid enthalpy} - \text{enthalpy of water at } t}{\text{enthalpy of vaporization at } t}.$$

If the enthalpy of the fluid is the same or lower than that of water saturated with steam at the aquifer temperature, then no steam is present in the aquifer, and the concentrations of mineral constituents owing to later steam separation are calculated from the following:

Original concentration = concentration in complete discharge = (analyzed concentration in water) X (fraction of water in separator 1) X (fraction of water in separator 2) X (fraction of water in silencer).

If, however, the enthalpy of the fluid is higher than that of steam-saturated water at the aquifer temperature, the presence of steam in the aquifer is indicated. The presence of steam causes the mineral constituents in the original waters as calculated above to be too low, so that the following correction factor is applied:

$$\text{Concentration in original water} = \frac{\text{concentration in complete discharge}}{\text{fraction of water in the aquifer}}.$$

The presence of steam is often the result of lowered pressure owing to extensive production. Because CO_2 and H_2S are strongly partitioned into the steam phase, the development of steam in the aquifer may result in a decrease in gas pressures and an increase in aquifer pH with the possibility of carbonate scale deposition in the aquifer and in the well casing.

Because of instrumental inaccuracies, measurement of the enthalpy of drillhole discharges is necessarily somewhat approximate; therefore, samples with fluid enthalpies within ±28 cal/g (50 Btu/lb) of the enthalpy of water in equilibrium with steam at the aquifer temperatures are recalculated assuming exact equilibrium.

GAS PARTIAL PRESSURES

If the gas (CO_2, H_2S) contents of the sampled steam and the fraction of steam in the fluid at the sampling point are known, the total gas contents of the aquifer fluids may be calculated. If a single liquid phase exists in the aquifer, the gas partial pressures may be calculated directly from experimental data on the solubility of gas in water at high temperatures (Ellis and Golding, 1963; Kozintseva, 1964). If both steam and water exist in the aquifer, a large fraction of the gas partitions into the aquifer steam phase, and the partial pressure of the gas is a quadratic function of the total gas content.

CHEMICAL MODEL

The calculation of the chemistry of the aquifer fluids requires knowledge of the total content of all solution components and of the dissociation constants of all weak acids and bases and all ion pairs. The total contents of components other than gases and hydrogen ions are easily calculated from the water analysis with allowance for the effects of steam separation and of steam in the aquifer as described earlier. The contents of dissolved gases in the water may be calculated from their solubilities, their contents in the separated steam, the steam fraction, and if there is excess enthalpy, from the fractions of steam and water in the aquifer. For the calculation

of the total content of hydrogen ion, the state of ionization of all weak acids and bases under the conditions of analysis must first be ascertained. This is done through the calculations of a chemical model (Garrels and Thompson, 1962; Ellis, 1967).

SOLUTION OF MASS ACTION AND MASS BALANCE EQUATIONS

In the chemical model for the water as analyzed, the analytical concentrations, experimental dissociation constants, mass balances, and the measured pH are used to calculate the distribution of weak acid species and experimental dissociation constants, and mass balance equations are used to calculate that of ion pairs. Weak acids dissociate to form hydrogen ions by equations such as those for silicic acid as follows:

$$H_4SiO_4 = H^+ + H_3SiO_4^-,$$

and

$$H_3SiO_4^- = H^+ + H_2SiO_4^{-2}.$$

The concentration of each species is determined by the total concentration, the pH, the activity coefficients of the species, and the equilibrium constants for distribution of species at chemical equilibrium. For the preceding reactions we can write the equilibrium equations as follows:

$$K_1 = \frac{m_{H_3SiO_4^-}\,\gamma_{H_3SiO_4^-}\,10^{-pH}}{m_{H_4SiO_4}\,\gamma_{H_4SiO_4}},$$

$$K_2 = \frac{m_{H_2SiO_4^{-2}}\,\gamma_{H_2SiO_4^{-2}}\,10^{-pH}}{m_{H_3SiO_4^-}\,\gamma_{H_3SiO_4^-}}.$$

The mass balance equation for total silica (silicic acid and silicate ions) is

$$m_{Si\ total} = m_{H_4SiO_4} + m_{H_3SiO_4^-} + m_{H_2SiO_4^{-2}}.$$

The mass action equations can be combined with the mass balance equation to solve for $m_{H_4SiO_4}$.

$$m_{H_4SiO_4} = \frac{m_{Si\ total}}{1+\gamma_{H_4SiO_4}\left(\frac{K_1\ 10^{pH}}{\gamma_{H_3SiO_4^-}} + \frac{K_1\ K_2\ 10^{2pH}}{\gamma_{H_2SiO_4^{-2}}}\right)}.$$

The value of $m_{H_4SiO_4}$ is then substituted into the mass action equations to solve for $m_{H_3SiO_4^-}$ and $m_{H_2SiO_4^{-2}}$. Activity coefficients are calculated from the extended Debye-Huckel equation as described later, and the ionic strength is calculated by iteration. Calculation of the concentration of ion pairs is accomplished by a slightly different procedure, which is illustrated by the calculation of the calcium ion species. The mass action expressions,

$$K_1 = \frac{m_{Ca^{+2}}\,\gamma_{Ca^{+2}}\,m_{SO_4^{-2}}\,\gamma_{SO_4^{-2}}}{m_{CaSO_4}\,\gamma_{CaSO_4}}$$

and

$$K_2 = \frac{m_{Ca^{+2}}\,\gamma_{Ca^{+2}}\,m_{CO_3^{-2}}\,\gamma_{CO_3^{-2}}}{m_{CaCO_3}\,\gamma_{CaCO_3}},$$

are combined with the mass balance expression,

$$m_{Ca\ total} = m_{Ca^{+2}} + m_{CaSO_4} + m_{CaCO_3},$$

to produce an expression for free (uncomplexed) Ca^{+2} ion,

$$m_{Ca^{+2}} = \frac{m_{Ca\ total}}{1+\gamma_{Ca^{+2}}\left(\frac{m_{SO_4^{-2}}\,\gamma_{SO_4^{-2}}}{K_1\,\gamma_{CaSO_4}} + \frac{m_{CO_3^{-2}}\,\gamma_{CO_3^{-2}}}{K_2\,\gamma_{CaCO_3}}\right)}.$$

The value of $m_{Ca^{+2}}$ may be substituted into the mass action expressions to solve for the ion pairs. In these equations Ca total is from the analysis, the dissociation constants depend only on temperature, and the activity coefficients are calculated from the ionic strength, which changes slowly during iteration. The molalities of the anions (SO_4^{-2}, CO_3^{-2}) are corrected in each iteration loop by summing the calculated species (for example, $m_{SO_4^{-2}} + m_{HSO_4^-} + m_{KSO_4^-} + \ldots$) and comparing the sum with the analytical concentration of total anion. If the sum calculated differs from the analytical concentration by more than 0.1 percent, the free anion concentration is corrected by an amount depending on the difference. When all anions have been checked (and corrected if necessary), the program iterates if corrections have been made to any of them. Thus, the program leaves the loop when the concentrations of all species satisfy the mass balances to 0.1 percent.

TOTAL IONIZABLE HYDROGEN ION CONTENT

The total content of hydrogen ions in an aqueous solution includes not only free ions but also those in combination in weak acids and in water itself. Only part of these can be ionized under the range of conditions found in natural waters.

This part, the total "ionizable" hydrogen ion content, is calculated by summing the contents of H^+ ion and of all the undissociated and partly dissociated weak acids—HCO_3^-, HBO_2, H_2S, NH_4^+, HSO_4^-, HF, HCl, $H_3SiO_4^-$, $H_4SiO_4^-$, (two times), and H_2CO_3 (two times). When the total ionizable hydrogen ion content has been corrected for electrolyte concentration changes due to steam separation and the presence of aquifer steam as discussed earlier, the H_2S and CO_2 originally dissolved in the water are added (the CO_2 two times as H_2CO_3).

AQUIFER CHEMICAL MODEL

The aquifer chemical model is calculated using the analysis corrected for steam separation and aquifer steam contents, values of dissociation constants at the aquifer temperature and saturated water vapor pressure, and the total ionizable hydrogen ion content. The method of calculation of the chemical model is the same as before except that the pH is now a dependent rather than an independent variable. Because almost all of the hydrogen ion occurs in complexes, changes in the calculated pH cause relatively large changes in the anion mass balances, and the program converges very slowly. A change in the criteria of convergence from 1 percent to 0.1 percent of the anion mass balances doubles the number of iterations and changes the final calculated pH by 0.1 to 0.15 units.

The correctness of the calculated model is dependent on the existence and validity of high-temperature quartz solubility values, gas solubility constants, and dissociation constants for the weak acids and bases and ion pairs present in the water. The data used in the program are given in tables 4 and 5 with their sources. They are of uneven quality, and as better data become available, the program can be easily updated. Tabular data are interpolated by a program written by P. C. Doherty of the U.S. Geological Survey. Single-ion activity coefficients have been calculated from the extended Debye-Hückel equation, with a small hydration coefficient (the "B." of Helgeson, 1969) assumed constant with temperature. This equation differs little from that suggested by Davies (1962). The ionic strength (I) of most geothermal waters is moderate ($<0.08m$), and the ionic activity coefficients are not very sensitive to the ion size ($\mathring{a}$) and hydration parameters chosen. The equation used is:

$$\log \gamma_i = \frac{-A z_i^2 I^{1/2}}{1 + \mathring{a}_i B I^{1/2}} + 0.04 I.$$

The constants A and B are from a tabulation by Helgeson (1967) and are for molal units. Values of $\mathring{a}$ are taken from Kielland (1937).

Table 4.—*Solubility constants and dissociation constants in* KA(I) *and* KT(I) *arrays, analytical expressions*

	Reaction	Analytical expression if used (T in K, t in °C)	Log K 25°	Log K 250°	Note	Reference
1	H_2CO_3 app=H^++HCO_3^-	Log K= -2382.3/T+8.153-0.02194T	-6.38	-7.88	(1)	Ryzhenko (1963).
2	H_2S=H^++HS^-	Log K= -3279.0/T+11.17-0.02386T	-6.94	-7.6		D'yachkova and Khodakovskiy (1968).
3	HBO_2+OH^-=$H_2BO_3^-$	Log K=1573.21/T+28.6059+0.012078T -13.2258 log T	+4.76	+1.98	(2)	Mesmer, Baes, and Sweeton (1972).
4	H_4SiO_4=H^++$H_3SiO_4^-$	See table 5	-9.63	-9.63	(3)	Cobble (1964); Ryzhenko (1967).
5	HF=H^++F^-	....do	-3.18	-5.80	(4)	Ellis (1963).
6	HSO_4^-=H^++SO_4^{-2}	Log K= -557.2461/T+5.3505-0.0183412T	-1.99	-5.31		Lietzke, Stoughton, and Young (1961).
7	H_2O=H^++OH^-	Log K= -4470.99/T+6.0875-0.01706T	-13.995	-11.38		Harned and Owen (1958, p. 645).
8	$NH_3(H_2O)$=NH_4^++OH^-	See table 5	-4.75	-6.00		Wright, Lindsay, and Druga (1961).
9	HCl=H^++Cl^-	....do	-6.10	-.67		Helgeson (1969).
10	NaCl=Na^++Cl^-	....do	+1.60	-.25	(5)	Pearson, Copeland, and Benson (1963); Dunn and Marshall (1969); Hanna, Pethybridge, and Prue (1971).
11	KCl=K^++Cl^-	....do	+1.59	-.1		Helgeson (1969); Hanna, Pethybridge, and Prue (1971).
12	$MgSO_4$=Mg^{+2}+SO_4^{-2}	....do	-2.25	-5.7	(6)	Do.
13	$CaSO_4$=Ca^{+2}+SO_4^{-2}	....do	-2.30	-4.1	(3)	Do.
14	KSO_4^-=K^++SO_4^{-2}	....do	-.83	-2.35	(3)	Quist and others (1963); Truesdell and Hostetler (1968).
15	$NaSO_4^-$=Na^++SO_4^{-2}	....do	-.83	-2.35	(6)	
16	$CaCO_3$=Ca^{+2}+CO_3^{-2}	....do	-2.30	-5.90	(3)	Helgeson (1969).
17	$MgOH^+$=Mg^{+2}+OH^-	....do	-2.60	-4.65	(3)	Do.
18	$H_3SiO_4^-$=H^++$H_2Sio_4^{-2}$	Log K= -3450/T+6.34-0.0216T	-11.7	-11.5		Naymov, Ryzhenko, and Kodakovskii (1971).
19	HCO_3^-=H^++CO_3^{-2}	Log K=-2730.7/T+5.388-0.02199T	-9.12	-11.34		Ryzhenko (1963).
KS	H_2S gas = H_2S aq	K=357+15.688t-0.038253t^2	+2.86	+3.28		Kozintseva (1964).
K	CO_2 gas+H_2O=H_2CO_3 app	See table 5	+3.21	+3.72	(1)	Ellis and Golding (1963).

[1] H_2CO_3 apparent includes H_2CO_3 and CO_2 aqueous.
[2] H_2BO_3 given in print out as BO_2. Reaction written by Mesmer, Baes, and Sweeton (1972) as $B(OH)_3$+OH^-=$B(OH)_4^-$.
[3] Extrapolated above 200°C.
[4] Extrapolated above 200°C. Agrees with Ryzhenko (1965) to 200°C.
[5] Extrapolated below 100°.
[6] Assumed identical to K KSO_4^-.

Table 5.--*Log* K(pK), *and* CO_2 *and quartz solubility, data in tabular form interpolated by look-up subroutine*
[For reaction equations and source of data, see table 4]

°C	(4) $H_4SiO_4°$	(5) $HF°$	(8) $NH_3(H_2O)°$	(9) $HCl°$	(10) NaCl°	(11) KCl°	(12) $MgSO_4°$	(13) $CaSO_4°$	(14) KSO_4^-	(16) $CaCO_3°$	(17) $MgOH^+$	CO_2 solubility	Quartz solubility[1] (p/m)
0	10.2	2.96	4.87	-7.5	-1.65	-1.65	2.05	2.3	0.65	3.0	2.58	700	2.4
10	9.94	3.00	4.80	-6.8	-1.63	-1.62	2.10	2.3	.71	3.05	2.58	1000	3.6
25	9.63	3.18	4.75	-6.1	-1.60	-1.59	2.25	2.3	.83	3.20	2.60	1630	6.6
35	9.48	3.25	4.70	-5.7	-1.40	-1.50	2.35	2.35	.90	3.27	2.63	2100	8.6
50	9.30	3.40	4.70	-5.0	-1.20	-1.40	2.60	2.40	1.00	3.40	2.7	2900	13.5
75	9.11	3.64	4.75	-3.8	-.90	-1.20	2.90	2.55	1.15	3.65	2.9	4000	27
100	9.03	3.85	4.85	-2.9	-.55	-1.00	3.20	2.7	1.30	3.90	3.1	5200	48
125	9.03	4.09	4.97	-2.0	-.55	-.90	3.55	2.9	1.45	4.15	3.33	6000	80
150	9.10	4.34	5.10	-1.23	-.45	-.75	3.90	3.1	1.60	4.50	3.6	6600	125
175	9.23	4.59	5.33	-.60	-.30	-.60	4.40	3.35	1.78	4.85	3.85	6800	190
200	9.36	4.89	5.53	-.07	-.15	-.40	4.80	3.6	1.93	5.20	4.1	6400	265
225	9.48	5.3	5.73	.30	.05	-.20	5.25	3.8	2.10	5.55	4.35	5900	367
250	9.63	5.8	6.0	.67	.25	.10	5.7	4.1	2.35	5.90	4.65	5300	490
275	9.83	6.2	6.3	.95	.60	.30	6.1	4.3	2.55	6.20	4.9	4600	615
300	10.2	6.8	6.75	1.2	.95	.6	6.4	4.5	2.75	6.45	5.15	3900	680
325	10.5	7.1	7.25	1.6	1.35	1.0	6.7	4.75	2.9	6.65	5.45	3100	720
350	11.0	7.4	8.0	2.5	2.0	1.7	7.0	5.0	3.1	7.0	5.7	2100	(750)

[1]Quartz solubility in water at saturated water vapor pressure. 0°–240°C from Morey, Fournier, and Rowe (1962); 260°–325°C from Kennedy (1950). An incorrect 350° value is included because the look-up subroutine requires a monotonic function.

The algol version of this program (Truesdell and Singers, 1973) has just been published.

REFERENCES CITED

Cobble, J. W., 1964,The thermodynamic properties of high temperature aqueous solutions–[part] VI, Application of entropy correspondence to thermodynamics and kinetics: Am. Chem. Soc. Jour., v. 86, p. 5394–5401.

Davies, C. W., 1962, Ion association: London, Butterworths, 190 p.

Dawson, G. B., and Dickinson, D. J., 1970, Heat flow studies in thermal areas of the North Island of New Zealand–U.N. symposium on the development and utilization of geothermal resources: Geothermics special issue 2, v. 2, pt. 1, p. 466–473.

Dunn, L. A., and Marshall, W. L., 1969, Electrical conductances and ionization behavior of sodium chloride in dioxane-water mixtures at 100° C: Jour. Phys. Chemistry, v. 73, p. 2619–2622.

D'yachkova, I. B., and Khodakovskiy, I. L., 1968, Thermodynamic equilibria in the systems S-H_2O, Se-H_2O and Te-H_2O in the 25–300° C temperature range and their geochemical interpretations: Geochemistry Internat., p. 1108–1125.

Ellis, A. J., 1963, The effect of temperature on the ionization of hydrofluoric acid: Chem. Soc. [London] Jour., p. 4300–4304.

—— 1967, The chemistry of some explored geothermal systems, Chapter 2 *in* Barnes, H. L., ed., Geochemistry of hydrothermal ore deposits: New York, Holt, Rinehart and Winston, p. 465–514.

—— 1970, Quantitative interpretation of chemical characteristics of hydrothermal systems–U.N. symposium on the development and utilization of geothermal resources: Geothermics special issue 2, v. 2, pt. 1, p. 516–528.

Ellis, A. J., and Golding, R. M., 1963, The solubility of carbon dioxide above 100° C in water and in sodium chloride solutions: Am. Jour. Sci., v. 261, p. 47–60.

Ellis, A. J., and McFadden, I. M., 1972, Partial molar volumes of ions in hydrothermal solutions: Geochim. et Cosochim. Acta. v. 36, p. 413–426.

Ellis, A. J., Mahon, W. A. J., and Ritchie, J. A., 1968, Methods of collection and analysis of geothermal fluids. New Zealand Dept. Sci. and Indus. Research Chemistry Div. Rept. CD2103, 51 p.

Fournier, R. O., and Rowe, J., 1966, Estimation of underground temperatures from the silica content of water from hot springs and wet-steam wells: Am. Jour. Sci., v. 264, p. 685–697.

Fournier, R. O., and Truesdell, A. H., 1973, An empirical Na-K-Ca geothermometer for natural waters: Geochim. et Cosmochim. Acta, v. 37, p. 1255–1275.

Garrels, R. M., and Thompson, M. E., 1962, A chemical model for sea water at 25° C and one atmosphere total pressure: Am. Jour. Sci., v. 260, p. 57–66.

Glover, R. B., 1970, Interpretation of gas compositions from the Wairakei field over 10 years–U.N. symposium on the development and utilization of hydrothermal resources: Geothermics, special issue 2, v. 2, pt. 2, p. 1355–1366.

Grindley, G. W., 1965, The geology, structure, and exploitation of the Wairakei geothermal field Taupo, New Zealand: New Zealand Geol. Survey Bull. 75, 130 p.

Hanna, E. M., Pethybridge, A. D., and Prue, J. D., 1971, Ion association and the analysis of precise conductivity data: Electrochim. Acta, v. 16, p. 677–686.

Harned, H. S., and Owen, B. B., 1958, The physical chemistry of electrolyte solutions: New York, Reinhold, 801 p.

Helgeson, H. C., 1967, Solution chemistry and metamorphism, *in* Abelson, P. H., ed., Researches in geochemistry, volume 2: New York, John Wiley and Sons, p. 362–404.

——1969, Thermodynamics of hydrothermal systems at elevated temperatures and pressures: Am. Jour. Sci., v. 267, p. 729–804.

Hemley, J. J., 1959, Some mineralogical equilibria in the system K_2O-Al_2O_3-SiO_2-H_2O: Am. Jour. Sci., v. 257, p. 241–270.

Keenan, J. H., Keyes, F. G., Hill, P. G., and Moore, J. G., 1969, Steam tables, Thermodynamic properties of water including vapor, liquid, and solid phases: New York, John Wiley and Sons, 162 p.

Kennedy, G. C., 1950, A portion of the system silica-water: Econ. Geology, v. 45, p. 629–653.

Kielland, J., 1937, Individual ion activity coefficients of ions in aqueous solutions: Am. Chem. Soc. Jour., v. 50, p. 1675–1678.

Kozintseva, T. N., 1964, Solubility of hydrogen sulfide in water at elevated temperatures: Geochemistry Internat., p. 750–756.

Lietzke, M. H., Stoughton, R. W., and Young, T. F., 1961, The bisulfate acid constant from 25° to 225° as computed from solubility data: Jour. Phys. Chemistry, v. 65, p. 2247–2249.

Mahon, W. A. J., 1966, Silica in hot water discharged from drillholes at Wairakei, New Zealand: New Zealand Jour. Sci., v. 9, 135–144.

—— 1970, Chemistry in the exploration and exploitation of hydrothermal systems–U.N. symposium on the development and utilization of geothermal resources: Geothermics, special issue 2, v. 2,

pt. 2, p. 1310–1322.

Mesmer, R. E., Baes, C. F., Jr., and Sweeton, F. H., 1972, Acidity measurements at elevated tempreatures: VI. Boric acid equilibria: Inorganic Chemistry, v. 11, p. 537–543.

Morey, G. W., Fournier, R. O., and Rowe, J. J., 1962, The solubility of quartz in water in the temperature interval from 25° to 300°C: Geochim. et Cosmochim. Acta, v. 26, p. 1029–1043.

Naymov, G. B., Ryzhenko, B. N., and Kodakovskii, I. L., 1971, Spravochnik termodinamicheckikh velichin dlia geology: Moskow, Atomizdat, 239 p.

Pearson, D., Copeland, C. S., and Benson, S. W., 1963, The electrical conductance of aqueous sodium chloride in the range 300° to 383°C: Am. Chem. Soc. Jour., v. 85, p. 1044–1047.

Quist, A. S., Franck, E. U., Jolley, H. R., and Marshall, W. L., 1963, Electrical conductances of aqueous solutions at high temperatures and pressures–[part] I, The conductances of potassium sulfate–water solutions from 25° to 800°C and at pressures up to 4000 bars: Jour. Phys. Chemistry, v. 67, p. 2453–2459.

Ryzhenko, B. N., 1963, Determination of dissociation constants of carbonic acid and the degree of hydrolysis of the CO_3^{-2} and HCO_3^- ions in solutions of alkali carbonates and bicarbonates at elevated temperatures: Geochemistry, no. 2, p. 151–164.

——1965, Determination of the dissociation constant of hydrofluoric acid and the conditions for the replacement of calcite by fluorite· Geochemistry Internat., v. 2, p. 196–200.

——1967, Determination of the hydrolysis of sodium silicate and calculation of dissociation constants of orthosilicic acid at elevated temperatures: Geochemistry Internat., v. 4 p. 99–107.

Truesdell, A. H., and Hostetler, P. B., 1968, Dissociation constants of KSO_4^- from 10°–50°C: Geochim. et Cosmochim. Acta, v. 32, p. 1019–1022.

Truesdell, A. H., and Singers, Wendy, 1973, Computer calculation of downhole chemistry in geothermal areas: New Zealand Dept. Sci. Indus. Research, Chemistry Div. Rept. CD2136, 145 p.

White, D. E., 1965, Saline waters of sedimentary rocks, *in* Fluids in subsurface environments–a symposium: Am. Assoc. Petroleum Geologists Mem. 4, p. 342–366.

—— 1970, Geochemistry applied to the discovery, evaluation, and exploitation of geothermal energy resources–U.N. symposium on the development and utilization of geothermal resources: Geothermics special issue 2, v. 1.

Wright, J. M., Lindsay, W. T., Jr., and Druga, T. R., 1961, The behavior of electrolytic solutions at elevated temperatures as derived from conductance measurements: Washington, D.C., U.S. Atomic Energy Comm. R&D WAPD-TM-204, 32 p.

Jour. Research U.S. Geol. Survey
Vol. 2, No. 3, May-June 1974, p. 279—288

SOME MORPHOMETRIC PROPERTIES OF EXPERIMENTALLY CRATERED SURFACES

By H. J. MOORE, R. V. LUGN, and E. B. NEWMAN,
Menlo Park, Calif.

Abstract.—Terrain descriptors and crater-frequency distributions for five experimental steady-state cratered surfaces are compared with analogous lunar data. In the experiments, craters were produced in granular materials by projectiles that impacted the surface with three frequency distributions. Values of terrain descriptors describing roughness of the surfaces are functions of the crater-production frequency distributions and initial slope. Relatively smooth surfaces are produced when the exponent of crater-production frequency distribution has a large negative value; relatively rough steady-state surfaces are produced when the exponent has a small negative value. When the initial slope is large, terrain descriptors reflect the initial slope. Steady-state crater-frequency distributions are functions of the crater-production distributions. Small negative exponents on the production distributions produce small negative exponents on the steady-state distributions. A large initial slope has little effect on the steady-state crater distribution. Visual impressions and terrain descriptors of the experimental surfaces agree with those of lunar surfaces. In all experiments, the steady-state crater-frequency distributions lie close to the lunar one, but the slopes of frequency curves differ slightly.

Imagery of the Moon taken by unmanned spacecraft such as Ranger (U.S. National Aeronautics and Space Administration, 1966, p. 170, fig. P-12), Luna (Akademiya Nauk S.S.S.R., 1966), Surveyor (U.S. Natl. Aeronautics and Space Administration, 1969, p. 63–69), and Lunar Orbiter (National Space Science Data Center, 1969), as well as photographs taken during the manned Apollo missions (see, for example, U.S. National Aeronautics and Space Administration, 1971, p. 47, fig. 3–14) have shown that craters characterize the lunar surface at the fine scale (fig. 1). Most of the highest resolution photographs show that the surfaces have reached a steady-state crater-frequency distribution with a continuum of crater sizes, up to some limiting size, in a continuum of states of preservation. Such steady-state surfaces probably result from bombardment of the lunar surface by meteors and micrometeoroids through eons of time.

Theory and empirical data show that on the moon smaller craters form at a much greater rate than larger craters and that the total number of craters increases with continued bombardment (Moore, 1964; Soderblom, 1970; Gault, 1970; Marcus, 1970; Shoemaker and others, 1969; and Trask, 1966). As a result of the high production rate of small craters in the regolith, the area of small craters 0.1 cm across and less, calculated from their diameters, exceeds the area on which they

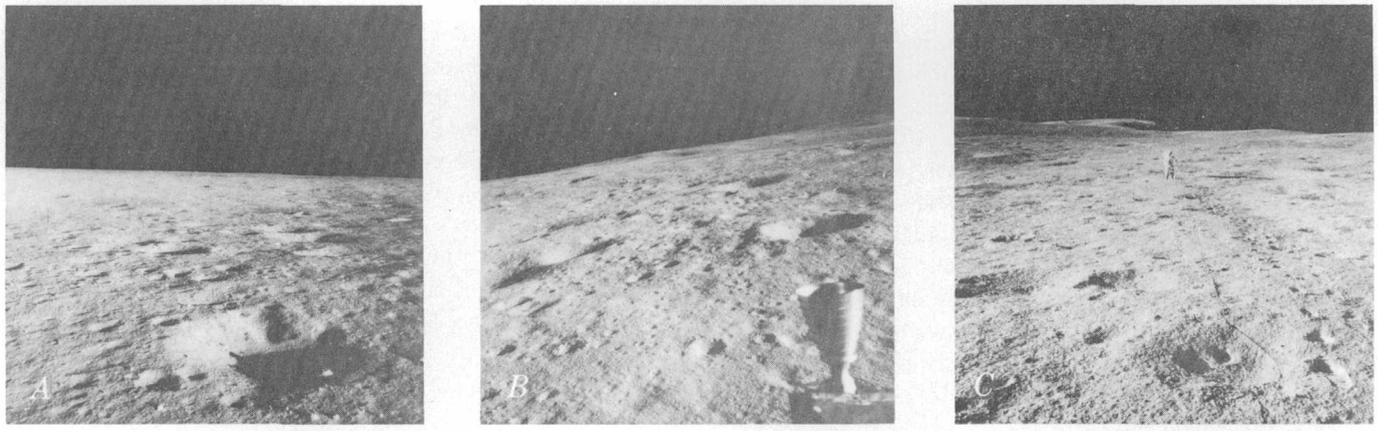

Figure 1.—Apollo photographs of lunar surfaces showing steady-state distribution of craters in various states of preservation. *A*, Surface at Apollo 12 landing site (AS-12-48-7029), large crater in foreground is about 6 m across. B, Surface at Apollo 14 landing site (AS-14-65-92031), crater beyond nozzle is about 5 m across. *C*, Surface at Apollo 14 landing site (AS-14-67-9374). Depressions from lower right to astronaut are footprints.

Table 1.—*Frequency of craters produced on five experimental surfaces*
[See text for explanation of 1/6, 1/10, and 1/16]

Experiment	Crater diameter, in centimeters							Initial surface
	0.52	1.1	2.5	4.2	13	30	60	
Terra Alta (1/6)	46,656	7,776	1,296	216	36	6	1	Level.
Mare Exemplum 1 (1/10)	1,000,000	100,000	10,000	1,000	100	10	1	Do.
2 (1/10)	1,000,000	100,000	10,000	1,000	100	10	1	Do.
3 (1/10)	1,000,000	100,000	10,000	1,000	100	10	1	15° slope.
Mare Nostrum (1/16)	16,777,216	1,048,576	65,533	4,096	256	16	0	Level.

are produced after about 10^4 yr. Thus, craters must be destroyed and obliterated by one another, achieving a steady-state condition. The resulting steady-state surface has three characteristics: (1) Craters of any given size, up to some limiting size, vary in their geomorphic age, (2) the frequency distribution is constant below the limiting size, and (3) craters smaller than the limiting size are destroyed as rapidly as they are produced. Steady-state conditions obtain for the smallest craters first and then, with continued time or bombardment, extend to larger size craters. The limiting size increases with time or the age of the surface (Moore, 1964; Shoemaker and others, 1969; and Soderblom and Lebofsky, 1972). At resolutions below the limiting size, the general appearance of the cratered surface remains the same and is independent of time, although the details are continually changing. Frequency distributions of craters larger than the limiting size directly reflect the crater-production frequency distribution and duration of cratering.

Mare Cognitum (U.S. National Aeronautics and Space Administration, 1965, p. 200) at the fine scale[1] is one such steady-state surface, and fine-scale topography of Mare Cognitum is used later to compare experimental surfaces with lunar ones. Mare Cognitum, like other lunar surfaces, has small craters in each size class with a continuum of geomorphic ages, and the frequency distribution curve has the form expected for a steady-state surface. Additionally, the form and magnitude of the frequency distributions of eumorphic or fresh craters (Trask, 1966, p. 257) are in reasonable agreement with the expectations for fresh, deep, high-rimmed craters on a steady-state surface (Moore, 1971, p. 15, 16).

This experimental study was conducted because steady-state surfaces are so widespread at the fine scale on the Moon, and data on meteors and micrometeors combined with data on experimental impact craters form a rational explanation for the lunar steady-state surfaces. Terrain descriptors and crater-frequency distributions of the experimental steady-state surfaces were compared with those of the lunar surface to test quantitatively the similarities suggested by visual comparisons of the experimental and lunar surfaces.

[1] The term "fine scale" applies to lengths on the lunar surface of about 1 cm to about 10 m.

Acknowledgments.—The authors thank R. J. Pike, Jr., and G. E. Ulrich for their helpful and critical reviews of this paper. The work was performed under NASA contracts R-66 and W-13,130.

PROCEDURES

Laboratory experiments

Five experiments were conducted at Ames Research Center[2] using surfaces underlain by cohesionless sand and coarse carborundum powder. A square box 2.44 m on an edge and 30 cm deep was filled with sand and, for three of the experiments, topped with a layer of carborundum powder about 2 cm thick. For four of the experiments, the initial surfaces were smooth and level, and for the fifth experiment, the initial slope of the surface was 15°.

Three frequency distributions for the production of craters were employed in the five experiments. For three experiments, the frequency of craters produced for a given size was one-tenth the frequency of the next smaller size; for the fourth experiment, one-sixth the frequency; and for the fifth experiment, one-sixteenth the frequency. These experimental conditions are summarized in table 1.

Projectiles impacted the surface according to the schemes just described, and the sequence of impact was repeated until a steady state was achieved. Cupfuls of No. 12 and No. 8 lead shot were dropped from a height of 7.6 m to yield the planned crater production frequencies described above. Individual craters produced by the No. 12 and No. 8 shot were 0.52 and 1.1 cm across. This procedure was followed by firing No. 12 shot from a sawed-off 22-caliber rifle at the central 1.22 m square. Impact of this shot produced craters 2.5 cm across. Only the central square, 1.22 m on an edge, received the required number of shot. Larger craters, 4.2, 13, and 30 cm across, were produced one at a time by firing a BB air gun, a

[2] The five experiments were conducted under the direction of D. E. Gault, Ames Research Center. The first experiment, Mare Exemplum 1, was suggested by U.S. Geological Survey and conducted jointly with Ames Research Center. Stereoscopic photographs of the subsequent four experiments were kindly furnished to the authors for this study. The chief experimenters were V. R. Oberbeck, W. L. Quaide, B. G. Ponseggi, and David West of Ames Research Center.

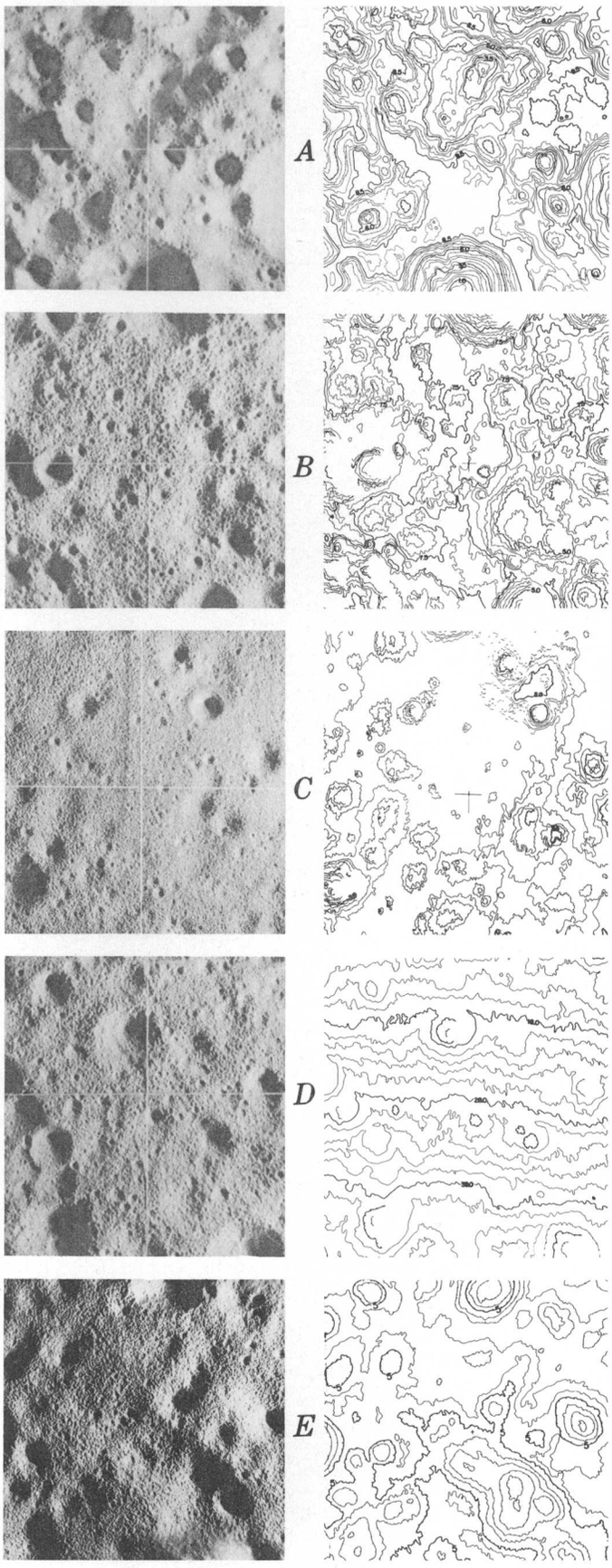

22-caliber rifle, and a 30-caliber rifle. The entire box received the required number of projectiles producing the large craters. A small explosive charge was used to produce craters 60 cm across. The frequencies of larger craters produced were guided by the intended crater-production frequency distribution, and their impact points were selected using a table of random numbers to generate coordinates matching those on the side of the box. The large craters were then produced by aiming and firing at the intersection of the proper grid coordinates.

Photographs of each surface were taken periodically so that the evolution of each surface could be traced. Photographs of the steady-state surfaces are shown in figure 2.

Topographic maps

After each experiment was completed, topographic maps (fig. 2) were prepared from vertical stereoscopic photographs taken with a 60-mm focal length Hasselblad camera. Diapositives were made in a Besseler printer to yield nearly equal vertical and horizontal scales in the stereomodel (Lugn, 1964). Even if the camera and stereoplotter geometry are not entirely compatible, accurate maps can be made by using vertical stereopairs (Marsden, 1952). The diapositives were then placed in an ER 55 anaglyphic stereoplotter (Hopkins and others, 1966), and the stereomodel was cleared and leveled. Measured box dimensions were compared with corresponding model dimensions to establish the scales of the stereomodels. Vertical, horizontal, and compilation scales are listed in table 2.

Table 2.—*Model scales*

Experiment	Scales			Contour intervals (cm)
	Horizontal	Vertical	Compilation	
Terra Alta	1:6.81	1:6.85	1:6.81	0.5
Mare Exemplum 1 . . .	1:5.80	1:4.76	1:10	1.0
2 . . .	1:6.83	1:6.85	1:6.83	.5
3 . . .	1:7.05	1:8.56	1:7.05	2.0
Mare Nostrum	1:5.80	1:4.76	1:5.80	.4

Each stereomodel was then tested, using the edges of the box and crossed strings stretched across the box to insure that the model was both level and flat. Lens distortions from the

Figure 2.—Photographs and topographic maps of experimental steady-state surfaces. *A*, Terra Alta; contour interval, 0.5 cm. *B*, Mare Exemplum 2; contour interval, 0.5 cm. *C*, Mare Nostrum; contour interval, 0.4 cm. *D*, Mare Exemplum 3; contour interval, 2 cm. *E*, Mare Exemplum 1; contour interval, 1 cm. Large craters are dominant in Terra Alta and absent from Mare Nostrum. On the contour maps, Terra Alta shows greater roughness than Mare Nostrum. General appearance of Mare Exemplum 1 and 2 is similar to Mare Exemplum 3, despite 15° regional slope of latter surface. Slope of Mare Exemplum 3 dictates form of contours that are subparallel to edge of map. Only central square, 1.22 m on an edge, that received the required impacts is shown. Areas of shadow are not contoured in *B*, *C*, and *D*.

camera and Besseler printer were not readily apparent. Thus, reasonably good geometry was attained. Additionally, relief of the surfaces far outshadows such lens distortions.

Topography of the lunar surface was obtained from a contour map of part of Mare Cognitum (H. A. Pohn and others, unpub. map, 1965). This map was prepared at a scale of 1:80 with a contour interval of 10 cm from the last P_3 camera frame of Ranger VII. It was made with a combination of photometric and photogrammetric procedures that are outlined in more detail elsewhere (Shoemaker, 1965, p. 129–130).

Terrain descriptors

In order to calculate terrain descriptors, elevations were obtained from the topographic maps using several sample designs. For Terra Alta, Mare Exemplum 2, and Mare Nostrum, a rectangular spiral[3] was placed in the central square, 1.18 m on an edge (fig. 3); then, elevations were read from the contour maps by interpolation every 2.0 cm (at full scale). Elevations were read starting near the center of the square and proceeding outward until about 650 elevations were obtained. For Mare Exemplum 1, a rectangular grid with 10.0 cm between grid lines was laid out in the central square 1.2 m, on an edge, and diagonals with 14.14 cm between lines were then added. Slope angles were computed for every 5.0-cm slope length so that 1,032 angles were obtained. In addition to the rectangular spiral, a rectangular grid with 10.0 cm between grid lines was laid out in the central square of the Mare Exemplum 2, and slope angles were then, computed for each 5.0-cm slope length so that 624 angles were obtained. A rectangular grid with 5.0 cm between lines was placed in the central square, 1.2-m on an edge, for Mare Exemplum 3. Grid lines were parallel to the direction of slope and at right angles to it. Six-hundred and twenty elevations were obtained along the grid lines, chiefly parallel to the contours of the 15° slope, and 630 elevations were obtained along grid lines chiefly parallel to the direction of slope. To attain continuity, a few elevations were obtained perpendicular to the principal direction of the traverses.

Elevation and slope angles for the fine-scale lunar surface were obtained from the topographic map of part of Mare Cognitum. A total of 2,987 slope angles was obtained from a rectangular grid with 100 cm between grid lines and for a slope length of 100 cm.

Elevation data were then put on punched cards, and topographic descriptors computed in the U.S. Geological Survey terrain-analysis computer program.[4] This program calculates slopes from elevations of points separated by a fixed horizontal interval (slope length) and obtains frequency distributions for both algebraic and absolute slopes (Rowan and others, 1971). Additional terrain descriptors, such as algebraic means, medians, and standard deviations, and absolute means and medians, are calculated. The algebraic standard deviation, σ_{AL}, is

$$\sigma_{AL} = \sqrt{\frac{\Sigma(X_i - \bar{X})^2}{n-1}}$$

where n is the total number of slope angles,

X_i is a (+) or (-) slope angle, and

$\bar{X}$ is the algebraic mean.

The absolute mean, $|\bar{X}|$, is equal to $\frac{1}{n} \Sigma |X_i|$ where $|X_i|$ is the absolute value of individual slope angles and n is the total number of slope angles in the sample.

All slope parameters are calculated from the same elevation data set for multiples of the fixed sampling interval. Power spectral densities (Rozema, 1969) are obtained from the same program.

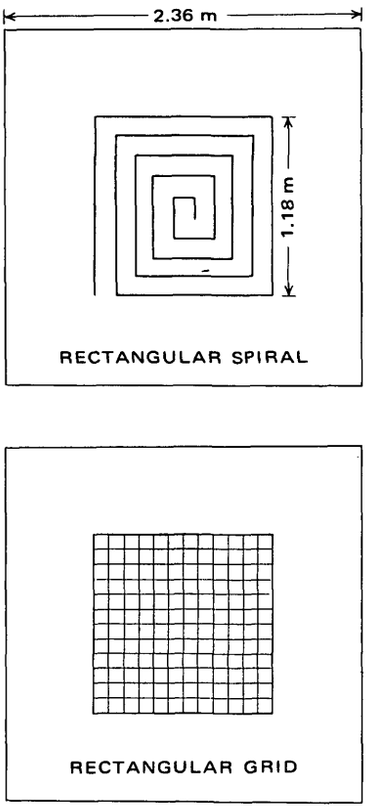

Figure 3.—Sample designs used to obtain elevations from experimentally cratered surfaces.

Crater frequencies

Crater frequencies of the surfaces were obtained within a square grid on 1:8.73-scale photographs taken at the end of

[3] Elevation data were read by L. I. Middlestorb along rectangular spirals designed by R. J. Pike.

[4] This program was written by Richard Godson, Gary Selner, Wesley Rozema, Dennis McMacken, and Stephen Wilson under the general supervision of R. J. Pike. It was completed April 1970.

each experiment. The edges of the grid corresponded to 1.2 m at full scale, and the center of the square grid corresponded to the center of the box so that craters in the appropriate part of the experiment were included. The square grid was divided into 100 equal squares. Craters larger than 6.94 cm (0.8-cm photoscale) were counted within the entire area of the grid. Twenty-five squares, 12.2 cm on an edge at full scale, were selected from a table of random numbers (Korn and Korn, 1961, p. 1070–1074), and craters 3.47 to 6.94 cm across (0.4- to 0.8 cm photoscale) were counted in these squares. Twelve and one-half squares, 12.2 cm on an edge, were selected from a table of random numbers to count craters 0.87 to 3.47 cm across (0.1- to 0.4-cm photoscale). The crater counts for the various sizes were then normalized for the area and combined to give the cumulative frequencies of craters per square meter (table 3).

Table 3.—*Cumulative frequencies of craters, per square meter, produced on experimental surfaces*

Crater diameter (cm)	Terra Alta[1]	Mare Exemplum			Mare Nostrum	
		[2]1	[1]2	[1]3	([1])	([3])
0.87	712	[4]1500	2580	1780	2209	2708
1.74	220	220	496	315	183	231
3.47	40.7	53	71.8	53.0	28.5	27.8
6.94	22.8	14	13.9	13.7	11.5	7.84
13.89	11.6	8.9	5.82	6.76	6.5	3.78
27.78	1.86	2.5	.421	1.50	.4	.405
55.55	.506	---	.084	---	---	---

[1] By E. B. Newman.
[2] By N. J. Trask.
[3] By H. J. Moore.
[4] Estimated by extrapolation.

RESULTS

Visual

All five surfaces looked somewhat alike after bombardment was completed. They were pocked with craters of all the sizes produced; the crater morphologies ranged from fresh appearing to so subdued that they were barely discernible. Mare Exemplum 1, 2, and 3 were very similar in appearance, and the 15° slope apparently had little effect on the craters (fig. 2*E*, *B*, *D*).

In detail, the Mare Exemplum 1, 2, and 3, Terra Alta, and Mare Nostrum were strikingly different. Topography of Terra Alta was dominated by larger craters; smaller ones were noticeable but not as obvious as the larger craters. For the Mare Exemplum 1, 2, and 3, craters of all sizes were equally apparent in the photographs. The smallest craters dominated Mare Nostrum, and larger craters were generally very subdued. Thus, the different crater-production frequencies produced noticeably different surfaces. These differences are manifested in the terrain analysis results and crater-frequency distributions.

Terrain analysis

With the exception of Mare Exemplum 3, the roughness of the surfaces correlates with visual impressions of the photographs. This correlation is shown by the absolute-slope-frequency distributions obtained at a slope length of 2.0 cm (fig. 4). For Terra Alta the cumulative fraction of absolute

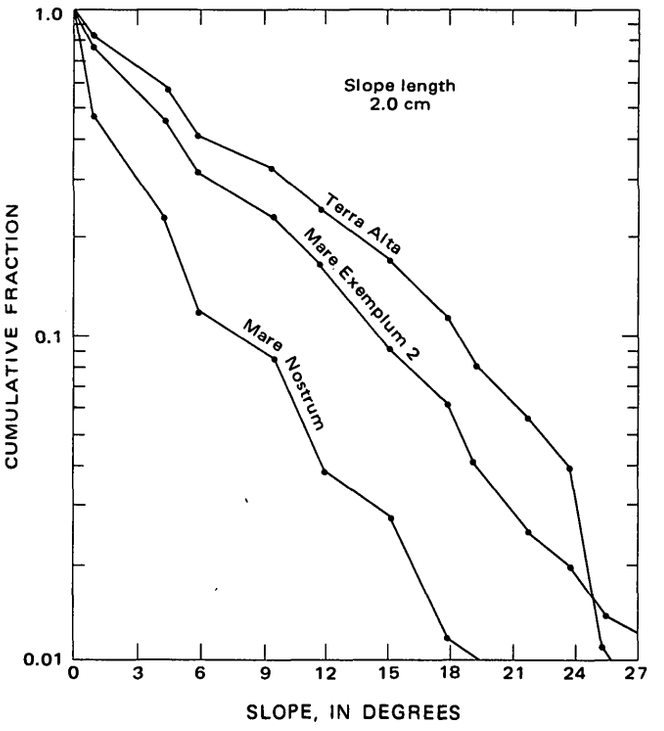

Figure 4.—Cumulative frequency distributions of absolute slopes larger than a given slope for Terra Alta, Mare Exemplum 2, and Mare Nostrum. Slope length is 2.0 cm. Relative positions of the curves correlate directly with crater-production frequencies.

slopes larger than a given slope angle was larger than those for Mare Exemplum 2 (except at 25.5° and larger) and Mare Nostrum. In turn, the cumulative fraction of slopes larger than a given slope angle for Mare Exemplum 2 was larger than for Mare Nostrum. This difference persists to slope lengths of 40 cm. For Terra Alta, mean absolute slopes, median absolute slopes, and algebraic standard deviations for slope lengths between 2 and 40 cm are larger than those of Mare Exemplum 2 and Mare Nostrum (fig. 5). Similarly, the data show that Mare Exemplum is rougher than Mare Nostrum. Mean absolute slopes, median absolute slopes, and algebraic standard deviations depend on slope length—a result consistent with lunar data (Rowan and others, 1971). To see if slope-frequency distributions for Mare Exemplum 1 and 2 were virtually the same, the data were obtained by hand computation, identical sampling grids, and a slope length of 5.0 cm. From absolute slope distributions in figure 6, it is evident that Exemplum 1 and 2 are very similar.

Mean and median absolute-slope values at various slope lengths for Mare Exemplum 3, which had an initial slope of 15°, are strongly dependent on the direction in which the

slopes are measured (fig. 7). Mean and median absolute slopes computed from measurements chiefly parallel to the direction of slope are near 13° to 15° and are weakly dependent on slope length. Values less than 15° are obtained because of the sampling procedure used, which required the inclusion of some slopes measured perpendicular to the direction of slope. From measurements chiefly perpendicular to the direction of slope, mean and median absolute slopes are strongly dependent on slope length and are substantially smaller than those measured parallel to the direction of slope. Values of mean and median absolute slopes measured perpendicular to the direction of slope at each slope length are larger than those for Mare Exemplum 2 because of the sampling procedures used, which required the inclusion of some slopes measured parallel to the direction of slope.

Power spectral densities (Rozema, 1969) reveal differences in roughness between Terra Alta, Mare Exemplum 2, and Mare Nostrum (fig. 8). In figure 8, the values of filtered power spectral densities (PSD) and frequencies have been scaled up so that they may be compared with lunar data. PSD curves for Mare Cognitum, a grass runway (Jaeger and Schuring, 1966), and a blocky crater excavated in basalt, Danny Boy (Nordyke and Wray, 1964), have been included in figure 8 for comparison. For frequencies of 0.1 cycle/m and less, Terra Alta has larger PSD values than Mare Exemplum 2, while for higher frequencies they are generally comparable. This is due to greater abundance of large craters in Terra Alta than in Mare Exemplum 2. Mare Nostrum PSD values are lower than those for Mare Exemplum and Terra Alta at all frequencies.

Linear trends fitted to the filtered PSD curves in figure 8 also show the relative roughness between the three surfaces. The constants K and α for an equation of the form PSD = Kf^{α}, where PSD is in square meters per cycle per meter and f is in cycles per meter, are tabulated below. By virtue of both K and α, Terra Alta is the roughest surface, Mare Exemplum is the next roughest surface, and Mare Nostrum is the smoothest surface. Here again, the linear trends correlate with crater-production frequencies.

	K	α
Terra Alta	$10^{-3.30}$	-2.84
Mare Exemplum 2 . . .	$10^{-3.46}$	-2.77
Mare Nostrum	$10^{-3.92}$	-2.75

Crater frequencies

All steady-state crater-frequency distributions for the five experimental surfaces (see fig. 9) exhibit three things in common: (1) The slopes of the curves are less than those of the crater-production curve, (2) they are reasonably close to the lunar steady-state curve (see for example, Trask, 1966), and (3) they all have a flexure corresponding to a flexure in the crater-production frequency distribution. Additionally, the number of craters counted at the 10-cm size is largest for Terra Alta and smallest for Mare Nostrum; Mare Exemplum 2 falls in

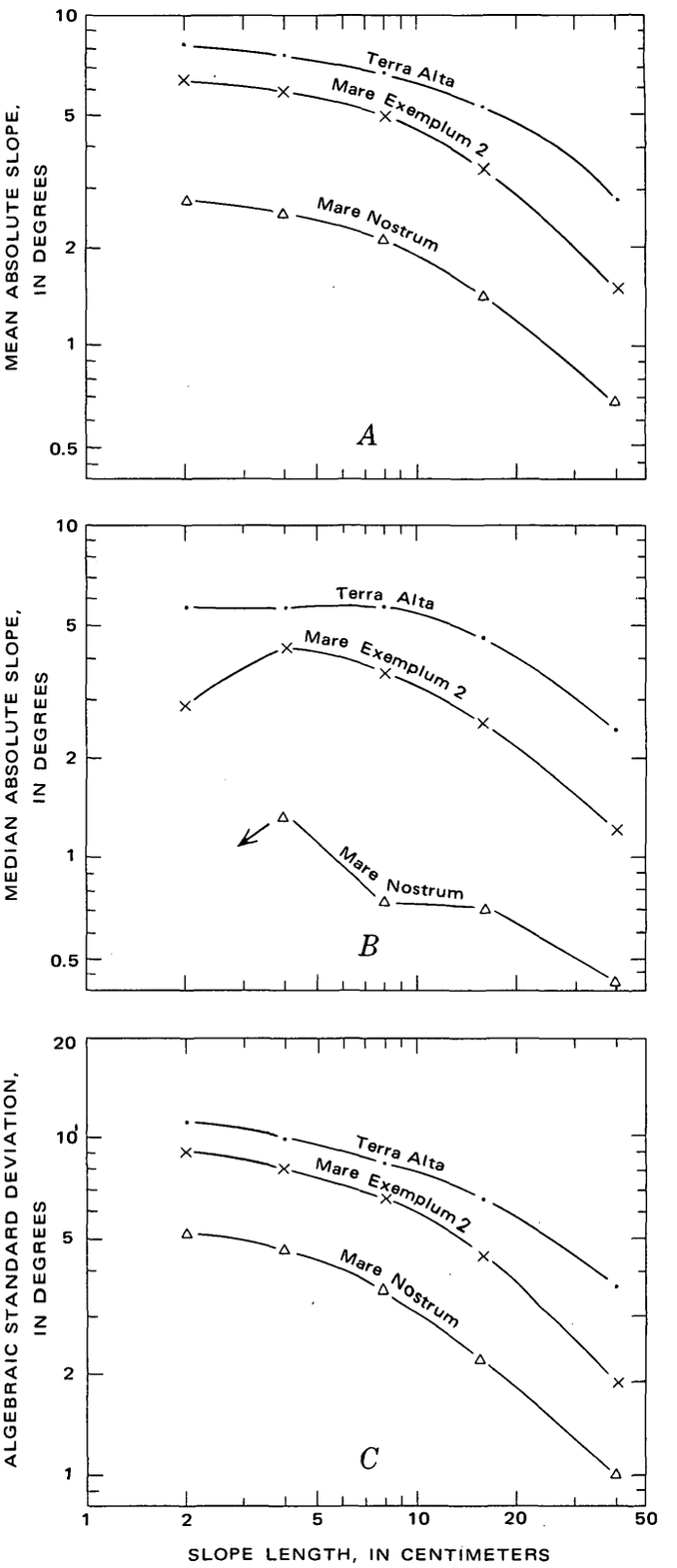

Figure 5.—Graphs comparing (*A*) mean absolute slopes, (*B*) median absolute slopes, and (*C*) algebraic standard deviations with slope length for Terra Alta, Mare Exemplum 2, and Mare Nostrum. Relative positions of curves correlate directly with crater-production frequencies.

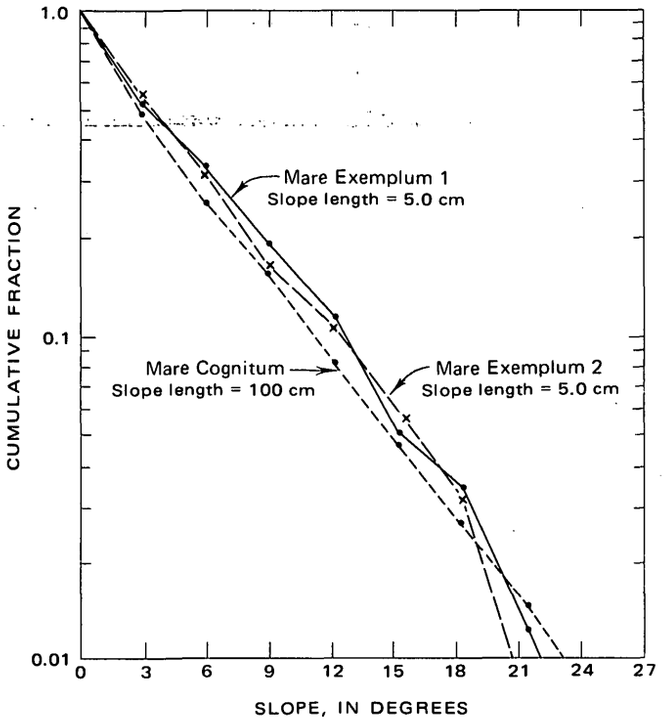

Figure 6.—Cumulative frequency distribution of absolute slopes larger than a given value for a slope length of 5.0 cm for Mare Exemplum 1 and 2; distributions of these two separate experiments with nearly identical crater-production frequencies correspond closely. Cumulative slope-frequency distributions of Mare Cognitum at a slope length of 1.0 m compare well in form and magnitude with those of Mare Exemplum 1 and 2.

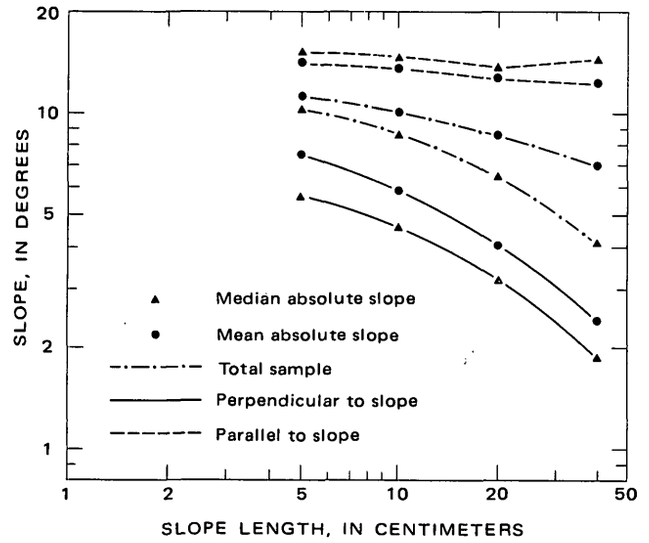

Figure 7.—Median and mean absolute slopes as a function of slope length for Mare Exemplum 3 (which had an initial slope of 15°). Slope values were obtained chiefly parallel to direction of slope, chiefly perpendicular to direction of slope, and for total sample.

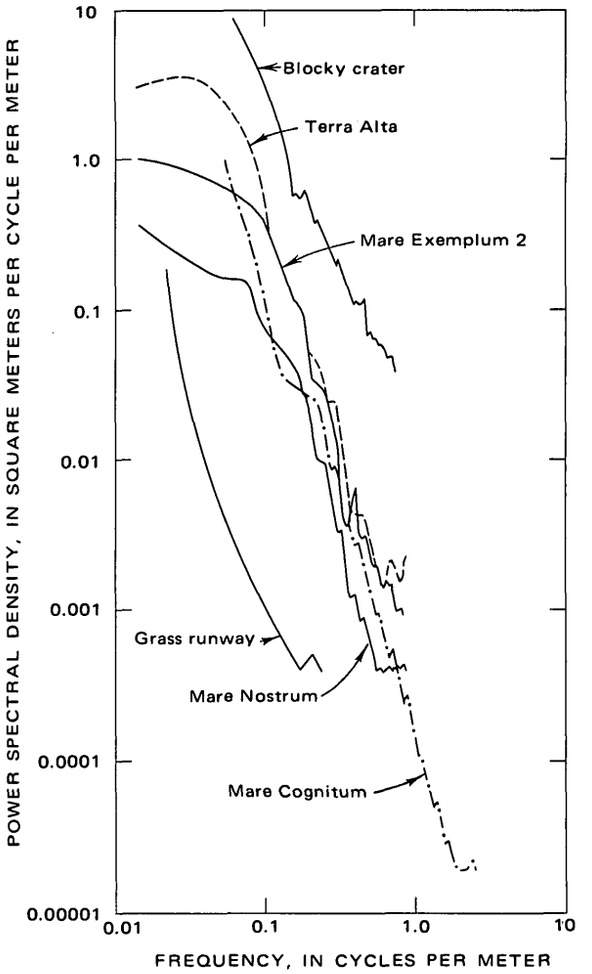

Figure 8.—Filtered power spectral densities for Terra Alta, Mare Exemplum 2, Mare Nostrum, Mare Cognitum, grass runway, and blocky crater. Power spectral densities for the three experimentally cratered surfaces have been scaled up for direct comparison with the three natural terrains. PSD curves for Mare Cognitum and grass runway from Jaeger and Shuring (1966). PSD curve for blocky crater taken from unpublished data of R. J. Pike.

between. Terra Alta has more craters at the largest size and fewer at smallest size than both Exemplum 2 and Nostrum. Although the number of larger craters for Nostrum is the same at the 30-cm size as for Exemplum, the larger craters of Nostrum are very subdued. For sizes between about 2 and 20 cm, Mare Nostrum has fewer craters than Exemplum. For the 0.8-cm size, they have about the same number.

These frequency distributions are consistent with the previous observations. Terra Alta has the roughest surface—particularly at the smaller frequencies as shown by the PSD curves. Mare Nostrum is the smoothest and has the lowest PSD curve, which is consistent with the crater counts.

Crater frequencies for the steady state of level Mare Exemplum 2 and the steady-state surface of Mare Exemplum 3 (fig.

9*F*), which had an initial slope of 15°, are nearly the same for craters 13.98 cm and less. The similarity of the two crater-frequency distributions might be expected because the crater-production frequency distributions were the same.

The flexure in the steady-state crater-frequency distributions near craters of 6-cm diameter correlates with a flexure in the crater-production frequency distribution (see fig. 9*A*–*D*). Inspection of the diameters listed in table 1 shows the cause of the flexure. For a more uniform crater-production frequency distribution, the diameters of the craters in each adjacent class should have a ratio of 2 for the frequency scheme employed. This clearly is not true for the craters 4.2 cm across. The ratio

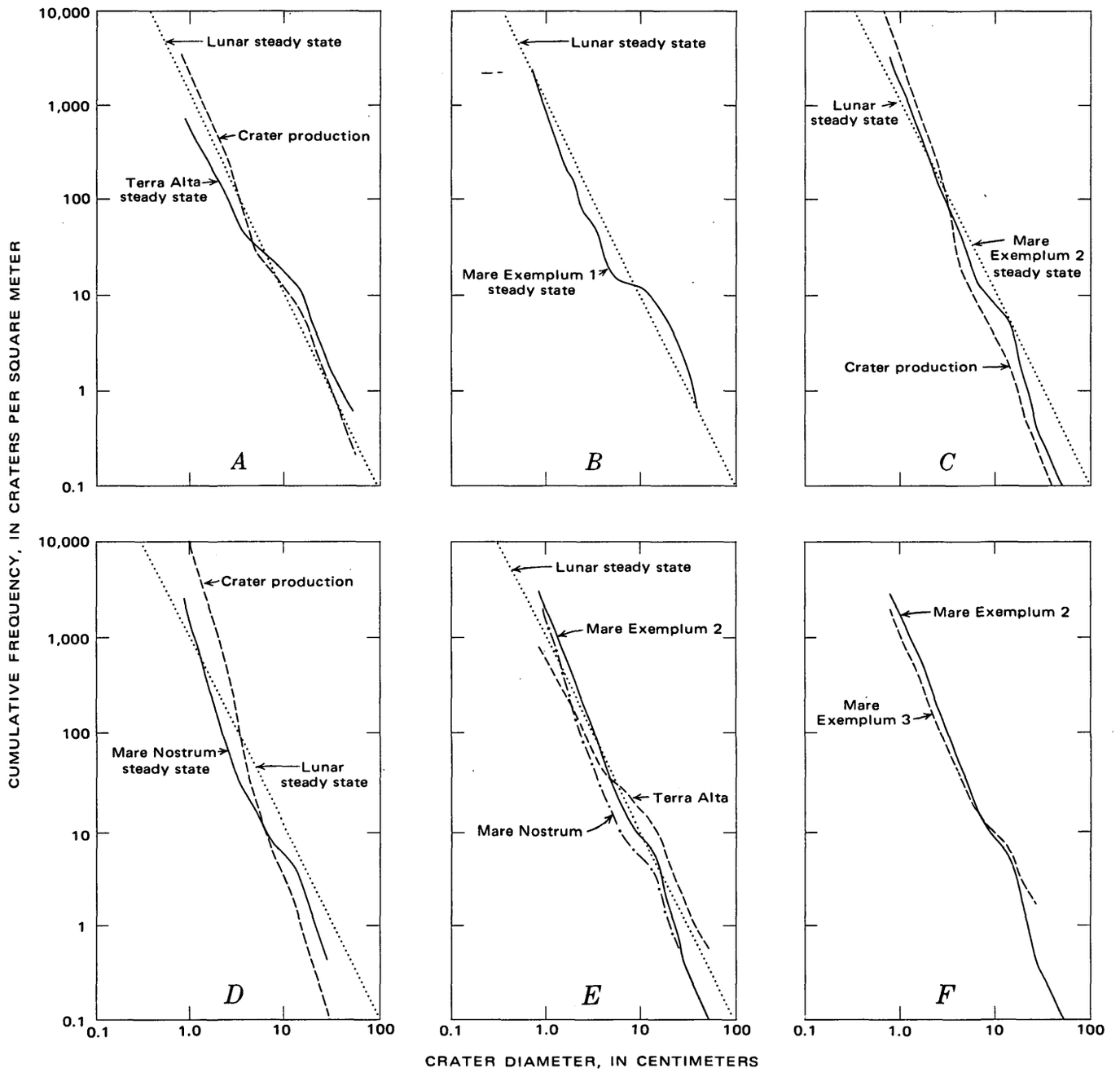

Figure 9.—Steady-state cumulative frequency distributions of craters. *A*–*D*, For experimental surfaces (solid lines), Moon (dotted lines), form of crater-production frequency distributions (dashed lines); *A*, Terra Alta; *B*, Mare Exemplum 1; *C*, Mare Exemplum 2; *D*, Mare Nostrum. *E*, Experimental and lunar steady state. *F*, Mare Exemplum 2 and 3.

with the next larger size crater (13-cm diam) is 3.1, and for the next smaller size crater (2.5-cm diam), the ratio is 1.7. Thus, the flexure arises from the fact that 4.2-cm-diameter craters were too small for their corresponding frequencies.

COMPARISON WITH LUNAR DATA

The experimental surfaces are very Moon-like in many respects. In particular, the surfaces are characterized by craters, below a limiting size, with a continuum of states of preservation. Surfaces imaged by the three Ranger Spacecraft are good examples of analogous terrains. All three surfaces, at the fine scale, have craters ranging in form from eumorphic or fresh to very subdued (Trask, 1966). Surfaces around the Surveyor Spacecraft are similar (Shoemaker and others, 1967). In the near field of Surveyor I, craters 6 m across and less have a continuum of crater morphologies; near Surveyor VII, craters 1 or 2 m across and less range from fresh to very subdued (Shoemaker and others, 1967). The continuum of crater morphologies is also evident in Apollo photographs. Thus, the experimental surfaces are a good miniature simulation of the lunar surface.

Terrain descriptors are similar for the experimental surfaces and the fine-scale lunar surface represented by Mare Cognitum. Cumulative slope-frequency distributions for the experimental surfaces, Mare Exemplum 1 and 2 and Mare Cognitum, can be approximately described by an exponential function for 97 percent of the sample (fig. 6). This is also true for Terra Alta, but Mare Nostrum deviates from the simple exponential function at very small slope angles (fig. 4). Power spectral densities also show similarities between the experimental and lunar surfaces. As shown in figure 8, power spectral densities for Mare Cognitum are similar in form and magnitude to scaled-up power spectral densities for the experimental surfaces. Indeed, the value of the intercept of the PSD curve at 1.0 cycle/m is near $10^{-3.75}$, which compares well with the value of K for Mare Nostrum and is one-half of the value of K for Mare Exemplum 2. Additionally, the PSD curves for the experimental surfaces bracket the curve of Mare Cognitum between 0.2 and 0.6 cycle/m. Had the scaling factor of PSD for the experimental surfaces been one-tenth that employed in figure 8, the PSD curves of the experimental surfaces would still bracket the curve for Mare Cognitum because the slope of most of the lowermost part of the Cognitum curve is near -3.

Crater-frequency distribution curves for the experimental steady-state surfaces are all close to the lunar steady-state crater-frequency distribution (fig. 9). However, the form of the distributions differs from each other and the idealized lunar steady-state curve. Both the Nostrum and Exemplum 2 curves are below the lunar curve at the large sizes, whereas the Terra Alta curve is above it. At the smallest sizes, Terra Alta crater frequencies are below the lunar curve, whereas Nostrum and Exemplum 2 are above it. All three steady-state curves show a flexure just below the 13-cm size that corresponds to a flexure in the crater-production curve. Despite these minor shortcomings, the steady-state crater-frequency distributions are close in form and magnitude to the lunar steady-state curve. Additionally, the frequency distribution for Mare Exemplum 3, which had an initial 15° slope, is well above the expectations for lunar surfaces with comparable slopes. Thus, we must call upon another mechanism of destruction of craters on lunar slopes. Such mechanisms might include seismic accelerations and thermal expansion and contraction.

CONCLUSIONS

The experimental steady-state surfaces are reasonably good simulations of lunar steady-state surfaces in at least four ways: (1) Craters of each size range from fresh-appearing ones to those so subdued that they are barely discernible, (2) the form of cumulative slope-frequency distributions tends to be an exponential form, (3) power spectral densities are similar in form and, when the experimental surfaces are scaled up, are similar in magnitude, and (4) the steady-state crater-frequency distributions are similar.

The main differences between the experimental and lunar surfaces are: (1) The range of crater sizes produced in the experiment falls far short of those expected for the Moon, (2) a continuum of crater sizes are produced on the Moon, whereas seven discrete crater sizes were produced in the experiments, and (3) the frequencies of impacts producing craters between 4.2 and 13 cm across were inconsistent with the expectations for the Moon and the intended distributions for the experiments. The effects of these shortcomings are clear. Absence of craters smaller than 0.52 cm clearly affects the destruction of craters that size and larger. Such craters exist on the Moon as the small microcraters on lunar rocks (Morrison and others, 1972). The presence of larger craters on the Moon also affects crater lifetimes. It is difficult to assess the effect of a continuum of crater sizes on the production curve. However, we believe that a more regular crater-frequency distribution would be obtained if the experiment had included a continuum of crater sizes. The difference between intended and actual craters produced for sizes between 4.2 and 13 cm across correlates with the flexure in the crater-count curves. Despite these differences, the experimental surfaces adequately simulate the lunar surface.

REFERENCES CITED

Akademiya Nauk SSSR, 1966, The first panoramic views of the lunar surface: U.S. Natl. Aeronautics and Space Adm. Tech. Translation F-393, 125 p.

Gault, D. E., 1970, Saturation and equilibrium conditions for impact cratering on the lunar surface—criteria and implications: Radio Science, v. 5, no. 2, p. 273–291.

Hopkins, B. T., Friedman, S. J., Halbrook, J. W., 1966, Double projection direct-viewing plotting instruments, Chap. 13, *in* Manual of

photogrammetry, v. 2 [3d ed.]: Falls Church, Va., Am. Soc. Photogrammetry, p. 557–628.

Jaeger, R. M. and Schuring, D. J., 1966, Spectrum analysis of terrain of Mare Cognitum: Jour. Geophys. Research, v. 71, no. 8, p. 2023–2028.

Korn, G. and Korn, T., 1961, Mathematical handbook for scientists and engineers [2d ed.]: New York, McGraw Hill Book Co., p. 1070-1074.

Lugn, R. V., 1964, Photogrammetric mapping of experimental craters: Photogramm. Eng., v. 30, p. 55–58.

Marcus, A. H., 1970, Comparison of equilibrium size distributions for lunar craters: Jour. Geophys. Research, v. 75, no. 26, p. 4977–4984.

Marsden, L. E., 1952, Experimental local length variation for multiplex plotting: U.S. Geol. Survey Topog. Div. Bull., v. 2, no. 1, p. 5–7.

Moore, H. J., 1964, Density of small craters on the lunar surface: U.S. Geol. Survey open-file rept., p. 34–51.

——1971, Geologic interpretation of lunar data: Earth-Sci. Rev., v. 7, p. 5–33.

Morrison, D. A., McKay, D. S., Moore, H. J., and Heiken, G. H., 1972, Microcraters on lunar rocks, *in* Criswell, D. R., ed., Proceedings, 3d Lunar Sci. Conf., v. 3, Physical properties, supp. 3: Cambridge, Mass., The MIT Press, p. 1767–2791.

National Space Science Data Center, 1969, Lunar Orbiter photographic data: Natl. Space Sci. Data Center, Data Users' Note N55DC 69-05, 37 p, Greenbelt, Md.

Nordyke, M. D., and Wray, W., 1964, Cratering and radio-activity results from a nuclear cratering detonation in basalt: Jour. Geophys. Research, v. 69, no. 4, p. 675–689.

Rowan, L. C., McCauley, J. F., and Holm, E. A., 1971, Lunar terrain mapping and relative-roughness anlaysis: U.S. Geol. Survey Prof. Paper 599-G, 32 p.

Rozema, W. J., 1969, The use of spectral analysis in describing lunar surface roughness, *in* Geological Survey research 1969: U.S. Geol. Survey Prof. Paper 650-D, p. D180–D188.

Shoemaker, E. M., 1965, Preliminary analysis of the fine structure of the lunar surface in Mare Cognitum, *in* Ranger VII, Part II, Experimenters' analyses and interpretations: California Inst. Technology Jet Propulsion Lab. Tech. Rept. 32-700, 154 p., Pasadena, Calif.

Shoemaker, E. M., Morris, E. C., Batson, R. M., Holt, H. E., Larson, K. B., Montgomery, D. R., Rennilson, J. J., and Whitaker, E. A., 1969, Television observations from Surveyor, *in* Surveyor program results: U.S. Natl. Aeronautics and Space Adm. Spec. Pub. SP-184, p. 19–128.

Soderblom, L. A., 1970, A model for small-impact erosion applied to the lunar surface: Jour. Geophys. Research, v. 75, no. 14, p. 2655–2661.

Soderblom, L. A., and Lebofsky, L. A., 1972, A technique for rapid determination of relative ages of lunar areas from orbital photography: Jour. Geophys. Research, v. 77, no. 2, p. 279–296.

Trask, N. J., 1966, Size and spatial distribution of craters estimated from Ranger photographs, *in* Ranger VIII and IX, Experimenters' analyses and interpretations: California Inst. Technology Jet Propulsion Lab. Tech. Rept. 32-800, p. 252–263, Pasadena, Calif.

U.S. National Aeronautics and Space Administration, 1965, Ranger VII photographs of the Moon, Part III, Camera "P" series: U.S. Natl. Aeronautics and Space Adm. Spec. Pub. SP-63, 200 p.

—— 1966, Ranger IX photographs of the Moon, Cameras A, B, and P: U.S. Natl. Aeronautics and Space Adm., Spec. Pub. SP-112, 170 p.

—— 1969, Surveyor program results: U.S. Natl. Aeronautics and Space Adm. Spec. Pub. SP-184, 432 p.

—— 1971, Preliminary science report–Apollo 14: U.S. Natl. Aeronautics and Space Adm. Spec. Pub. SP-272, 309 p.

Jour. Research U.S. Geol. Survey
Vol. 2, No. 3, May-June 1974, p. 289—302

TECTONIC TRANSITION ZONE IN THE NORTHEASTERN CARIBBEAN

By MICHAEL S. MARLOW; LOUIS E. GARRISON, RAY G. MARTIN,
JAMES V. A. TRUMBULL; and ALAN K. COOPER;
Menlo Park, Calif.; Corpus Christi, Tex.; Menlo Park, Calif.

Abstract.—Seismic reflection data indicate that the Atlantic plate has been underthrust beneath the Caribbean plate east of the Lesser Antilles. The data further reveal that the transition from underthrust to strike-slip plate motion occurs near lat 19.3° N. and long 62° W. in alinement with the Anegada Trough. Oceanic basement and reflectors above basement have not been detected beneath the landward wall of the Puerto Rico Trench west of the transition zone. Southeast of the zone, the horizontal distance over which the reflectors and basement can be traced beneath the landward wall (outer part of the Lesser Antilles rise) systematically increases from a few kilometers in the north to as much as 37 km near lat 16.5° N. If a thrust fault emerges at the landward trench wall, the data suggest that a décollement exists between reflectors above basement and an overlying acoustically transparent zone. Gravity and seismic refraction data indicate a thick accumulation of low-density, low-velocity material beneath the Lesser Antilles rise, possibly sediments scraped off the underthrusting Atlantic plate, although massive slumping might cause a similar low-density configuration. The magmatic history of the Lesser Antilles arc suggests two periods of underthrusting, one in the Mesozoic or early Cenozoic and a second in the late Cenozoic. Although the magmatic history of the Lesser Antilles apparently began in the Mesozoic, its Cenozoic history is remarkably similar to the Cenozoic histories of circum-Pacific arcs. Magmatic histories in both areas suggest that island arc evolution in the Cenozoic may have worldwide synchroneity.

Recent seismicity studies indicate that the northeastern Caribbean is a tectonic transition zone between underthrusting and strike-slip segments of the Caribbean-Atlantic (Americas) plate boundary (Sykes and Ewing, 1965; Molnar and Sykes, 1969). Seismic reflection data (Chase and Bunce, 1969; Bunce and others, 1971) show that apparent oceanic basement and overlying sedimentary beds underlie the landward wall of the southeastern Puerto Rico Trench. Earlier refraction data (Ewing and others, 1957; Officer and others, 1957, 1959) also indicated that the Atlantic crust dips beneath the island arc of the eastern Lesser Antilles.

Because reflection studies of the circum-Pacific trenches (except perhaps off the Washington-Oregon coast, Silver, 1972) have not clearly demonstrated underthrusting of oceanic crust beneath landward trench walls (Scholl and others, 1968, 1970; Marlow, Scholl, and Buffington, 1973, Marlow, Scholl, Buffington, and Alpha, 1973; von Huene and Shor, 1969; von Huene, 1972) and because the new theories of global tectonics predict that trenches are sites of crustal assimilation (underthrusting), we investigated the "type area" of underthrusting in the northeast Caribbean. Delineation of trench structures in the best documented area of underthrusting in the Atlantic will perhaps lead to a better understanding of the structures of the Pacific trenches.

Acknowledgments.—This study was part of the International Decade of Ocean Exploration (IDOE) program in the Caribbean area, partly supported by the National Science Foundation. The senior author is indebted to the U.S. Geological Survey for providing a Postdoctoral Research Associateship to complete this work. J. E. Newcombe assisted in manuscript preparation; D. W. Scholl and E. A. Silver aided immeasurably in critical review of the manuscript by contributing thought-provoking discussion.

GEOLOGIC SETTING

Only a brief summary of the geologic history of the Lesser Antilles arc is presented here. For a complete review of Caribbean geology, the reader is referred to the thorough work of Nagle (1971) and for the most recent summary of the Lesser Antilles to the work of Martin-Kaye (1969).

North of Dominica Island the islands of the Lesser Antilles are divided into two chains (fig. 1). The outer or eastern islands are referred to as the Limestone Caribbees (including Anguilla, St. Martin, Antigua, Grand Terre, La Desirade, and Marie Galante, fig. 1). They are composed of middle Eocene to late Oligocene volcanic rocks (except La Desirade, see below) capped by late Oligocene and early Miocene limestones, and they were uplifted in the late Miocene (Nagle, 1971). The inner or western Lesser Antilles are referred to as the Volcanic Caribbees (including St. Christopher, Montserrat, and Guadeloupe, fig. 1) and are composed of latest Miocene or early Pliocene to Holocene volcanic rocks (Nagle, 1971). Dominica is geologically similar to the youngest Volcanic Caribbees, although it is not known if older rocks underlie the island. South of Dominica the two periods of volcanism are represented by rocks forming the single island chain that extends as far south as Grenada Island (see Nagle, 1971, fig. 3).

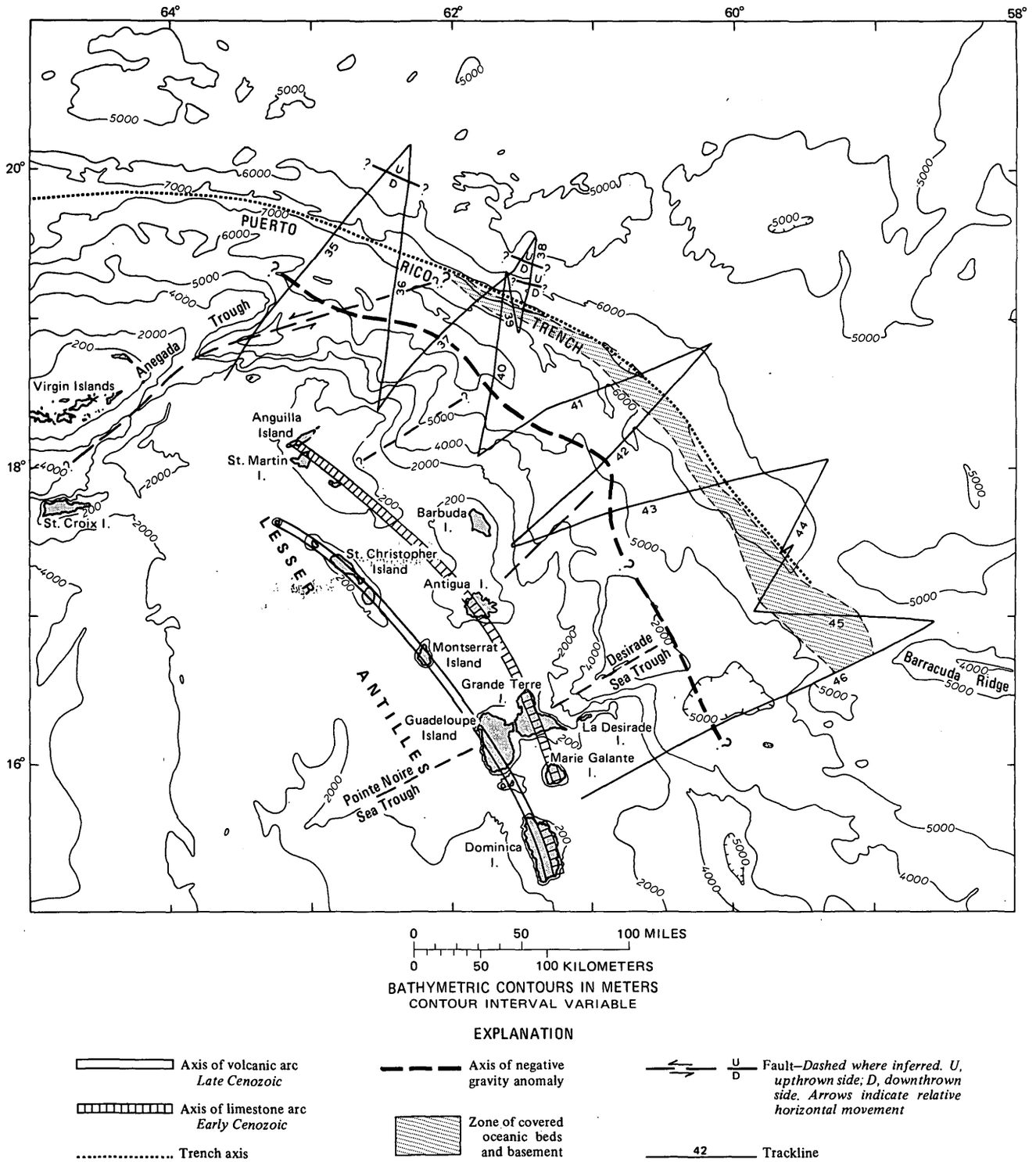

Figure 1.–Bathymetric chart of the northeastern Caribbean showing location of track lines (numbers refer to profiles U-35, U-36, and so on). Axes of volcanic and limestone arcs from Fink (1972). Faults from Tomblin (1974) and this study.

The only known intrusive rocks are small exposures of diorite of latest Eocene or early Oligocene age on St. Martin and St. Bartholomew Islands, probably older trondhjemite on La Desirade (described below), and an occurrence on Grenadine Island of possible Miocene or Pliocene age (Martin-Kaye, 1969). Major tectonic activity occurred in the Lesser Antilles arc during two periods, the Eocene and Oligocene(?) and the late Miocene to early Pliocene (Martin-Kaye, 1969), although Martin-Kaye doubted the evidence of Oligocene tectonism. Remarkably similar timing of tectonism and magmatism has been noted in some circum-Pacific island arcs (Mitchell and Reading, 1971; Marlow, Scholl, Buffington, and Alpha, 1973).

The only published radiometric dates from the Lesser Antilles are from La Desirade (Fink, 1970, 1972; Nagle, 1971), where dating of a spilite-keratophyre sequence and an intrusive trondhjemite unit revealed an age range of from 50 to 140 m.y., much older than any previous age estimates based on paleontologic control. The arc could thus have been an older feature continuous with the Greater Antilles island arc (Fink, 1970; Nagle, 1971).

MARINE GEOPHYSICAL INVESTIGATIONS

Seismic reflection, magnetic, and free-air gravity profiles

Lesser Antilles Ridge.—On the eastern edge of the Lesser Antilles Ridge crest, seismic reflection records from four crossings (fig. 1) reveal a few hundred meters (0.2–0.3 s) of stratified sediments overlying acoustic basement (U-35, U-36, and U-37, fig. 2). Only one line, U-46 (fig. 9), which crosses most of the eastern half of the ridge crest, shows a thick sequence, about 1.8 km (2 s), of sedimentary deposits above an acoustic basement; this basement rises under the eastern edge of the ridge crest and is associated with a gravity high and magnetic low (fig. 9). The basement high may form part of an eastern spur of a topographic ridge that emerges as La Desirade Island farther north (fig. 1).

On all the profiles except U-46, the free-air gravity anomaly over the eastern Lesser Antilles Ridge increases from about -150 to -100 mGal near the base of the ridge to as much as 100 mGal over the edge of the ridge crest. To the west beyond the limits of the profiles, the anomalies continue to increase (see Bowin, 1971, for profiles across the entire ridge crest). The anomaly on line U-46 (fig. 9) crests at about 120 mGal over the outer basement high associated with La Desirade (fig. 1).

Lines that extend westward more than 10 km over the ridge crest, U-35 and U-46 (figs. 2, 9), show magnetic anomalies of slightly more than 200 gammas over the outer ridge crest. Such anomalies are expected over a volcanic arc and in fact have been observed across the entire outer or eastern limestone arc as well as the inner volcanic arc (Bunce and others, 1971).

Lesser Antilles rise.—As used informally in this paper, the Lesser Antilles rise refers to the gently sloping topographic ramp between the base of the Lesser Antilles Ridge and the southeastern extension of the Puerto Rico Trench (fig. 1). The rise is underlain by two structural provinces, an inner province about 50 km wide that skirts the base of the ridge and an outer one that extends to the axis of the trench. The inner province is characterized by flat-lying or gently dipping beds that average about 1.0 to 1.5 km (1.0–1.5 s) thick; they are thickest near the base of the ridge (figs. 2–9). On two profiles, U-35 and U-42 (figs. 2, 6), the dip of these layers appears to increase with depth, but on other profiles the deposits of the inner province are relatively undeformed; they presumably are partly of Neogene age. In contrast, the outer province of the rise is characterized by a lack of well-defined reflectors. A notable exception is the area of inner trench wall crossed on profiles U-40 to U-46; here ridgeward-dipping beds and oceanic basement underlie the outer part of the rise (figs. 3–9). Scattered coherent reflection horizons elsewhere in the outer province suggest layered deposits; refraction and gravity data also indicate low-velocity, low-density material beneath the outer rise. These deposits have apparently been deformed to such a degree that only discontinuous internal reflecting horizons remain.

The minimum in the free-air gravity anomaly is generally centered over the central area of the rise except along lines U-41, 43, and 46 (figs. 5, 7, and 9), where the low occurs closer to the Lesser Antilles Ridge and over the inner part of the rise. The rise is magnetically quiet except for a 100-gamma anomaly along line U-45 (fig. 8), where a basement high of oceanic crust underlies the outer part of the rise.

Southeastern Puerto Rico Trench.—The seaward edge of the outer part of the rise forms the inner or landward flank of the Puerto Rico Trench. On two northerly profiles, U-35 and U-36 (figs. 1, 2), neither oceanic basement nor reflecting horizons above basement extend landward beneath the inner trench flank (note that the apparent 2-km-wide "overlap" of subtrench reflecting surfaces beneath the inner wall is a crossover effect caused by the recording of slant-angle seismic signals, see Marlow, Scholl, and Buffington, 1973). The trench here is filled with about 800 to 900 m (0.9–1.0 s) of flat-lying pelagic or hemipelagic sediments. To the south, however, landward-dipping oceanic basement and overlying reflecting horizons can be traced beneath the inner trench flank (figs. 2–9). On lines U-41 and U-43 the pelagic fill in the trench dips gently landward (figs. 5, 7). The horizontal distance over which oceanic basement can be traced beneath the inner flank of the trench increases southward from a few kilometers on line U-37 (fig.2) to a maximum of 33 to 37 km on lines U-45 and U-46 (figs. 8, 9). Where reflecting horizons occur beneath the inner flank, they are conformable to the underlying basement, suggesting pelagic-type deposits (figs. 5–9). Above these beds is an acoustically transparent zone in which only a few scattered internal reflectors are observed (figs. 2–9).

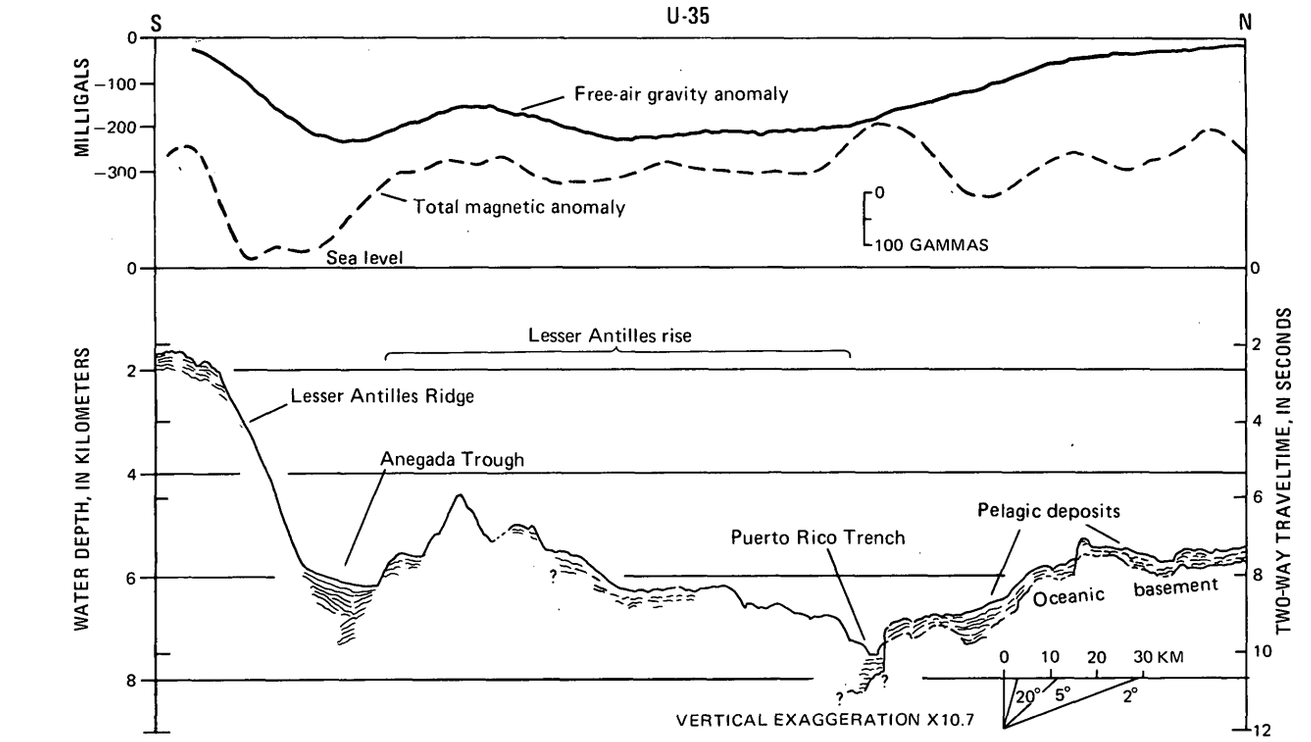

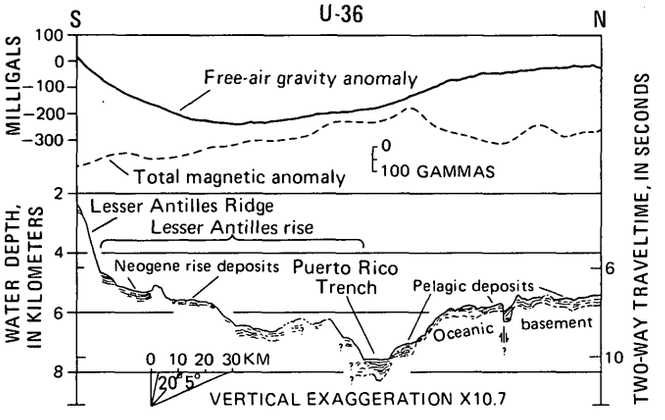

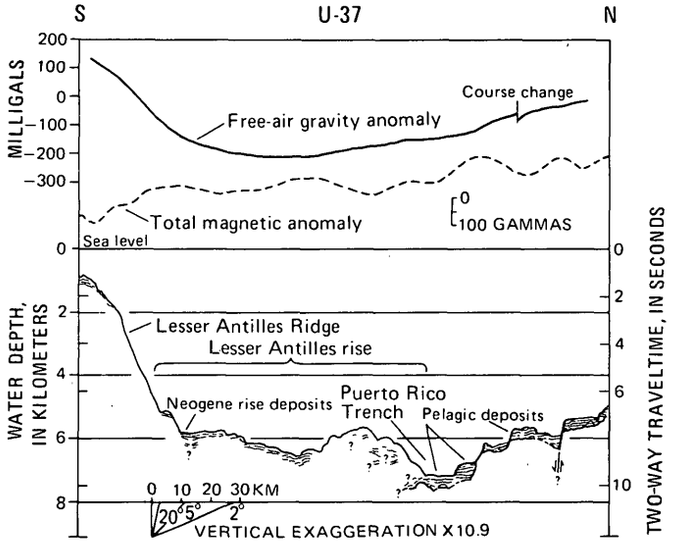

Figure 2.—Gravity and magnetic profiles and interpretative drawing of seismic reflection profiles U-35, U-36, and U-37 which cross the eastern edge of the Lesser Antilles Ridge, the Anegada Trough, the Lesser Antilles rise, and the Puerto Rico Trench. See figure 1 for location. Scale in seconds in two-way traveltime; scale in kilometers is for water depth only and is based on an assumed seismic velocity in water of 1.5 km/s. True slope angles are indicated by diagram under horizontal scale. Bottom is indicated by a heavy line, coherent reflectors by fine lines. Acoustic basement, where distinguishable, is shown by a heavy line; at many places it is represented by the tops of curved hyperbolic reflection signatures.

The seaward or outer flank of the trench is underlain by as much as 1 km (1.1 s) of pelagic deposits conformably overlying oceanic basement. Strong, linear reflecting horizons suggestive of turbidite deposits are observed only in the southernmost profiles, U-45 and the eastern end of U-46 (figs. 8, 9), where the Puerto Rico Trench is poorly formed as

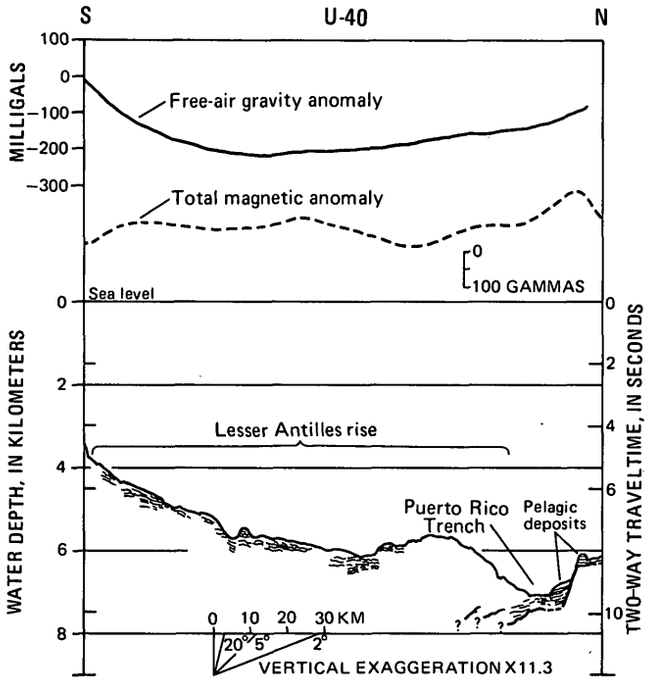

Figure 3.—Gravity and magnetic profiles and interpretative drawing of seismic reflection profile U-40 across the Lesser Antilles rise and Puerto Rico Trench. See figure 1 for location, figure 2 for explanation of symbols.

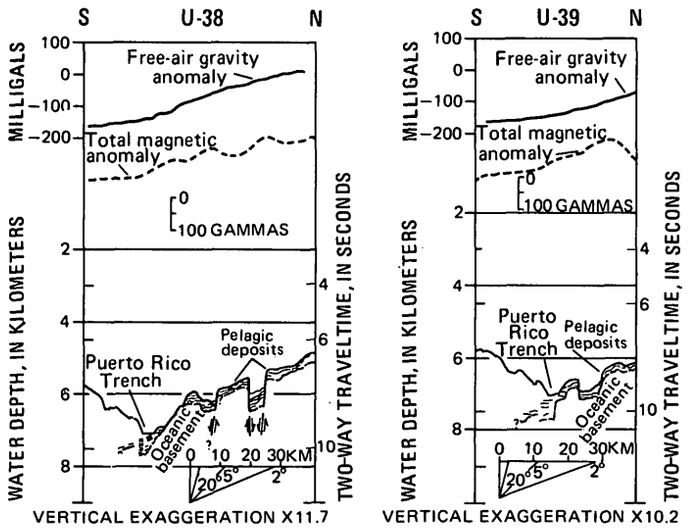

Figure 4.—Gravity and magnetic profiles and interpretative drawing of seismic reflection profiles U-38 and U-39 across the outer part of the Lesser Antilles rise and Puerto Rico Trench. See figure 1 for location, figure 2 for explanation of symbols.

a geomorphic feature. These turbidite beds are apparently part of the deposits of the western distal end of the Barracuda Abyssal Plain (Birch, 1970; Embly and others, 1970).

Several normal faults offset the oceanic basement and overlying pelagic sediments on the seaward flank of the trench near lat 19° to 20° N. (figs. 1, 2, 4); farther south the seaward flank is underlain by undeformed pelagic deposits and oceanic basement, both unfaulted and gently dipping toward the trench axis (figs. 5–9). Oceanic basement crops out at Barracuda Ridge near lat 16.7° N. on profile U-46 (figs. 1, 9), from which basalt has been dredged (Birch, 1970; Bonatti, 1971).

No magnetic anomalies are associated with the trench or trench flanks or with the configuration of oceanic basement, except for the magnetic high above a basement high under the outer part of the rise or the inner flank of the trench on line U-45 (fig. 8). The oceanic basement high is apparently a continuation of Barracuda Ridge. As noted above, the axis of the free-air gravity anomaly low does not coincide with the axis of the trench but rather is displaced towards the rise.

Gravity models

Two profiles, U-36 and U-46, across the northern and southeastern Puerto Rico Trench, respectively (fig. 1), were used to construct the theoretical two-dimensional gravity models shown in figures 10–12. A 32-km-thick standard sea-level section with a total average section density of 2.87 g/cm^3 and oceanic mantle density of 3.5 g/cm^3 was assumed (Talwani and others, 1959; Rose and others, 1968; Hayes, 1966). The upper sedimentary layers with densities of 2.0 g/cm^3 and less are based on the seismic reflection data (figs. 2, 9). The refraction data of Officer, Ewing, and coworkers, 1957, 1959; (Ewing and others, 1957), were used to constrain the configuration of the crustal layers and the M discontinuity.

Two slightly different models were derived for the northerly profile, U-36 (figs. 10, 11). Both models show a thinning of the crust seaward of the trench (at a distance of 0–40 km in the models), which is also supported by the published refraction data. Landward of the trench the upper crust thickens considerably beneath the rise (layers with densities of 2.3, 2.6, and 2.9 g/cm^3 at a distance of -80 to 0 km both models), and the M discontinuity dips down toward the arc. In order to match the steep gradient of the gravity curve at the rise-ridge boundary, a shallowing of high-density, lower crust and mantle is required. For the first model (fig. 10) the surface of the lower crust (3.1 g/cm^3 rises from a depth of about 20 to 25 km to about 10 to 15 km and is underlain by dense mantle (3.5 g/cm^3). The mantle dips landward, and the upper crustal layers (2.7, 2.8 g/cm^3) thicken to form a root beneath the arc.

Since published refraction control is not complete enough to substantiate the first model and since refraction data are the main constraints on gravity models, a second one (fig. 11) was derived for the same profile but with a different crust-mantle configuration at the rise-ridge boundary. A slab of upper mantle (3.3 g/cm^3) less dense than typical oceanic mantle (3.5 g/cm^3) dips beneath the arc in place of less dense upper crust. A choice between the models cannot be made without greater refraction coverage.

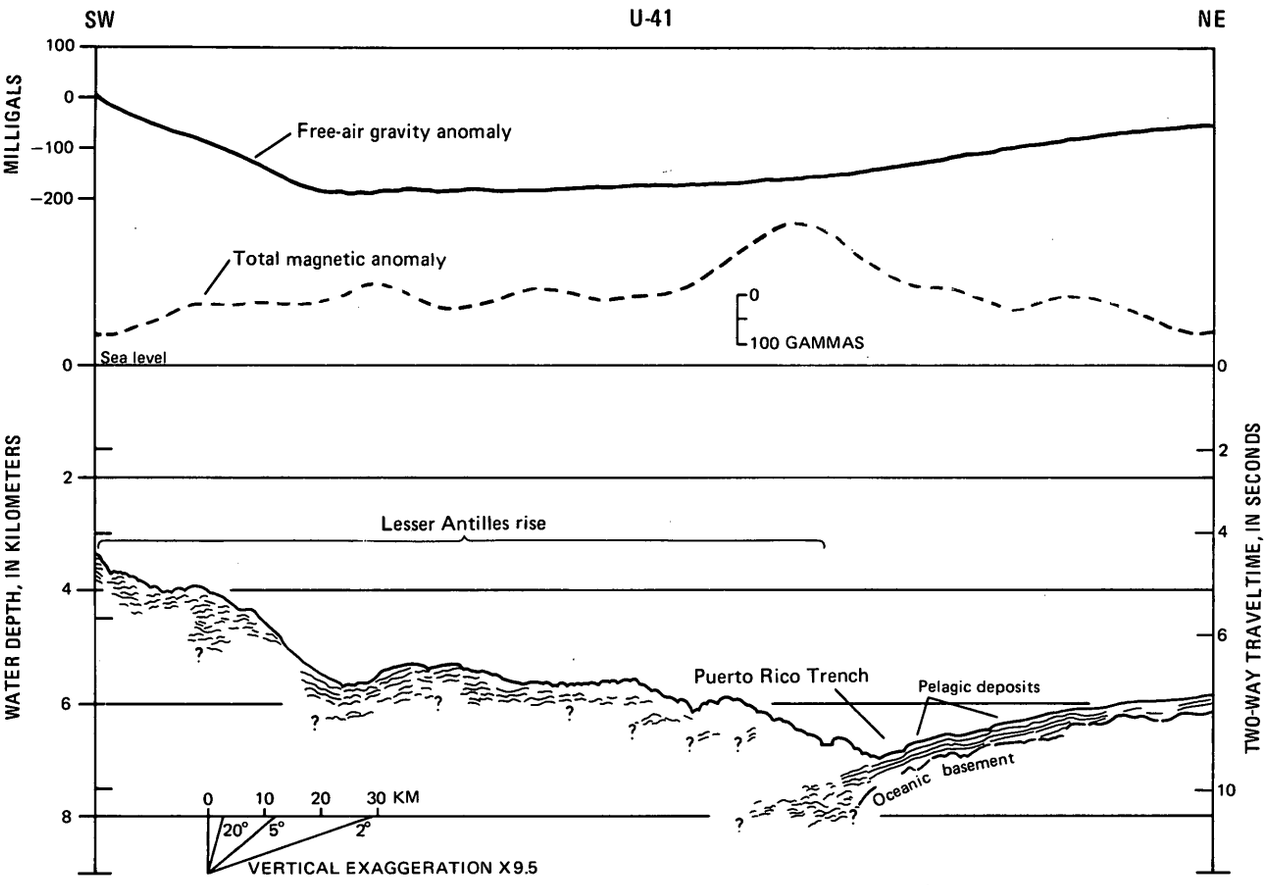

Figure 5.—Gravity and magnetic profiles and interpretative drawing of seismic reflection profile U-41. See figure 1 for location, figure 2 for explanation of symbols.

The more southerly model, for profile U-46 (fig. 12) is similar to that for line U-36 except that it was not necessary to raise high-density material at the rise-ridge boundary because of the more gradual decrease in water depth and gravity gradient. Also, as in the northern profile, the crust thickens landward beneath the rise, and the M discontinuity dips towards the arc. A root of thickened lower crust (3.1 g/cm^3) forms the core of the ridge. A thinner crust beneath the trench is not required on the basis of the gravity data, but unfortunately, there is no refraction coverage in this area to confirm the derived crustal configuration.

DISCUSSION

Formation of the Lesser Antilles Ridge

Until the discovery of a Late Jurassic trondhjemite unit on La Desirade by Fink (1970, 1972) the oldest known rocks in the Lesser Antilles Islands were early or middle Eocene (Martin-Kaye, 1969; Nagle, 1971). Fink (1972) notes many similarities between the basement rocks of La Desirade and those of the Greater Antilles, which led him to suggest that the arc of the Lesser Antilles may have a continuous Mesozoic core extending from the Greater Antilles to at least Guadeloupe-La Desirade and possibly farther south to the Venezuelan Antilles off South America. Further sampling, especially in submerged areas, is needed to establish this likelihood, as well as to date firmly the origin of the ridge.

Fink (1972) also suggests that north of Dominica the inner volcanic arc began to form by middle or late Miocene volcanism along the western flank of the older arc. He further supposes that the older arc rifted extensionally during the interruption of volcanism in the Oligocene or early Miocene in a manner similar to the crustal dilation models for frontal arcs of the Pacific (Karig, 1970, 1971). To explain the superposition of younger and older arcs south of Dominica, Fink proposes that a filled Lesser Antillean trench (Hurley, 1966; Chase and Bunce, 1969), which may be a filled southeastern extension of the Puerto Rico Trench, produced a buttressing effect and limited crustal extension in the southern half of the arc.

A major transverse fault should have developed north of Dominica as a result of different extension rates in the two island-arc segments. Fink (1972, fig. 5) cites as evidence for

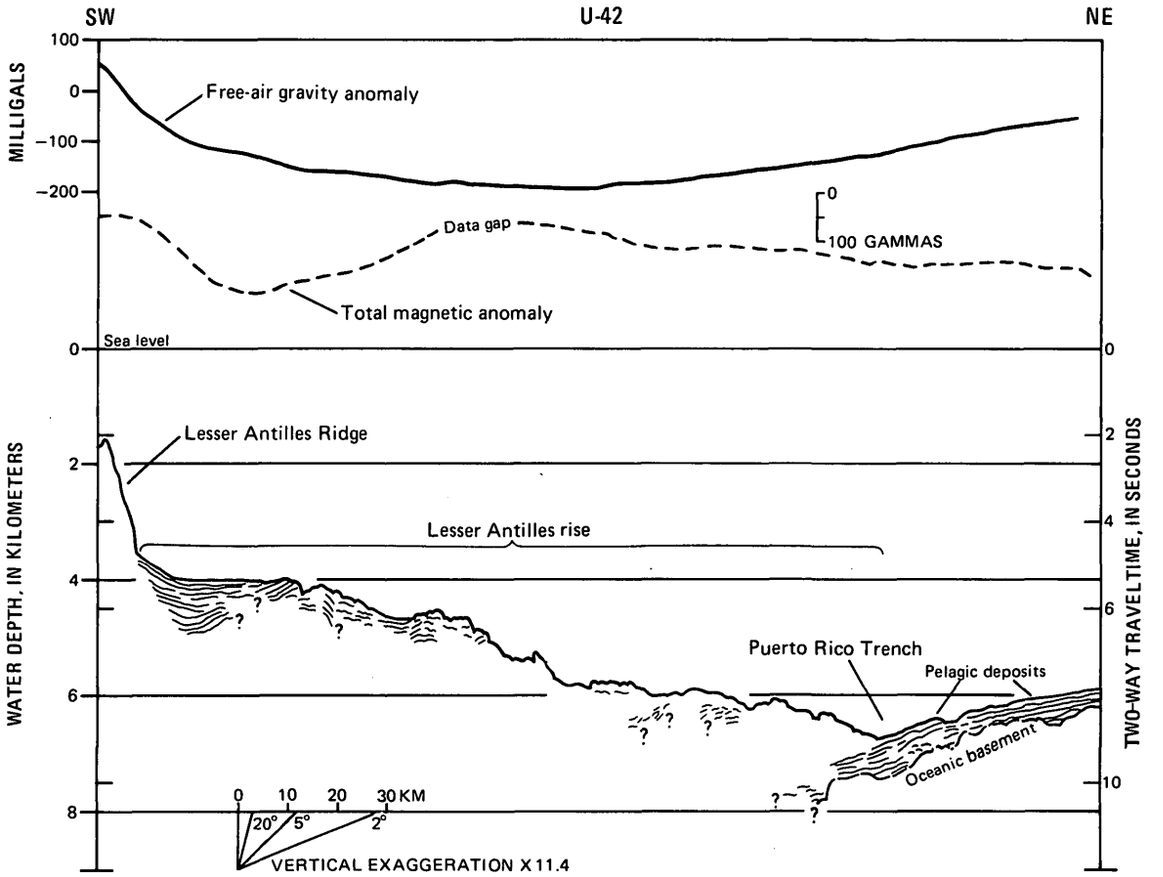

Figure 6.—Gravity and magnetic profiles and interpretative drawing of seismic reflection profile U-42. See figure 1 for location, figure 2 for explanation of symbols.

this fault the alinement of Desirade Sea Trough and Pointe Noire Sea Trough on opposite sides of the ridge crest (fig. 1) and a major contrast in coherency of subbottom reflectors beneath the Lesser Antilles rise on a north-south profile taken by Collette, Ewing, Lagaay, and Truchan (1969). We also note an apparent alinement of epicenters along Fink's proposed fault zone (Tomblin, 1974), suggesting a transverse fault zone here (fig. 1).

Although none of our profiles crossed Fink's proposed fault zone, two of them (U-43, fig. 7 and U-46, fig. 9) crossed the Lesser Antilles rise north and south of the fault zone; no difference in subbottom reflectivity was noted. The difference in subbottom reflectivity on the profile of Collette, Ewing, Lagaay, and Truchan (1969, figs. 8 and 10) appears to result from the fact that the southern end of their profile is over the northern nose of Barbados Ridge, a much shallower feature than the Lesser Antilles rise, which the northern half of their profile crosses. The smooth, undeformed reflection horizons resolved under the Barbados Ridge, but not under the rise, may be relatively young draped sedimentary beds derived from the ridge; more deformed beds may occur at depths beneath the smoothly layered upper beds of the ridge.

Whether the core of the entire Lesser Antilles Ridge is Mesozoic and early Tertiary in age is unknown; however, it is certain that the volcanism that formed the older arc continued into the lower Oligocene and that parts of the arc had appeared above water somewhat earlier in the Eocene (Martin-Kaye, 1969; Nagle, 1971). During the Miocene the arc subsided, and the limestone cap formed on the older islands. Renewed volcanism and uplift occurred at the end of the Miocene or the beginning of the Pliocene, forming the younger or inner volcanic arc and exposing parts of the older ridge. Tectonic activity has continued to the present (Martin-Kaye, 1969; Nagle, 1971). If volcanic activity is related to underthrusting of the Atlantic beneath the Lesser Antilles, then two periods of underthrusting are suggested, one in Mesozoic(?)

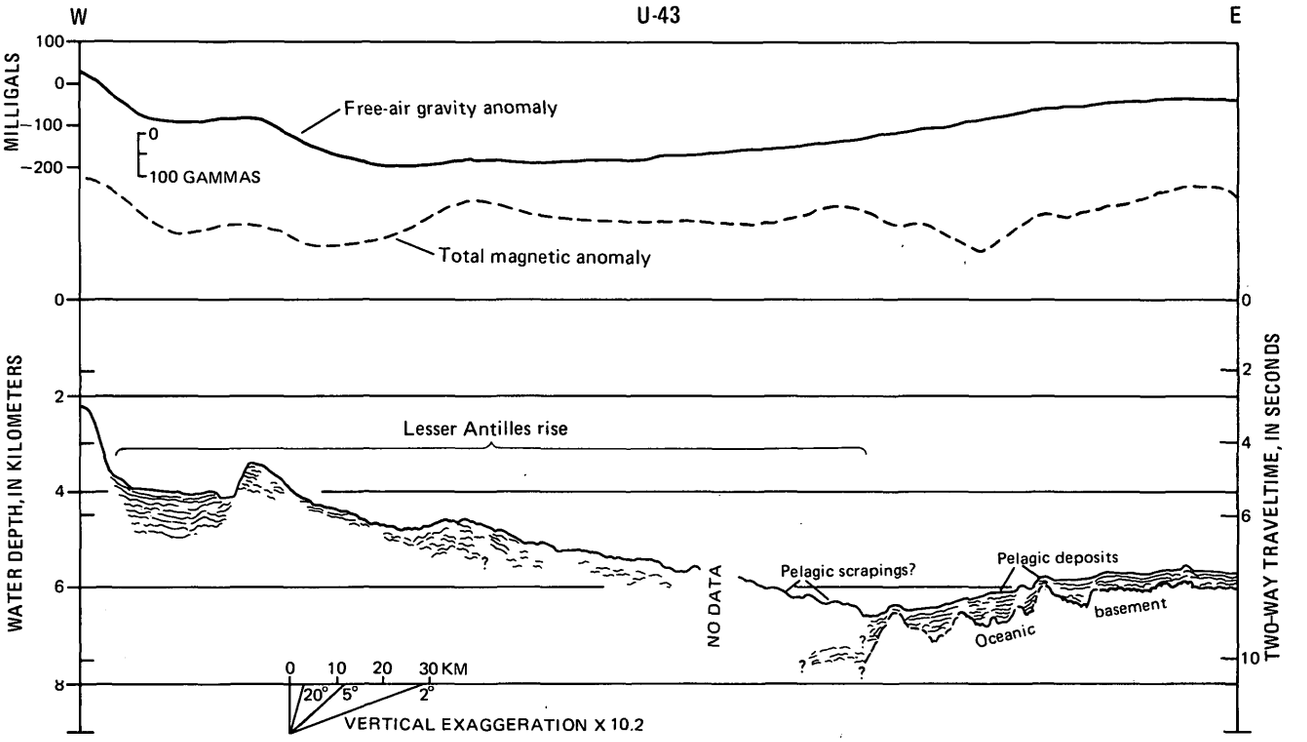

Figure 7.—Gravity and magnetic profiles and interpretative drawing of seismic reflection profile U-43. See figure 1 for location, figure 2 for explanation of symbols.

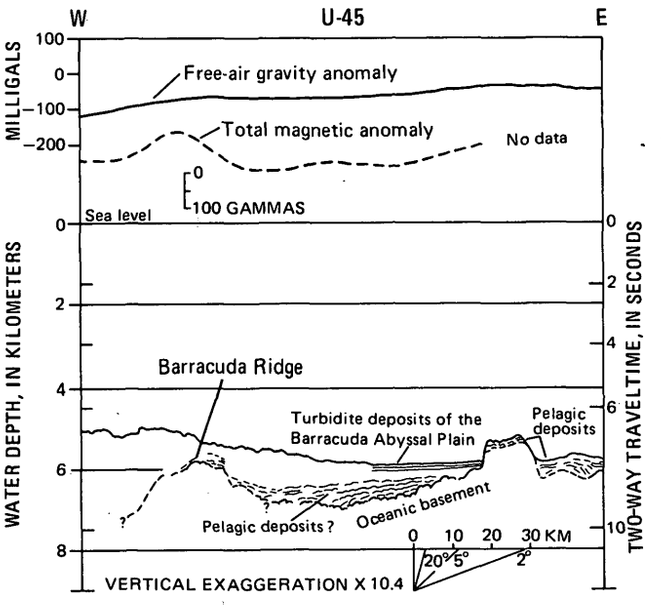

Figure 8.—Gravity and magnetic profiles and interpretative drawing of seismic reflection profile U-45 which crosses the outer part of the Lesser Antilles rise, Barracuda Ridge and the Puerto Rico Trench. Here the trench is poorly formed as a geomorphic feature and is partly underlain by turbidite deposits of the Barracuda Abyssal Plain. See figure 1 for location, figure 2 for explanation of symbols.

through early Tertiary time and one since the late Miocene (Fink, 1971). Remarkably similar Cenozoic magmatic histories have been deduced for the Aleutian arc (except for the likelihood of Mesozoic volcanism, Marlow, Scholl, Buffington, and Alpha and others, 1973; Scholl and others, 1973) and other circum-Pacific arcs (Mitchell and Bell, 1970; Mitchell and Reading, 1971).

Formation of the Lesser Antilles rise and southeastern Puerto Rico Trench

Evidence for the transition from strike-slip to underthrust motion between the Caribbean and Atlantic (Americas) plates predicted by the seismicity studies of Molnar and Sykes (1969) near lat 19° N. is apparent in the structure of the outer part of the rise. On profiles U-37 to U-46 (figs. 2–9) oceanic basement and overlying reflection horizons can be traced landward from the trench between the outer part of the rise, and the horizontal distance over which these reflectors can be traced beneath the rise increases systematically southward from a few kilometers on profile U-37 (lat 19° N.) to about 37 km on profile U-36 (lat 16.5° N.). The two northernmost profiles, U-35 and U-36 (fig. 2), show no oceanic basement or dipping beds beneath the outer rise. Hence the transition in relative plate motion, as indicated by the reflection profiles, lies somewhere between lines U-36 and U-37 in the vicinity of

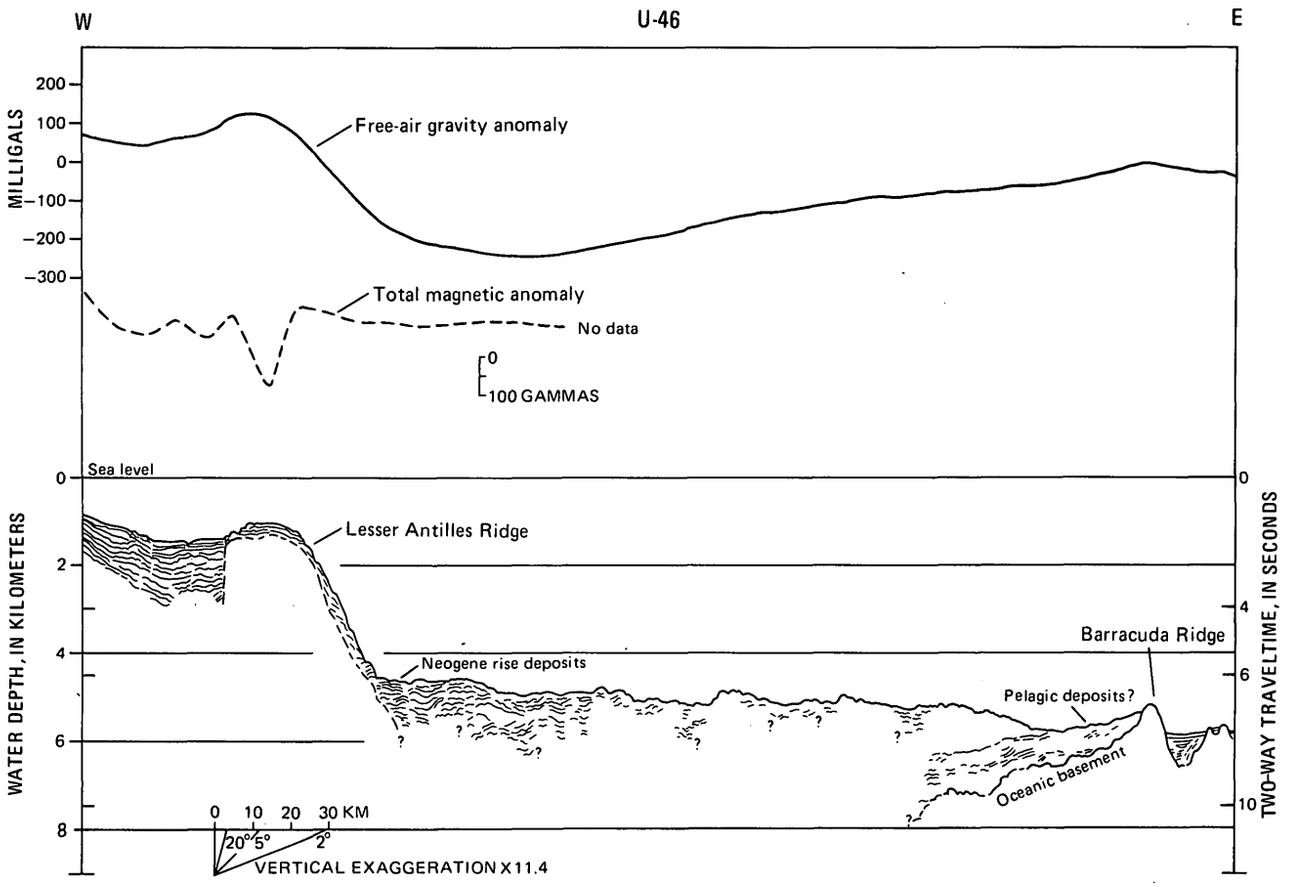

Figure 9.—Gravity and magnetic profiles and interpretative drawing of seismic reflection profile U-46. Here the southeastern extension of the Puerto Rico Trench is a swale in the sea floor immediately west of Barracuda Ridge. See figure 1 for location, figure 2 for explanation of symbols.

the outer rise and trench (fig. 1). This zone is alined with the Anegada Trough, an active fault zone (Donnelly, 1964; Sykes and Ewing, 1965) separating the Greater and Lesser Antilles Island arcs. One profile (U-35; fig. 2) across the trough shows a stratified sequence composed of divergent dipping units, a relation indicative of tectonic activity. It is not clear whether the Anegada Trough marks a zone of hinge (scissor) faulting between the Caribbean and Atlantic plates (which Molnar and Sykes, 1969, suggest for the southern end of the Lesser Antilles) or whether the plate boundary lies north of the trough near the Puerto Rico Trench. With only two profiles in the area presumed for transitional plate motions, it is difficult to make more than an estimate of its location.

The age of the Lesser Antilles rise is unknown. The relatively flat-lying and undisturbed upper beds beneath the inner part of the rise at the base of the ridge suggest a Neogene age. Reflection data show that deformed sediment underlies the upper 1 to 2 km of the outer part of the rise. However, both refraction and gravity data imply that a large volume of low-density, low-velocity material underlies the central part of the rise and that it is possibly 5 km thick or more. Thus, the basal layers of the rise may be early Tertiary or older.

If the outer part of the rise has not formed by massive slumping of debris from the ridge (Meyerhoff and Meyerhoff, 1972), then, as Chase and Bunce (1969) note, the reflection records can be interpreted as revealing offscraped sediment from the underthrust Atlantic plate. The width of both the zone of covered oceanic basement and overlying beds and the entire rise increases southward toward the zone of direct plate convergence. Such a systematic increase in width would not be expected if this section of the rise is composed entirely of massive slumps. However, if the outer part of the rise is a subduction zone, then a systematic increase in width (hence volume) of offscraped sediments would be expected toward the zone of direct plate convergence. Two problems are associated with this idea—the undeformed nature of beds above overlying basement rock beneath the outer part of the rise, and the continuation of both the axis of the gravity low over the rise and the rise itself into the zone of postulated strike-slip plate motions north of Puerto Rico. On the

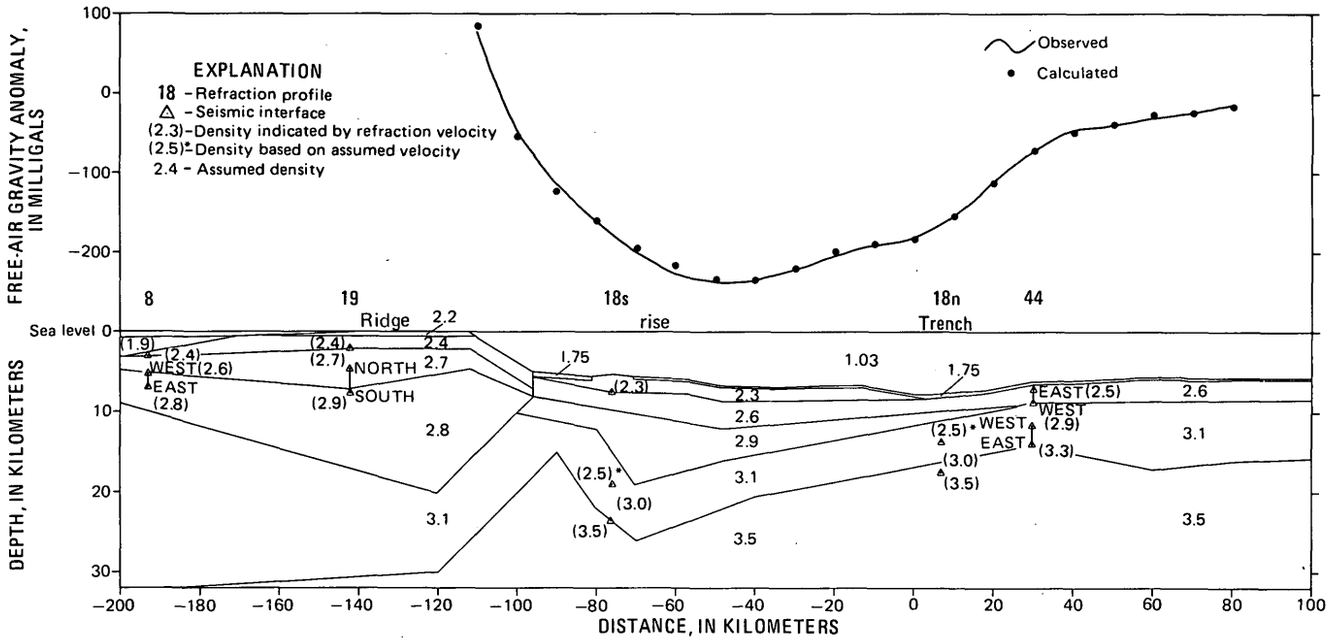

Figure 10.—Gravity model of the Lesser Antilles Ridge and rise, and the Puerto Rico Trench based on profile U-36 (see text for construction procedure and figure 1 for location). Numbers refer to densities picked from the Nafe-Drake curve (Talwani and others, 1959). Vertical exaggeration is 2:1.

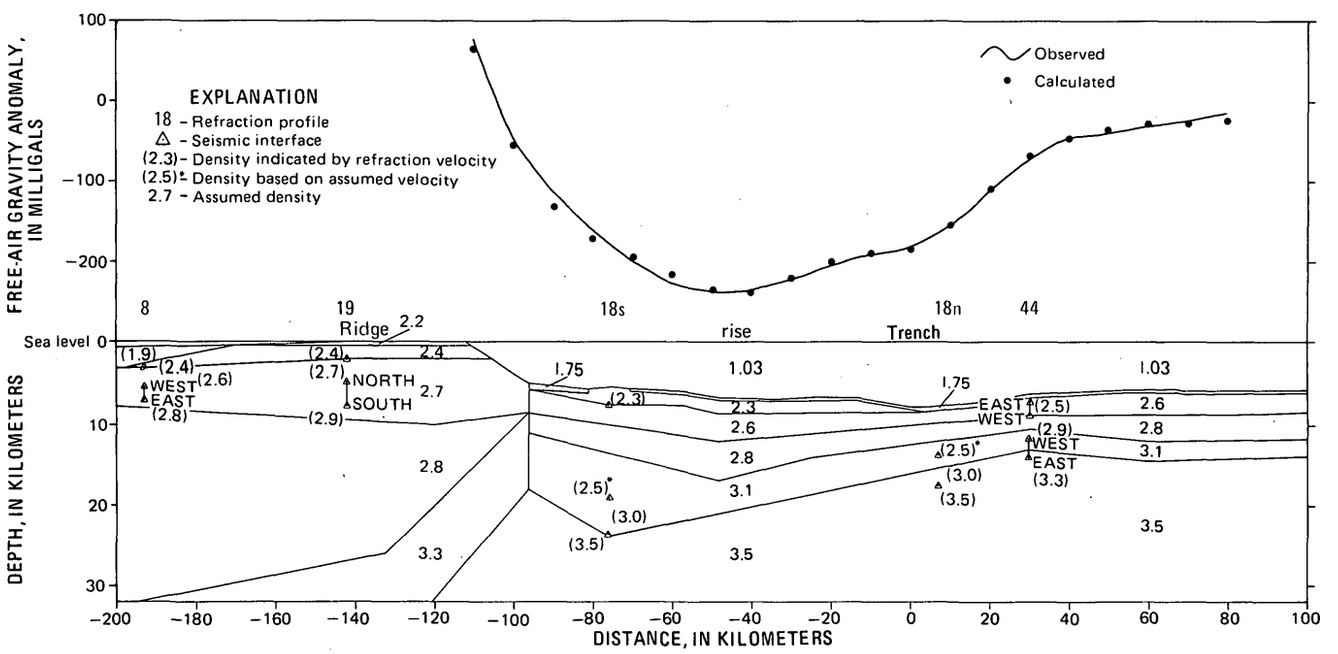

Figure 11.—Alternative gravity model based on profile U-36. See figure 1 for location and figure 10 for other explanations. Vertical exaggeration is 2:1.

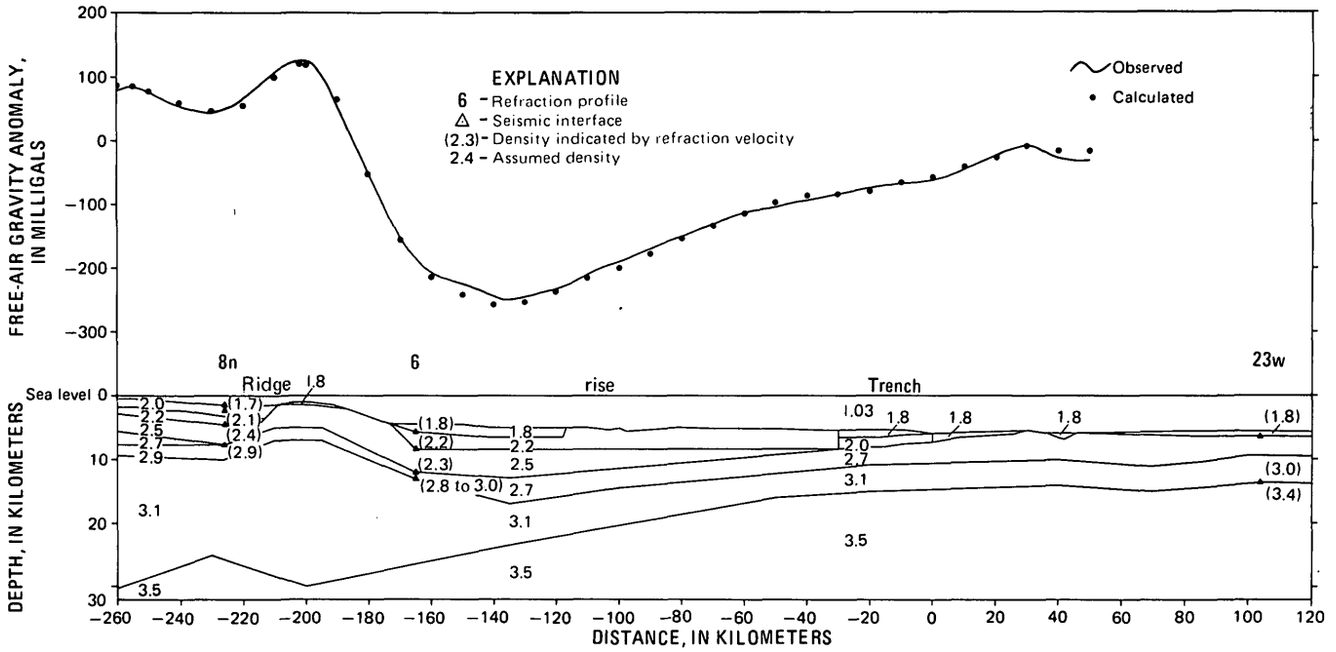

Figure 12.—Gravity model of the Lesser Antilles Ridge and rise, and southeastern Puerto Pico Trench based on profile U-46. See figure 1 for location and figure 10 for other explanations. Vertical exaggeration is 2:1.

reflection profiles that show basement dipping beneath the outer part of the rise, the overlying strata dip conformably to basement (see especially lines U-45 and U-46, figs. 8, 9). An acoustically unresolvable zone above the conformable beds may be part of the offscraped debris; therefore, a décollement must occur between the conformable reflectors and the structurally unresolvable upper zone. In other words, disruption of strata resulting from offscraping is confined to the upper zone, whereas undeformed sediment is passively "rafted" by the basement beneath it. The same acoustic effects would be created by massive slumping, with the toes of large slump bodies migrating seaward over dipping sediments on a downbowed oceanic basement. Perhaps both processes are going on simultaneously.

The second difficulty in assuming that the rise is composed mainly of offscraped sediment is that the axis of the gravity low, which presumably partly delineates a thick accumulation of low-density sediments, continues uninterrupted around the westward bend in the rise toward the Greater Antilles (Bowin, 1971). As Hatherton (1971) points out, the gravity low associated with the Greater and Lesser Antilles arcs is nowhere lower than north of Puerto Rico, along a line landward of the trench axis and in the zone of postulated strike-slip plate motion. Perhaps the rise and its associated gravity low off the Greater Antilles resulted from offscraping of sediments during an earlier period of different relative plate motions, when the Atlantic plate underthrust the Greater Antilles from a northerly or northeasterly direction. Such motion would have ceased by the Eocene, as volcanic activity in the Greater Antilles ceased by this time (Martin-Kaye, 1969; Nagle, 1971; Donnelly, 1964; Fink, 1971).

An alternative explanation for the displaced gravity low off the Greater Antilles is that the south wall of the Puerto Rico Trench is part of a downfaulted block containing a thick accumulation of sedimentary debris derived from the Greater Antilles (Talwani and others, 1959; Bunce and Falquist, 1962; Glover, 1967). The age of faulting (and presumably formation of the adjacent trench) is middle Eocene or younger because horizon A, which here is middle Eocene (Hersey, 1966; Bader and others, 1970), dips beneath the turbidite sequences in the trench. The trench could be a pull-apart structure that resulted from slight rifting along the strike-slip boundary separating the Atlantic and Caribbean plates. As discussed earlier, the history of volcanism along the Lesser Antilles requires two periods of underthrusting—one in the late Mesozoic or early Tertiary and a second in the late Cenozoic. In contrast, volcanic activity in the Greater Antilles had ceased by the Eocene. Therefore, if the trench northwest of the Lesser Antilles is an extensional structure of post-Eocene age, it must have formed in response to the renewed underthrusting in the Lesser Antilles that began in the late Miocene. Seismic activity indicates that the trench is continuing to form (Sykes and Ewing, 1965; Molnar and Sykes, 1969; Tomblin, 1974).

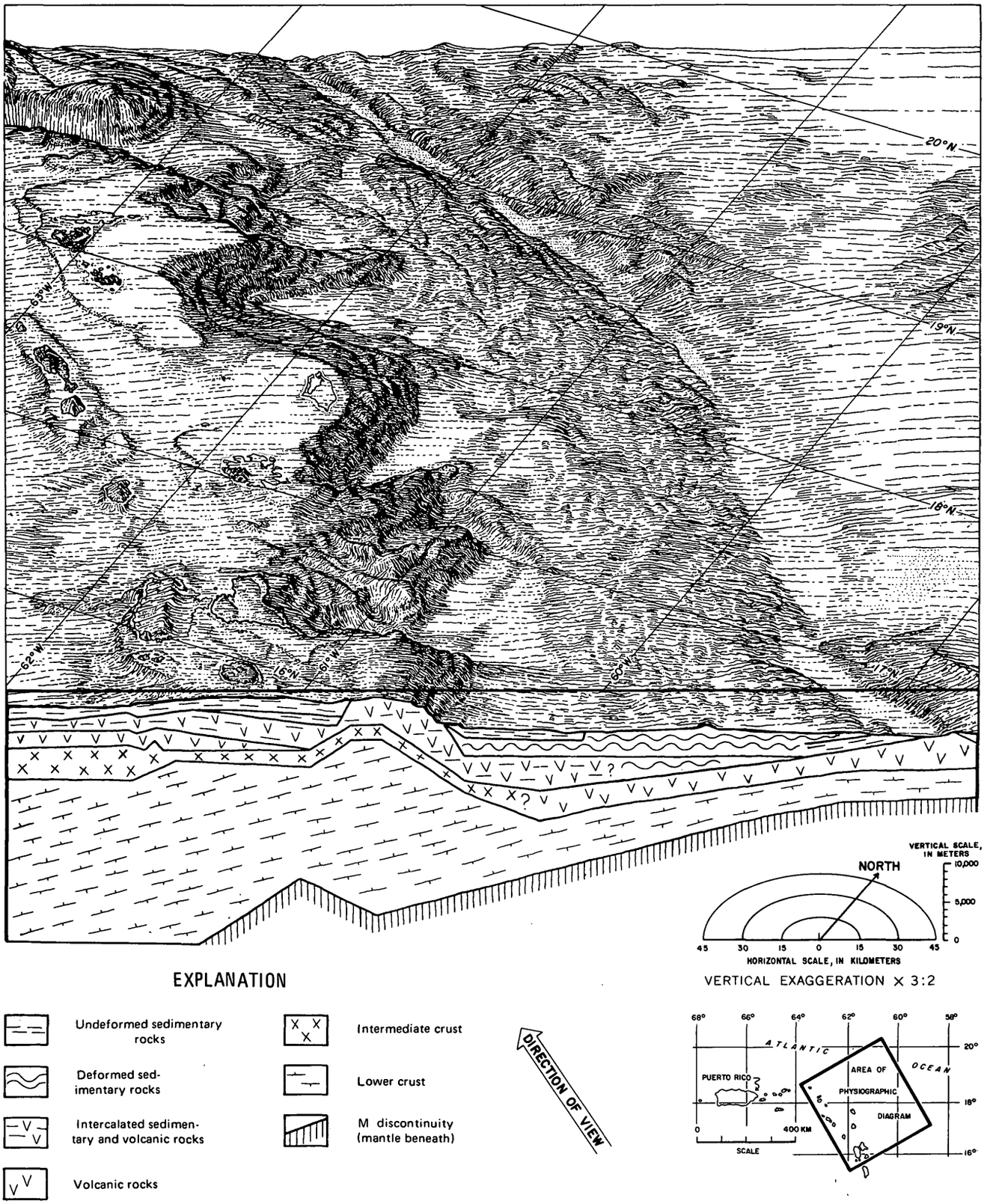

Figure 13.—Combined crustal section and physiographic diagram of the northeastern Caribbean. Crustal section is based on figure 12. Orthographic drawing by Tau Rho Alpha.

SUMMARY AND CONCLUDING REMARKS

Seismic reflection profiles can be interpreted as evidence that underthrusting of the Atlantic beneath the Lesser Antilles takes place along the eastern Caribbean and that strike-slip motion occurs between the Caribbean and Atlantic plates north of lat 19.3° N., along either the Puerto Rico Trench or the Anegada Trough, or both. The principal evidence is that along the southern underthrust zone, oceanic basement and overlying beds are clearly definable beneath the landward slope of the southeastern Puerto Rico Trench (outer part of the Lesser Antilles rise). This is in sharp contrast to the central Aleutian Trench, a zone of presumed plate convergence, where structures beneath the inner trench slope are rarely defined on reflection records, and where resolvable, appear to be related to normal faulting (Marlow, Scholl, Buffington, and Alpha, 1973). Rates of underthrusting in the Aleutian Trench are estimated to be 6 to 8 cm/yr (Morgan, 1968; McKenzie and Parker, 1967), whereas those in the eastern Caribbean are only 0.5 to 2.2 cm/yr (Molnar and Sykes, 1969). Perhaps as a consequence, the slope angles of the inner trench slope are gentler for the southeastern Puerto Rico Trench (2°–12°) than for the Aleutian Trench (10°–35°), a factor that enhances acoustic resolution of the inner slope in the Lesser Antilles area. Paradoxically, available data indicate that the central Aleutian Trench is best interpreted as a young half graben (Marlow, Scholl, Buffington, and Alpha, 1973), whereas the southeastern Puerto Rico Trench can be more successfully related to a thrust-zone feature (Chase and Bunce, 1969; Molnar and Sykes, 1969). Multichannel reflection data and deep-sea sampling are needed to resolve the structures of these inner trenches.

Refraction data and the gravity low centered over the Lesser Antilles rise indicate a thick accumulation of sediment landward of the southeastern Puerto Rico Trench. The rise is an area of thickened low-density crust landward of the trench (fig. 13). It is not clear why the gravity low continues landward of the trench in the western zone of postulated strike-slip plate boundary, rather than shifting seaward to follow the topographic axis of the trench. And, as Molnar and Sykes (1969) and Hatherton (1971) note, the mere existence of the Puerto Rico Trench in a zone of strike-slip plate motion remains enigmatic. The same enigma holds for the Aleutian Trench, which is continuous from an eastern zone of plate convergence to a western zone of strike-slip plate motion.

The magmatic and tectonic history of the Lesser Antilles indicates two periods of underthrusting—one in the late Mesozoic or early Tertiary and a second in the late Cenozoic. Similar Cenozoic histories are becoming apparent for circum-Pacific arcs (Mitchell and Bell, 1970; Mitchell and Reading, 1971), lending credence to the idea that island arc evolution in the Cenozoic may have worldwide synchroneity.

REFERENCES CITED

Bader, R. G., and others, 1970, Initial reports of the Deep Sea Drilling Project, v. IV: Washington, D.C., U.S. Govt. Printing Office, 753 p.

Birch, F. S., 1970, The Barracuda fault zone in the western North Atlantic—geological and geophysical studies: Deep-Sea Research, v. 17, p. 847–859.

Bonatti, Enrico, 1971, Rocks and sediments from the Barracuda fault zone [abs.]: Caribbean Geol. Conf., 5th, St. Thomas, Trans., p. 45.

Bowin, Carl, 1971, Some aspects of the gravity field and tectonics of the northern Caribbean region: Caribbean Geol. Conf., 5th, St. Thomas, Trans., p. 1–6.

Bunce, E. T., and Fahlquist, D. A., 1962, Geophysical investigation of the Puerto Rico Trench and outer ridge: Jour. Geophys. Research, v. 67, no. 10, p. 3955–3972.

Bunce, E. T., Phillips, J. D., Chase, R. L., and Bowin, C. O., 1971, The Lesser Antilles arc and the eastern margin of the Caribbean Sea, *in* Maxwell, A. E., ed., The sea, v. 4, pt. 2: New York, John Wiley and Sons, Inc., p. 359–385.

Chase, R. L., and Bunce, E. T., 1969, Underthrusting of the eastern margin of the Antilles by the floor of the western North Atlantic Ocean, and origin of the Barbados Ridge: Jour. Geophys. Research, v. 74, no. 6, p. 1413–1420.

Collette, B. J., Ewing, J. I., Lagaay, R. A., and Truchan, M., 1969, Sediment distribution in the oceans—The Atlantic between 10° and 19° N.: Marine Geology, v. 7, p. 279–345.

Donnelly, T. W., 1964, Evolution of the eastern Greater Antillean island arc: Am. Assoc. Petroleum Geologists Bull., v. 48, p. 680–696.

Embley, R. W., Ewing, J. I., and Ewing, M., 1970, The Vidal Deep-Sea Channel and its relationship to the Demerara and Barracuda Abyssal Plains: Deep-Sea Research, v. 17, p. 539–552.

Ewing, J. I., Officer, C. B., Johnson, H. R., and Edwards, R. S., 1957, Geophysical investigations in the eastern Caribbean—Trinidad shelf, Tobago Trough, Barbados Ridge, Atlantic Ocean: Geol. Soc. America Bull., v. 68, p. 897–912.

Fink, L. K., Jr., 1970, Evidence for the antiquity of the Lesser Antilles Island Arc [abs.]: EOS (Am. Geophys. Union Trans.), v. 51, p. 326–327.

——1971, Evidence in the eastern Caribbean for mid-Cenozoic cessation of sea-floor spreading [abs.]: EOS (Am. Geophys. Union Trans.), v. 52, no. 4, p. 251.

——1972, Bathymetric and geologic studies of the Guadeloupe region, Lesser Antilles Island Arc: Marine Geology, v. 12, p. 267–288.

Glover, L., 1967, Geology of the Coamo area Puerto Rico—with comments on Greater Antillean volcanic island arc-trench phenomena: Princeton Univ., Ph. D. thesis, 110 p.

Hatherton, T., 1971, Plate consumption—some comments from an island arc: Nature, v. 234, p. 294–295.

Hayes, D. E., 1966, A geophysical investigation of the Peru-Chile Trench: Marine Geology, v. 4, p. 309–351.

Hersey, J. B., 1966, Marine geophysical investigations in the West Indies, *in* Continental margins and island arcs: Canada Geol. Survey Paper 66-15, p. 151–164.

Hurley, R. J., 1966, Geological studies of the West Indies, *in* Continental margins and island arcs: Canada Geol. Survey Paper 66-15, p. 139–150.

Karig, D. E., 1970, Ridges and basins of the Tonga-Kermadec island arc system: Jour. Geophys. Research, v. 75, p. 239–254.

——1971, Structural history of the Marianas island arc system: Geol. Soc. America Bull., v. 82, p. 323–344.

Marlow, M. S., Scholl, D. W., and Buffington, E. C., 1973, Comments on paper by M. L. Holmes, R. E. von Huene, and D. A. McManus, 'Seismic reflection evidence supporting underthrusting beneath the

Aleutian arc near Amchitka Island': Jour. Geophys. Research, v. 78, p. 3517–3522.

Marlow, M. S., Scholl, D. W., Buffington, E. A., and Alpha, T. R., 1973, Tectonic history of the central Aleutian arc: Geol. Soc. America Bull., v. 84, p. 1555–1574.

Marlow, M. S., Scholl, D. W., and Garrison, L. E., 1972, Evidence(?) of underthrusting from seismic reflection profiles across the Puerto Rico and Aleutian Trenches [abs.]: EOS (Am. Geophys. Union Trans.), v. 53, p. 1114.

Martin-Kaye, P. H. A., 1969, A summary of the geology of the Lesser Antilles: Overseas Geology and Mineral Resources, v. 10, p. 172–206.

McKenzie, D. P., and Parker, R. L., 1967, The North Pacific–an example of tectonics on a sphere: Nature, v. 216, p. 1276–1280.

Meyerhoff, A. A., and Meyerhoff, H. A., 1972, The new global tectonics–major inconsistencies: Am. Assoc. Petroleum Geologists Bull., v. 56, p. 269–336.

Mitchell, A. H., and Bell, J. D., 1970, Volcanic episodes in island arcs: Geol. Soc. London Proc., no. 1662, p. 9–12.

Mitchell, A. H., and Reading, H. G., 1971, Evolution of island arcs: Jour. Geology, v. 79, p. 253–284.

Molnar, Peter, and Sykes, L. R., 1969, Tectonics of the Caribbean and Middle America regions from focal mechanisms and seismicity: Geol. Soc. America Bull., v. 80, p. 1639–1684.

Morgan, W. J., 1968, Rises, trenches, great faults, and crustal blocks: Jour. Geophys. Research, v. 73, p. 1959–1982.

Nagle, F., 1971, Caribbean Geology, 1970: Bull. Marine Sci., v. 21, no. 2, p. 375–439.

Officer, C. B., Ewing, J. I., Edwards, R. S., and Johnson, H. R., 1957, Geophysical investigations in the eastern Caribbean–Venezuelan basin, Antilles island arc, and Puerto Rico Trench: Geol. Soc. America Bull., v. 68, p. 359–378.

Officer, C. B., Ewing, J. I., Hennon, J. F., Hardrider, D. G., and Miller, P. E., 1959, Geophysical investigations in the eastern Caribbean–summary of 1955 and 1956 cruises, [chap.] 2 *in* V. 3, *of* Ahrens., L. H., and others, eds., Physics and chemistry of the earth: London, Pergamon Press, p. 17–109.

Rose, J. C., Wollard, G. P., and Malahoff, A., 1968, Marine gravity and magnetic studies of the Solomon Islands, *in* Knopf, L., Drake, C. L., and Hart, P. J., eds., The crust and upper mantle of the Pacific area: Am. Geophys. Union Geophys. Mon., v. 12, p. 379–410.

Scholl, D. W., Buffington, E. C., and Marlow, M. S., 1974, Plate tectonics and the structural evolution of the Aleutian-Bering Sea region, *in* Forbes, R. B., ed., The geophysics and geology of the Bering Sea region: Geol. Soc. America Mem. (In press.)

Scholl, D. W., Christensen, M. N., von Huene, R. E. and Marlow, M. S., 1970, Peru-Chile Trench sediments and sea-floor spreading: Geol. Soc. America Bull., v. 81, p. 1339–1360.

Scholl, D. W., von Huene, R. E. and Ridlon, J. B., 1968, Spreading of the ocean floor–undeformed sediments in the Peru-Chile Trench: Science, v. 159, p. 869–871.

Silver, E. A., 1972, Pleistocene tectonic accretion of the continental slope off Washington: Marine Geology, v. 13, p. 239–249.

Sykes, L. R., and Ewing, Maurice, 1965, The seismicity of the Caribbean region: Jour. Geophys. Research, v. 70, p. 5065–5074.

Talwani, Manik, Sutton, G. H., and Worzel, J. L., 1959, A crustal section across the Puerto Rico Trench: Jour. Geophys. Research, v. 64, no. 10, p. 1545–1555.

Tomblin, J. F., 1974, Seismicity and plate tectonics of the eastern Caribbean: 6th Caribbean Geol. Conf., Margarita Island, Venezuela, Trans. (In press.)

von Huene, R. E., 1972, Structure of the continental margin and tectonism at the eastern Aleutian Trench: Geol. Soc. America Bull., v. 83, p. 3613–3626.

von Huene, R. E., and Shor, G. G., Jr., 1969, The structure and tectonic history of the eastern Aleutian Trench: Geol. Soc. America Bull., v. 80, p. 1889–1902.

Jour. Research U.S. Geol. Survey
Vol. 2, No. 3, May-June 1974, p. 303–310

SILICOFLAGELLATE ZONATION OF UPPER CRETACEOUS TO LOWER MIOCENE DEEP-SEA SEDIMENT

By DAVID BUKRY and JOHN H. FOSTER, La Jolla, Calif.

Abstract.—A stratigraphic zonation based on silicoflagellates is proposed for the division of Upper Cretaceous to lower Miocene deep-sea sediments into eight independent zones. The occurrence of silicoflagellate siliceous microfossils from Mesozoic and lower Cenozoic sediment has been poorly known in all but the middle Eocene. The most diagnostic occurrences in deep-sea sediment are here used to define a sequence of zones, which are correlated with the more widely recognizable zonation of coccoliths. The silicoflagellate zones defined include the *Lyramula furcula* Zone of Late Cretaceous age, the *Corbisema hastata* Zone of Paleocene age, the *Naviculopsis constricta* Zone and *Dictyocha hexacantha* Zone of Eocene age, the *Dictyocha deflandrei* Zone and *Rocella gemma* Zone of Oligocene age, and the *Naviculopsis quadrata* Zone and *Distephanus octacanthus* Zone of early Miocene age.

Initial biostratigraphic study in deep-sea sediment of the distribution of silicoflagellates—microscopic siliceous skeletons produced by unicellular marine algae—has revealed that minor structural variation within species is common, and many species have long stratigraphic ranges. Establishing a detailed biostratigraphic zonation based on silicoflagellates is hindered by a lack of continuously preserved developmental sequences that would provide the ranges of fossil silicoflagellates. Also, substantial variation in skeletal form within a single species, due to environmental responses, is characteristic of this group and has led to a proliferation of overlapping taxonomy. Variation in ranges and in form is difficult to evaluate stratigraphically because the thin tubular construction of silicoflagellate skeletons makes them especially susceptible to solution. Moreover, compiling and comparing the ranges of silicoflagellates over large areas is difficult because silicoflagellates seem to be geographically limited to areas of upwelling that are rich in nutrients. Despite these limitations, silicoflagellates do provide general stratigraphic markers that supplement other stratigraphically important marine microfossil groups. An independent silicoflagellate zonation based on known silicoflagellate ranges is described here.

For the present summary of biostratigraphic distribution in deep-sea sediment, species identifications are used in a broad sense. Some particularly diagnostic species are shown in figures 1 and 2. For the genus *Naviculopsis*, the species concepts of Ling (1972) have been used because they offer the most logical organization of this genus. Excellent recent discussions of the stratigraphic significance and taxonomy of other genera of Late Cretaceous to early Miocene silicoflagellates include those of Glezer (1966), Loeblich and others (1968), Mandra (1968), and Ling (1972).

STUDY METHOD

Unprocessed dried sediment slurries cemented on glass slides with synthetic balsam were examined at X 400. Abundance of silicoflagellates in the samples is variable. For example, 4 slides were needed to obtain a count of 100 specimens for DSDP sample 214-38-3-top, whereas only 6 mechanical-stage traverses on a single slide were necessary to count 300 specimens for DSDP 275-1-2, 75–76 cm. Actual counts are converted to percentages for easy comparison between samples.

SAMPLE LOCALITIES

Atlantic Ocean:
- USGS-LM-5-2-4 (04°07′ N., 07°27′ W.)
- DSDP 6 (30°50′ N., 67°39′ W.)
- DSDP 13 (06°02′ N., 18°14′ W.)
- DSDP 29 (14°47′ N., 69°19′ W.)
- DSDP 140 (21°45′ N., 21°48′ W.)

Pacific Ocean:
- Scripps JYN V-16P (07°44′ N., 149°44′ W.)
- Scripps MSN-149P (09°23′ N., 145°15′ W.)
- DSDP 66 (02°24′ N., 166°07′ W.)
- DSDP 206 (32°01′ S., 165°27′ E.)
- DSDP 208 (26°07′ S., 161° 13′ E.)
- DSDP 274 (69°00′ S., 173°26′ E.)
- DSDP 275 (50°26′ S., 176°19′ E.)
- DSDP 280 (48°57′S., 147°14′ E.)

Indian Ocean:
- DSDP 214 (11°20′ S., 88°43′ E.)
- DSDP 216 (01°28′ N., 90°12′ E.)

SILICOFLAGELLATE ZONES

Eight silicoflagellate zones are proposed for the Upper Cretaceous to lower Miocene (table 1) wherein boundary species are indicated and a composite assemblage is established for each zone. A temperature-dependent provincialism found for the Neogene, which requires cold- and warm-water zonal

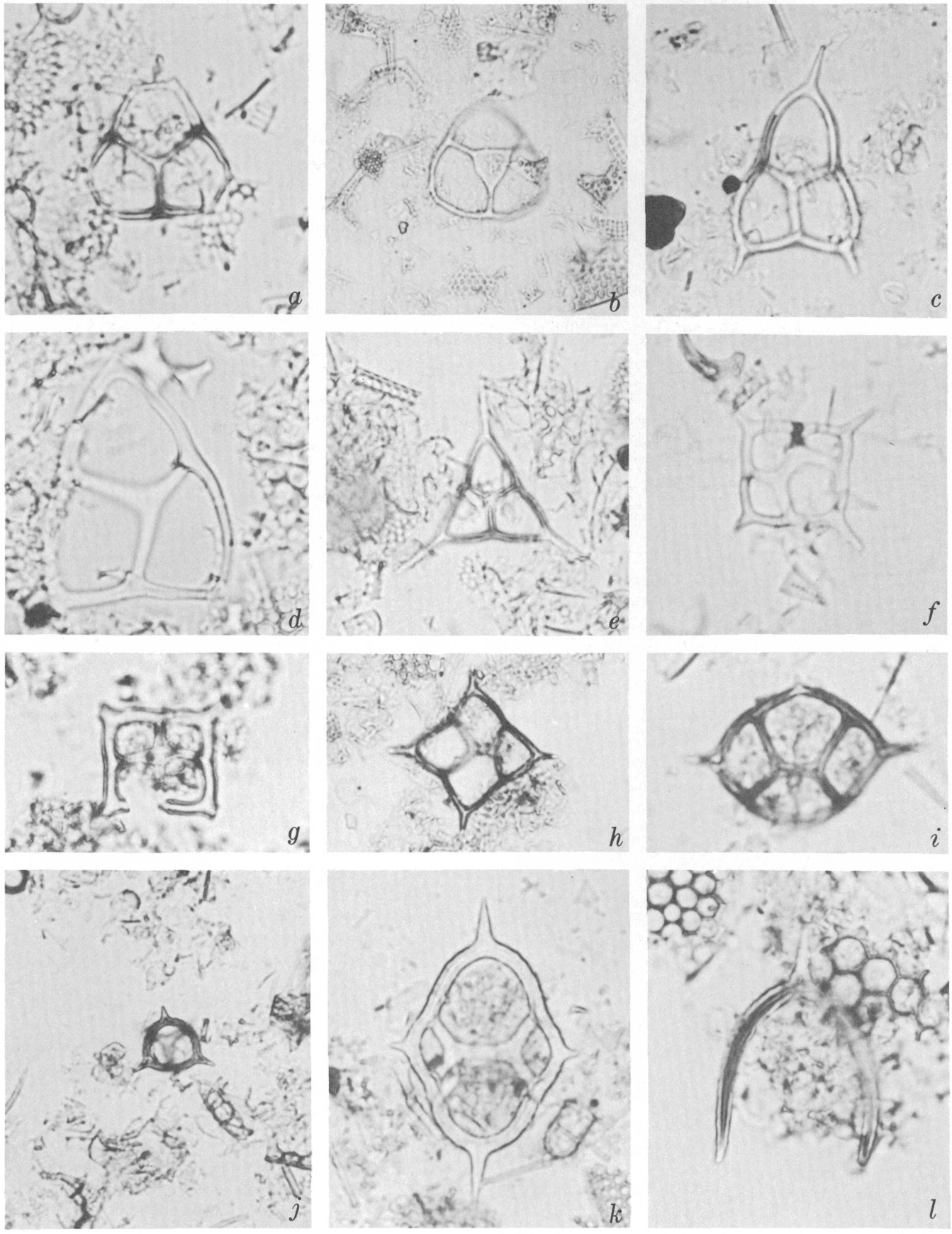
a
b
c
d
e
f
g
h
i
j
k
l

systems (Bukry, 1973), is not evident for the Upper Cretaceous and Paleogene because fewer localities are available for comparison.

Lyramula furcula Zone

Boundary species:
Top: *Corbisema hastata*, first occurrence
Bottom: *Lyramula furcula*, first occurrence
Assemblage: *Corbisema archangelskiana, C. geometrica, Cornua trifurcata, Lyramula furcula, L. simplex, Vallacerta hannai, V. hortonii, V. tumidula*

Comment.—The *Lyramula furcula* Zone assemblage is typically dominated by *Lyramula furcula. Corbisema geometrica* is generally the second most abundant species, and *Vallacerta tumidula* is the third. Other species have variable but small abundance levels.

Cores recovered by the Deep Sea Drilling Project show occurrences of the *Lyramula furcula* Zone at site 216 in the Indian Ocean and site 275 in the Pacific Ocean. Distribution of species at these sites is shown in table 2; correlation with coccolith zones is shown in table 1. At site 216, the zone is associated with the Late Cretaceous *Nephrolithus frequens* Zone of coccoliths. Occurrences in land sections of the key *Vallacerta* species and *Lyramula furcula* (and its varieties) also are from Late Cretaceous strata (Hanna, 1938; Schulz, 1928; Glezer, 1959, 1966; Mandra, 1968; Ling, 1972).

Figure 1.—Photomicrographs of fossil silicoflagellates from deep-sea localities. Magnification ranges from × 700 to × 1100, as indicated.

a. Corbisema bimucronata Deflandre, USGS-LM-5-2-4; X1100.
b. Corbisema geometrica Hanna, DSDP 275-1-4, 75–76 cm; X 700.
c. Corbisema hastata (Lemmermann), DSDP 214-38-3, top; X 800.
d. Corbisema recta (Schulz), DSDP 13-3-1, 103–104 cm; X 1100.
e. Corbisema triacantha (Ehrenberg), USGS-LM-5-2-4; X 800.
f. Dictyocha aspera (Lemmermann), USGS-LM-5-2-4; X 1100.
g–i. Dictyocha fibula Ehrenberg s. ampl.
g. DSDP 208-29-5, 110–111 cm; X 800.
h. USGS-LM-5-2-4; X 700.
i. DSDP 140-2-6, 114–115 cm; X 1100.
j. Dictyocha hexacantha Schulz, USGS-LM-5-2-4; X 700.
k. Dictyocha rhombica (Schulz), DSDP 140-2-6, 114–115 cm; X 800.
l. Lyramula furcula Hanna, DSDP 208-31-3, 110–111 cm; X 1100.

Corbisema hastata Zone

Boundary species:
Top: *Naviculopsis constricta*, first occurrence
Bottom: *Corbisema hastata*, first occurrence
Assemblage: *Corbisema archangelskiana, C. geometrica, C. hastata, C. schulzii, C. triacantha, Dictyocha fibula* s. ampl., *Lyramula furcula*

Comment.—Assemblages of the *Corbisema hastata* Zone are dominated by the genus *Corbisema. Corbisema archangelskiana, C. geometrica,* and *Lyramula furcula* persist from the underlying *Lyramula furcula* Zone; however, *L. furcula* is rare and may represent minor reworking. In either case, the first appearance of *C. hastata,* which is common throughout the zone, provides a good marker for the base of the zone that approximates the Late Cretaceous-Paleocene boundary. Only the lower part of the zone has been observed, because upper Paleocene and lower Eocene silicoflagellates have not been found in available deep-sea sediment cores. The lower assemblage of the zone at sites 208 and 214 in the Pacific and Indian Oceans is associated with coccoliths of the lower Paleocene *Cruciplacolithus tenuis* Zone. Both silicoflagellate assemblages lack the genus *Naviculopsis*, which appears later and becomes a prominent member of middle Eocene assemblages.

The *Corbisema hastata* Zone is distinguished from the underlying *Lyramula furcula* Zone by the first occurrence of *Corbisema hastata* and by the essential disappearance of *Lyramula furcula.* Although the top of the zone has not been observed in deep-sea sediment, the first occurrence of *Naviculopsis constricta* later in Paleocene or possibly in early Eocene time is designated as the top of the zone.

The dominance of *Corbisema* in the *Corbisema hastata* Zone and later in the middle Eocene and middle Miocene corresponds to intervals of warm oceanic paleotemperature and suggests that this genus of silicoflagellates, like *Discoaster* among the coccoliths, is a good indicator for warm environments. *Corbisema* is notably rare during the later Neogene, a time of generally declining oceanic paleotemperature.

Naviculopsis constricta Zone

Boundary species:
Top: *Dictyocha hexacantha*, first occurrence
Bottom: *Naviculopsis constricta*, first occurrence
Assemblage: *Corbisema archangelskiana, C. geometrica, C. hastata, C. triacantha, Dictyocha deflandrei, D. fibula* s. ampl.[1], *Distephanus crux* s. ampl., *D. speculum* s. ampl., *Naviculopsis constricta, N. foliacea, Mesocena circula*

Comment.—Glezer's (1966) compilation of silicoflagellate distribution lists 35 varieties for the early Eocene. The list is distinctive for the presence of *Naviculopsis biapiculata minor* Glezer [syn. *N. constricta* (Schulz) and ?*N. foliacea* Deflandre of Ling, 1972] and for the absence of *Dictyocha hexacantha.*

[1] In a broad sense (botanical nomenclature).

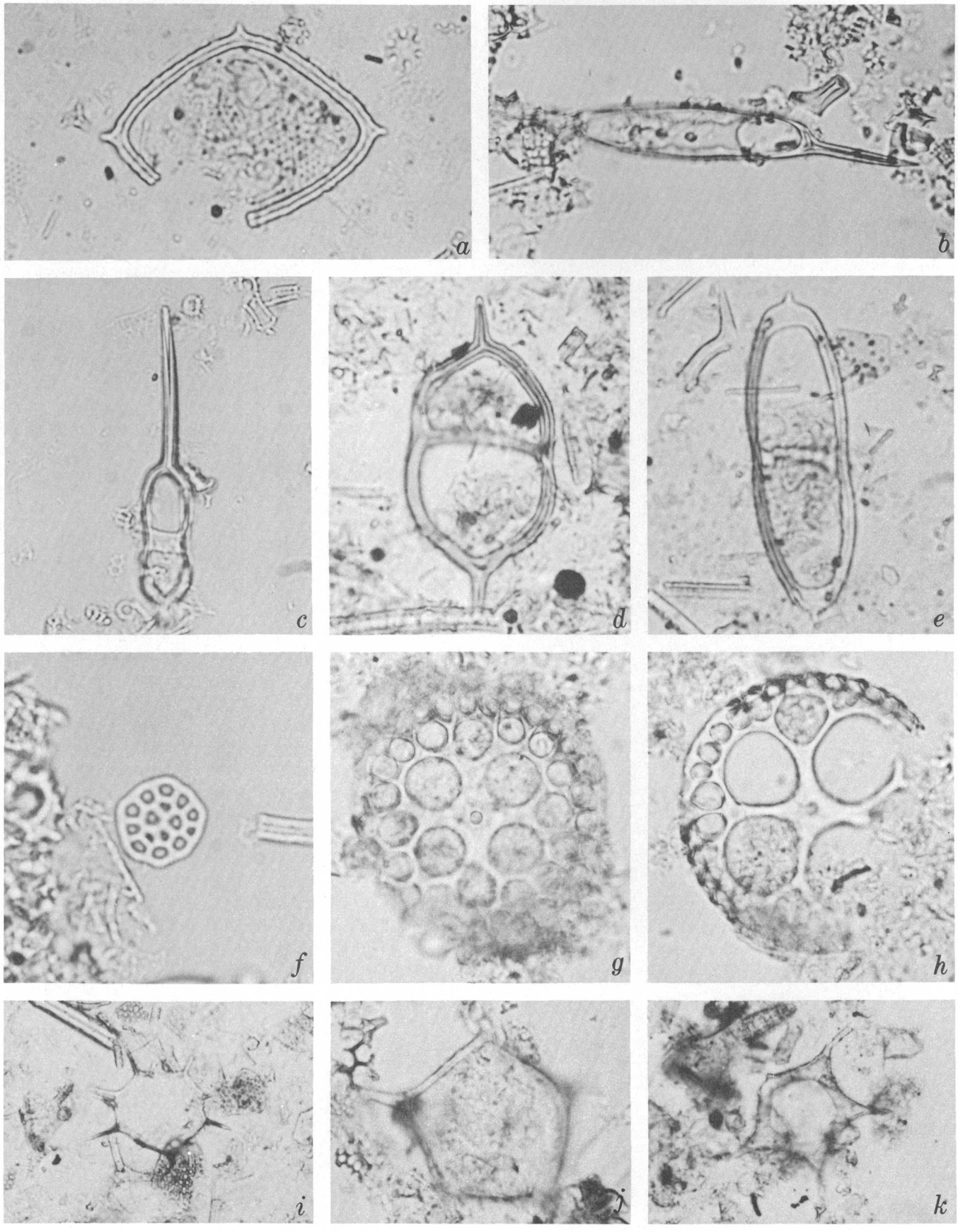
a
b
c
d
e
f
g
h
i
j
k

The next higher zone in deep-sea cores includes *D. hexacantha* and occurs with coccoliths and radiolarians of middle Eocene age.

Although not evident in the available deep-sea samples, it seems clear that a *Naviculopsis constricta* Zone and possibly an *N. foliacea* Zone can be established within the lower Eocene, because the first appearance of *Naviculopsis* occurs stratigraphically between the first appearances of *Corbisema hastata* in lower Paleocene and *D. hexacantha* in the middle Eocene. The assemblage of species has been generalized from Glezer (1966), who listed many varietal forms.

Dictyocha hexacantha Zone

Boundary species:
Top: *Dictyocha hexacantha*, last occurrence
Bottom: *Dictyocha hexacantha*, first occurrence
Assemblage: *Corbisema bimucronata, C. geometrica, C. recta, C. triacantha* s. ampl., *Dictyocha aspera* s. ampl., *D. fibula* s. ampl., *D. hexacantha, Distephanus crux, Mesocena oamaruensis, M. apiculata, Naviculopsis biapiculata, N. constricta, N. foliacea, Pseudorocella barbadensis.*

Comment.—The first widespread and common occurrence of silicoflagellates in deep-sea sediment is in the middle Eocene. A series of samples from various cores shows a generally consistent occurrence of *Corbisema bimucronata, C. triacantha*, and *Dictyocha hexacantha*. However, other species are often found to predominate, although their occurrence is more sporadic. For example, *Corbisema recta, Naviculopsis constricta, N. foliacea*, and *Pseudorocella barbadensis* exhibit great local abundance in one or two of the samples studied.

Figure 2.—Photomicrographs of fossil silicoflagellates from deep-sea localities. Magnification is × 800 except for *i* and *k*, × 700, and *f*, × 1100.

a. Mesocena elliptica Ehrenberg, DSDP 140-2-3, 109–110 cm.
b. Naviculopsis foliacea Deflandre, DSDP 208-27-5, 103–104 cm.
c. Naviculopsis constricta (Schulz), USGS-LM-5-2-4.
d. Naviculopsis lata (Deflandre), DSDP 140-2-6, 114–115 cm.
e. Naviculopsis quadrata (Ehrenberg), DSDP 140-2-6, 114–115 cm.
f. Pseudorocella barbadensis Deflandre, DSDP 29-9-4, 74–75 cm.
g, h. Rocella gemma Hanna, DSDP 206C-6C-3, 35–36 cm.
i. Vallacerta hannai Deflandre, DSDP 275-2-1, 75–76 cm.
j. Vallacerta hortonii Hanna, DSDP 216-31-1, 90–91 cm.
k. Vallacerta tumidula Glezer, DSDP 216-31-1, 90–91 cm.

The *Dictyocha hexacantha* Zone is distinguished from the underlying *Naviculopsis constricta* Zone by the first occurrence of *Dictyocha hexacantha*. It is distinguished from the higher *Dictyocha deflandrei* Zone by the restricted occurrence of both *D. hexacantha* and *N. foliacea* and by the apparent absence of *D. deflandrei*.

Dictyocha deflandrei Zone

Boundary species:
Top: *Rocella gemma*, first occurrence
Bottom: *Dictyocha hexacantha*, last occurrence
Assemblage: *Corbisema hastata, C. triacantha* s. ampl., *Dictyocha deflandrei, D. fibula, D. frenguellii, Distephanus crux, D. speculum pentagonus, D. speculum speculum, Mesocena elliptica* s. ampl., *M. apiculata, Naviculopsis regularis, N. trispinosa.*

Comment.—This assemblage contains taxa from the Eocene and upper Oligocene to lower Miocene. It is characterized by the predominance of quadrate species *Dictyocha deflandrei* and *Distephanus crux*. The *Dictyocha deflandrei* Zone is distinguished from the *Dictyocha hexacantha* Zone by the absence of *Dictyocha hexacantha* and *Naviculopsis foliacea* and by the common occurrence of *D. deflandrei*. It is distinguished from the higher *Rocella gemma* Zone by the absence of *Rocella gemma*.

At present, the *Dictyocha deflandrei* Zone is known only from DSDP site 274, core 21, in the Ross Sea, and DSDP site 280, near New Zealand, in cores 1A–7A. Our preliminary study of the latter cores shows little variation in the assemblage. Details appear in the initial report series of the Deep Sea Drilling Project.

Rocella gemma Zone

Boundary species:
Top: *Navicula quadrata*, first occurrence
Bottom: *Rocella gemma*, first occurrence
Assemblage: *Distephanus boliviensis major, D. speculum speculum, Mesocena apiculata, Naviculopsis regularis, Rocella gemma*

Comment.—The stratigraphic significance of *Rocella gemma* was first indicated by Ling (1972), who considered it to be restricted to an interval of short duration at the beginning of the early Miocene. Our investigation of Scripps Cores JYN V-16P and MSN-149P supports this observation. These cores contain rare *Naviculopsis regularis* and rare-to-common *Rocella gemma*. However, strong dissolution has restricted siliceous phytoplankton occurrences in these cores. At DSDP site 206C in the Tasman Sea, slightly less dissolution has permitted the identification of some additional rare associated species such as *Distephanus boliviensis major, D. speculum speculum, and Mesocena apiculata* (table 2).

Rocella gemma, strictly speaking, is probably not the skeleton of a silicoflagellate. Owing to the breadth and thickness of *R. gemma* skeletons, faint lines due to refraction can resemble tubular construction in some photographs. However, if one examines the fossil microscopically, focusing up and down through the fossil shows solid rather than tubular construction. Although *R. gemma* may be more closely related

Table 1.—*Proposed deep-sea silicoflagellate zones and their suggested correspondence with coccolith zones and subzones*

Series or subseries	Coccolith zone	Coccolith subzone	Silicoflagellate zone
Lower Miocene	*Helicopontosphaera ampliaperta*		*Distephanus octacanthus*
	Sphenolithus belemnos		*Naviculopsis quadrata*
	Triquetrorhabdulus carinatus	*Discoaster druggii*	
		Discoaster deflandrei	
		Cyclicargolithus abisectus	*Rocella gemma*
Oligocene	*Sphenolithus ciperoensis*		
	Sphenolithus distentus		
	Sphenolithus predistentus		*Dictyocha deflandrei*
	Helicopontosphaera reticulata	*Reticulofenestra hillae*	
		Cyclococcolithina formosa	
		Coccolithus subdistichus	
Upper Eocene	*Discoaster barbadiensis*		
Middle Eocene	*Reticulofenestra umbilica*	*Discoaster saipanensis*	*Dictyocha hexacantha*
		Discoaster bifax	
	Nannotetrina quadrata	*Coccolithus staurion*	
		Chiasmolithus gigas	
		Discoaster strictus	
	Discoaster sublodoensis	*Rhabdosphaera inflata*	*Naviculopsis constricta*
		Discoasteroides kuepperi	
Lower Eocene	*Discoaster lodoensis*		
	Tribrachiatus orthostylus		
	Discoaster diastypus		
Paleocene	*Discoaster multiradiatus*	*Campylosphaera eodela*	*Corbisema hastata*
		Chiasmolithus bidens	
	Discoaster nobilis		
	Discoaster mohleri		
	Heliolithus kleinpellii		
	Fasciculithus tympaniformis		
	Cruciplacolithus tenuis		
Upper Cretaceous	*Nephrolithus frequens*		*Lyramula furcula*
	Lithraphidites quadratus		
	Tetralithus trifidus		?
	Broinsonia parca		
	Eiffellithus augustus		

to diatoms than to silicoflagellates, it is employed in silicoflagellate zonation as is the incertae sedis genus *Discoaster* in coccolith zonation and as are some silicoflagellates such as *Mesocena elliptica* in diatom zonation (Burckle, 1972; Schrader, 1973).

Rocella gemma is predominant in the lower part of the *Rocella gemma* Zone, which is here identified in sediment of the upper Oligocene *Sphenolithus ciperoensis* Zone of coccoliths (DSDP 206C-5C-2 to 7C-1, 440–480 m) and in the upper Oligocene or lower Miocene lower *Triquetrorhabdulus carinatus* Zone of coccoliths (JYN V-16P; 0–106 cm). A lack of continuous silicoflagellate-bearing deep-sea section between the *Rocella gemma* Zone and the higher *Naviculopsis quadrata* Zone prevents characterization of the upper part of the zone at this time.

Naviculopsis quadrata Zone

Boundary species:
Top: *Distephanus octacanthus*, first occurrence
Bottom: *Naviculopsis quadrata*, first occurrence

Assemblage: *Cannopilus sphaericus, Corbisema triacantha, Dictyocha aspera, D. fibula, D. rhombica, Distephanus boliviensis major, D. crux, D. speculum binoculus, D. speculum speculum, Mesocena elliptica, Naviculopsis lata, N. quadrata*

Comment:—A diverse group of long-ranging species dominates this assemblage characterized by the short-ranging species *Naviculopsis quadrata*, which has distinctly angular corners. *Distephanus crux* is predominant. The *N. quadrata* Zone occurs in samples assigned to the early Miocene *Sphenolithus belemnos* Zone and *Helicopontosphaera ampliaperta* Zone of coccoliths at DSDP site 140 in the Atlantic Ocean off Cap Blanc, Africa.

Schulz (1928) described *Naviculopsis rectangularis*, a synonym of *N. quadrata*, from the Miocene of Maryland, and Bachmann (1970) illustrated it in an assemblage from Austria considered to be upper Oligocene. The taxonomic concept of Ling (1972) for *Naviculopsis* is used here and is recommended for stratigraphic purposes.

Table 2.—*Distribution of species in deep-sea sediment samples recorded as percent*

Series or sub-series	Zone	Sample number (depth in centimeters given in parentheses)	*Corbisema archangelskiana*	*C. geometrica*	*Cornua* sp. cf. *C. trifurcata*	*Lyramula furcula* s. ampl.	*L. simplex*	*Vallacerta tumidula*	*V. hortonii*	*V. hannai*	*Corbisema hastata*	*C. triacantha* s. ampl.	*Dictyocha fibula* s. ampl.	*Corbisema schulzii*	*Dictyocha pentagona*	*D. aspera* s. ampl.	*D. hexacantha* s. ampl.	*Mesocena elliptica* s. ampl.	*Naviculopsis constricta*	*N. foliacea*	*Pseudorocella barbadensis*	*Corbisema bimucronata*	*Naviculopsis biapiculata*	*Distephanus crux*	*Mesocena mutica*	*M. oamaruensis*	*M. apiculata*	*Corbisema recta*	*Dictyocha deflandrei*	*Distephanus speculum pentagonus*	*D. speculum speculum*	*Naviculopsis regularis*	*N. trispinosa*	*Distephanus boliviensis major*	*Naviculopsis iberica*	*Rocella gemma*	*Dictyocha rhombica*	*Distephanus octangulatus*	*Naviculopsis lata*	*N. quadrata*	*Cannopilus sphaericus*	*Distephanus speculum binoculus*	Total specimens
Lower Miocene	*Naviculopsis quadrata*	140-2-3 (109–110)										6	3			2		5			<1			67						3			2			5		2	3	<1	2	194
		140-2-6 (114–115)										7	4			1		5	<1		<1			66						<1			<1			4	<1	5	5			245
Oligocene	*Rocella gemma*	206C-6C-3 (35–36)																	3					<1			2			1	12		1	<1	80							156
	Dictyocha deflandrei	280A-7A-4 (75–76)									1	13	4					<1						25			16		32	1	5	2	1									303
Middle Eocene	*Dictyocha hexacantha*	USGS-LM-5-2-4		<1							2	67	2			3	15		3			4		2																		359
		29-9-4 (74–75)										3									96	<1																					300
		13-3-1 (103–104)										6					7			37		2						48														112
		206C-15C-2 (28–29)	1	4								14	2			3	16		45			2	5	<1	3	3																160
		6-3-Core catcher										34	1				5			5	51	2	2																			102
		208-27-5 (63–64)		3								44	9			3	<1	1	7	31	2																					116
Lower Paleocene	*Corbisema hastata*	214-38-3, top		28							48	22		1	1																											117
		208-29-5 (110–111)	3	52		2					22	7	15																													120
		208-31-3 (110–111)	3	29		5					47	17																														101
Upper Cretaceous	*Lyramula furcula*	216-30-1 (70–71)		5	4	90		2																																		266
		216-31-1 (90–91)	<1	3	4	89		2	1																																	325
		216-32-1 (116–117)	5	3	<1	88		1	1																																	216
		216-32-4, top		2	2	94		<1	1																																	340
		275-1-2 (75–76)		11	<1	83	2	3	<1																																	300
		275-1-4 (75–76)	<1	8	4	85	1	3	<1																																	300
		275-2-1 (75–76)		14		80	1	2	2	<1																																	300
		275-2-3 (75–76)		14	6	82	1		<1																																	300
		275-2-5 (75–76)	<1	8	4	84	<1	3																																		300

Distephanus octacanthus Zone

Boundary species:
Top: *Corbisema triacantha,* acme occurrence
Bottom: *Distephanus octacanthus,* first occurrence
Assemblage: *Cannopilus hemisphaericus, Corbisema triacantha, Dictyocha aspera, D. fibula, D. octagona, D. rhombica, Distephanus crux, D. octacanthus, Mesocena elliptica.*

Comment:—The *Distephanus octacanthus* Zone is probably short and possibly local and occurs near the boundary between lower and middle Miocene between the *Naviculopsis quadrata* Zone and *Corbisema triacantha* Zone. Martini (1971), at both the experimental Mohole site and at DSDP site 66, recorded a short interval within his tropical *Corbisema triacantha* Zone that contained *Distephanus octacanthus.* Within its range, *D. octacanthus* is more common than *Corbisema triacantha.* Martini's data show 3 and 12 percent *D. octacanthus* and only 2 and 4 percent *C. triacantha* in DSDP samples 66.1-7-5 and 66.1-7-6, respectively. The data of Ling (1972) and Bukry and Foster (1973), for the experimental Mohole, show the same relation.

Naviculopsis, which flourished in the Eocene and early Miocene, is missing in the middle Miocene to Holocene of the central Pacific (Martini, 1971). A similar situation is evident in coeval sediment from the eastern equatorial Pacific, where only minor occurrences are indicated by examination of silicoflagellates in cores of DSDP Leg 16 (see *Dictyocha navicula* in Bukry and Foster, 1973). The general absence of *Naviculopsis* in or above the level of the *Distephanus octacanthus* Zone provides a useful stratigraphic guide.

The overlying *Corbisema triacantha* Zone is distinguished from the *Distephanus octacanthus* Zone by the absence of *Distephanus octacanthus* and by a greater abundance of *C. triacantha* there. The widespread early middle Miocene acme of *C. triacantha* provides a useful stratigraphic marker at both low and middle latitude. Originally identified in the central Pacific (Martini, 1971), the *C. triacantha* Zone is reported from the Panama Basin (Bukry and Foster, 1973) and off Cape Mendocino, Calif. (Bukry, 1973).

ACKNOWLEDGMENT

The samples examined in this study are from the National Ocean Sediment Coring Program of the National Science Foundation, the Scripps Institution of Oceanography core collection, and the USGS-IDOE cruises. We thank George W. Moore, U.S. Geological Survey, and Harald S. Poelchau, Scripps Institution of Oceanography, for constructive suggestions.

REFERENCES CITED

Bachmann, A., 1970, Silicoflagellaten aus dem oberösterreichischen Egerien (Oberoligozän): Osterreichische Geol. Bundesanst. Verh., v. 2, p. 275–305.

Bukry, David, 1973, Coccolith and silicoflagellate stratigraphy, Deep Sea Drilling Project Leg 18, eastern North Pacific: Deep Sea Drilling Proj. Initial Repts., v. 18, p. 817–831.

Bukry, David, and Foster, J. H., 1973, Silicoflagellate and diatom stratigraphy, Leg 16, Deep Sea Drilling Project: Deep Sea Drilling Proj. Initial Repts., v. 16, p. 815–871.

Burckle, L. H., 1972, Late Cenozoic planktonic diatom zones from the Eastern Equatorial Pacific: Nova Hedwigia Beihefte, v. 39, p. 217–246.

Glezer, Z. I., 1959, Nekotorye novye dannye o semeistve Vallacertaceae Deflandre (Silicoflagellatae) [Some new data on the Family Vallacertaceae Deflandre (Silicoflagellatae)]: Vses. Nauchno-Issled. Geol. Inst. Inform. Sbornik., v. 10, p. 103–113.

——1966, Silicoflagellatophyceae, *in* Gollerbakh, M. M., ed., Cryptogamic plants of the U.S.S.R.: Akad. Nauk SSSR, V. A. Komarova Bot. Inst.; translated from Russian by Israel Program for Scientific Translations, Ltd., Jerusalem, 1970, v. 7, 363 p.

Hanna, G. D., 1928, Silicoflagellata from the Cretaceous of California; Jour. Paleontology, v. 1, p. 259–273.

Ling, H. Y., 1972, Upper Cretaceous and Cenozoic silicoflagellates and ebridians: Bulls. Am. Paleontology, v. 62, p. 135–229.

Loeblich, A. R., 3d, Loeblich, L. A., Tappan, H., and Loeblich, A. R., Jr., 1968, Annoted index of fossil and recent silicoflagellates and ebridians with descriptions and illustrations of validly proposed taxa: Geol. Soc. America Mem. 106, 319 p.

Mandra, Y. T., 1968, Silicoflagellates from the Cretaceous, Eocene, and Miocene of California, U.S.A.: California Acad. Sci. Proc., v. 36, p. 231–277.

Martini, E., 1971, Neogene silicoflagellates from the equatorial Pacific: Deep Sea Drilling Proj. Initial Repts., v. 7, p. 1695–1708.

Schrader, H. J., 1973, Cenozoic diatoms from the northeast Pacific, Leg 18: Deep Sea Drilling Proj. Initial Repts., v. 18, p. 673–797.

Schulz, P., 1928, Beitrage zur Kenntnis fossiler und rezenter Silicoflagellaten: Bot. Archiv, v. 21, p. 15–292.

Jour. Research U.S. Geol. Survey
Vol. 2, No. 3, May-June 1974, p. 311—321

GENERALIZED GEOLOGY AND STRUCTURE OF THE WINKELMAN 15-MINUTE QUADRANGLE AND VICINITY, PINAL AND GILA COUNTIES, ARIZONA

By M. H. KRIEGER, Menlo Park, Calif.

Abstract.—A northwest-trending belt of steeply east-dipping Precambrian and Paleozoic sedimentary rocks extends across the Winkelman 15-minute quadrangle and separates areas of contrasting structures. To the southwest for 60 mi is an expanse of Precambrian basement, largely granite; to the northeast the Precambrian and Paleozoic sedimentary rocks are gently tilted and intricately faulted. The structure within the Winkelman 15-minute quadrangle is interpreted as a monocline separated into en echelon segments by strike-slip and normal faults. Other monoclines lie to the north and northwest. Most of the tilting that formed the monoclines occurred after deposition of the early(?) Miocene San Manuel Formation. Structural features that repeat the Precambrian and Paleozoic sedimentary rocks within the area and that resemble high-angle faults are believed to have formed as low-angle thrusts, tilted to their present nearly vertical position during development of the monoclines. Structural features that are younger than the monoclines include low-angle gravity slide surfaces which are older than the high-angle normal faults that formed the basin-and-range topography on which the Pliocene sediments were deposited.

This paper describes and interprets the geologic structure within and adjacent to the Winkelman 15-minute quadrangle (fig. 1). The four 7½-minute quadrangles that make up the 15-minute quadrangle are being published in the quadrangle-map series at a scale of 1:24,000 (Krieger, 1974a-d). The interested reader is referred to these maps for more details on the structure and for fuller descriptions of the stratigraphy of the area. The most obvious structural features are en echelon belts of steeply dipping Precambrian and Paleozoic sedimentary rocks that contrast with structural features to the northeast and southwest. Southwest of the 15-minute quadrangle, Precambrian basement rocks are extensively exposed; northeast of it, Precambrian and Paleozoic sedimentary rocks are gently tilted and intricately faulted. The northwest-trending en echelon belts within the 15-minute quadrangle are interpreted as a single monocline later separated into segments by strike-slip and high-angle normal faults.

Acknowledgments.—I thank my colleagues in the U.S. Geological Survey, particularly Max D. Crittenden, Jr., and Norman G. Banks, for stimulating discussion, for many suggestions concerning the structural interpretations, and for critical review of the manuscript.

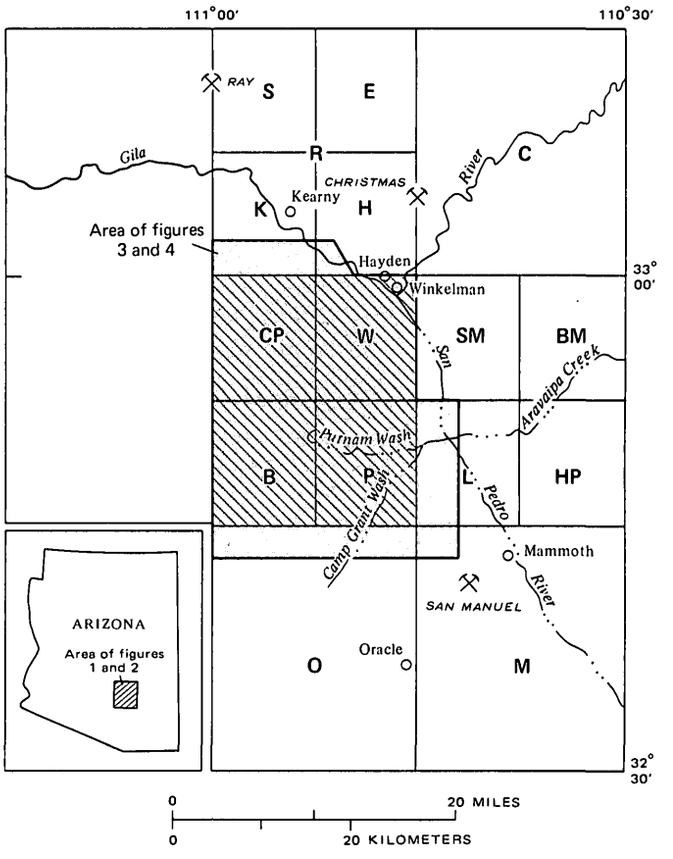

Figure 1.—Index map showing location of the Winkelman 15-minute quadrangle (hatched and shaded) and other quadrangles in southeastern Arizona, and showing location of features referred to in text. Quadrangle names and published data identified as follows: B, Black Mountain (Krieger, 1974c); BM, Brandenburg Mountain (Krieger, 1968a); C, Christmas (Willden, 1964); CP, Crozier Peak (Krieger, 1974b); E, El Capitan; H. Hayden (Ransome, 1919; N. G. Banks and M. H. Krieger, unpub. data, 1973); HP, Holy Joe Peak (Krieger, 1968b); K, Kearny, (Cornwall and Krieger, 1974); L. Lookout Mountain (Krieger, 1968c); M, Mammoth (Creasey, 1965, 1967); O, Oracle (from aerial photographs by U.S. Soil Conservation Service and from Creasey and others, 1961); P, Putnam Wash (Krieger, 1974d); R, Ray (Ransome, 1919); S, Sonora (Cornwall and others, 1971); SM, Saddle Mountain (Krieger, 1968d); W, Winkelman 7½-minute (Krieger, 1974a).

STRATIGRAPHY

Rocks in the area discussed (figs. 2,3) range in age from Precambrian to Holocene. The oldest Precambrian rocks are the Pinal Schist and intrusive rocks, mostly the Ruin Granite (Oracle Granite of Peterson, 1938). Batholithic masses of Ruin Granite, dated at about 1,430 m.y., by Silver, (1968) and Damon, Livingston, and Erickson (1962), were intruded after a period of intense deformation that produced nearly vertical east-trending foliation and bedding in the schist. The schist and granite are overlain with profound angular unconformity by unmetamorphosed Precambrian sedimentary rocks of the Apache Group and the disconformably overlying Troy Quartzite. Diabase, about 1,200 m.y. old (Silver, 1960; Damon and others, 1962), forms dikes and sills in the Apache Group and Troy Quartzite and sill-like masses in the schist and granite parallel to the pre-Apache erosion surface. The sills inflated the Precambrian sedimentary section but apparently did not perceptibly tilt the strata. Because of their abundance and narrow outcrop width due to steep dips, diabase sills in sedimentary rocks are not shown in figure 3. Sills in granite and schist are shown with exaggerated width to illustrate their relation to the pre-Apache erosion surface.

After a long period of erosion, Cambrian formations were deposited disconformably on the Precambrian sedimentary rocks and diabase. Devonian, Mississippian, and Pennsylvanian rocks overlie the Cambrian strata.

Volcanic rocks of Late Cretaceous age that disconformably overlie older rocks in the area are (1) the Williamson Canyon Volcanics (fig. 3) of andesitic composition, most abundant northeast of the Winkelman quadrangle, (2) the Cloudburst Formation, composed of volcanic rocks of probable latitic composition, fanglomerate, and sedimentary breccias in the southern part of the area and now standing nearly vertically and underlain by a gently dipping gravity slide surface, and (3) a rhyodacitic to quartz latitic pyroclastic unit, found only

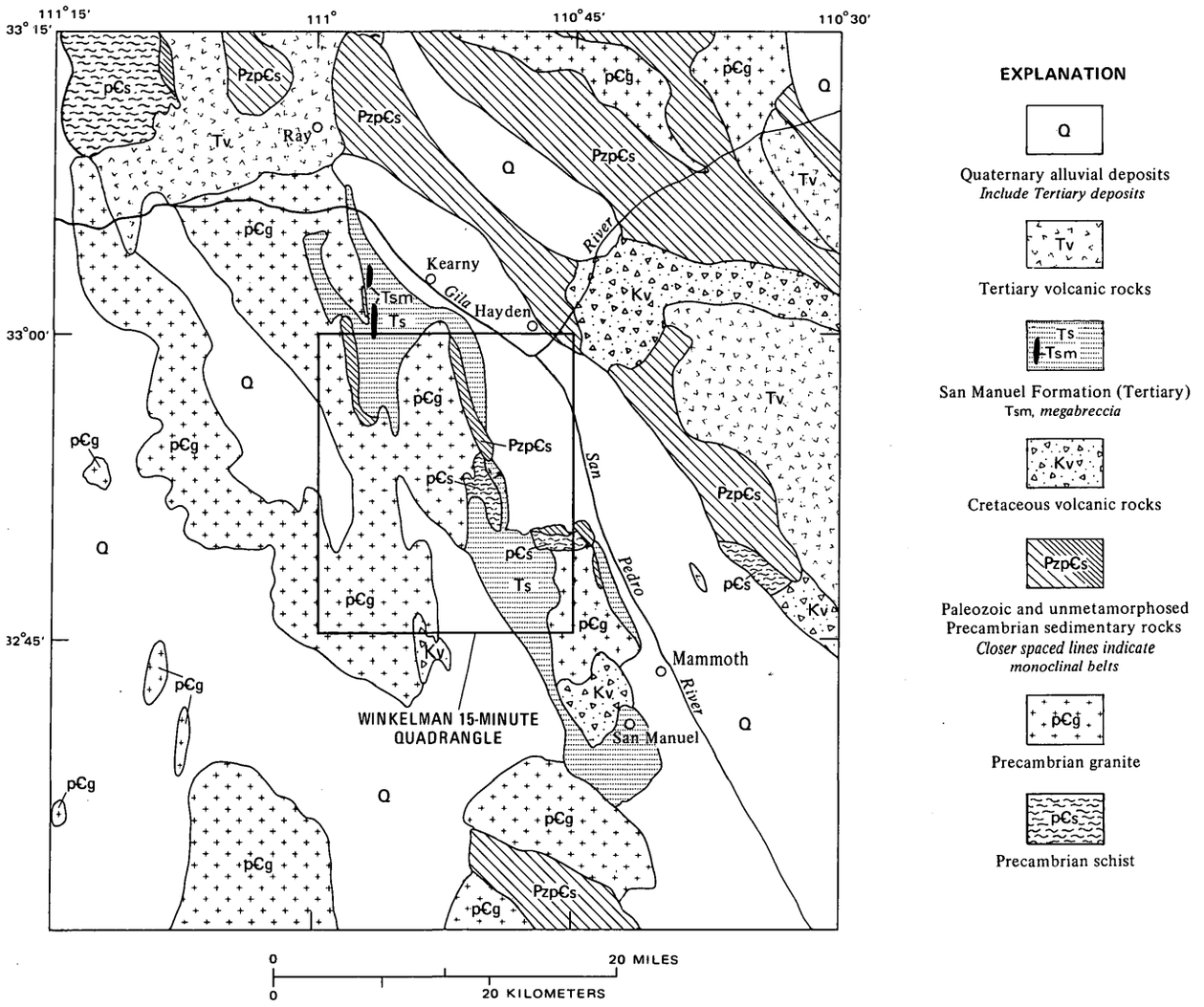

Figure 2.—Regional geologic setting of the Winkelman 15-minute quadrangle. Modified from Wilson, Moore, and Cooper (1969).

in the northwest part of the Crozier Peak quadrangle. The Williamson Canyon Volcanics was considered to be Late Cretaceous by Willden (1964) and Late Cretaceous or early Tertiary by Creasey (1965, 1967). It is now considered to be Late Cretaceous because in the Crozier Peak quadrangle it is intruded by Late Cretaceous diorite (Krieger, 1974b). The Cloudburst Formation is also designated as Late Cretaceous because Creasey (1965, 1967) considered it to be probably the same age as the Williamson Canyon Volcanics in the Christmas quadrangle. The rhyodacitic to quartz latitic volcanic rocks are considered to be Late Cretaceous in age because some of them resemble the Glory Hole Volcanics (east of the area of fig. 3), which is intruded by 69-m.y.-old granodiorite (Simons, 1964; Creasey, 1967).

Late Cretaceous diorite and granodiorite and Late Cretaceous and (or) early Tertiary (Laramide) porphyry masses and dikes of several lithologic types, but largely rhyodacite porphyry, intrude the older rocks. Only the diorite is shown in figure 3. Many of the porphyry dikes and masses are east trending, but older porphyry masses, some possibly of Early Cretaceous age, are conformable and probably were intruded as sills in the Precambrian sedimentary rocks before tilting.

According to the new nomenclature for Cenozoic stratigraphy in eastern Pinal County (Krieger and others, 1974), Tertiary sedimentary deposits in the area (fig. 3), formerly called the Gila Conglomerate or Group, are now divided into the San Manuel Formation (oldest), the Big Dome Formation, and the Quiburis Formation (youngest). Pleistocene and Holocene alluvial deposits, also formerly included in the Gila Conglomerate or Group, overlie these formations.

The San Manuel Formation consists of alluvial and playa deposits and interbedded andesite and megabreccias (not shown separately in fig. 3). The playa deposits and megabreccias are well developed in the Kearny quadrangle (Cornwall and Krieger, 1974). The San Manuel is Miocene (probably early Miocene) in age. Discordant dates on biotite and sanidine from a rhyodacite tuff bed in the upper part of the formation in the Crozier Peak quadrangle are 18 and 24 m.y., respectively. The San Manuel Formation is overlain unconformably by the alluvial Big Dome Formation in the Kearny and Crozier Peak quadrangles. In the Kearny quadrangle, north of the map area, a nonwelded ash-flow tuff in the Big Dome Formation yielded late Miocene K-Ar ages of 14 m.y. on biotite and 17 m.y. on hornblende (Banks and others, 1972). The Quiburis Formation consists of both alluvial and lakebed facies and was deposited in the basin now occupied by the San Pedro River. It contains Hemphillian vertebrate fossils, indicating a middle Pliocene age (John Lance, oral commun., 1963, in Krieger, 1974a). Tertiary volcanic rocks shown in figure 2 include the Galiuro Volcanics (Krieger, 1968, a-d) east of the San Pedro River and the volcanic rocks in the Ray-Superior area. The Galiuro Volcanics has been dated at 22-26 m.y. and probably is about the same age as the San Manuel Formation. The Apache Leap Tuff (part of the volcanic rocks shown in the northwest part of fig. 2) has been dated at 20 m.y. It is older than the Big Dome Formation and probably younger than the San Manuel Formation. Beneath the Apache Leap Tuff is the Whitetail Conglomerate, which contains near its top in the Ray area (Cornwall and others, 1971) a rhyolite tuff bed dated at 32 m.y. (Oligocene).

STRUCTURE

The most obvious structural features in the area are belts of steeply dipping Precambrian and Paleozoic sedimentary rocks that form a series of en echelon ridges separating extensive exposures of Precambrian granite and minor schist on the west from tilted Tertiary sedimentary rocks and gently tilted and intricately faulted Precambrian and Paleozoic sedimentary rocks on the east (figs. 3,4). The steeply dipping belts formed as monoclines, not as the eastern limbs of anticlines. The belts within the Winkelman 15-minute quadrangle are interpreted as parts of a single monocline, later separated by strike-slip and high-angle normal faults. Monoclinal folding commenced before, but continued during and after, deposition of the early(?) Miocene San Manuel Formation.

Within the steeply dipping belts, the section is locally repeated by faults with steep dips which are considered to have formed as low-angle thrusts and to have been tilted to their present nearly vertical position during monoclinal folding. These thrusts and related tears are the oldest structures recognized. They are intruded by Laramide porphyries that are older than the San Manuel Formation. All the other structures are mainly younger than the San Manuel. Possibly some movement on strike-slip faults that segmented the monocline commenced before San Manuel time, but much of it was later. Low-angle gravity slide surfaces underlie the Cloudburst Formation and part of the San Manuel Formation. North-trending high-angle normal faults cut older structural features; some are younger than the Big Dome Formation.

Structural Features Older Than The San Manuel Formation

Thrusts

Faults interpreted to be tilted thrusts (fig. 4) include (1) Ripsey Wash fault, an imbricate structure in the Crozier Peak and southwestern Kearny quadrangles, (2) Romero Wash fault in the Winkelman 7½-minute quadrangle, (3) a thrust extending southward from the Crozier Peak into the Black Mountain quadrangle, and (4) possibly a thrust in the northwestern part of the Lookout Mountain quadrangle. All now have steeply dipping attitudes that closely follow beds of the monoclinal fold. The Ripsey Wash and Romero Wash faults are intruded by Cretaceous porphyries (not shown in fig. 3). Because the folding occurred largely after deposition of the San Manuel Formation, as shown by steep dips in that formation, and because the San Manuel contains clasts of the porphyries, the structural features cannot have formed as high-angle normal or strikeslip faults after formation of the monocline. The Ripsey Wash and Romero Wash faults may

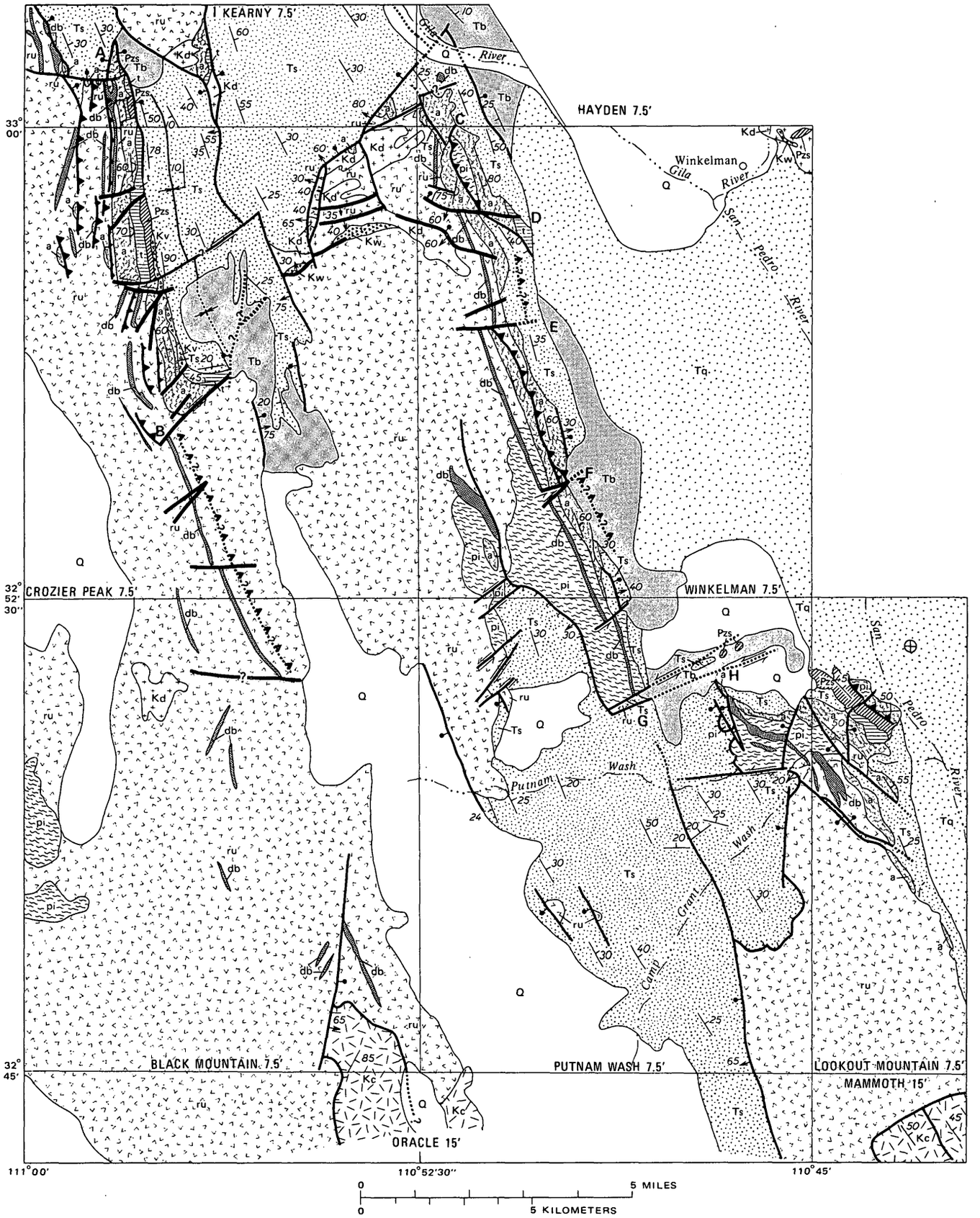

Figure 3.—Generalized geologic map of the Winkelman 15-minute quadrangle and adjacent areas.

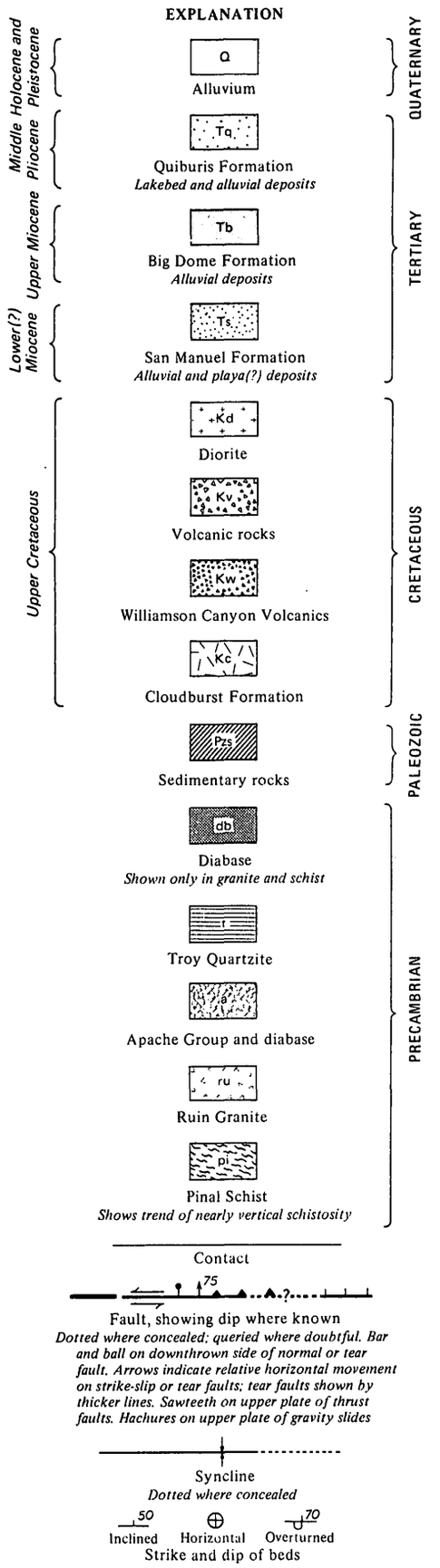

have been part of a single thrust zone, cut and displaced by strike-slip and high-angle normal faults that segmented the monocline.

Ripsey Wash fault.—A north-trending belt of nearly vertical faults that extends from the southwestern part of the Kearny quadrangle (point A, fig. 4) to the central part of the Crozier Peak quadrangle (point B, fig. 4). This zone consists of several fault strands that separate thin east-facing slices of the basal part of the Apache Group, resting with sedimentary contact on the underlying basement (Ruin Granite), from similar slices to the west. Just north of point B at least three such slices, too small and too poorly exposed to show even on the detailed map (Krieger, 1974b), are spaced at distances of 50–100 ft. It is difficult to interpret this series of faults as anything other than a zone of imbricate thrusts that was later tilted. If the monocline extended upward indefinitely, high-angle normal faults could have downdropped the tilted slivers, but the presence of Cretaceous porphyries in some of the faults proves that faulting preceded tilting. If the monocline flattened upward, as it must have and as is suggested for the separate monocline in the Kearny quadrangle discussed below, the slivers should be nearly horizontal or tilted in discordant directions. Figure 5 represents diagrammatic sections across the fault zone, showing relations before and after tilting.

Romero Wash fault.—This fault (fig. 4) is exposed in two segments, a northern segment from south of point C (Hayden quadrangle) to west of point D (Winkelman quadrangle) and a southern segment from west of point E to west of point F. In the northern segment east of the fault the Apache Group rests on the Pinal Schist, and the beds dip steeply east; west of the fault the Apache rests on granite, and the beds are overturned but still occur in normal sequence, except where broken by small faults, most of which are not shown in figures 3 or 4. Some of these faults may be imbricate structures related to the major thrust, not younger high-angle faults as shown on the detailed map (Krieger, 1974a). In the southern segment the beds both east and west of the fault dip steeply east. West of the fault the Apache rests on granite to the north and schist to the south. East of the fault it rests on granite, except at the southern end, where the section is repeated without intervening granite. At the southern end of this segment (point F), two strands of the fault repeat the Apache Group. The southern segment of the fault (points E to F) is occupied by a tabular body of Cretaceous porphyry, whose nearly vertical dip and concordant relations show that the fault formed before or during Cretaceous time. Figure 6 represents a diagrammatic section across the fault, showing relations before and after tilting.

Other thrusts.—The occurrence of diabase as sill-like masses in granite and schist parallel to, and generally not more than 500 ft below, the pre-Apache erosion surface is well illustrated in the Winkelman and parts of the Crozier Peak and Putnam Wash 7½-minute quadrangles (fig. 3). This relationship was recognized by Shride (1967, p. 56), who stated that at depths

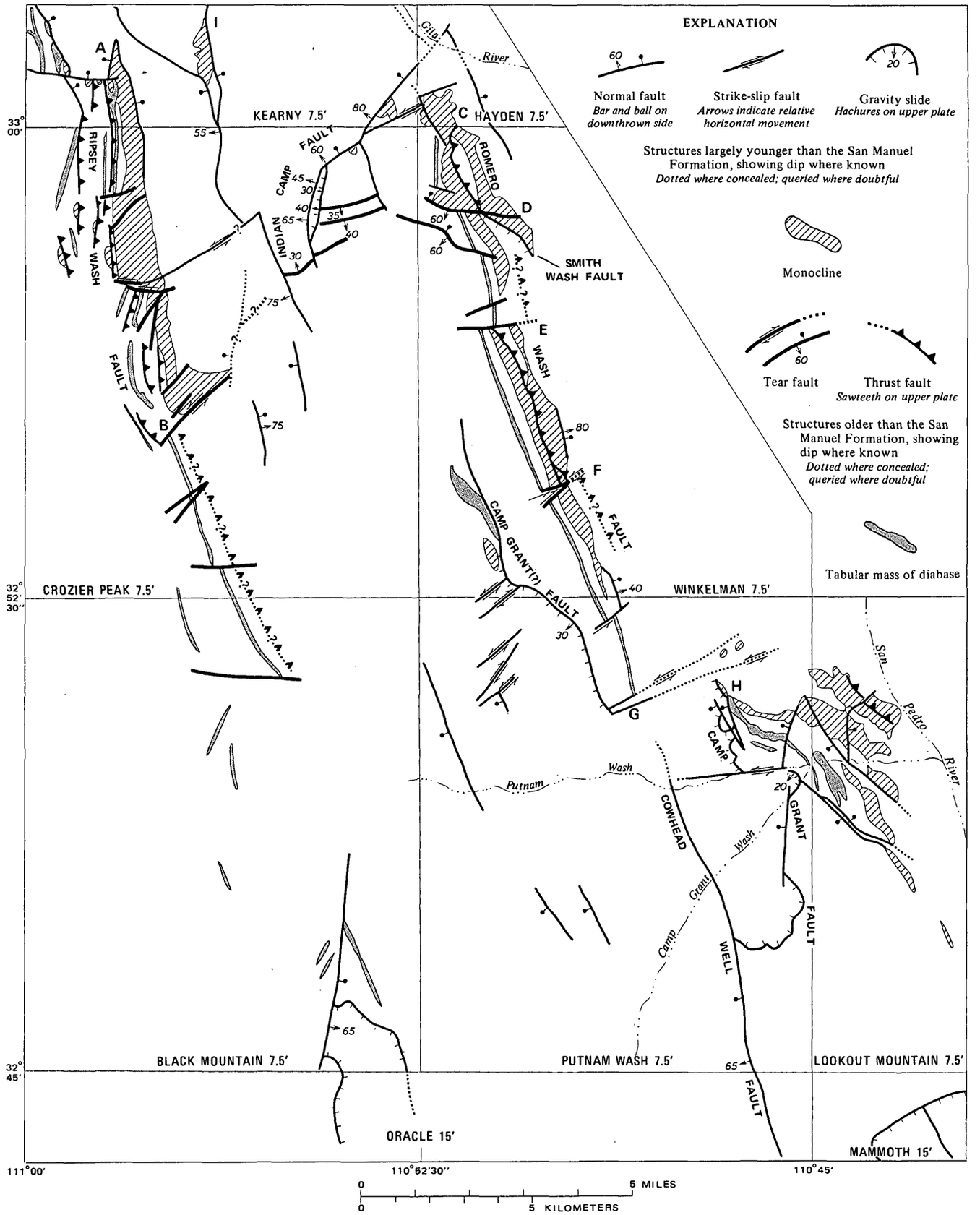

Figure 4.—Generalized structure map of the Winkelman 15-minute quadrangle and adjacent areas.

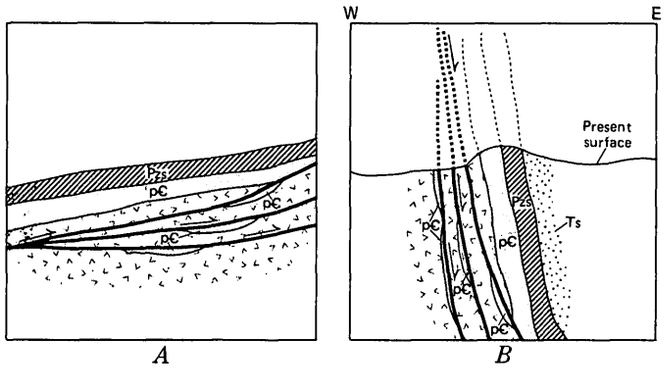

Figure 5.—Diagrammatic sections across Ripsey Wash fault showing suggested relations (*A*) before, and (*B*) after tilting. Ts, sedimentary strata; Ps, Paleozoic strata; pC, Precambrian sedimentary strata.

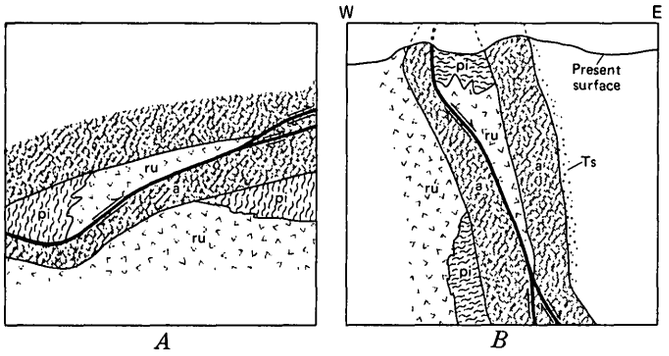

Figure 6.—Diagrammatic sections across Romero Wash fault showing suggested relations (*A*) before, and (*B*) after tilting. Ts, sedimentary strata; a, Apache Group; ru, Ruin Granite; pi, Pinal Schist.

of more than 500 ft below the base of the Apache Group extensive intrusions of diabase are practically nonexistent. It seems likely that the tabular mass of diabase that extends south of point B into the Black Mountain quadrangle may be such a sill originally intruded into the Ruin Granite within 500 ft of the pre-Apache surface. I explain its presence here, apparently miles "below" the nearest Apache Group, as the result of a thrust (fig. 4) perhaps related to a deeper strand of the Ripsey Wash fault; unrecognized normal faults in the granite may complicate the structure. Other tabular masses of diabase, mostly in the Black Mountain quadrangle, may owe their position to unrecognized tilted thrusts, or they may represent feeders to the diabase sills and sill-like masses.

In the northwestern part of the Lookout Mountain quadrangle, the section of steeply dipping Precambrian and Paleozoic rocks is repeated by a series of faults. Some of these faults cut the San Manuel Formation and therefore cannot be thrusts similar to the Ripsey Wash and Romero Wash faults. The beds face east and become progressiely younger, except in the northeasternmost exposures where the beds are overturned and face west or south. This was shown on the map of the Lookout Mountain quadrangle (Krieger, 1968c, sec. *AA'*) as a steeply east-dipping thrust that moved from east to west, or as a high-angle reverse fault. The structure was throught to represent the east limb of a tight syncline in which the west limb had been sheared out. Its relation to the thrusts to the northwest is unknown.

Tears

Numerous northeast-, east-, and southeast-trending, steeply dipping cross faults cut Precambrian and Paleozoic rocks. Some of them exhibit features characteristic of tear faults related to thrusting; they terminate at a thrust or transfer movement from one thrust surface to another. If they are tears that have been rotated almost 90° during development of the monocline, the typical tear-type displacement, which originally would have been strike slip, may now appear as high-angle dip-slip movement. Examples of this are two east-southeast-trending high-angle faults with apparent reverse movement in the northwest part of the Winkelman quadrangle, west and southwest of point D. They dip about 60° to the south, and both show relative uplift on the south. These same relations may also be obtained by strike-slip or oblique-slip, rather than reverse movement. The northern fault appears to offset the Romero Wash fault but not enough to account for the offset of the Apache Group. Where the fault offsets the San Manuel Formation, the south side has been relatively downdropped; that is, the movement is in the opposite sense.

Structural Features Younger Than the San Manuel Formation

Structural features that are mostly younger than the San Manuel Formation include (1) folds that tilted the thrusts and the Precambrian and Paleozoic sedimentary rocks to form north-trending, steeply dipping, east-facing monoclines, (2) east- to northeast-trending strike-slip faults that separate the major monocline into en echelon segments, (3) gently dipping gravity slides that placed tilted Cretaceous and Tertiary rocks on the Ruin Granite, and (4) north-trending high-angle normal faults. Folding may have commenced before, but much of it occurred during and after deposition of the San Manuel. Movement on some of the strike-slip faults may also have commenced before, but most of it ocurred after San Manuel time, and some of it is younger than the gravity sliding that postdates the San Manuel. High-angle normal faults are mostly related to deformation that produced the basin and ranges; one of these basins was filled with the Pliocene Quiburis Formation on which the San Pedro River now flows.

Monoclines

Three north-northwest-trending, en echelon belts of steeply dipping to overturned Precambrian and Paleozoic sedimentary rocks (figs. 3, 4) extend from the Lookout Mountain to the

southwest part of the Kearny quadrangle. A remnant of another belt is exposed in the south-central part of the Kearny quadrangle (figs. 2, 3, and Cornwall and Krieger, 1974). A fourth belt of tilted Precambrian sedimentary rocks is found 15–20 mi northwest of the Kearny quadrangle (fig. 2, and Schmidt, 1966).

The belts that lie mainly within the Winkelman 15-minute quadrangle (from points A to B, points C to G, and southeast of point H, fig. 4) are interpreted to have originally been part of a single monocline later segmented by strike-slip and high-angle normal faults. The steeply dipping Apache Group rocks are not exposed continuously in the middle segment (points C to G). Their presence beneath the San Manuel Formation, however, is suggested by the tabular mass of diabase in granite and schist, which elsewhere lies within 500 ft of the pre-Apache surface; it is also confirmed by small patches of Apache Group (not shown in fig. 3), north of point G.

The monocline near point I is a separate but probably contemporaneous feature. This monocline extends from southwest of point I northward across the Kearny quadrangle (Cornwall and Krieger, 1974) for over 6 mi. Remnants of Precambrian sedimentary rocks resting on granite lie west of the steeply dipping San Manuel Formation near point I. North of point I nearly vertical tabular masses of diabase lie a short distance west of the fault that separates Ruin Granite from the San Manuel Formation and indicate the northward extension of the monocline. The suggestion is untenable that the monocline was originally part of the monocline in the Winkelman 15-minute quadrangle and was moved from point A to south of point I along a southeast-trending strike-slip fault. Two belts of east-trending porphyry dike swarms show no evidence of offset. One belt extends from the northwest part of the Kearny quadrangle (Cornwall and Krieger, 1974), westward across the northeast part of the adjacent Grayback Mountain quadrangle (H. R. Cornwall and M. H. Krieger, unpub. data, 1973); the other extends from the southwestern part of the Kearny quadrangle into the southeast part of the Grayback Mountain quadrangle. The apparent strike-slip fault is a high-angle normal fault that bounds the southwest side of a younger horst block.

These tilted belts are interpreted as the eroded remnants of east-facing monoclinal folds that separate vast areas of granite on the west from Tertiary sediments on the east. The almost complete absence of west-facing beds, as well as the absence of Precambrian or Paleozoic sedimentary rocks for more than 60 mi to the southwest, appear to rule out the possibility that the monocline is the east limb of an anticline. Isolated examples of west-facing beds—southwest part of the Winkelman quadrangle (Krieger, 1974a), northwest part of the Lookout Mountain quadrangle, (Krieger, 1968c), and northwest part of the Crozier Peak quadrangle (Krieger, 1974b, sec 23, T. 5 S., R. 13 E.)—are interpreted as the result of drag or later deformation. The alternate view that the tilted belts are the result of drag along high-angle faults appears improbable because the Apache Group is in normal sedimentary contact with granite and schist and because diabase in the basement, within 500 ft of the base of the Apache, precludes the existence of large high-angle faults west of the belts. In the west-central part of the Kearny quadrangle (Cornwall and Krieger, 1974), a nearly horizontal mass of diabase trends westward from a north-trending diabase mass that marks the trend of the monocline in this area. It is interpreted as a sill intruded not more than 500 ft below the pre-Apache surface and representing the area where the monocline flattened westward. The overlying Precambrian and Paleozoic sedimentary rocks were eroded after formation of the monocline.

The folding occurred before and continued after deposition of the San Manuel Formation because, adjacent to the monoclinal ridges, the San Manuel Formation also dips steeply, though generally 20°–30° less than the older rocks. Although some of the tilting of the San Manuel Formation could have been caused by drag along the faults that separate the San Manuel from older rocks, the extensive areas of tilted San Manuel east of the faults could not have been formed by drag. Deposits of claystone and mudstone with abundant mud cracks and curled mud chips indicate deposition of part of the San Manuel Formation in a flat playa environment. In the Kearny quadrangle (Cornwall and Krieger, 1974), megabreccias (landslide blocks) slid from the west or southwest out onto interfingering playa and alluvial deposits and were immediately buried by additional playa and alluvial deposits. The sediments and interbedded megabreccias now dip steeply to almost vertically east. Away from the monocline the San Manuel Formation dips less steeply because of the eastward flattening of the monocline. Attitudes of the San Manuel Formation away from the monocline may be partly due to later structural features. The fact that the oldest unit in the San Manuel in the Putnam Wash quadrangle is composed largely of clasts of Ruin Granite indicates that Precambrian basement was exposed, before San Manuel time, somewhere west and southwest of the Winkelman 15-minute quadrangle. Likewise, much of the San Manuel Formation in the northwestern half of the Kearny quadrangle is composed of granitic clasts, derived from the northwest and west. However, Paleozoic and Precambrian sedimentary rock clasts are abundant in the San Manuel Formation and form extensive megabreccias, especially in the Kearny quadrangle (Cornwall and Krieger, 1974), proving that these sedimentary rocks had not been entirely stripped from the granite and schist basement by San Manuel time.

Strike-slip faults

Two major left-lateral strike-slip faults appear to separate into segments what is interpreted to have been a single monoclinal ridge (fig. 4). The northern fault moved the

monoclinal ridge from points B to C, and the southern one moved it from point G to east of point H.

Although conclusive proof is lacking that the northern and middle segments were originally continuous, the following evidence suggests this interpretation: (1) In the Crozier Peak quadrangle, east of point B (fig.3) the strike of vertical to steeply overturned strata changes abruptly from a north to an east-west trend with a gentler northward dip, suggesting drag, and (2) The small patches of Apache Group, not entirely in normal stratigraphic sequence, west of point C (southeast corner of Kearny quadrangle and northeast part of Crozier Peak quadrangle), may have been dragged into their present position by the fault. In this area the fractured condition of granite and diorite bedrock may have been caused by the strike-slip fault. The position of the strike-slip fault across or beneath the San Manuel Formation, northeast of point B, is uncertain because of concealement both by the Big Dome Formation and by colluvial slumping of the San Manuel Formation and because of offset by younger north-northwest-trending high-angle faults. How much of the movement on the strike-slip fault is older than the San Manuel Formation and how much is younger is uncertain. The fold in the older rocks is reflected in the younger deposits, which also swing east.

The following evidence supports a southern strike-slip fault: (1) Small exposures of Paleozoic rocks north of point H lie considerably west of the main outcrops in the northwest part of the Lookout Mountain quadrangle (fig. 3), (2) Apache Group, assumed to be buried beneath the San Manuel Formation, north of point G, is west of the Apache Group near point H, and (3) what is interpreted to be the continuation of the post-San Manuel Camp Grant fault (fig. 4), northwest of point G, is offset westward from the northern exposure of Camp Grant fault near point H. Movement on this strike-slip fault appears to be younger than the Camp Grant fault, which cuts the San Manuel Formation.

Gravity slides

Gravity slides—décollements or detachments—are concave-upward surfaces that separate sedimentary or volcanic rocks from older rocks. The younger rocks generally dip in the opposite direction from the fault surface. The best example of a gravity slide in the Winkelman 15-minute quadrangle is Camp Grant fault in the Putnam Wash quadrangle. Other probable gravity slides are beneath the Cloudburst Formation (fig. 3) in the Black Mountain and Mammoth quadrangles and involve San Manuel Formation in the northern part of the Winkelman 15-minute quadrangle. The Cloudburst Formation in the southeast part of the Black Mountain quadrangle is nearly vertical and is surrounded on at least the west, north, and east sides by the Ruin Granite. The contact between the Cloudburst and granite is concealed by alluvium, except on the west where it is an east-dipping normal fault. The gravity slide is assumed to be a nearly horizontal concave-upward surface (Krieger, 1974c, sec. *AA'*). In the Mammoth quadrangle, Creasey (1965, 1967) interpreted the structure as a gently east-dipping thrust; the overlying Cloudburst Formation dips mostly 35°–65° eastward. The Indian Camp fault in the northeastern part of the Crozier Peak quadrangle and the Smith Wash fault in the northwest part of the Winkelman 7½-minute quadrangle are questionably interpreted as gravity slides.

A low-dipping gently curved fault surface (fig. 7) is well exposed on the north side of Camp Grant Wash about 2,000 ft southwest of its junction (at the quadrangle boundary) with Putnam Wash. This surface, interpreted as a gravity slide plane, dips 20° west and separates Ruin Granite on the east from the San Manuel Formation on the west. The surface on granite is remarkably smooth. Conglomeratic gouge a few inches thick separates the granite from the overlying conglomerate. Fracture cleavage in the gouge indicates that the upper block moved from east to west. The conglomerate dips about 35° northeast and is cut by by subparallel cycloidal (in section) faults and by steeper west-dipping faults. The steeper faults end downward at the gravity slide plane or at the cycloidal faults. These features are similar to what Anderson (1971, p. 43) has called "thin-skinned distension" in Tertiary rocks in Nevada in which Tertiary volcanic rocks are cut by "a system of closely spaced north- to northwest-striking shingling normal faults (many of which are low angle) that displace younger over older rocks in a west to southwest direction * . * . * . The structural units are floored at or near the present level of exposure by complex low-angle zones of detachment or decollement into which the numerous shingling normal faults merge." Absence of recognizable small stratigraphic units and difficulty in tracing faults in the San Manuel Formation make it impossible to determine whether or not the apparently great thickness of the formation in the Putnam Wash quadrangle is caused by repeated low-angle slicing and rotation.

Camp Grant fault is offset to the west by an eastward-trending strike-slip fault along Putnam Wash and probably by a major strike-slip fault near point G; it is cut by north-trending normal faults (discussed below). What is interpreted to be the offset part of the Camp Grant fault is exposed in the northwest part of the Putnam Wash quadrangle. It separates Pinal Schist on the east from northeast-dipping San Manuel Formation on the west. The fault dips about 30° west. Camp Grant fault was questionably extended into the southwestern part of the Winkelman quadrangle. If the fault in that area is part of the Camp Grant fault, it is unusual in that it involves Precambrian rocks. Most of the gravity slides are believed to flatten downward and for the most part not to extend far into the basement. The attitude of the small mass of Apache Group suggests drag that might accompany faulting or gravity sliding. The Apache is cut by a north-trending fault (not shown in figs. 3, 4). West of the fault the Apache dips steeply eastward; east of the fault it also dips steeply eastward, but the dip flattens

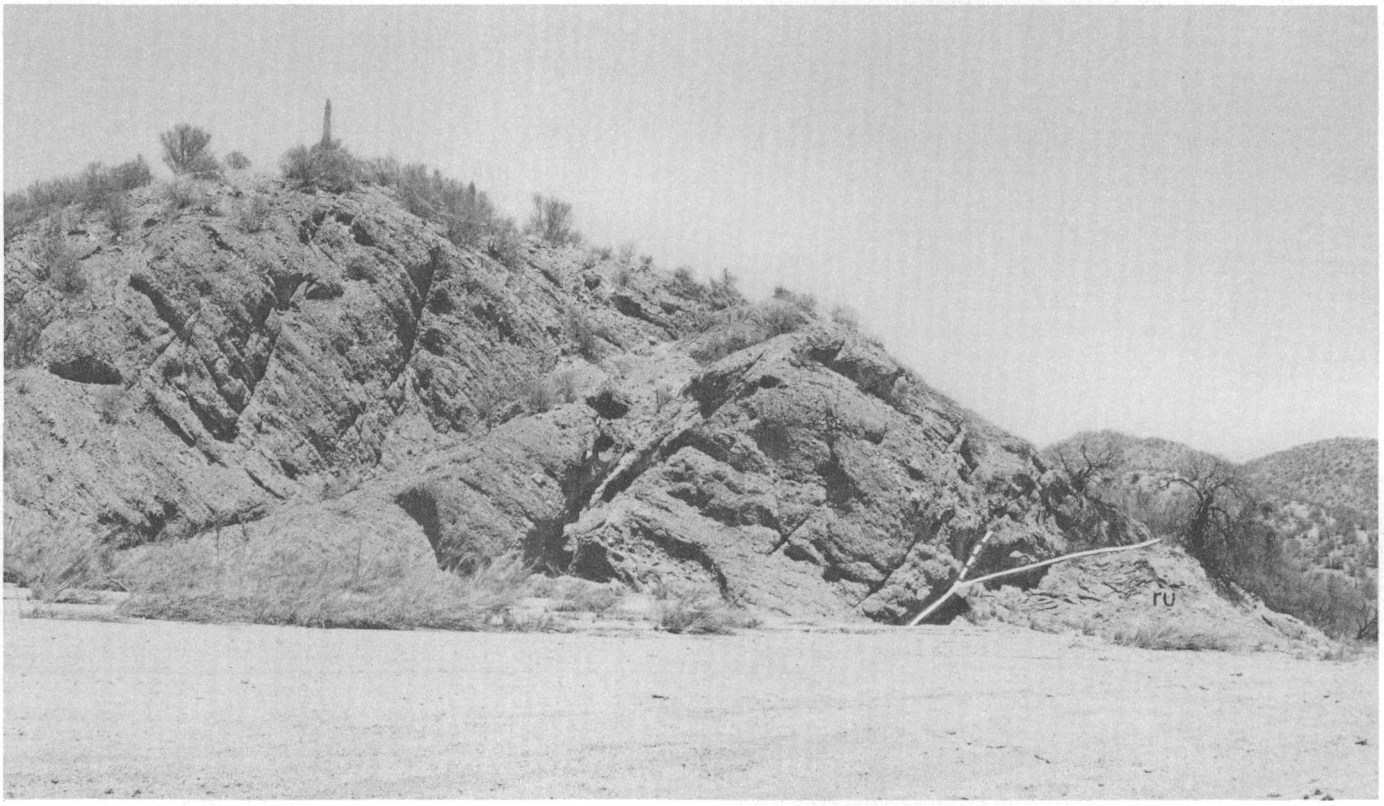

Figure 7.—Camp Grant fault, exposed on north side of Camp Grant Wash, about 2,000 ft southwest of junction of Camp Grant and Putnam Washes. Light-colored outcrop at right is Ruin Granite (ru). Fault surface here dips about 20° west. Overlying conglomerate of San Manuel Formation dips about 35° northeast and is cut by subparallel cycloidal faults and by steeper west-dipping faults that end downward at the cycloidal faults. The fault surface appears to steepen where it approaches the wash, but this is an optical illusion due to foreshortening because of the angle at which it is viewed and to removal of some of the younger rocks, where cut by one of the more steeply dipping small faults at the creek level.

rapidly (Krieger, 1974d, sec. *DD'*), and along the eastern margin of the outcrop, beds dip gently westward.

High-angle normal faults

High-angle, mostly north-northwest-trending normal faults cut the San Manuel Formation and older rocks. Renewed movement has also occurred since deposition of the Big Dome Formation, and some has occurred since deposition of the Quiburis Formation (east of the San Pedro River). Some of these faults are downthrown on the east, and some on the west. A few of these faults deserve special mention.

The Cowhead Well fault (fig. 4) extends for at least 12 mi, from north of Putnam Wash into the western part of the Mammoth quadrangle (south of the map area). It is younger than both the San Manuel Formation and the Camp Grant fault.

The fault that cuts off the Cloudburst Formation and the thrust that underlies the Cloudburst in the Southeastern part of the Black Mountain quadrangle may also be younger than the San Manuel Formation.

Faults occur between the San Manuel Formation and Precambrian and Paleozoic bedrock in many places, but the amount of displacement within the Winkelman 15-minute quadrangle in most places is believed to be small. The attitude of the San Manuel Formation, therefore, is likely due to folding (tilting), not to drag on the faults. In the Kearny quadrangle, however, considerable post-San Manuel displacement has occurred on the bounding faults. The bedrock mass west of point I is clearly a horst. Uplift on this block may have been responsible for development of the syncline in the San Manuel Formation that extends from the Crozier Peak quadrangle into the southwest part of the Kearny quadrangle. Playa deposits on the east side of the syncline are identical with those east of point I and at one time extended across at least the southern end of the block.

These high-angle normal faults are part of the Basin and Range fault system. Major faults, at least on the east side of the San Pedro River (fig. 2), produced the basin in which the Pliocene Quiburis Formation was deposited. This faulting took place largely after deposition of the San Manuel Formation, and some of it occurred after deposition of the Big Dome

Formation. The early Miocene Galiuro Volcanics east of the San Pedro River has been downdropped at least 5,000 ft from its position at the northern end of the Galiuro Mountains and was later buried by the Quiburis Formation (Krieger, 1968b,c). The change from low-angle gravity sliding and associated low-angle normal faults indicating major extension to high-angle normal faults indicating predominantly vertical displacement took place in the late Tertiary, as noted in Anderson (1971, p. 3534), in southwestern Nevada.

CONCLUSIONS

Structural features in the Winkelman 15-minute quadrangle are believed to have developed in the following sequence: Imbircate thrusts and related tears were formed in a flat environment and were later tilted, when an east-facing monoclinal fold developed a linear belt of steeply dipping to overturned Precambrian and Paleozoic sedimentary rocks. This folding, which began before but continued after deposition of the Miocene San Manuel Formation, developed other monoclinal folds to the north and northwest of the quadrangle. East-trending strike-slip faults separated the monocline in the Winkelman quadrangle into three en echelon segments. Some of this faulting apparently occurred after large areas of the San Manuel Formation became detached and moved over basement rocks on a low-angle gravity slide surface. All these structures are broken by north-trending high-angle normal faults.

The structural complexity of the area contrasts markedly with the structural features northeast of the Gila and San Pedro Rivers, as was noted by Ransome (1919, p. 82) and as can be seen in figure 2 and by examining published geologic maps of the area (see fig. 1 for references; also Wilson and others, 1969). Northeast of the rivers the beds are mainly gently tilted and intricately faulted; monoclinal flexures, where present, face both east and west. A major northwest-trending fault, approximately beneath the Gila and San Pedro Rivers, follows the boundary between the two blocks.

REFERENCES CITED

Anderson, R. E., 1971. Thin skin distension in Tertiary rocks of southeastern Nevada: Geol. Soc. America Bull., v. 82, p. 43–58; reply, p. 3533–3536.

Banks, N. G., Cornwall, H. R., Silberman, M. L., Creasey, S. C., and Marvin, H. R., 1972. Chronology of intrusion and ore deposition at Ray, Arizona. Part I, K-Ar ages: Econ, Geology, v. 67, p. 864–878.

Cornwall, H. R., Banks, N. G., and Phillips, C. H., 1971. Geologic map of the Sonora quadrangle, Pinal and Gila Counties, Arizona: U.S. Geol. Survey Geol. Quad. Map GQ-1021, scale 1:24,000.

Cornwall, H. R., and Krieger, M. H., 1974. Geologic map of the Kearny quadrangle, Pinal County, Arizona: U.S. Geol. Survey Geol. Quad. Map GQ-1188, scale 1:24,000. (In press.)

Creasey, S. C., 1965, Geology of the San Manuel area, Pinal County, Arizona: U.S. Geol. Survey Prof. Paper 471, 64 p.

—— 1967, General geology of the Mammoth quadrangle, Pinal County, Arizona: U.S. Geol. Survey Bull. 1218, 94 p.

Creasey, S. C., Jackson, E. D., and Gulbrandsen, R. A., 1961, Reconnaissance geologic map of parts of the San Pedro and Aravaipa Valleys, south-central Arizona: U.S. Geol. Survey Mineral Inv. Field Studies Map MF-238.

Damon, P. E., Livingston, D. E., and Erickson, R. C., 1962, New K-Ar dates for the Precambrian of Pinal, Gila, Yavapai, and Coconino Counties, Arizona, *in* Guidebook of the Mogollon Rim Region, east-central Arizona, New Mexico Geol. Soc., 13th Field Conf.: Socorro, New Mexico Bur. Mines and Mineral Resources, p. 56–57.

Krieger, M. H., 1968a, Geologic map of the Brandenburg Mountain quadrangle, Pinal County, Arizona: U.S. Geol. Survey Geol. Quad. Map GQ-668, scale 1:24,000.

—— 1968b, Geologic map of the Holy Joe Peak quadrangle, Pinal County, Arizona: U.S. Geol. Survey Geol. Quad. Map GQ-669, scale 1:24,000.

—— 1968c, Geologic map of the Lookout Mountain quadrangle, Pinal County, Arizona: U.S. Geol. Survey Geol. Quad. Map GQ-670, Scale 1:24,000.

—— 1968d, Geologic map of the Saddle Mountain quadrangle, Pinal County, Arizona: U.S. Geol. Survey Geol. Quad. Map GQ-671, scale 1:24,000.

—— 1974a, Geologic map of the Winkelman quadrangle, Pinal and Gila Counties, Arizona: U.S. Geol. Survey Geol. Quad. Map GQ-1106, scale 1:24,000. (In press.)

—— 1974b, Geologic map of the Crozier Peak quadrangle, Pinal County, Arizona: U.S. Geol. Survey Geol. Quad. Map GQ-1107, scale 1:24,00. (In press.)

—— 1974c, Geologic map of the Black Mountain quadrangle, Pinal County, Arizona:: U.S. Geol. Survey Geol. Quad. Map GQ-1108, scale 1:24,000. (In press.)

—— 1974d, Geologic map of the Putnam Wash Quadrangle, Pinal County, Arizona: U.S. Geol. Survey Geol. Quad. Map GQ-1109, scale 1:24,000. (In press.)

Krieger, M. H. Cornwall, H. R., and Banks, N. G., 1974, The Big Dome Formation and revised Tertiary stratigraphy in the Ray-San Manuel area, Arizona: U.S. Geol. Survey Bull. 1394-A, 93 p.

Peterson, N. P., 1938, Geology and ore deposits of the Mammoth mining camp area, Pinal County, Arizona: Arizona Bur. Mines Bull. 144, Geol. ser. 11 (Arizona Univ. Bull., v. 9, no. 2), 63 p.

Ransome, F. S., 1919, The copper deposits of Ray and Miami, Arizona: U.S. Geol. Survey Prof. Paper 115, 192 p.

Schmidt, E. A., 1966, Geologic map of the Mineral Mountain quadrangle, Pinal County, Arizona: Arizona Univ., Tucson, M.S. thesis.

Shride, A. F., 1967, Younger Precambrian geology in southern Arizona: U.S. Geol. Survey Prof. Paper 566, 89 p.

Silver, L. T., 1960, Age determinations on Precambrian diabase differentiates in the Sierra Ancha, Gila County, Arizona [abs.]: Geol. Soc. America Bull., v. 71, no. 12, pt. 2, p. 1973–1974.

—— 1968, Precambrian batholiths of Arizona [abs.]: Geol. Soc. America, Cordilleran Sec., 64th Ann. Mtg., Tucson, Ariz., Program, p. 109–110.

Simons, F. S., 1964, Geology of the Klondyke quadrangle, Graham and Pinal Counties, Arizona: U.S. Geol. Survey Prof. Paper 461, 173 p.

Willden, Ronald, 1964, Geology of the Christmas quadrangle, Gila and Pinal Counties, Arizona: U.S. Geol. Survey Bull. 1161-E, p. E1–E64.

Wilson, E. D., Moore, R. T., and Cooper, J. R., 1969, Geologic map of Arizona: Arizona Bur. Mines and U.S. Geol. Survey, scale 1:500,000.

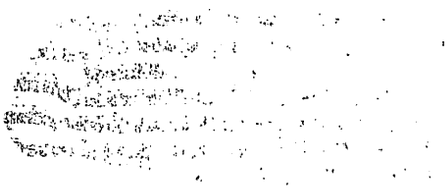

Jour. Research U.S. Geol. Survey
Vol. 2, No. 3, May-June 1974, p. 323—329

THE BORDER RANGES FAULT IN SOUTH-CENTRAL ALASKA

By E. M. MacKEVETT, JR., and GEORGE PLAFKER,
Menlo Park, Calif.

Abstract.—The Border Ranges fault, a major fault of southern Alaska, can be traced for more than 1,000 km arcuately eastward from Kodiak Island to the St. Elias Mountains. Throughout its extent, the fault juxtaposes upper Paleozoic and lower Mesozoic rocks on the north against upper Mesozoic and Tertiary rocks. This report describes the Border Ranges fault and its geologic setting along an approximately 245-km-long segment in the McCarthy and Valdez quadrangles. It also summarizes information relevant to other parts of the fault and discusses its significance and tectonic implications. In the McCarthy and Valdez quadrangles the fault strikes between N. 60° W. and west. Its dips change from vertical and steeply northward in its eastern part to between 20° and 60° north throughout most of the Valdez quadrangle and reflect the transition from a high-angle reverse fault to a northward-dipping thrust. The Border Ranges fault is interpreted to mark a plate boundary that developed near the close of the Mesozoic or in the early Tertiary.

A major fault, here named the Border Ranges fault, can be traced discontinuously for more than 1,000 km along the Pacific border of Alaska. The fault extends from west of Kodiak Island arcuately eastward along the northern flanks of the Kodiak, Kenai, and Chugach Mountains to the St. Elias Mountains (fig. 1). Throughout its length, the fault juxtaposes upper Paleozoic and lower Mesozoic rocks on the north against upper Mesozoic and Tertiary rocks. Although parts of the fault have been known or inferred for many years, the fault is incompletely mapped, mainly because it extends through remote, rugged terrain that has been sparingly investigated; consequently, it has received little recognition in the geologic literature. This report describes the fault and its geologic setting along an approximately 245-km-long segment in the Chugach Mountains in the McCarthy and Valdez quadrangles. Also, the report summarizes information relevant to other parts of the fault and discusses significance and tectonic implications of the entire fault.

PREVIOUS INVESTIGATIONS

Most earlier data relevant to the Border Ranges fault are incidental products of geologic studies near the western parts of the fault. According to Capps (1937), a large northeast-striking, nearly vertical fault transects northwestern Kodiak Island and Afognak Island (fig. 1) and separates a greenstone-schist complex on the north from a thick sequence of upper Mesozoic graywacke, slate, and argillite. Capps reported some pillow lavas in the greenstone-schist complex and correlated the complex with similar rocks on the Kenai Peninsula that, according to Martin and others (1915), range in age from late Paleozoic to Jurassic. Fossiliferous middle Permian limestone and associated volcanic rocks at Puale Bay on the Alaska Peninsula opposite Kodiak Island (Hanson, 1957) probably also correlate with parts of the greenstone-schist complex. Moore's (1967) map of Kodiak Island shows the fault as a northeast-striking thrust with Triassic and Jurassic volcanic and marine sedimentary rocks and ultramafic rocks to the northwest thrust over Cretaceous sedimentary rocks. D. L. Jones and S. H. B. Clark (oral commun., 1972) after brief reconnaissance examinations report that at several places the basal rocks north of the fault on Kodiak Island include an ophiolite sequence of ultramafic rock, gabbro, and overlying pillow basalts. Evidence for southwestward continuation of the fault beyond Kodiak Island is meager.

The trace of the fault in the Kenai Peninsula is accurately known at only a few localities. In the western Kenai Mountains the fault separates a thick heterogeneous upper Paleozoic to Jurassic sequence from upper Mesozoic flysch to the southeast. The rocks northwest of the fault mainly comprise schist, pillow lava, tuff, chert, and limestone (Martin and others, 1915), and they include some blueschist that has been radiometrically dated as Late Triassic or Early Jurassic (Forbes and Lanphere, 1973). The relations between the ultramafic masses at Red Mountain and Claim Point and the fault are not known, but similar ultramafic rocks near the fault elsewhere are invariably associated with the older rocks of the upper plate. In the absence of more specific data, we favor including the Kenai Mountains ultramafic rocks with the older rocks and speculate that they occur near the extremities of a southward-projecting lobe of the fault.

In the northeastern Kenai Peninsula and near Anchorage, the fault is mantled by surficial deposits. Extensive ground breakage in surficial deposits along a northeast-striking zone in the northwestern part of the Kenai Peninsula that developed during the 1964 Alaska earthquake may reflect movement along a buried fault (Foster and Karlstrom, 1967, p. F24).

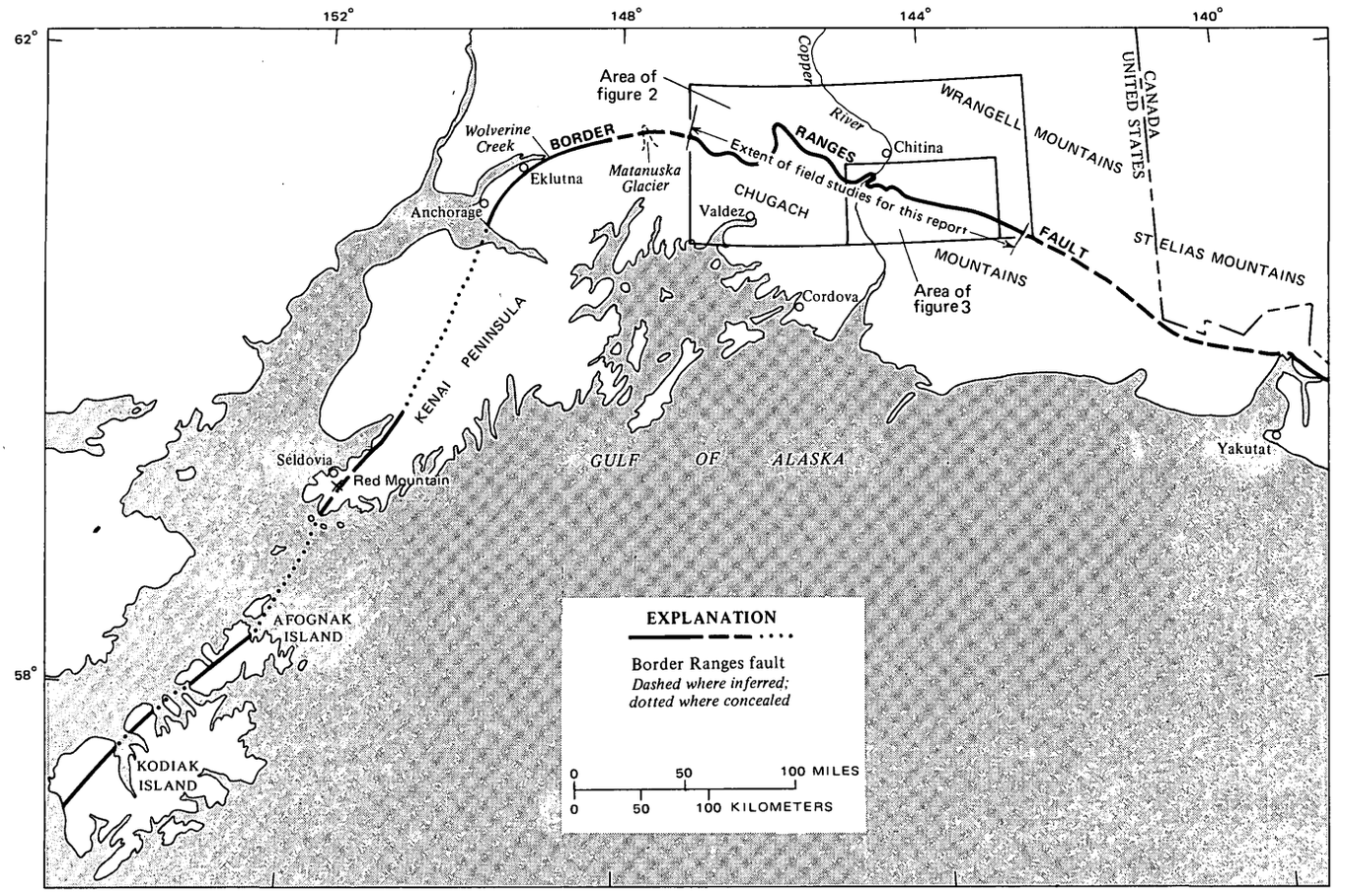

Figure 1.—Location and extent of the Border Ranges fault, southern Alaska.

Although much of the breakage zone lies northwest of the inferred position of the Border Ranges fault, the disruptive effects may be a manifestation of it or a related fault. The fault reappears along the northwestern front of the Chugach Mountains about 25 km northeast of Anchorage where it has been mapped by Clark (1972a) as the Knik fault. Eastward from this locality, Clark (1972a,b) has traced the fault intermittently along the range front and across intervening valleys approximately 50 km to near the 148°30′ meridian. Clark (1972a,b) reports that the Knik fault separates Permian to Jurassic(?) metamorphosed volcanic and sedimentary rocks, ophiolitic assemblages, and Jurassic plutons from upper Mesozoic rocks of the McHugh Complex and Valdez(?) Group to the south. The McHugh Complex consists of two distinctive submarine sequences, one metaclastic and the other metavolcanic, that in places are chaotically juxtaposed and locally contain exotic blocks. The Valdez(?) Group in Clark's map area constitutes a slightly metamorphosed flysch that has yielded a few fossils of Late Cretaceous (Maestrichtian) age. According to Clark (1972a), the Knik fault occupies a complex zone with little or no topographic expression.

The limited information on the fault between the 148°30′ meridian and the 147° meridian (the western boundary of our map) is from brief reconnaissance examinations by Arthur Grantz. Grantz (oral commun., 1973) observed the fault about 12 km above the terminus of the Matanuska Glacier where the fault strikes east and dips about 85° north. The fault juxtaposes the Talkeetna Formation, a predominantly marine volcanic and sedimentary unit of Early Jurassic age, on the north against Tertiary terrestrial sedimentary rocks, which unconformably overlie the weakly metamorphosed Valdez Group about 3 km to the south. A probably similar relationship was observed by Grantz west of Nelchina Glacier during airborne reconnaissance.

Moffit (1914, 1938) delineated the approximate contact between the upper Paleozoic rocks and the Valdez Group throughout the area of our mapping. Although his maps do not show the contact as a fault, Moffit's (1914, p. 19; 1938, p. 26) descriptions indicate that, in places, he interpreted the contact as a fault.

The southeastward continuation of the fault from near the junction of the Tana River and the southern boundary of the McCarthy quadrangle (the limit of our mapping) is not well known. The fault projects into a contact in the northern part

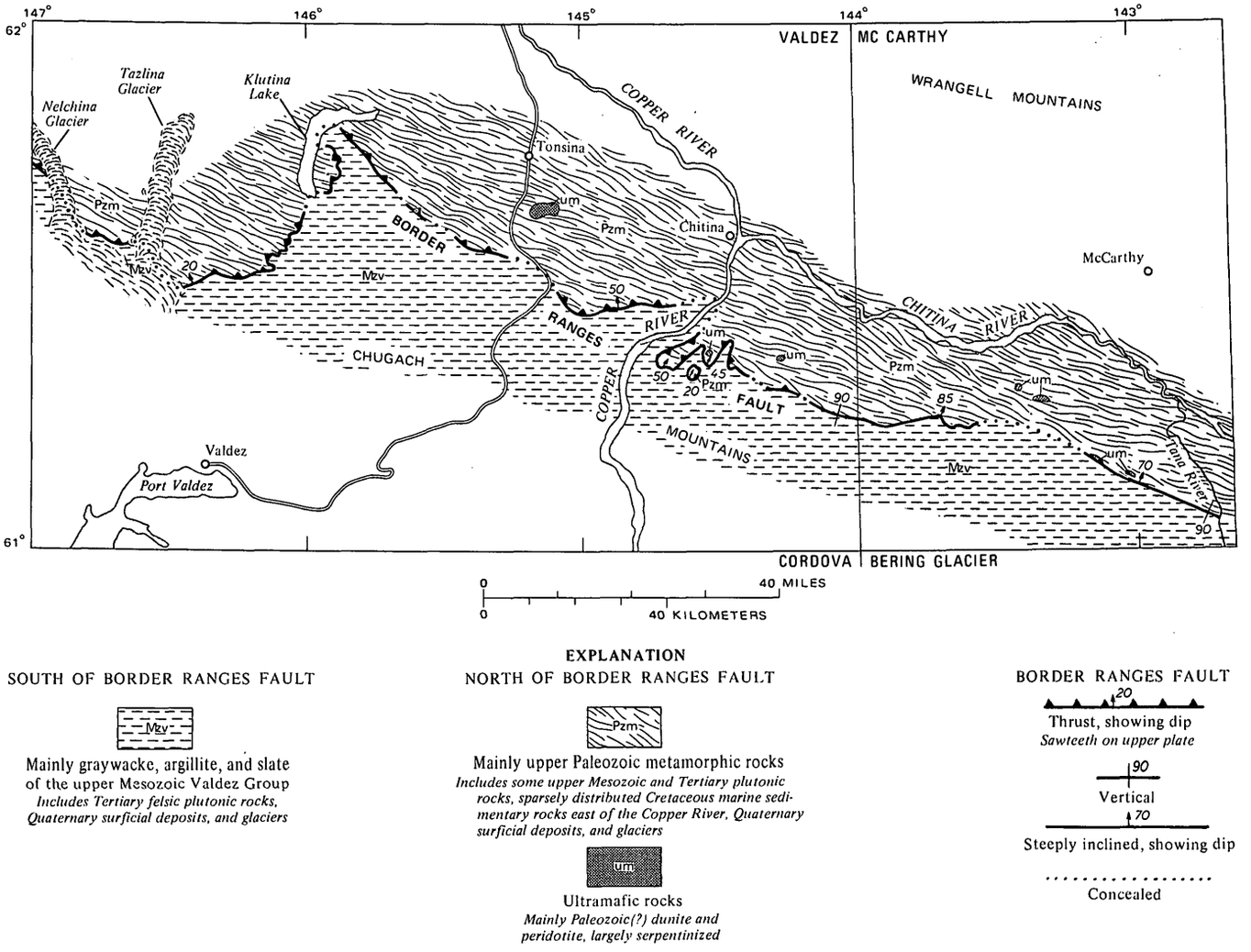

Figure 2.—Generalized geologic map showing the Border Ranges fault in the McCarthy and Valdez quadrangles. Base from U.S. Geological Survey 1:250,000-scale McCarthy and Valdez quadrangle maps, 1960.

of the Bering Glacier quadrangle that is shown on a reconnaissance strip map across the eastern Chugach Mountains (Brabb and Miller, 1962). This contact was mapped for approximately 8 km across the mapped strip. It separates nearly vertical late Paleozoic rocks on the north from the nearly vertical Valdez Group and probably marks a steep northwest-striking fault. Farther to the southeast the Border Ranges fault projects into unmapped parts of the Bering Glacier quadrangle, and distally, it may connect with one of the major faults that have been mapped by Plafker (unpub. data, 1974) in the St. Elias Mountains north of Yakutat.

PRESENT INVESTIGATION

This report is based on 3 weeks of helicopter-supported reconnaissance geologic mapping during August 1972 and 1 day in August 1971. During these periods we mapped the fault from the south-central edge of the McCarthy 1:250,000-scale quadrangle northwestward to the western edge of the Valdez quadrangle (fig. 2). The fault trace is along the remote and rugged northern front of the Chugach Mountains where it is partly obscured by surficial deposits and glaciers. One road, the Richardson Highway, and one major river, the Copper, cross the fault in the region of our investigation. Throughout its mapped length, the fault juxtaposes a thick upper Paleozoic metamorphic sequence that contains subordinate gabbro, diorite, and ultramafic rocks against upper Mesozoic flysch of the Valdez Group. Our descriptions of rocks near the fault are mainly based on hand-specimen examinations.

Characteristics and relations of the fault

In the McCarthy quadrangle and northwestward to near Spirit Mountain, about 25 km west of the eastern boundary of the Valdez quadrangle, the fault mainly dips between 70° north and vertical or, rarely, steeply southward (fig. 3). Strikes

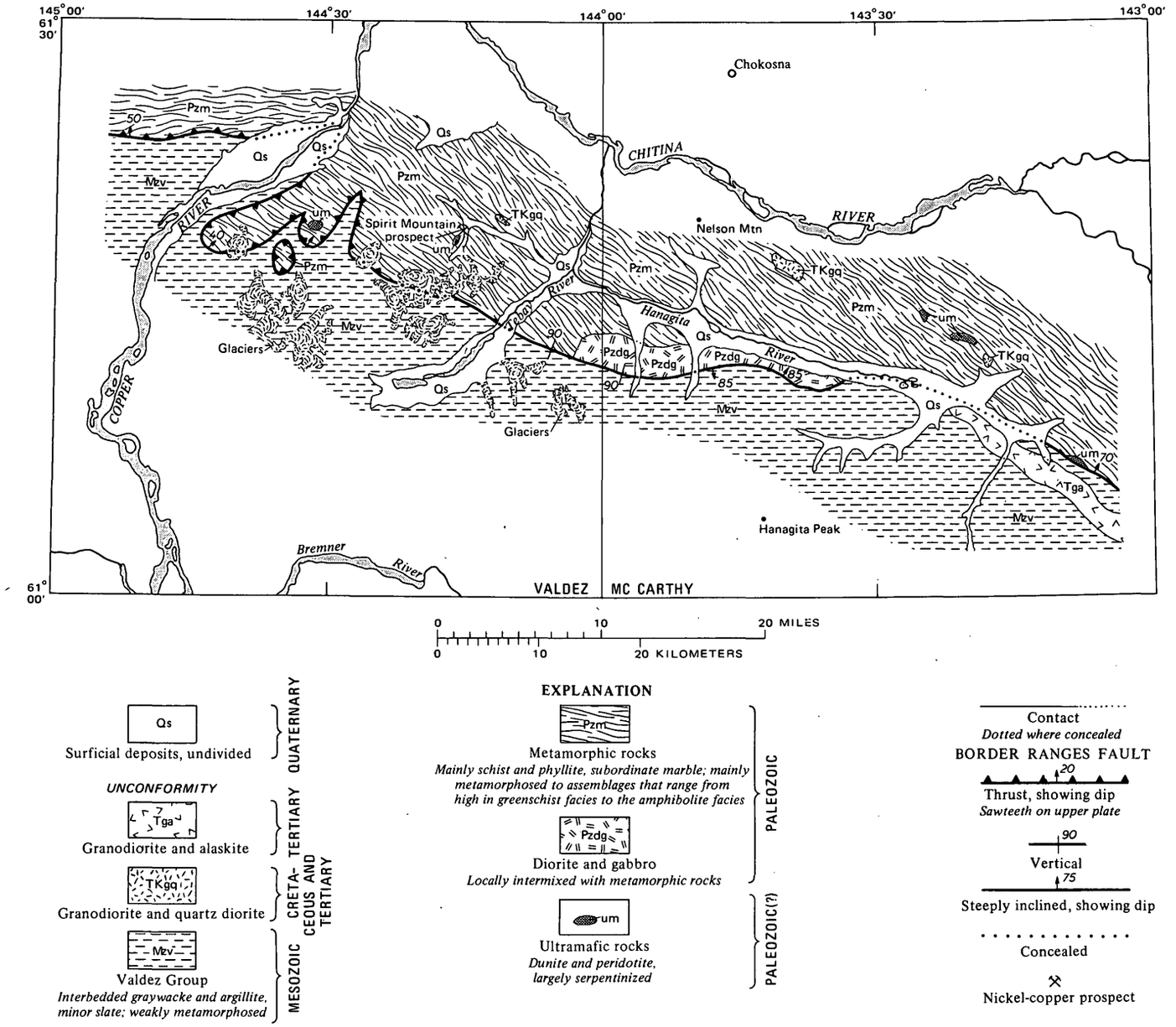

Figure 3.—Geologic setting along and near the Border Ranges fault in the western part of the McCarthy quadrangle and the eastern part of the Valdez quadrangle. Base from U.S. Geological Survey 1:250,000-scale McCarthy and Valdez quadrangle maps, 1960.

along this fault segment are mostly N. 70° W. to west. The westward continuation of the fault across the greater part of the Valdez quadrangle is a thrust that dips between 20° and 60° to the north (fig. 4). The thrust generally maintains the northwest to west strike, but in places where it is subhorizontal, its trace is irregular, and it strikes northeastward. The disparity in style of faulting, indicated by the transition from steep- to gentle-dipping attitudes, may reflect exposures of a folded thrust at different structural levels. Likewise, attitudes of the rocks that border the fault may have locally influenced the style of faulting. This is suggested by the fact that the fault generally is a low- or moderate-angle thrust where the bedding of its wallrock dips gently, and, conversely, it is a high-angle reverse fault where bounded by steeply dipping rocks. Locally, notably along the Copper River, the trace of the thrust fault across steep-walled valleys is marked by large irregular reentrants. The fault contacts range from sharp and nearly knife edged (fig. 5*A*) to shear zones as much as 20 m wide that contain abundant breccia and gouge. The sharp contacts appear to be best developed where attitudes of the adjacent rocks are similar to those of the fault, and, conversely, the broad contacts are best developed where the bordering rocks

Figure 4.—Upper Paleozoic metamorphic rocks (Pzm) thrust over Valdez Group (Mzv) in eastern part of Valdez quadrangle. View is to the east.

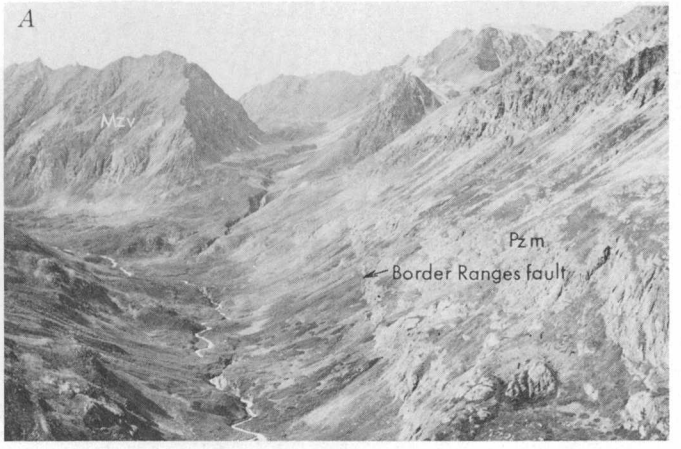

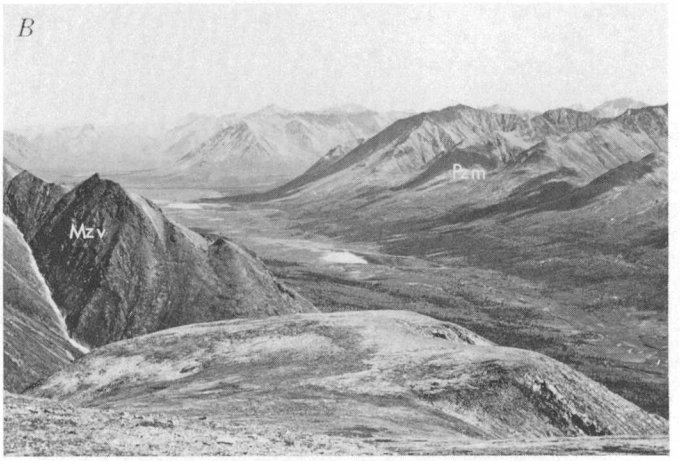

Figure 5.—*A*, Steep, sharp contact that marks the Border Ranges fault near the eastern edge of the Valdez quadrangle; view is to the west; Pzm, upper Paleozoic metamorphic rocks; Mzv, flysch of the Valdez Group. *B*, Northwestward view of the Hanagita Valley; Pzm, mainly metamorphosed upper Paleozoic rocks; Mzv, Valdez Group; the trace of the Border Ranges fault is south of the valley, behind the hills in the foreground.

trend obliquely to the fault. However, more detailed work is required to substantiate these impressions. Except for the local development of saddles and knolls, the fault has scant topographic expression. With the possible exception of the extreme eastern part of Hanagita Valley (fig. 5*B*), none of the conspicuous northwest-trending linear topographic troughs of the region are controlled by the fault. Subsidiary faults that are probably related to the Border Ranges fault occur in the older rocks north of it. These faults are of small extent and include thrusts that in places are imbricate and steep faults that strike obliquely to the Border Ranges fault. Faults of the Spirit Mountain thrust zone (Herreid, 1970, p. 6) exemplify the thrusts in the upper plate. A few short, steep faults cut the Valdez Group near the Border Ranges fault. Above gently dipping segments of the Border Ranges fault, rocks of the upper plate have formed local nappes with recumbent folds and a few klippen (fig. 6). Although only one klippe is shown on our maps (figs. 2 and 3), we recognized a few other small klippen, and more detailed investigations will probably reveal others.

Rocks of the upper plate

The upper plate, which underlies the region north of the fault, is characterized by a thick upper Paleozoic sequence of metamorphosed marine sedimentary and volcanic rocks that is associated with subordinate gabbro and diorite, and less abundant ultramafic rocks (figs. 2 and 3). A few small plutons of Cretaceous quartz diorite and shallow-seated Tertiary rocks cut the metamorphic sequence. The upper Paleozoic assemblage constitutes the regional basement for most of eastern south-central Alaska between the Border Ranges and Denali faults. This basement probably extends westward throughout south-central Alaska to beyond the longitude of Anchorage, but evidence for its westward extent is spotty.

The metamorphic rocks consist mainly of compositionally diverse schist and phyllite and sporadically distributed marble. These rocks indicate metamorphic grades high in the greenschist facies, the greenschist-amphibolite transition facies, or the amphibolite facies. They are strongly foliated and, in places, intricately folded and sheared. Moffit (1938, p. 22–29) assigned the metamorphic rocks along the north flank of the Chugach Mountains to the Strelna Formation, which he considered to be Mississippian in age. Recent investigations by MacKevett and coworkers indicate that fossil assemblages that provided the main basis for the Mississippian age assignment are Permian and that the Strelna Formation is a metamorphosed equivalent of the Permian(?) and Permian Skolai Group of Smith and MacKevett (1970). Where it is weakly metamorphosed in the Wrangell Mountains (fig. 2), the Skolai Group consists of at least 3,000 m of submarine lavas and

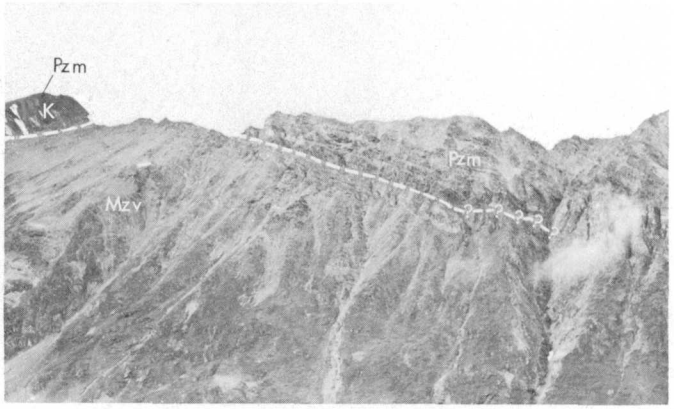

Figure 6.—Klippe (K) along gently dipping part of Border Ranges fault. View is to the west near Spirit Mountain in the eastern Valdez quadrangle. Pzm, upper Paleozoic metamorphic rocks; Mzv, Valdez Group.

volcaniclastic rocks and a superjacent, approximately 500-m-thick section of Early Permian marine sedimentary rocks. Some of the lavas have pillow structures. Correlatives of the Skolai Group are widespread in south-central Alaska south of the Denali fault and include the Mankomen Formation and abundant sedimentary and volcanic rocks in the northeastern part of the McCarthy quadrangle (White River drainage). Recent work at the type locality of the Mankomen (Richter and Dutro, 1974) indicates that the lower, predominantly volcanic part of the sequence contains intercalated sedimentary rocks that yield Pennsylvanian fossils and that the sedimentary upper part is characterized by Early Permian fossils.

Gabbro and diorite form discrete masses and local intermixed complexes throughout the metamorphic terrane. One of the complexes that is intermixed with inliers of metamorphic rocks is contiguous to the Border Ranges fault for about 20 km in the extreme western part of the McCarthy quadrangle (fig. 3). The gabbro and diorite are generally foliated and altered. They are interpreted to be an integral, mainly older part of the upper Paleozoic terrane, although some gabbro elsewhere in the McCarthy and Nabesna quadrangles represents feeders for the Nikolai Greenstone of middle and (or) Late Triassic age.

Ultramafic rocks crop out in several small masses north of the fault between the eastern limit of our mapping and about 3 km east of the Richardson Highway (figs. 2 and 3). Other small ultramafic bodies probably occur in scantily explored areas north of the fault. Only one of the known ultramafic bodies is in contact with the Border Ranges fault; the others are sporadically distributed within ¾ to 10 km of the fault. Most of the ultramafic masses appear to have been tectonically emplaced along faults within the upper plate, although parts of some bodies suggest dikelike intrusion. The ultramafic rocks consist of partly serpentinized dunite and peridotite with lesser amounts of pyroxenite. Layering and cumulate textures are crudely developed in some of the ultramafic rocks. The westernmost ultramafic mass shown in figure 2 has been investigated by Hoffman (1972), who reports that it consists largely of dunite with small amounts of peridotite and pyroxenite. Hoffman noted that the ultramafic body is largely fault bounded and that the dunite contains locally abundant chromite. Herreid (1970, p. 13) reports that the small ultramafic body at the Spirit Mountain prospect (fig. 3) is a peridotite dike that locally contains massive and disseminated copper and nickel sulfides. Several of our ultramafic rock samples contain disseminated pyrrhotite and chalcopyrite, and a few contain chromite.

The ultramafic rocks are lithologically similar to layered ultramafic masses north of and proximal to the Border Ranges fault northeast of Anchorage. These masses, which include a layered ultramafic complex near the headwaters of Wolverine Creek (Clark, 1972b) and a complex near Eklutna (Rose, 1966), consist largely of peridotite and dunite and are mainly bounded by faults. Clark (1972b, p. 3) suggests that the layered gabbro in the complex of Wolverine Creek is localized in the upper part of the complex and that the complex is overturned and stratigraphically overlain by greenstone.

Layered ultramafic rocks on the Kenai Peninsula consist mainly of dunite and pyroxenite (Guild, 1942) and, accordingly, are lithologically similar to other ultramafic bodies near the Border Ranges fault. However, the spatial relations between these ultramafic rocks and the fault are not known.

Although no age data are available for the ultramafic rocks, we tentatively favor interpreting them as remnants of an ophiolite sequence at the base of the upper Paleozoic terrane.

Rocks of the lower plate

The lower plate lies south of the fault and is dominated by a thick flysch, the Valdez Group, but it also contains subordinate intrusive rocks that form small stocks, dikes, and sills (figs. 2 and 3), and some quartz veins. Stratigraphic contacts of the Valdez have not been observed, but it probably is at least a few thousand meters thick. The Valdez consists of interbedded graywacke and argillite with minor amounts of slate. Typically, the beds vary in thickness from a few centimeters to about 15 m. The Valdez is highly deformed and weakly metamorphosed. It is marked by steep foliation that strikes northwestward and by folds that include tight isoclinal types and broad open varieties. Structural and textural features indicative of flysch deposits are locally well developed. Most of the Valdez is probably metamorphosed to grades low in the greenschist facies, but our limited petrographic data preclude further refinement of metamorphic details. The graywacke is typically light or medium gray and composed of fine- to coarse-grained aggregates of poorly sorted subangular clasts. The clasts are bounded by an extremely fine grained turbid phyllosilicate matrix. They consist chiefly of plagioclase, quartz, mafic minerals, and lithic fragments, including chips of Valdez argillite and slate. The argillite and slate are very fine grained rocks that typically are

dark gray and have incipient to well-developed cleavage.

No fossils were found in the Valdez Group within our study area. The late Mesozoic age of the group is inferred from faunal evidence in lateral equivalents that indicates a Cretaceous, mainly Late Cretaceous (Maestrichtian), age (Jones and Clark, 1973, p. 129).

Intrusive rocks in the Valdez terrane (fig. 3) include granodiorite that generally forms small stocks and alaskite that mainly forms dikes and sills. Although conclusive chronologic data are lacking, these rocks are probably Tertiary in age.

TECTONIC IMPLICATIONS

The Border Ranges fault is interpreted to mark a plate boundary that developed near the close of the Mesozoic or in the early Tertiary. During this time, the deep-water deposits of the Valdez Group buckled against, and probably locally were subducted beneath, terrane underlain by an upper Paleozoic island arc that previously had accreted to the continent. The island-arc terrane is believed to have formed directly on oceanic crust (Richter and Jones, 1971; Jones and others, 1971). Its superjacent rocks consist of subaerial volcanic rocks and widespread fossiliferous, largely clastic, Mesozoic rocks that were deposited on the continental shelf or in shallow epicontinental marine embayments. Some of these rocks are coeval with the Valdez Group. The Valdez Group reflects rapid turbidite-type sedimentation, probably largely on oceanic crust in a deep marginal trench.

Activity on the Border Ranges fault apparently waned after the early Tertiary, subsequent to uplift and emergence of the Valdez Group and its accretion to the continental margin. However, at least local post-early Tertiary activity on the fault is indicated by Arthur Grantz's (oral commun., 1972) observation that the fault cuts Tertiary rocks near the Matanuska Glacier.

Active seismicity and deformation along the Gulf of Alaska margin (Plafker, 1969) in combination with Cenozoic igneous activity, indicated by widespread Tertiary plutons (both north and south of the fault) and by the Tertiary and Quaternary lavas of the Wrangell Mountains and Alaska Peninsula (north of the fault), reflect a late Cenozoic tectonic regime in which oceanic crust continues to be relatively underthrust beneath the continental margin in the eastern part of the Aleutian arc.

REFERENCES CITED

Brabb, E. E., and Miller, D. J., 1962, Reconnaissance traverse across the eastern Chugach Mountains, Alaska: U.S. Geol. Survey Misc. Geol. Inv. Map I-341.

Capps, S. R., 1937, Kodiak and adjacent islands, Alaska: U.S. Geol. Survey Bull. 880-C, p. 111–184.

Clark, S. H. B., 1972a, Reconnaissance bedrock geologic map of the Chugach Mountains near Anchorage, Alaska: U.S. Geol. Survey Misc. Field Studies Map MF-350.

——1972b, The Wolverine complex, a newly discovered layered ultramafic body in the western Chugach Mountains, Alaska: U.S. Geol. Survey open-file rept. 522, 10 p.

Forbes, R. B., and Lanphere, M. A., 1373, Tectonic significance of mineral ages of blueschists near Seldovia, Alaska: Jour. Geophys. Research, v. 78, no. 8, p. 1383–1386.

Foster, H. L., and Karlstrom, T. N. V., 1967, Ground breakage and associated effects in the Cook Inlet area, Alaska, resulting from the March 27, 1964, earthquake: U.S. Geol. Survey Prof. Paper 543-F, 28 p.

Guild, P. W., 1942, Chromite deposits of Kenai Peninsula, Alaska: U.S. Geol. Survey Bull. 931-G, p. 139–173.

Hanson, B. M., 1957, Middle Permian limestone on Pacific side of Alaska Peninsula: Am. Assoc. Petroleum Geologists Bull., v. 41, p. 2376–2378.

Herreid, Gordon, 1970, Geology of the Spirit Mountain nickel-copper prospect and surrounding area: State of Alaska geologic rept. 40, 19 p.

Hoffman, Barry, 1972, Geology of the Bernard Mountain area, Alaska: Alaska Univ., M.S. thesis.

Jones, D. L., and Clark, S. H. B., 1973, Upper Cretaceous (Maestrichtian) fossils from the Kenai-Chugach Mountains, Kodiak and Shumagin Islands, southern Alaska: U.S. Geol. Survey Jour. Research, v. 1, no. 2, p. 125–136.

Jones, D. L., MacKevett, E. M., Jr., and Plafker, George, 1971, Speculations on Late Mesozoic tectonic history of part of southern Alaska [abs.]: Internat. Symposium Arctic Geology, 2d, San Francisco, Calif., 1971, p. 30.

Martin, G. C., Johnson, B. L., and Grant, U. S., 1915, Geology and mineral resources of Kenai Peninsula, Alaska: U.S. Geol. Survey Bull 587, 243 p.

Moffit, F. H., 1914, Geology of the Hanagita-Bremner region, Alaska: U.S. Geol. Survey Bull. 576, 56 p.

——1938, Geology of the Chitina Valley and adjacent area, Alaska: U.S. Geol. Survey Bull. 894, 137 p.

Moore, G. W., 1967, Preliminary geologic map of Kodiak Island and vicinity, Alaska: U.S. Geol. Survey open-file rept. 271.

Plafker, George, 1969, Tectonics of the March 27, 1964, Alaska earthquake: U.S. Geol. Survey Prof. Paper 543-I, p. I1–I74.

Richter, D. H., and Dutro, J. T., Jr., 1974, Revision of the type Mankomen Formation and the Permian-Pennsylvanian boundary, Eagle Creek area, eastern Alaska Range: U.S. Geol. Survey Bull. 1395-B. (In press.)

Richter, D. H., and Jones, D. L., 1971, Structure and stratigraphy of eastern Alaska range, Alaska [abs.] *in* Internat. Symposium Arctic Geology, 2d, San Francisco, Calif., 1971, p. 45.

Rose, A. W., 1966, Geology of chromite-bearing ultramafic rocks near Eklutna, Anchorage quadrangle, Alaska: Alaska Div. Mines and Minerals Geologic Rept. 18, 20 p.

Smith, J. G., and MacKevett, E. M., Jr., 1970, The Skolai Group in the McCarthy B-4, C-4, and C-5 quadrangles, Wrangell Mountains, Alaska: U.S. Geol. Survey Bull. 1274-Q, p. Q1-Q26.

Jour. Research U.S. Geol. Survey
Vol. 2, No. 3, May-June 1974, p. 331—337

PALEOZOIC TECTONICS IN THE EDNA MOUNTAIN QUADRANGLE, NEVADA

By R. L. ERICKSON and S. P. MARSH, Denver, Colo.

Abstract.—Geologic mapping at scale 1:24,000 of the Edna Mountain 15-minute quadrangle, Humboldt County, Nev., revealed two episodes of pre-Mesozoic deformation that are difficult to reconcile with either the Antler or the Sonoma orogeny. We believe that the older episode predated the Antler orogeny and may be as old as Late Cambrian. The younger episode may have been more localized, predated the Sonoma orogeny, and was probably Late Pennsylvanian to Permian in age. Deformation related to Antler and Sonoma orogenies also occurred. These four episodes suggest that cycles of uplift, folding, faulting, and erosion began early in the development of the southern Cordillera and continued intermittently throughout Paleozoic time. West of the continental shelf was a broad subsiding basin marked by narrow troughs and elongate structural highs which emerged, matured, and diminished at different times. Waxing and waning deformation in various parts of the geosyncline acting upon local "highs" and troughs can explain the seemingly erratic distribution in north-central Nevada of different facies of time-correlative stratigraphic units and structural blocks of Paleozoic age. Telescoping of facies by thrust faulting certainly took place, but large displacements within brief periods are not essential to the validity of the explanation.

This paper records some clearly exposed structural relations in Paleozoic rocks in the Edna Mountain quadrangle, Humboldt County, Nev. (fig. 1), that cannot be reconciled with regional concepts of early Cordilleran structural and stratigraphic history which are firmly entrenched in the geologic literature of north-central Nevada. These regional concepts have been developed through years of fieldwork by many geologists (Roberts and others, 1958; Roberts, 1964, 1968, 1972; Silberling and Roberts, 1962) and are well known and generally accepted by students of Basin-Range geology. The following synthesis of the early development of the Cordilleran foldbelt in Nevada is paraphrased from the references listed above. Mesozoic and Tertiary history is not pertinent to this discussion.

The Cordilleran geosyncline was an unsymmetrical zone of subsidence that extended from the craton to the open ocean and in which sediments accumulated almost uninterruptedly, except for local disturbances, from Late Cambrian until Late Devonian time. Three lithologic facies are recognized from east to west: (1) Chiefly carbonate assemblage (miogeosynclinal), (2) transitional facies, and (3) detrital volcanic assemblage

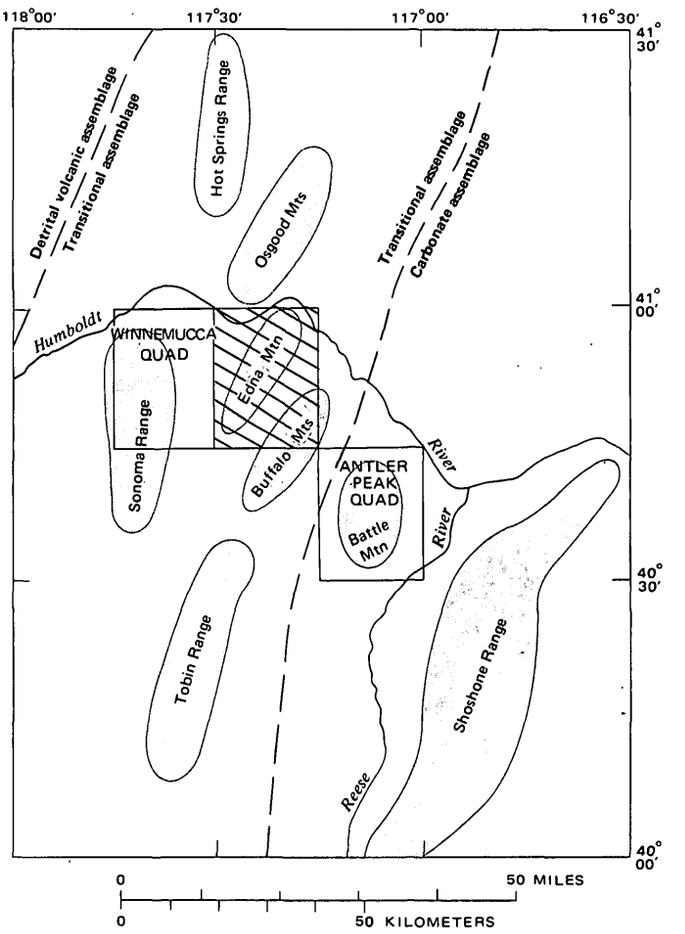

Figure 1.—Map showing geographic distribution of mountain ranges and inferred Paleozoic facies boundaries (based on Roberts, 1964) discussed herein. Edna Mountain quadrangle shown by line pattern.

(eugeosynclinal). This persistent deposition pattern was terminated during Late Devonian or Early Mississippian time by the Antler orogeny, a period of intense folding and faulting during which the two extreme facies were brought into contact by telescoping along a thrust fault of great magnitude, the Roberts Mountains, which carried the detrital volcanic

assemblage eastward over the carbonate assemblage. During the remainder of Paleozoic time, clastic sediments were shed both east and west from emergent areas in the orogenic belt in relatively shallow marine straits and embayments. These sediments have been called the overlap assemblage. West of the orogenic belt, eugeosynclinal sedimentation (Pumpernickel and Havallah Formations) persisted well into the Permian until terminated by the Sonoma orogeny. Again, widely divergent facies were telescoped by a thrust fault of great magnitude, the Golconda thrust, which carried the Pumpernickel and Havallah Formations (detrital volcanic assemblage) eastward over the overlap assemblage and the older Roberts Mountains thrust plate. Recently Roberts (1972) modified this (his) synthesis of the regional geology of Paleozoic rocks in north-central Nevada. He now traces the development of the Cordilleran foldbelt in three principal phases that took place over a span of more than 500 m.y. The first phase, orthogeosynclinal, was a single stage of sedimentation lasting from late Precambrian to middle Paleozoic. The second phase, orogenic-late geosynclinal, included the Antler and Sonoma orogenies as well as deposition in secondary basins and troughs and lasted from middle Paleozoic to early Mesozoic time. Phase three, post-geosynclinal, was characterized by distinctive depositional environments controlled by the interaction of oceanic plates. Thus Roberts reaffirmed the geotectonic cycle to explain the early evolution of the Cordilleran foldbelt—"The fundamental cause of orogeny along a continental margin is sedimentation" (Roberts, 1968, p. 114). In his view, plate tectonics did not influence evolution of the foldbelt until Mesozoic and Tertiary time (his phase III).

In contrast, Burchfiel and Davis (1972) related the entire evolution of the Cordilleran foldbelt to the new global tectonics. They divided the evolution of the foldbelt into three periods—late Precambrian through late Paleozoic, early Mesozoic through early Tertiary, and middle Tertiary to Holocene. Obviously the drastically shortening timespan of each succeeding "period" reflects our degree of knowledge of the geologic history of each period. The older the episode, the less is known about it. Burchfiel and Davis (1972, p. 115) stated that

> all major east-directed thrusts in the southern Cordillera can be interpreted as compressional features related to eastward underthrusting of oceanic crust beneath the North American plate. Eastward thrusting of oceanic rocks atop miogeosynclinal strata during the Mid-Paleozoic Antler and Early Mesozoic Sonoma orogenies can be attributed to stages in the compressive closing of a small inner-arc ocean basin off the continental margin. These orogenic events are thought to be related to episodic(?) eastward subduction of oceanic crust beneath a Paleozoic Klamath-Sierran island arc.

It is to phases I and II of Roberts (1972) and period I of Burchfiel and Davis (1972) that we address this paper. At times the results of detailed geologic mapping (quadrangle scale) do not fit neatly into regional concepts of geologic history. When this happens, we usually conclude that the detailed mapping is

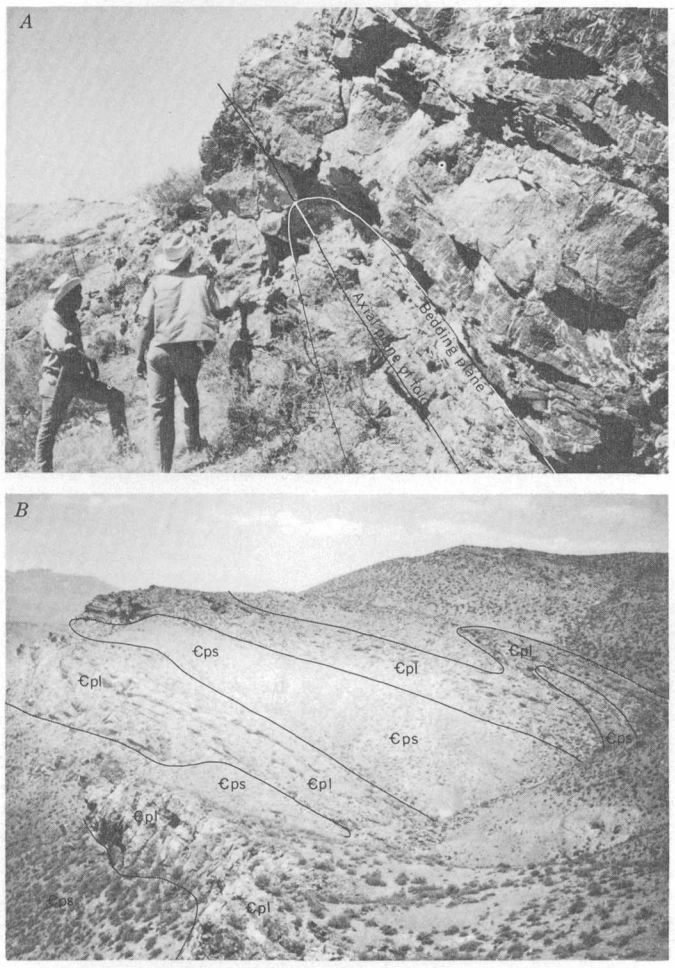

Figure 2.—Overturned folds in the Preble Formation of Cambrian age, NW¼ sec. 31, T. 36N., R. 41 E., Edna Mountain quadrangle. *A*, Nose of asymmetric overturn in limestone strata. Both limbs dip east. View north. *B*, Nearly recumbent folds in limestone (Cpl) strata. Slopes between limestone ledges are intensely sheared phyllitic shale (Cps). Beds are overturned to the west. View north.

suspect and needs reinterpretation, or that the detailed mapping simply demonstrates a local aberration which is not significant in our understanding of the regional setting. The geology of the Edna Mountain quadrangle is one of these aberrations—perhaps not so local and perhaps critical in regional studies. Our detailed geologic mapping (scale 1:24,000) of the four 7½-minute quadrangles that make up the Edna Mountain 15-minute quadrangle in Humboldt County, Nev., has revealed two periods of pre-Mesozoic deformation in Paleozoic rocks that cannot be reconciled with either the Antler or Sonoma orogeny. We believe that the older of these two episodes predated the Antler orogeny and may have been as old as Late Cambrian or Early Ordovician. The second episode of deformation may have been more localized, predated the Sonoma orogeny, and was probably

Late Pennsylvanian to Permian in age. Deformation related to the Antler and Sonoma orogenies is also present.

PRE-ANTLER DEFORMATION

In the Edna Mountain quadrangle the Preble Formation and underlying Osgood Mountain Quartzite, of Cambrian and Cambrian(?) age respectively, are regionally metamorphosed and folded into south-plunging asymmetric folds overturned to the west (fig. 2). Commonly, limestone beds have slid over phyllite units in the overturned parts of the folds. The exposed part of the foldbelt is about 60 km long and as much as 10 km wide; it extends north-northeastward along the east flank of the Sonoma Range, across the north end of Edna Mountain, and forms the core of the Osgood Mountains farther north. The mechanism of this westward-directed deformation is uncertain, but deformation clearly predated deposition of the Battle Formation of Early Pennsylvanian age which overlies unconformably the deformed Preble and Osgood Mountain. The westward-overturned folds in the Osgood Mountain and Preble may be drag folds on the east limb of a north-trending anticlinorium. Although the west limb is not exposed in the Edna Mountain quadrangle, Hotz and Willden (1964) mapped a west limb for a short distance on the west flank of the Osgood Mountains. Hotz and Willden inferred the anticlinal structure elsewhere from bedding attitudes in the Osgood Mountain Quartzite. They also reported (1964, p. 69) that development of the major anticline took place prior to deposition of the Lower Pennsylvanian beds. There can be no doubt that a strong structural and topographic high existed in this part of Nevada during middle Paleozoic (post-Preble, pre-Battle) time.

Although development of this structure has not been specifically assigned to the Antler orogeny, one can infer from Roberts (1968, p. 106) that he would assign it to the earliest stage of the Antler orogeny characterized by upwarping of the thick accumulation of sediments along the boundary between continental slope and the eugeosynclinal environment. As uplift proceeded, gravity or glide plates broke away from the crest of the upwarp and moved eastward (Roberts Mountains thrust). This interpretation of the origin of the structure in Cambrian rocks does not satisfy the stratigraphic and structural observations made in the field in the Edna Mountain area, for the following reasons:

1. The westward-overriding foldbelt in Osgood Mountain Quartzite and Preble Formation cannot have resulted from simple upwarping of the sedimentary section. There must have been a strong westward-directed compressive force regardless of whether the structure was a westward-moving plate or the east limb of a major drag-folded anticline. These compressive forces are not compatible with either early simple upwarp or later eastward-directed Antler orogenic events.
2. An isolated fault-bounded block of tightly folded siliceous clastic rocks of Middle Ordovician age at the northeast end of Edna Mountain is interpreted by us as a remnant of eastward-directed thrust plates related to the Antler orogeny. This Ordovician block was mapped earlier as the Comus Formation (Ferguson and others, 1952), assigned to the transitional facies, and believed to be autochthonous or parautochthonous. Our detailed geologic mapping disclosed two distinctly different lithologic and structural units in the block of Ordovician rocks. One unit, to which we tentatively refer as the Vinini Formation, is composed of isoclinally and recumbently folded beds of chert, siliceous shale, and quartzite. Overriding of beds was from west to east (Antler orientation). The second lithologic unit in the Ordovician block, the Comus Formation, is about 2,000 ft thick and is composed of finely laminated dolomitic siltstone and silty dolomite in the upper part, giving way to interbedded chert and dolomite and graptolite-bearing tuffaceous siltstone in the lower part. The beds dip westward, from moderately to steeply to slightly overturned but are not tightly folded; however, autobreccias and quartz-rich shear zones parallel or subparallel to bedding are common, particularly in the lower part, and probably have tectonic significance. The contrast between the Vinini(?) and Comus in lithology and structural style suggests that the Vinini(?) Formation belongs to the eugeosynclinal facies and has moved into the area as a thrust sheet from the west. The lithology and structural style of the Comus Formation suggest that it belongs to the transitional facies and has not moved far from its site of deposition. We interpret the Comus exposure to be a window in the thrust sheet that carried the Vinini(?) into this area. Deformation and sliding within the Comus and the eastward-directed overriding thrust sheet of Vinini(?) are here assigned to the Antler orogeny. Strict definition of the Roberts Mountains thrust requires that the lower plate be the miogeosynclinal carbonate facies. Nevertheless, although the Edna Mountain area is in the transitional part of the geosyncline near the change to eugeosynclinal deposition, we are reluctant to introduce a new name for the Ordovician plate.

These relations (1 and 2, above) are the crux of the problem of Paleozoic tectonism in the region. If the Comus has not been moved far and has not been tightly folded, what is its relation to the Cambrian(?) Osgood Mountain and Cambrian Preble Formations? Hotz and Willden (1964) reported that all contacts of the Comus Formation with other Paleozoic formations in the Osgood Mountains are fault contacts. The isolated Comus exposure on the east flank of Edna Mountain is also a fault-bounded block. We believe that the strong contrast between the tightly folded, metamorphosed, westward-overriding rocks of the Osgood Mountain

Quartzite and Preble Formation and the uniformly west-dipping unmetamorphosed rocks of the Comus Formation demands deformation and metamorphism of the Cambrian rocks prior to and unrelated to deformation of the Comus and Vinini. We thus interpret the Ordovician block to be a remnant of eastward-directed thrust plates related to the Antler orogeny. The Vinini(?) was thrust over the Comus, and the Comus itself has moved, but probably not far. Therefore the folding, metamorphism, and uplift of the Cambrian rocks must have been earlier than the Antler orogeny.

3. The Osgood Mountain Quartzite and Preble Formation were assigned to the transitional facies (Roberts and others, 1958, p. 282b); however, they stated that the Preble Formation shows closer affinities with the eastern assemblage than with the western. The time-correlative Scott Canyon Formation (Lower or Middle Cambrian), exposed in the Antler Peak quadrangle at Battle Mountain southeast of Edna Mountain, clearly belongs in the eugeosynclinal assemblage; therefore, its original site of deposition, in Roberts' model, must have been west of our Cambrian structural high. The Scott Canyon rocks must then have moved up and over the ancestral Antler upwarp—rather than being a detached gravity or glide block that slid off the upwarp.
4. If we assume that the Osgood Mountain and Preble are autochthonous or parautochthonous and that deposition in the geosyncline was continuous through Devonian time, where is the record of overlying and younger rock units of Late Ordovician through Devonian age? Gilluly (1967, p. 4) remarked on the

   very puzzling problems of paleogeography [in the nearby Winnemucca quadrangle] which cannot be solved until much more large-scale mapping has been done in adjacent areas. The inadequacy of our information is underlined by the fact that none of the eugeosynclinal formations of Silurian and Devonian age which are so widespread in the upper plate of the Roberts thrust to the east * * * has yet been identified anywhere to the west of the Reese River Valley, whence they must surely have been derived during the Antler orogeny.

   There is no record of Silurian and Devonian transitional or eugeosynclinal rocks in the Edna Mountain area, the Osgood Mountains to the north, or the Sonoma Range to the west. The oldest rocks in depositional contact with the Osgood Mountain and Preble are everywhere in these ranges Early to Middle Pennsylvanian in age.
5. The Upper Cambrian Harmony Formation is not present in the Edna Mountain area but is widespread to the east in the Antler Peak area and to the west and northwest in the Sonoma Range and Hot Springs Range. However, in none of these areas has the Harmony been found in depositional contact on the Osgood Mountain or Preble. Nevertheless, Roberts, Hotz, Gilluly, and Ferguson (1958, p. 2828) stated that folds in the Harmony Formation in the Hot Springs Range are generally accordant with folds in the Osgood Mountain Quartzite and Preble Formation in the Osgood Mountains. Hotz and Willden (1964, p. 76) wrote of the intricate folds in the Harmony in the Hot Springs Range and stated that although the true pattern of folds is not known, in general the structure "is a series of north-plunging asymmetrical anticlines and synclines whose axial planes dip moderately east; some of the folds are isoclinal." This fold orientation (overturning to the west) therefore is the same as we find in the Osgood Mountain and Preble in the Edna Mountain area. Also Hotz and Willden's cross sections show that the Hot Springs Range cannot be the west limb of an anticline that forms the Osgood Mountains, as inferred by Roberts, Hotz, Gilluly, and Ferguson (1958, p. 2828). It may be, however, the east limb of another major drag-folded anticline.

The preponderance of feldspathic sandstone in the Harmony Formation sets it apart from other lower Paleozoic formations. Roberts, Hotz, Gilluly, and Ferguson (1958, p. 2828) stated that the feldspathic rocks "have clearly been derived from a granitic source near the basin of deposition. Determination of the age of detrital zircon from the Harmony gave 680 million years, and it is therefore probable that the source rock was upper Precambrian, though no Precambrian rocks have yet been recognized in north-central Nevada." Of course, the lithology of the Harmony is compelling evidence that uplift did take place somewhere in this part of the Cordilleran geosyncline at least as early as Late Cambrian. We suggest that folding of the Osgood Mountain Quartzite and Preble Formation in the Osgood Mountains, Edna Mountain area, and east flank of the Sonoma Range preceded or accompanied Late Cambrian uplift. As uplift proceeded, siliceous and feldspathic sediments were spread both east and west into flanking basins to form the Upper Cambrian Harmony Formation. Hotz and Willden (1964) recorded a basal shale member 75–150 ft thick and suggested that the source area at that time was an area of low relief which shortly was subjected to rapid uplift to produce the overlying coarse clastic units. Gilluly (1967, p. 2) stated that "I know of no evidence that the Harmony in the lower plate of the Sonoma thrust has been moved far from its site of deposition." We suggest that the source of the Harmony was an emergent structural high located somewhere between the Sonoma Range and Battle Mountain. Further, we believe that the foldbelt in Cambrian rocks in the Edna Mountain area is a part of that old structural high.

Carrying this speculation further, we might assume that this old structural and topographic high persisted during much of Paleozoic time. Trenches deepened with time on both sides of the high and accumulated mixed transitional and eugeosynclinal sediments, but Silurian

and Devonian rocks never were deposited on the upwarp itself. During the Antler orogeny the thick accumulations of sediments in the narrow trenches were squeezed like a tube of toothpaste, and "globs" or plates moved east and west away from the central uplift. Gilluly (1967) has mapped all thrusts in the Sonoma Range farther west as having had east-to-west transport; however, he also stated that all the thrusts are "oviously post-Triassic." To our knowledge, however, all known westward-directed thrusting in the region occurred west of our structural high; east of the high, all plates identified with the Antler orogeny were east directed.

6. Let us assume, for sake of argument, the usually accepted model of a geosynclinal basin extending from the continent westward at least to the position of the present Klamath-Sierran arc and receiving miogeosynclinal, transitional, and eugeosynclinal sediments relatively uninterrupted from late Precambrian through Devonian time: then Silurian and Devonian rocks of transitional or eugeosynclinal facies must have been deposited in the Edna Mountain area, Osgood Mountains, and Sonoma Range. If the foldbelt in the Cambrian rocks is related to an early stage of the Antler orogeny (Late Devonian), then Silurian and Devonian rocks were also arched upward. Because these rocks are no longer evident along the upwarp or on the west side of the upwarp, we must assume that they were removed from the upwarp by erosion or as thrust plates, or possibly were buried by later thrust plates on the west. Erosion is an unacceptable explanation because there is no record of detritus from Silurian and Devonian rocks either to the west or to the east. The oldest rocks in conformable contact with the Cambrian rocks are coarse conglomerates of Early Pennsylvanian age (Battle Formation) composed at Edna Mountain and in the Osgood Mountains exclusively of Osgood Mountain Quartzite. Intraformational conglomerate in the Highway Limestone overlying the Battle Formation is composed of fragments of both the Preble Formation and the Osgood Mountain Quartzite. Theoretically, if the Cordilleran geosyncline developed along classical lines, the conglomeratic units should contain fragments of Silurian and Devonian formations.

   If we assume that the Silurian and Devonian rocks were removed from the Edna Mountain area as thrust plates, then the thrusting mechanism was extremely efficient, delicately removing all traces of the plates' former existence over an area of about 2,000 km^2 and without removing any slices of Comus Formation or older Cambrian rocks (Osgood Mountain Quartzite and Preble Formation). Yet to the east in the Battle Mountain area and farther east in the Shoshone Range, the upper plate of the Roberts thrust is described as a complex block of siliceous clastic sedimentary rocks and volcanics ranging in age from Cambrian through Devonian; the Ordovician Valmy and Vinini Formations are probably the thickest and most widespread part of this plate. Such a stratigraphically coherent block could not have been originally deposited in the Edna Mountain area. Correlative eastward-moving sheets from the Edna Mountain area would have had to include the Ordovician Comus Formation and, conceivably, slivers of Cambrian Prebel Formation and Cambrian(?) Osgood Mountain Quartzite. No such structural block is known to exist. If the "western assemblage" (Cambrian through Devonian rocks) now present in the Shoshone Range was originally deposited to the west of the Edna Mountain area, this block, on its eastward journey, must have encountered the structural ridge in the Edna Mountain area, moved up and over the ridge to consume the Silurian and Devonian rocks that originally should have been deposited there, and then continued its eastward migration without leaving evidence of its passing.

   The presence of Ordovician eugeosynclinal Valmy lithology both east (Battle Mountain area and Shoshone Range) and west (Sonoma Range) of the Edna Mountain structural high has been cited often as evidence of eastward plate movement of great magnitude. We suggest that Valmy lithology was deposited in troughs both east and west of the high (similar to the original distribution of the Upper Cambrian Harmony). Subsequent intense folding and thrusting of Valmy rocks during the Antler orogeny shifted Valmy plates, but displacement was of much smaller magnitude than usually postulated. All Valmy lithology need not have originated somewhere west of the Sonoma Range.

The Shwin Formation of Middle Cambrian age in the Shoshone Range is another example. Gilluly (Gilluly and Gates, 1965) mapped and described the Shwin Formation as intensely deformed with isoclinal folds and composed of abundant basic metavolcanics and phyllite in the lower part, giving way to argillite, slate, mudstone, and limestone in the upper part. Gilluly referred the Shwin to the eastern or miogeosynclinal facies but recognized that the abundance of volcanics also suggested reference to the western or eugeosynclinal facies. He further stated (Gilluly and Gates, 1965, p. 14), "If our assignment is correct and the formation is autochthonous or parautochthonous, it is obvious that the transition between carbonate and siliceous facies took place farther east in Middle Cambrian time than in either earlier or later parts of the Paleozoic.* * * there is no evidence whatever to suggest long thrust transport from the site of its deposition." When we contrast the lithology of the Shwin Formation with the lithology of the Osgood Mountain Quartzite and Preble Formation in the Edna Mountain area to the west, it is equally obvious that these latter formations are not a eugeosynclinal facies and actually have a closer affinity to the eastern or carbonate assemblage than does the Shwin

Formation. If Gilluly's original interpretation is correct that the Shwin has not been transported far, then Roberts' model of east-to-west facies changes—from continental margin westward to open ocean, telescoped by thrust faults of great magnitude—cannot be correct. If Roberts' model is correct, then the Shwin is far-traveled and must have been originally deposited west of the Edna Mountain area.

Gilluly (oral commun., 1973) now believes that the Shwin is more closely related to the western eugeosynclinal assemblage and therefore is probably far-traveled from the west. His reasoning derives from the traditional model of the early Paleozoic development of the Cordilleran geosyncline: if the lithology is a detrital volcanic (eugeosynclinal) assemblage, it must be far-traveled from the west, telescoped by thrust faults of great magnitude. If the Shwin did not move far, the transition between carbonate and detrital-volcanic facies took place farther east. Because the Osgood Mountain Quartzite and Preble Formation to the west are certainly not eugeosynclinal strata, the Shwin must therefore be far-traveled and have originally been deposited west of the Edna Mountain area.

This rigid model predetermines the interpretation of field observations because lithology alone dictates where facies changes occurred and whence and how far thrust plates were transported. Such a model also requires absence of any earlier (pre-Antler) orogenic episodes of significance that might have altered the facies distribution pattern from late Precambrian through Devonian time. The fold belt in Lower to Middle Cambrian rocks in the Edna Mountain area and the arkosic composition of the widespread Upper Cambrian Harmony Formation are, in our opinion, compelling evidence for pre-Antler orogenic episodes.

DEFORMATION OF LATE PENNSYLVANIAN OR EARLY PERMIAN AGE

The second pre-Mesozoic period of deformation that cannot be reconciled with either the Sonoma or Antler orogeny involved the Battle Formation, Highway Limestone, and Antler Peak Limestone ranging in age from Early Pennsylvanian to Early Permian. These rock units, together with the Edna Mountain Formation of Late Permian age, are part of the overlap assemblage that was deposited on the folded and faulted strata involved in the Antler orogeny, and are named the Antler sequence (Roberts and others, 1958).

In the Edna Mountain quadrangle the Battle, Highway, and Antler Peak have been asymmetrically folded, in places overturned, and now lie above the Cambrian Preble Formation as a plate (fig. 3).

The displacement of this plate upon what is here called the Iron Point thrust fault probably is of low magnitude—the plate is perhaps parautochthonous. However, recording this period of movement, deformation, and erosion is important because it predated deposition of the Upper Permian Edna Mountain Formation. The Edna Mountain Formation, underlying the

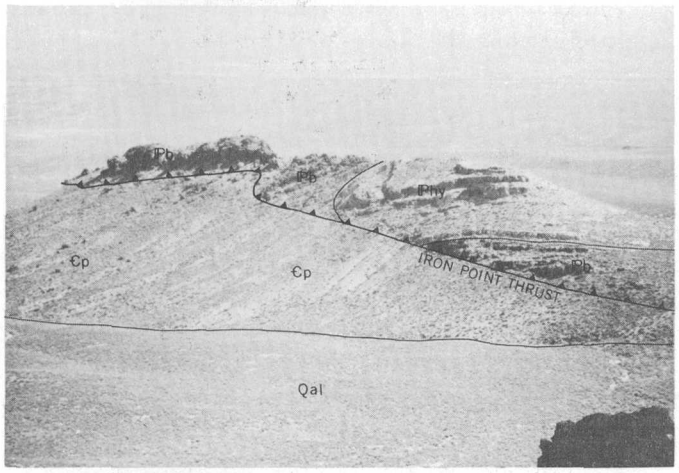

Figure 3.—Folded strata of the Battle Formation (IPb) and Highway Limestone (IPhy) of Early to Middle Pennsylvanian age thrust on the Preble Formation (€p) of Cambrian age. Qal, Quaternary alluvium.

Golconda thrust, has not been folded—only tilted—and occurs in depositional overlap contact on an erosion surface cut across the older folded rocks in the plate; locally the plate was completely eroded, and the Edna Mountain rests with angular unconformity on the Preble Formation of Cambrian age. Thus this Pennsylvanian or Early Permian time of deformation followed by extensive erosion predated both the Golconda thrust and the Edna Mountain Formation. Neither the upper plate of the Iron Point thrust nor the Edna Mountain Formation is present in contact with the Ordovician structural block, but presumably both once extended over the entire area.

The direction of transport of the Iron Point plate is not clear, but the plate could not have been moved far from its original site of deposition. The thickness of the combined Battle, Highway, and Antler Peak is measured only in hundreds of feet in the Edna Mountain area. In the Osgood Mountains farther north, Hotz and Willden (1964) reported more than 2,000 ft of Antler sequence strata. Correlative rocks are not known to the west or south. Hotz and Willden (1964, p. 81) also reported: "Marine deposition was interrupted in this region between Early and Middle Permian time, and the previously deposited sedimentary rocks were moderately deformed, uplifted, and subjected to erosion." Thus, recognition of late Paleozoic deformation and uplift unrelated to the younger Sonoma orogeny is certainly not new with us. What we stress here is that orogenic movements which do not conveniently relate to either the Antler or Sonoma orogeny deserve more attention and must be accounted for in the geologic history of the southern Cordillera. We suspect that similar "local aberrations" have been noted by other geologists elsewhere in north-central Nevada but perhaps have been deemphasized.

We propose that the term "Antler sequence" be dropped or at least modified. "Sequence" implies depositional continuity. The Edna Mountain Formation clearly was deposited on an erosion surface cut on folded strata also assigned to the "Antler sequence."

SUMMARY

In the course of geologic studies in the Edna Mountain quadrangle, we encountered problems in fitting our observations to the regional model of early development of the southern Cordillera. The traditional model calls for relatively uninterrupted sedimentation in the subsiding geosyncline from late Precambrian to Late Devonian time and recognizes no significant orogenic movements prior to the beginning of the Antler orogeny in Late Devonian time. Sedimentation followed the Antler orogeny and was terminated by the Sonoma orogeny. Both orogenies are characterized by thrust faults of great magnitude (Roberts Mountains thrust and Golconda thrust, respectively). It seems clear to us that cycles of uplift, folding, faulting, and erosion in the Edna Mountain area began at least as far back as Late Cambrian time and continued intermittently throughout Paleozoic time. Field evidence at Edna Mountain is compelling for deformation in Late Cambrian to Early Ordovician, Late Devonian to Mississippian (Antler orogeny), Late Pennsylvanian to Early Permian, and Late Permian to Early Triassic (Sonoma orogeny). Episodes of deformation of ages different from these probably occurred in other parts of the geosyncline. Willden and Kistler (1967) reported Ordovician tectonism in the miogeosynclinal carbonate assemblage in the Ruby Mountains in northeastern Nevada. Thus our model, admittedly based on detailed knowledge of a small area rather than general knowledge of a broad area, suggests a continental shelf that gave way westward to a broad subsiding basin whose monotony was interrupted by narrow deep troughs and elongate emergent structural highs. The various ridge-and-flanking trough areas probably emerged, matured, and diminished at different times. We would postulate intermittent but continuing deformation waxing and waning in various parts of the geosyncline throughout its history. This concept can explain the seemingly erratic distribution in north-central Nevada of different facies of time-correlative stratigraphic units and structural blocks of Paleozoic age. Telescoping of facies by thrust faulting certainly took place, but displacement of huge thicknesses of sediments for a distance of 140–160 km as a single plate over a ridge-and-trough terrane and during a restricted time interval is not necessary to explain the distribution of Paleozoic stratigraphic units.

REFERENCES CITED

Burchfiel, B.C., and Davis, G. A., 1972, Structural framework and evolution of the southern part of the Cordilleran orogen, western United States: Am. Jour. Sci., v. 272, no. 2, p. 97–118.

Ferguson, H.G., Roberts, R. J., and Muller, S. W., 1952, Geology of the Golconda quadrangle, Nevada: U.S. Geol. Survey Geol. Quad. Map GQ-15.

Gilluly, James, 1967, Geologic map of the Winnemucca quadrangle, Pershing and Humboldt Counties, Nevada: U.S. Geol. Survey Geol. Quad. Map GQ-656.

Gilluly, James, and Gates, Olcott, 1965, Tectonic and igneous geology of the northern Shoshone Range, Nevada: U.S. Geol. Survey Prof. Paper 465, 153 p.

Hotz, P. E., and Willden, Ronald, 1964, Geology and mineral deposits of the Osgood Mountains quadrangle, Humboldt County, Nevada: U.S. Geol. Survey Prof. Paper 431, 128 p.

Roberts, R. J., 1964, Stratigraphy and structure of the Antler Peak quadrangle, Humboldt and Lander Counties, Nevada: U.S. Geol. Survey Prof. Paper 459-A, 93 p.

——1968, Tectonic framework of the Great Basin: Missouri Univ. Rolla Tech. Ser., no. 1, p. 101–119.

——1972, Evolution of the Cordilleran fold belt: Geol. Soc. America Bull., v. 83, no. 7, p. 1989–2004.

Roberts, R.J., Hotz, P. E., Gilluly, James, and Ferguson, H. G., 1958, Paleozoic rocks of north-central Nevada: Am Assoc. Petroleum Geologists Bull., v. 42, no. 12, p. 2813–2857.

Silberling, N. J., and Roberts, R. J., 1962, Pre-Tertiary stratigraphy and structure of northwestern Nevada: Geol. Soc. America Spec. Paper 72, 58 p.

Willden, Ronald, and Kistler, R. W., 1967, Ordovician tectonism in the Ruby Mountains, Elko County, Nevada *in* Geological Survey research 1967: U.S. Geol. Survey Prof. Paper 575-D, p. D64–D75.

Jour. Research U.S. Geol. Survey
Vol. 2, No. 3, May-June 1974, p. 339—340

COLORADOITE, ACANTHITE, AND JAROSITE FROM THE CRIPPLE CREEK DISTRICT, TELLER COUNTY, COLORADO

By FRED A. HILDEBRAND and GARLAND B. GOTT, Denver Colo.

Abstract.—Coloradoite (HgTe), acanthite (Ag_2S), and jarosite ($KFe_3(SO_4)_2(OH)_6$) have been identified in rocks from the Cripple Creek district, Colorado. Neither acanthite nor jarosite has previously been reported from this mining district. Although the occurrence of coloradoite was reported, its identification was never actually verified. The presence of acanthite may explain a discrepancy between the relative proportions of gold and silver as shown by mill reports and geochemical data.

Since the discovery of gold at Cripple Creek in 1891, the district has produced about 21 million ounces of gold. The ore contained approximately 1 ounce of silver per 10 ounces of gold. A recent geochemical investigation, however, disclosed that in 282 surface samples of volcanic breccia, which is the host rock for the gold deposits, the silver-gold ratio is about 1.5:1 (Gott and others, 1969). Possibly, the discrepancy between the silver-gold ratio in the produced ore and the ratio in the surface breccias is caused by the presence of a silver mineral not spatially associated with the gold. This possibility prompted a study of the mineralogy of several available specimens that had been collected from the Cripple Creek district.

The assemblage of gold and silver tellurides that is well known to exist in the district includes calaverite ($AuTe_2$), krennerite ($AuTe_2$), sylvanite ($AgAuTe_2$), petzite (Ag_3AuTe_2), and hessite (Ag_2Te). Native gold occurs in the oxidized ores.

This limited mineralogical study resulted in the identification of three additional minerals to the Cripple Creek mineral assemblage: coloradoite (HgTe), acanthite (Ag_2S), and jarosite ($KFe_3(SO_4)_2(OH)_6$). Lindgren and Ransome (1906, p. 115) reported the possible presence of coloradoite many years ago, and Eckel (1961, p. 111) referred to newspaper accounts that commented on the presence of this mineral, but its actual occurrence in the district was never substantiated. Now, by means of modern mineralogical methods, the presence of coloradoite has been corroborated. Neither acanthite nor jarosite has previously been reported.

The gold deposits occur as fissure veins in a volcanic subsidence basin filled with brecciated volcanic rocks that are mainly of phonolite and latite-phonolite composition. Gold and silver tellurides and native gold constitute the ore minerals. In ore from the Cresson mine there was some contribution of gold from exsolved gold in the mineral melonite (NiTe) which presumably is pseudomorphous after calaverite. Quartz, the most abundant gangue mineral in the veins, is generally associated with dolomite and finely crystalline purple fluorite. Pyrite occurs in all the veins and is disseminated throughout the country rocks. Sphalerite, galena, chalcopyrite, stibnite, and molybdenite are associated with the ore minerals in some mines, but they are of no economic significance.

COLORADOITE

Coloradoite was identified during this study in a specimen collected about 40 yr ago from the 1,800-ft. level of the Cresson mine by A. H. Koschmann of the U.S. Geological Survey. The specimen consists of ore veins that surround and cut pieces of breccia. The veins minerals are mainly sphalerite, somewhat lesser amounts of galena and quartz, and still lesser amounts of purple fluorite and silvery krennerite.

Coloradoite in the specimen is black and is finely intergrown with grayish-black galena and silvery krennerite with a brass-yellow cast. In X-ray diffraction patterns of mixtures of mainly coloradoite and krennerite, the interplanar spacings of coloradoite are distinct and do not conflict with those of krennerite. The position and intensity of the coloradoite spacings are in excellent agreement with those of coloradoite reported by Berry and Thompson (1962, p. 50). Analysis of the sample shows that mercury and tellurium are major constituents.

ACANTHITE AND JAROSITE

Acanthite, jarosite, and native gold were identified in oxidized outcrop specimens kindly provided by Mr. Charles Carlton of the Golden Cycle Corp. of Colorado Springs. The specimens, Nos. 2112 and 2113, came from the northeast edge of a body of breccia close to its contact with Precambrian granitic rocks in sec. 21, T. 15 S., R. 69 W., Big Bull Mountain quadrangle. Analyses of the two specimens are shown in table 1.

Table 1.—*Results of analyses, in parts per million, of two specimens from Big Bull Mountain area*

[Au and Te determined by atomic absorption methods by A. E. Huber. All other elements determined by semiquantitative spectrographic analyses by J. M. Nishi]

Sample	2112	2113	Sample	2112	2113
Au	70	66	Sb	150	300
Te	22	88	Bi	10	15
Ag	7	150	Cu	5	15
Pb	100	500	Mo	70	50
Zn	200	200	V	200	100
Cd	20	20	Mn	200	300
Ba	500	5,000	As	700	200
Sr	500	300			

Small particles of native gold from specimen 2112 were identified by X-ray and atomic absorption techniques. The association of gold with any specific mineral could not be ascertained, although a very small piece of wire or ribbon gold was seen to be enclosed in a tiny chain of coalesced, opaline silica spheres.

Specimen 2113, an altered, silicified breccia, contains many druses lined with clear, terminated, prismatic quartz crystals. In areas of colorless massive quartz between the druses, small concentrations of soft black acanthite are associated with tiny crystals and clusters of crystals of native gold. The acanthite was identified by X-ray and atomic absorption methods.

Orange-brown, shiny crystals of normal potassium jarosite fill small quartz druses in specimen 2113. Most of the jarosite is associated with white, sugary barite that fills in around, and coats, clusters of jarosite crystals. Jarosite also occurs sparingly as a cubic pseudomorph after pyrite.

CONCLUSIONS

This limited mineralogical study suggests that the discrepancy between the relative proportions of gold and silver as indicated by mill reports and the geochemical data reported by Gott, McCarthy, VanSickle, and McHugh (1969) may result from the presence of acanthite in the district. This conclusion necessitates the further conclusion that the acanthite is more widespread than the gold.

REFERENCES CITED

Berry, L. G., and Thompson, R. M., 1962, X-ray powder data for ore minerals—the Peacock atlas: Geol. Soc. America Mem. 85, 281 p.

Eckel, E. B., 1961, Minerals of Colorado—A 100-year record: U.S. Geol. Survey Bull. 1114, 399 p.

Gott, G. B., McCarthy, J. H., Jr., VanSickle, G. H., and McHugh, J. B., 1969, Distribution of gold and other metals in the Cripple Creek district, Colorado: U.S. Geol. Survey Prof. Paper 625-A, p. A1-A17.

Lindgren, W. L., and Ransome, F. L., 1906, Geology and gold deposits of the Cripple Creek district, Colorado: U.S. Geol. Survey Prof. Paper 54, 516 p.

Jour. Research U.S. Geol. Survey
Vol. 2, No. 3, May-June 1974, p. 341—342

THALLIUM-BEARING ORPIMENT, CARLIN GOLD DEPOSIT, NEVADA

By ARTHUR S. RADTKE; CHARLES M. TAYLOR,[1] F. W. DICKSON;[1]
and CHRIS HEROPOULOS, Menlo Park, Calif.;
Palo Alto, Calif.; Menlo Park, Calif.

Abstract.—A variety of orpiment, As_2S_3, containing a significant amount of thallium has been identified in the unoxidized East ore body of the Carlin gold deposit. The mineral occurs in small veinlets with barite, calcite, quartz, and realgar.

Thallium-bearing orpiment occurs with epithermal minerals in the East ore body of the Carlin disseminated gold deposit (fig. 1), Eureka County, Nev. The gold ores developed by replacement of carbonate minerals, calcite and dolomite, in Silurian limestone of the Roberts Mountains Formation; the general geologic features of the Carlin gold deposit and descriptions of the mineralogy of the host rocks and ores have been presented by Hardie (1966), Hausen and Kerr (1968), Radtke and Scheiner (1970), and Radtke, Taylor, and Christ (1972).

The presence of thallium in the Carlin gold ores was first reported by Radtke, Heropoulos, Fabbi, Scheiner, and Essington (1972) in a paper summarizing data on major and minor elements in both unoxidized and oxidized gold ores at this deposit. The thallium-bearing orpiment was recognized by electron microprobe analyses done on grain mounts prepared from a hand sample that contained 150–200 p/m thallium. Optical and X-ray diffraction studies of these grains confirmed the fact that no phases were intergrown with the orpiment. Orpiment that contains thallium has not been previously reported, according to our search of the literature. Two other varieties of orpiment have been identified—one contains antimony (Radtke, Taylor, and Heropoulos, 1973) and the other is nearly pure As_2S_3.

Acknowledgments.—The writers thank T. G. Theodore and H. R. Cornwall of the U.S. Geological Survey and Prof. K. B. Krauskopf of Stanford University for their critical reviews of the manuscript. Perfecto Mary of Stanford University kindly prepared a photograph of the mineral specimen.

[1]Department of Geology, Stanford University.

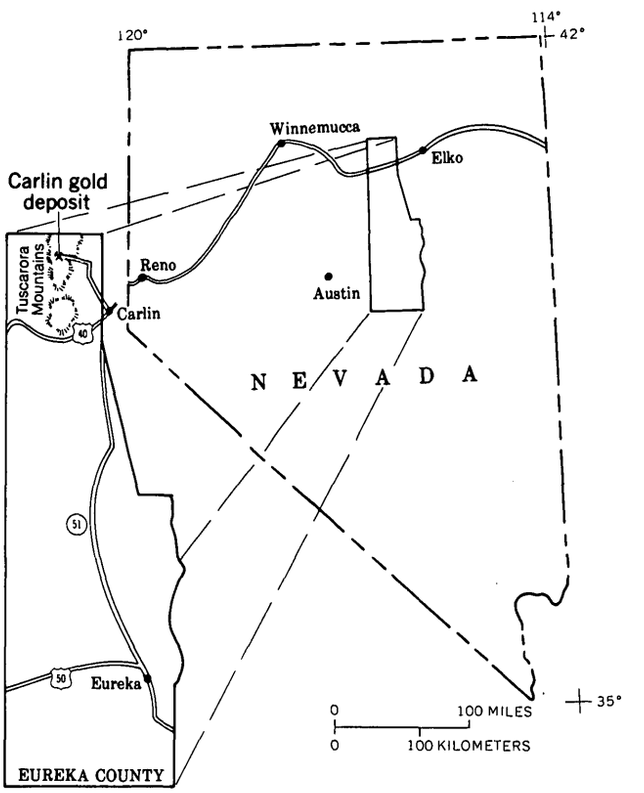

Figure 1.—Index map showing the location of the Carlin gold deposit in north-central Nevada.

ASSOCIATIONS AND COMPOSITION

Thallium-bearing orpiment is associated with barite, calcite, and minor amounts of quartz and realgar, in 20–30-mm-wide veinlets that transect the gold-bearing carbonaceous limestones. A photograph of a hand sample containing euhedral to subhedral crystals of thallium-bearing orpiment surrounded by barite is given in figure 2.

Except for an anomalous brownish-yellow color, other physical properties of the thallium-bearing variety of orpiment, including hardness, luster, and cleavage, are similar to those of ordinary orpiment. Optical properties of the mineral also correspond to those of ordinary orpiment. Results of electron microprobe analyses done on five grains of orpiment

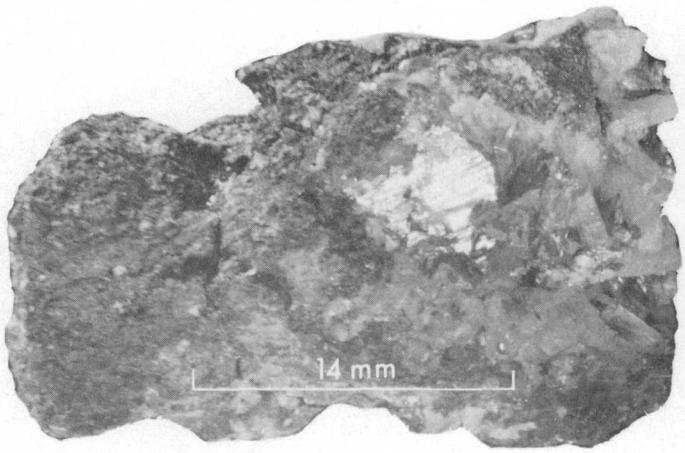

Figure 2.—Specimen containing thallium-bearing orpiment (white shiny crystals) intergrown with tabular gray barite crystals. Other associated minerals are not distinguishable in the photograph. Dark-gray areas are silicified carbonaceous limestone host rock.

show that the content of thallium is rather uniform within a single grain but that it varies significantly between grains. Among the five grains analyzed, the thallium content ranged from 0.1 to 0.35 weight percent. A semiquantitative spectrographic analysis of a large handpicked grain of thallium-bearing orpiment is given in table 1.

Table 1.—*Semiquantitative spectrographic analyses of thallium-bearing orpiment*

[Sought but not found: Au, B, Be, Bi, Cd, Ce, Cr, Eu, Ga, Ge, Hf, In, K, La, Li, Mo, Na, Nb, Pb, Pd, Pt, Re, Sb, Sc, Sn, Sr, Ta, Te, Ti, Th, U, V, W, Y, Yb, Zr. Values are in weight percent. Analyst: Chris Heropoulos]

Si 0.05	Mn .... <0.0001	Cu 0.0001
Al .... <.002	Ag .... <.00007	Hg .... [1]<.001
Fe .... .005	As .... >20.	Ni .... .0007
Mg .... <.0005	Ba .... .07	Tl 2
Ca .... <.001	Co .... <.0002	Zn .... .003

[1] Mercury was detected using a special spectrographic technique developed by Chris Heropoulos.

Two sulfide minerals that contain thallium as a major constituent have been recognized in the same part of the ore deposit. These two minerals are lorandite, $TlAsS_2$, and an unnamed thallium-mercury-arsenic sulfide (Radtke, Taylor, Erd, and Dickson, 1974). Neither of these two minerals occurs in the sample containing thallium-bearing orpiment; in samples that do contain these two minerals and orpiment, the thallium content of the orpiment is less than the lower limit of detection of the electron microprobe (700 p/m).

Artificial crystals of orpiment (grown from a glass with the composition 90 mol percent As_2S_3 and 10 mol percent Tl_2S that was held in a sealed evacuated Pyrex tube for 2 weeks at 250°C) proved to contain about 0.19 wt percent Tl by microprobe analysis. The range of Tl content in 10 grains of orpiment was 0.10 to 0.34 wt percent, essentially the same range as was found for the natural orpiment. We are continuing to study the system Tl_2S-As_2S_3 and related systems pertinent to epithermal gold deposits by melt and hydrothermal approaches.

Other experimental data on thallium-arsenic-sulfur systems are scarce. Canneri and Fernandes (1925), by melting-point measurements, attempted to determine equilibrium relations in the system Tl_2S-As_2S_3, but apparently they encountered serious experimental difficulties that cast doubts on much of their results.

The persistent presence of arsenic in epithermal disseminated replacement-type gold deposits, including the occurrence of arsenic sulfides in barite-calcite veins cutting gold ore bodies, implies a genetic relationship. The thallium that is associated with the arsenic minerals must also be part of the same hydrothermal process. Understanding the distribution of thallium in rocks and minerals of the ore deposits, together with information resulting from laboratory investigations on the physical chemical behavior of selected thallium-containing systems, may provide valuable insight in exploring for new ore bodies.

REFERENCES CITED

Canneri, G., and Fernandes, L., 1925, Contributo allo studio di alcuni minerali contenenti tallio. Analisi termica dei sistemi: Tl_2S-As_2S_3; Tl_2S-PbS: Reale Accad. Nazionale Dei Lincei Atti., 6th series, Rend., Classe di Scienze Fisiche, Matematiche e Naturali, v. 1, pt. 1, p. 671–676.

Hardie, B. S., 1966, Carlin gold mine, Lynn district, Nevada: Nevada Bur. Mines Rept. 13, pt. A, p. 73–83.

Hausen, D. M., and Kerr, P. F., 1968, Fine gold occurrence at Carlin, Nevada, *in* Ridge, J. D., ed., Ore deposits of the United States 1933–1967 (Graton-Sales Volume 1): New York, Am. Inst. Mining, Metall. Petroleum Engineers, Inc., p. 908–940.

Radtke, A. S., Heropoulos, Chris, Fabbi, B. P., Scheiner, B. J., and Essington, Mel, 1972, Data on major and minor elements in host rocks and ores, Carlin gold deposit, Nevada: Econ. Geology, v. 67, no. 7, p. 975–978.

Radtke, A. S., and Scheiner, B. J., 1970, Studies of hydrothermal gold deposition (I). Carlin gold deposit, Nevada—The role of carbonaceous materials in gold deposition: Econ. Geology, v. 65, no. 2, p. 87–102.

Radtke, A. S., Taylor, C. M., and Christ, C. L., 1972, Chemical distribution of gold and mercury at the Carlin deposit, Nevada [abs.]: Econ. Geology, v. 67, no. 7, p. 1009.

Radtke, A. S., Taylor, C. M., Erd, R. C., and Dickson, F. W., 1974, Occurrence of lorandite, $TlAsS_2$, at the Carlin gold deposit, Nevada: Econ. Geology. (In press.)

Radtke, A. S., Taylor, C. M., and Heropoulos, Chris, 1973, Antimony-bearing orpiment, Carlin gold deposit, Nevada: U.S. Geol. Survey Jour. Research, v. 1, no. 1, p. 85–87.

Jour. Research U.S. Geol. Survey
Vol. 2, No. 3, May-June 1974, p. 343—352

CHEMICAL VARIATIONS ACROSS THE ALASKA-ALEUTIAN RANGE BATHOLITH

By BRUCE L. REED and MARVIN A. LANPHERE,
Anchorage, Alaska, Menlo Park, Calif.

Abstract.—A study of 79 chemical analyses of plutonic rocks in the northern part of the Alaska-Aleutian Range batholith shows that K_2O and SiO_2 in Late Cretaceous and Tertiary rocks decrease toward the Pacific margin and that Al_2O_3 and CaO increase. Plots for Fe_2O_3, FeO, MgO, and TiO_2 suggest a possible increase toward the Pacific margin; Na_2O, H_2O+, and MnO show no significant trends across the batholith. Oxide trends for groups of plutons in the western and eastern parts of the batholith in general are opposite that of the groups combined. For the Jurassic plutonic rocks, K_2O may decrease toward the Pacific margin; other oxides show considerable scatter, and meaningful trends are not readily apparent. The oxide trends across the batholith are similar to trends across the central Sierra Nevada batholith of California, with the exception of SiO_2 and Al_2O_3, which show no significant changes. In the Coast Range batholith of British Columbia, potassium also increases away from the Pacific margin. The increase in K_2O toward the continent in the Alaska-Aleutian Range batholith is similar to that found across Quaternary volcanic island arcs, where K_2O content increases directly with increasing depth to inclined seismic zones. This increase suggests that generation of magma may have taken place along, or above, a paleoseismic zone. Geologic evidence supports such a model for the Jurassic plutonic rocks, which represent the roots of an early Mesozoic magmatic arc that probably formed above a descending oceanic plate. However, the hypothesis that magma for Late Cretaceous and Tertiary plutonic rocks was generated along seismic zones does not fit available geologic evidence, and an anatectic model cannot be ruled out.

Chemical trends within circum-Pacific batholiths bear directly on the relation of the batholiths to volcano-plutonic arcs, fossil subduction zones, and consequently, their relation to plate boundaries and plate motions in the past. Compositional trends across circum-Pacific batholiths have long been known (Buddington, 1927; Lindgren, 1915; Moore, 1959; Moore and others, 1963). In this paper we present new data on chemical trends within the Alaska-Aleutian Range batholith that provide additional insight on patterns of chemical variations in the granitic plutons of the Pacific basin.

Bateman and Dodge (1970), in a detailed study of chemical variations within the central part of the Sierra Nevada batholith, suggested that K_2O decreases systematically toward the Pacific margin. Their data showed that Fe_2O_3 and TiO_2 also may decrease toward the Pacific margin and FeO, MgO, and CaO increase. These chemical trends are consistent with the earlier definition by Moore (1959) of a hypothetical quartz diorite line separating quartz diorite near the Pacific margin from granodiorite and quartz monzonite farther inland. In British Columbia the quartz diorite line is not well defined, and the Coast plutonic complex, which contains abundant gneisses and migmatites, is relatively heterogeneous. The K-feldspar content of the plutonic rocks generally increases away from the continental margin (Roddick and Hutchison, 1972), a trend similar to that across the Sierra Nevada.

The potassium content of Quaternary volcanic rocks from circum-Pacific island arcs is spatially related to the position of volcanoes above an inclined seismic zone (Dickinson and Hatherton, 1967). The potassium variation across ancient magmatic arcs may also be related to the position of the magmas above paleoseismic zones (Dickinson, 1970).

GEOLOGIC SETTING OF THE ALASKA-ALEUTIAN RANGE BATHOLITH

The Alaska-Aleutian Range batholith, which lies on the northern part of the circum-Pacific orogenic belt, is about 500 km long and 15 to 80 km wide. (For a more complete discussion of the geology, age, and chemistry of the batholith, see Reed and Lanphere, 1973.) It trends northeast, essentially parallel to the mountain ranges (fig. 1). The batholith is a composite body composed chiefly of quartz-bearing rocks that range in composition from gabbro to granite. The granitic rocks occur as discrete plutons that generally are in sharp contact with one another. At about lat 62° N., the batholith terminates rather abruptly, but smaller plutonic bodies continue north and northeastward into the Mount McKinley area. South of lat 61° N., the batholith is composed chiefly of Jurassic plutonic rocks and is flanked by Mesozoic volcanic and sedimentary rocks. The early Mesozoic rocks are eugeosynclinal and consist of abundant andesite lava and volcaniclastic strata. These rocks, together with the Early Jurassic plutonic rocks, represent the roots of a magmatic arc of an early Mesozoic arc-trench system that extends for more than 1,300 km from the Talkeetna Mountains southwest into the Bering Shelf (Reed and Lanphere, 1973). The associated trench deposits lie about 140 km southeast of the batholith (Forbes and Lanphere, 1973).

Middle and late Mesozoic rocks, exposed chiefly on the east side of the batholith, consist of more than 4.5 km of

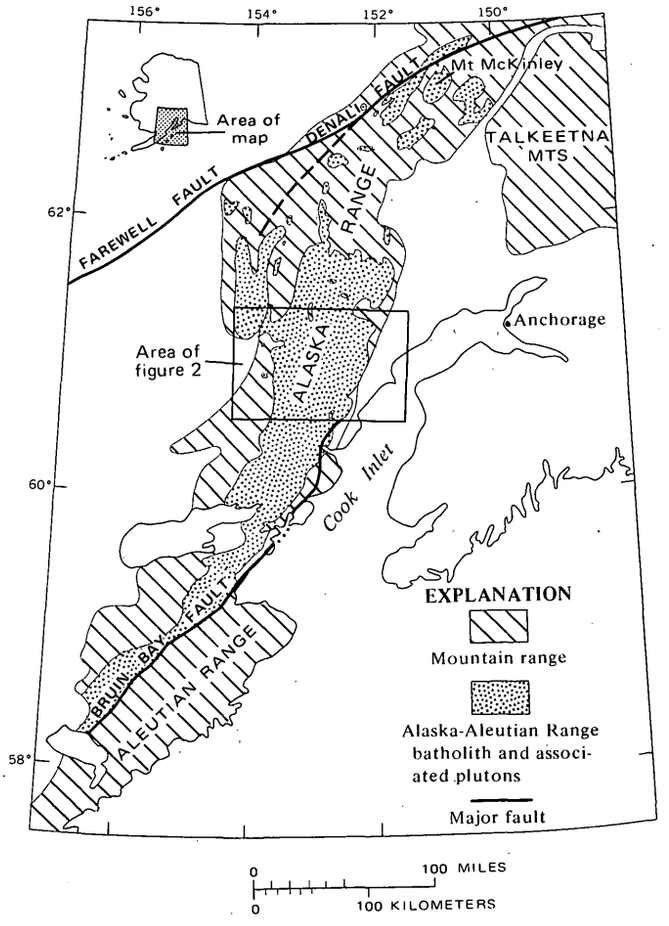

Figure 1.—Map showing boundaries of the Alaska-Aleutian Range batholith and area of figure 2.

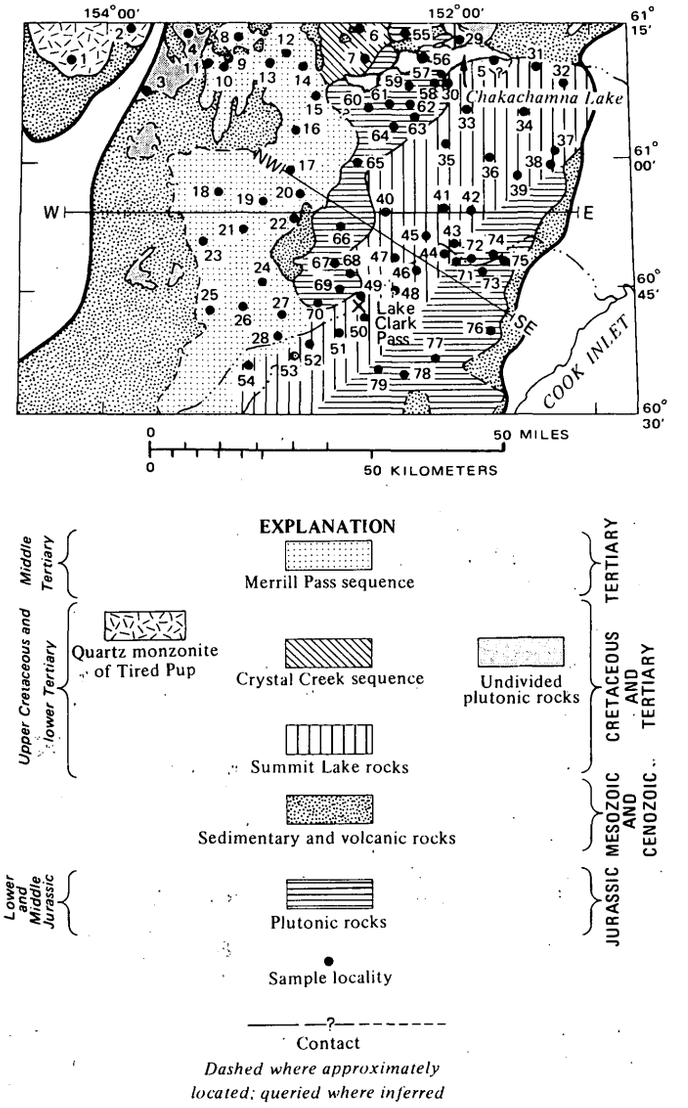

Figure 2.—Map of Alaska-Aleutian Range batholith south of Chakachamna Lake showing intrusive sequences and location of samples chemically analyzed. For analyses see table 1.

first-cycle plutonic and volcanic detritus shed into an adjacent arc-trench gap (the Matanuska geosyncline of Payne, 1955). The Bruin Bay fault, a postintrusive high-angle reverse fault, forms the southeastern side of the batholith for 160 km. The narrowing of the exposed part of the batholith in this area is due primarily to a cover of Tertiary volcanic and sedimentary rocks on the west side. From about lat 61° N., the northwest side of the batholith is flanked by a thick sequence of dark-colored graywacke, slate, and argillite thought to be correlative with Cretaceous rocks in southwestern Alaska.

In the southern part of the batholith, the larger plutons are elongate in a northeasterly direction, parallel to the long axis of the batholith (Reed and Lanphere, 1973). Contacts are generally concordant with the country rocks, and the country rocks are highly deformed locally due to forceful emplacement of the batholith. Late Cretaceous and Tertiary plutonic rocks occur mainly in the northern part of the batholith. The long axes of individual plutons trend in a northerly direction transverse to the regional northeast strike of the country rocks, and their contacts tend to be sharp and discordant.

The principal means of delineating plutonic episodes in the batholith is radiometric dating. Evaluation of concordant potassium-argon ages of coexisting biotite and hornblende indicates that the plutonic rocks were emplaced during three discrete intrusive epochs. The oldest, Early and Middle Jurassic in age, is represented by plutonic rocks consisting chiefly of diorite, quartz diorite, and granodiorite emplaced between 176 and 154 m.y. ago. These rocks make up the major portion of the southern part of the batholith (Reed and Lanphere, 1972). A large block of Jurassic rocks that extends south from Chakachamna Lake (fig. 2) ranges in composition from diorite to granodiorite and is chemically and petrologically similar to the southwest-trending belt of Jurassic rocks to the south. We believe that this block was continuous with the main belt of Jurassic rocks before intrusion of the Summit Lake rocks of Late Cretaceous and early Tertiary age. Coexisting biotite and hornblende from rocks in this block yield highly discordant mineral ages, owing to reheating by the adjacent younger intrusive bodies (Reed and Lanphere, 1973).

Table 1.—*Chemical analyses, norms, and differentiation indices of plutonic rocks of the Alaska-Aleutian Range batholith between lat 60° 30′ and 61° 15′ N.*

[Rapid chemical analyses of rocks by Lowell Artis, S. D. Botts, Gillison Chloe, P. L. D. Elmore, J. L. Glenn, James Kelsey, and Hezekiah Smith]

	Quartz monzonite of Tired Pup		Undivided plutonic rocks			Crystal Creek sequence		Merrill Pass sequence								
Sample No.	1	2	3	4	5	6	7	8	9	10	11	12	13	14	15	16
Field No.	68AR-208	68AR-212	64AR-596	69AR-377	66ALe-29	69AR-325	69AR-328	69AR-366	68AR-240	68AR-241	68AR-242	69AR-321	68AR-254	69AR-320	68AR-256	70AR-151
Chemical analyses (weight percent)																
SiO_2	69.8	70.1	63.6	69.6	74.5	70.5	75.2	77.7	73.6	77.7	71.4	75.6	75.4	74.9	76.3	74.8
Al_2O_3	14.2	14.5	15.1	15.6	14.1	15.5	13.2	13.1	13.6	14.4	14.1	13.2	13.2	13.7	12.5	13.2
Fe_2O_3	.70	.40	.53	3.1	.33	.92	.72	.54	1.0	.72	2.6	.70	.30	.54	.58	.52
FeO	3.0	3.0	4.2	.36	.50	1.8	.80	.60	.76	1.8	.06	.60	1.0	.88	.56	.80
MgO	.80	.70	4.2	.71	.25	.68	.14	.00	.30	.40	.60	.10	.30	.23	.30	.19
CaO	2.1	1.9	4.2	2.6	2.0	2.2	.79	.82	1.2	1.7	2.1	.82	1.0	1.4	.60	1.1
Na_2O	3.3	2.8	2.6	3.6	3.3	4.0	3.4	3.8	4.1	4.2	3.9	3.7	3.5	3.7	3.5	3.6
K_2O	3.8	4.7	2.8	3.8	3.8	3.4	4.8	4.1	3.5	3.5	3.3	4.4	4.2	3.7	4.3	4.2
H_2O+	1.4	.97	1.1	.74	.48	.85	.40	.47	.48	1.1	1.2	.35	.60	.58	.41	.46
H_2O-	.05	.00	.31	.07	.00	.07	.06	.08	.06	.05	.06	.03	.06	.08	.05	.04
TiO_2	.50	.50	.72	.47	.09	.37	.20	.11	.27	.30	.36	.11	.21	.16	.10	.15
P_2O_5	.17	.20	.21	.12	.02	.16	.03	.02	.00	.05	.06	.01	.00	.04	.03	.03
MnO	.14	.14	.09	.04	.05	.03	.00	.00	.14	.14	.18	.00	.07	.13	.00	.09
CO_2	.05	<.05	<.05	.17	<.05	.02	.02	.02	<.05	<.05	.05	.02	<.05	.08	.08	.06
Total	100	100	100	101	100	101	100	101	99	100	100	100	100	100	99	99
CIPW norms (weight percent)																
Q	29.01	29.20	19.97	28.04	36.10	27.97	35.15	37.56	33.52	28.65	31.03	35.40	35.83	35.67	38.16	35.24
or	22.46	27.80	17.23	22.25	22.59	20.00	28.45	23.92	20.90	20.68	19.52	26.10	24.87	21.86	25.60	25.02
ab	27.94	23.71	22.12	30.18	28.09	33.70	28.86	31.75	35.06	35.54	33.03	31.43	29.68	31.30	29.84	30.71
an	9.00	8.13	19.57	10.94	9.85	9.70	3.61	3.76	6.02	8.11	9.72	3.89	4.97	6.18	2.29	4.92
C	1.36	1.83	.55	1.5	.98	1.66	1.10	1.00	.89	.73	.55	.93	1.08	1.34	1.26	.95
ne	—	—	—	—	—	—	—	—	—	—	—	—	—	—	—	—
wo	—	—	—	—	—	—	—	—	—	—	—	—	—	—	—	—
en	1.99	1.74	10.52	1.75	.63	1.69	.35	—	.76	1.00	1.50	.25	.75	.57	.75	.48
fs	4.37	4.62	6.29	—	.59	1.98	.55	.47	.39	2.48	—	.34	1.37	1.15	.38	.97
fo	—	—	—	—	—	—	—	—	—	—	—	—	—	—	—	—
fa	—	—	—	—	—	—	—	—	—	—	—	—	—	—	—	—
mt	1.02	.58	.77	—	.48	1.33	1.05	.77	1.46	1.04	—	1.02	.44	.78	.84	.76
hm	—	—	—	3.07	—	—	—	—	—	—	2.60	—	—	—	—	—
il	.95	.95	1.38	.84	.17	.70	.38	.21	.52	.57	.51	.21	.40	.30	.19	.29
ap	.40	.47	.50	.28	.05	.38	.07	.05	—	.12	.14	.02	—	.10	.07	.07
cc	.11	—	—	.38	—	.04	.05	.04	—	—	.11	.05	—	.18	.18	.14
Differentiation index	79.40	80.72	59.33	80.48	86.77	81.68	92.46	93.23	89.48	84.86	83.57	92.93	90.39	88.82	93.60	90.97

The contact between Summit Lake rocks and the Jurassic block is well defined, but geologic mapping south of Lake Clark Pass is inadequate to establish a southern contact between the Summit Lake rocks and the main belt of Jurassic rocks. On the map of the batholith (fig. 2), the contact is arbitrarily drawn between the sample locations, and the trend of this should not be interpreted to indicate that the Summit Lake rocks necessarily trend northeast.

Late Cretaceous and early Tertiary plutonic rocks, emplaced between about 83 and 58 m.y. ago, form six mappable units in the northern part of the batholith. Compositionally these rocks fall into two categories: (1) Quartz monzonite and granite and (2) quartz diorite and granodiorite. Where sequences of intrusion of individual plutons have been established, the more mafic phases were the first to be emplaced. Two of these are the quartz monzonite of Tired Pup and the Crystal Creek sequence, shown on the map (fig. 2).

The youngest intrusive epoch is represented by middle Tertiary plutonic rocks that range in age from 38 to 26 m.y. and occur in two areas within the batholith and in the Mount McKinley area (Reed and Lanphere, 1972). The largest area of middle Tertiary plutonic rocks is the Merrill Pass sequence (fig. 2), a 150-km elongate body of quartz monzonite and granite on the western side of the batholith that yields mineral ages of 34 to 41 m.y.

CHEMICAL VARIATIONS ACROSS THE BATHOLITH

This paper is an initial attempt to determine whether major chemical variations exist across the part of the Alaska-Aleutian Range batholith south of Chakachamna Lake (between lat 60° 30′ and 61°15′ N., fig. 2). Our work in this part of the batholith was a reconnaissance study; difficulty of access to the region probably will limit detailed geologic investigations for some time. The 79 samples collected are though to be representative of the individual plutonic units, and the sample density probably is sufficient to show any chemical trends that may exist across the batholith. These samples (table 1) were chemically analyzed by the "rapid" method (Shapiro and Brannock, 1962) in the laboratories of the U.S. Geological Survey; sample locations are shown in figure 2.

Table 1.—*Chemical analyses, norms, and differentiation indices of plutonic rocks of the Alaska-Aleutian Range batholith between lat 60° 30′ and 61° 15′ N.*—Continued

	Merrill Pass sequence—Continued												Summit Lake rocks			
Sample No.	17	18	19	20	21	22	23	24	25	26	27	28	29	30	31	32
Field No.	70AR-164	68AR-244	68AR-245	68AR-246	70AR-165	70AR-166	68AR-248	70AR-181	68AR-251	70AR-182	70AR-159	70AR-170	69AR-393	70AR-137	70AR-180	70AR-134
Chemical analyses (weight percent)—Continued																
SiO_2	73.4	65.2	74.6	74.2	73.4	75.0	76.1	72.8	70.8	72.7	69.8	75.4	69.6	65.6	61.2	67.8
Al_2O_3	13.8	16.1	13.2	13.2	13.7	13.2	12.5	14.5	14.5	14.3	15.4	13.2	15.8	16.8	17.8	16.6
Fe_2O_3	.80	1.7	.89	1.1	.70	.54	.45	1.2	1.1	.90	1.4	.72	1.7	1.8	2.4	1.3
FeO	1.0	2.3	1.1	1.0	1.4	.88	.68	.96	2.1	1.4	1.6	.20	1.5	2.0	3.1	1.2
MgO	.32	2.2	.40	.40	.26	.13	.30	.42	.97	.51	.96	.06	1.1	1.5	1.8	.90
CaO	1.2	3.7	1.1	1.4	1.6	1.0	1.1	1.9	2.9	2.0	3.0	.39	3.0	3.9	6.0	3.1
Na_2O	3.8	3.9	3.7	3.7	4.0	3.5	3.9	4.0	3.8	4.0	3.9	4.4	4.2	4.4	4.1	4.7
K_2O	3.9	2.7	3.9	3.9	3.0	3.8	4.3	3.2	2.4	3.0	1.9	3.4	3.2	1.9	1.4	2.7
H_2O+	.50	.92	.62	.77	.61	.45	.20	.49	.69	.75	.51	.68	.53	.92	.90	.92
H_2O-	.09	.05	.04	.04	.05	.05	.15	.04	.06	.04	.05	.06	.04	.18	.04	.04
TiO_2	.21	.65	.24	.27	.25	.20	.13	.28	.39	.28	.36	.10	.46	.56	.62	.32
P_2O_5	.06	.17	.00	.00	.07	.05	.03	.09	.06	.09	.15	.05	.15	.23	.36	.15
MnO	.09	.18	.14	.03	.06	.06	.07	.06	.09	.09	.09	.09	.04	.09	.12	.09
CO_2	.04	<.05	<.05	.05	.06	.04	<.05	.02	.05	.02	.06	.04	.08	.06	.06	<.05
Total	99	100	100	100	99	99	100	100	100	100	99	99	101	100	100	100
CIPW norms (weight percent)—Continued																
Q	33.44	20.56	34.71	34.04	34.74	38.02	34.25	32.73	31.08	32.50	32.24	36.58	24.86	22.36	16.55	22.27
or	23.25	16.00	23.07	23.04	17.89	22.72	25.47	18.93	14.20	17.72	11.33	20.35	18.66	11.26	8.28	15.99
ab	32.44	33.09	31.34	31.30	34.15	29.96	33.08	33.87	32.20	33.83	33.29	37.71	35.06	37.32	34.74	39.86
an	5.36	17.29	5.46	6.63	7.16	4.43	3.91	8.72	13.70	9.20	13.64	1.37	13.22	17.51	26.07	14.43
C	1.39	.44	.89	.46	1.28	1.74	—	1.26	.64	1.10	1.99	1.81	.51	1.11	—	.67
ne	—	—	—	—	—	—	—	—	—	—	—	—	—	—	—	—
wo	—	—	—	—	—	—	.57	—	—	—	—	—	—	—	.42	—
en	.80	5.50	1.00	1.00	.65	.33	.75	1.05	2.42	1.27	2.41	.15	2.70	3.74	4.49	2.25
fs	1.00	2.08	1.15	.54	1.70	.96	.79	.42	2.48	1.53	1.37	—	.66	1.43	2.91	.77
fo	—	—	—	—	—	—	—	—	—	—	—	—	—	—	—	—
fa	—	—	—	—	—	—	—	—	—	—	—	—	—	—	—	—
mt	1.17	2.47	1.29	1.60	1.02	.79	.65	1.74	1.60	1.30	2.05	.66	2.43	2.62	3.48	1.89
hm	—	—	—	—	—	—	—	—	—	—	—	.28	—	—	—	—
il	.40	1.24	.46	.51	.48	.38	.25	.53	.74	.53	.69	.19	.86	1.07	1.18	.61
ap	.14	.40	—	—	.17	.12	.07	.21	.14	.21	.36	.12	.35	.55	.85	.36
cc	.09	—	—	.11	.14	.09	—	.05	.11	.04	.14	.09	.18	.14	.14	—
Differentiation index	89.13	69.66	89.13	88.39	86.78	90.69	92.81	85.53	77.49	84.06	76.85	94.65	78.58	70.94	59.58	78.12

Because plutonic rocks of various ages in the part of the Alaska-Aleutian Range batholith shown on the map (fig. 2) trend in different directions, we have projected the chemical data, plotted as a series of diagrams (fig. 3) for various oxides (expressed in weight percent), onto two lines that cross the trends of the plutonic belts at approximately right angles. Chemical data for the Late Cretaceous and early Tertiary rocks are projected onto line W–E, data for the Jurassic rocks onto line NW–SE (fig. 2). For W–E profiles, the data are separated into two groups: (1) Summit Lake rocks and (2) undivided plutonic rocks of Late Cretaceous and early Tertiary age, the Crystal Creek sequence, quartz monzonite of Tired Pup, and the Merrill Pass sequence.

Least-squares lines are fitted to the data on each oxide plot to assist in evaluation of possible trends. On the W–E profiles, least-squares lines are fitted to each group separately and for both groups as a whole. Standard deviations and correlation coefficients are given for each group of data (fig. 3). The trends of least-squares lines for the undivided group of rocks (dots) on the west side of the W–E profiles are largely controlled by the chemistry of the Merrill Pass sequence because 21 of the 28 samples are from this plutonic unit. Although the other three units are represented by only seven samples, the chemistry of these samples is not significantly different from that of the Merrill Pass sequence (table 1).

With the exception of K_2O, the trends for the oxides of the two groups on the W–E profile are not parallel, but these trends generally slope in a direction opposite that of the least-squares line fitted to all samples. It should be noted, however, that there is considerable scatter of points on either side of the least-squares line and many of the lines are nearly horizontal, a fact indicated also by the generally low correlation coefficient. Some profiles show distinct differences in the oxide content of the two groups, which suggests they may have been derived from different source materials. Compositional differences are further illustrated by a K_2O:SiO_2 plot (fig. 4), a composite K_2O:SiO_2 diagram for the rock units shown in figure 3. This diagram, however, includes all the samples collected from these rock units in the Alaska-Aleutian Range batholith and is not restricted to the samples from the

Table 1.—*Chemical analyses, norms, and differentiation indices of plutonic rocks of the Alaska-Aleutian Range batholith between lat 60° 30′ and 61° 15′ N.*—Continued

	Summit Lake rocks—Continued															
Sample No. . .	33	34	35	36	37	38	39	40	41	42	43	44	45	46	47	48
Field No. . . .	68AR-258	68AR-257	68AR-259	70AR-188	66ALe-30	70AR-189	70AR-179	70AR-140	70AR-186	70AR-187	70AR-185	70AR-158	70AR-147	70AR-174	70AR-141	70AR-173
Chemical analyses (weight percent)—Continued																
SiO_2	61.4	64.7	68.2	64.5	55.4	68.4	58.5	62.6	65.6	68.4	68.1	62.6	66.2	61.8	68.1	56.1
Al_2O_3	17.8	18.0	17.0	17.9	18.8	15.9	17.6	17.2	17.4	16.3	15.6	16.5	17.8	17.4	17.2	18.3
Fe_2O_3	2.2	1.6	1.3	2.1	2.6	1.3	1.9	2.2	1.7	1.4	1.5	1.6	1.7	1.8	1.5	2.5
FeO	2.6	1.7	1.1	1.9	4.6	1.7	4.6	2.9	1.6	1.8	2.3	3.7	1.6	3.5	1.2	4.2
MgO	2.7	1.5	.90	1.4	4.0	.99	3.0	2.3	.83	1.2	1.2	2.6	1.0	1.6	.70	3.9
CaO	5.2	4.1	3.7	5.2	7.2	3.0	6.4	4.8	4.2	3.6	3.6	4.9	4.2	5.6	3.2	6.8
Na_2O	4.2	5.0	5.1	4.5	3.6	3.3	3.6	4.0	4.9	3.6	3.9	4.0	5.1	4.0	5.1	4.1
K_2O	1.9	1.7	1.3	1.4	1.2	3.0	1.6	1.8	1.4	2.6	2.4	1.8	1.4	1.6	2.2	1.0
H_2O+	.74	.75	.68	.64	1.1	.64	.95	1.1	.76	.57	.66	.72	.64	.86	.63	1.2
H_2O-	.04	.07	.05	.03	.02	.08	.05	.04	.02	.02	.02	.08	.03	.01	.04	.03
TiO_2	.66	.44	.34	.47	.94	.39	.83	.64	.44	.41	.56	.66	.41	.72	.32	.88
P_2O_5	.33	.23	.20	.30	.21	.15	.32	.25	.22	.19	.18	.22	.23	.27	.16	.36
MnO	.02	.05	.02	.07	.13	.07	.12	.12	.09	.07	.09	.16	.12	.12	.09	.12
CO_2	<.05	.05	<.05	.04	<.05	.06	.06	.04	.02	.06	.04	.08	.06	.04	.04	.08
Total	100	100	100	100	100	99	100	100	99	100	100	100	100	99	100	100
CIPW norms (weight percent)—Continued																
Q	14.63	18.38	24.70	20.10	7.41	30.04	12.24	18.34	21.81	27.92	26.19	16.99	20.91	17.42	22.30	7.80
or	11.26	10.06	7.69	8.24	7.11	17.92	9.50	10.64	8.34	15.33	14.15	10.69	8.24	9.52	12.94	5.94
ab	35.63	42.38	43.22	37.92	30.53	28.23	30.62	33.86	41.77	30.40	32.92	34.00	42.96	34.08	42.97	34.85
an	23.70	18.56	17.08	23.49	31.66	13.67	27.28	21.94	19.42	16.21	16.39	21.85	18.87	24.97	14.51	28.71
C	.17	1.15	.96	.34	—	2.29	—	.64	.77	1.61	.56	—	.94	—	1.08	—
ne	—	—	—	—	—	—	—	—	—	—	—	—	—	—	—	—
wo	—	—	—	—	1.15	—	.90	—	—	—	—	.26	—	.41	—	.96
en	6.74	3.74	2.24	3.47	9.98	2.49	7.51	5.73	2.08	2.98	2.98	6.50	2.48	4.01	1.74	9.76
fs	1.91	1.17	.42	1.10	5.00	1.55	5.76	2.68	1.17	1.60	2.41	4.70	1.08	4.00	.60	4.44
fo	—	—	—	—	—	—	—	—	—	—	—	—	—	—	—	—
fa	—	—	—	—	—	—	—	—	—	—	—	—	—	—	—	—
mt	3.20	2.32	1.89	3.03	3.78	1.91	2.77	3.19	2.48	2.03	2.17	2.33	2.45	2.63	2.16	3.64
hm	—	—	—	—	—	—	—	—	—	—	—	—	—	—	—	—
il	1.26	.84	.65	.89	1.79	.75	1.58	1.21	.84	.78	1.06	1.26	.78	1.38	.60	1.68
ap	.78	.55	.47	.71	.50	.36	.76	.59	.52	.45	.42	.52	.54	.64	.38	.86
cc	—	.11	—	.09	—	.14	.14	.09	.05	.14	.09	.18	.14	.09	.09	.18
Differentiation index	61.52	70.83	75.62	66.26	76.71	76.20	52.36	62.84	71.92	73.66	73.26	61.68	72.10	61.02	78.21	48.58

part of the batholith shown on the map (fig. 2). The K_2O:SiO_2 ratio of the Crystal Creek sequence, quartz monzonite of Tired Pup, and Merrill Pass sequence is about twice that of the Jurassic and Summit Lake rocks. A line passing through 45 percent SiO_2 at 0 percent K_2O and 75 percent SiO_2 at 4 percent K_2O roughly separates the Jurassic and Summit Lake rocks from the Crystal Creek sequence and quartz monzonite of Tired Pup, but this line transects the field defined by the Merrill Pass sequence. The facts that the fields of the Summit Lake rocks and Jurassic rocks overlap and that trends for some of the oxides of the Summit Lake rocks (W–E profile, fig. 3) are similar to trends for some of the oxides of the Jurassic rocks (NW–SE profile, fig. 3) suggest that these two units may have been derived from similar source materials.

The most pronounced chemical variations across the batholith are those for Al_2O_3 and K_2O. Eastward Al_2O_3 increases from about 14 percent to about 18 percent, whereas K_2O decreases from 4 percent to 1 percent. Plots for SiO_2 and CaO show a general, but not so well defined, variation. SiO_2 shows a decrease of about 10 percent eastward toward the Pacific; the CaO data scatter somewhat, but there is a general increase toward the Pacific. The plots for Fe_2O_3, FeO, MgO, and TiO_2 also suggest a possible, but by no means convincing (correlation coefficients are less than 0.3), increase eastward toward the Pacific margin. The plots for Na_2O, H_2O+, and MnO show no significant change across the batholith. Na_2O averages about 4 percent across the batholith, although the least-squares line on the Na_2O plot dips slightly to the west. The lack of variation in Na content is typical of circum-Pacific batholiths and volcanic arcs; Bateman and Dodge (1970) observed no variation in Na_2O with respect to SiO_2 across the Sierra Nevada batholith, and Hatherton (1969) and more recently Jakes and White (1972) likewise noted no significant variation in Na across volcanic arcs.

Most of the chemical data for Jurassic plutonic rocks plotted on the NW–SE line show considerable scatter, and meaningful trends are not readily apparent. The plot for K_2O, however, suggests a general decrease to the east. TiO_2 also decreases to the east. The plots of MnO, H_2O+, and Na_2O do not indicate any significant change across the batholith.

Table 1.—*Chemical analyses, norms, and differentiation indices of plutonic rocks of the Alaska-Aleutian Range batholith between lat 60° 30′ and 61° 15′ N.*—Continued

	Summit Lake rocks—Continued						Jurassic rocks									
Sample No. . .	49	50	51	52	53	54	55	56	57	58	59	60	61	62	63	64
Field No. . . .	70AR-146	70AR-172	70AR-167	70AR-168	70AR-171	70AR-169	69AR-330	66ALe-28	70AR-136	70AR-138	70AR-160	70AR-162	70AR-153	68AR-264	68AR-263	68AR-260
Chemical analyses (weight percent)—Continued																
SiO_2	69.8	64.8	61.2	60.0	54.6	69.8	61.5	54.5	55.5	50.6	59.8	61.8	60.1	59.3	55.5	59.6
Al_2O_3	17.4	17.2	17.0	18.1	18.0	15.8	16.8	17.8	18.6	18.8	17.4	17.8	17.2	17.6	18.2	17.5
Fe_2O_3	.90	2.1	2.5	2.2	3.0	1.2	1.6	1.0	3.0	3.2	2.1	1.4	1.9	2.8	2.9	2.5
FeO	.96	2.2	2.7	3.1	4.6	1.1	4.4	8.8	3.9	5.5	3.8	3.9	3.7	3.4	4.2	3.5
MgO	.42	1.4	2.0	1.8	4.0	.38	2.5	2.5	3.8	5.4	2.9	1.3	3.0	3.0	4.0	3.0
CaO	3.0	4.5	5.5	5.6	7.4	2.3	5.0	6.3	7.0	8.5	5.8	4.1	5.4	6.0	7.2	5.8
Na_2O	5.6	4.2	4.2	4.6	4.1	4.4	3.6	3.3	4.4	4.2	3.9	4.6	3.9	4.0	4.2	3.9
K_2O	1.1	1.8	1.6	1.2	1.2	3.9	2.6	1.9	1.0	.76	1.6	2.3	1.9	2.0	1.3	2.0
H_2O+	.64	.85	.88	.91	1.2	.71	.84	1.2	1.0	.96	.83	.90	.92	.89	.92	.90
H_2O-	.04	.03	.08	.09	.05	.04	.13	.05	.09	.04	.06	.10	.08	.08	.08	.05
TiO_2	.27	.59	.72	.74	.95	.31	.79	1.6	1.0	1.2	.78	.78	.78	.76	.91	.73
P_2O_5	.08	.26	.28	.36	.41	.14	.17	.62	.42	.68	.29	.28	.27	.24	.39	.24
MnO	.09	.09	.12	.12	.16	.09	.07	.25	.12	.16	.12	.12	.12	.00	.00	.12
CO_2	.04	.06	.08	.04	.06	.08	.01	<.05	.04	.06	.06	.04	.08	<.05	<.05	.05
Total	100	100	99	99	100	100	100	100	100	100	99	99	99	100	100	100
CIPW norms (weight percent)—Continued																
Q	25.88	21.96	16.68	13.96	4.93	24.04	14.50	6.58	6.04	———	13.68	14.26	13.44	11.38	5.42	12.21
or	6.48	10.63	9.57	7.18	7.11	23.00	15.38	11.25	5.92	4.49	9.51	13.68	11.31	11.82	7.70	11.84
ab	47.24	35.52	35.98	39.41	34.80	37.15	30.50	27.99	37.31	35.53	33.21	39.19	33.24	33.85	35.64	33.05
an	14.06	20.24	23.09	25.49	27.25	9.97	22.03	27.27	28.11	30.19	25.40	18.38	23.99	24.16	27.04	24.38
C	1.82	.92	—	.01	—	.68	—	.35	—	—	—	1.06	—	—	—	—
ne	—	—	—	—	—	—	—	—	—	—	—	—	—	—	—	—
wo	—	—	.91	—	2.72	—	.68	—	1.54	2.98	.53	—	.30	1.69	2.60	1.07
en	1.04	3.48	5.04	4.54	9.99	.94	6.23	6.24	9.48	8.40	7.27	3.26	7.53	7.47	9.99	7.48
fs	.74	1.50	1.95	2.91	4.71	.68	5.59	13.19	3.26	3.60	4.20	4.97	4.19	2.68	3.82	3.38
fo	—	—	—	—	—	—	—	—	—	3.54	—	—	—	—	—	—
fa	—	—	—	—	—	—	—	—	—	1.67	—	—	—	—	—	—
mt	1.30	3.04	3.67	3.23	4.36	1.74	2.32	1.45	4.36	4.64	3.06	2.04	2.78	4.06	4.22	3.63
hm	—	—	—	—	—	—	—	—	—	—	—	—	—	—	—	—
il	.51	1.12	1.38	1.42	1.81	.59	1.50	3.05	1.90	2.28	1.49	1.49	1.49	1.44	1.73	1.39
ap	.19	.62	.67	.86	.97	.33	.40	1.47	1.00	1.61	.69	.67	.64	.57	.93	.57
cc	.09	.14	.18	.09	.14	.18	.02	—	.09	.14	.14	.09	.18	—	—	.11
Differentiation index	79.61	68.11	62.23	60.54	46.86	84.19	60.38	45.82	49.27	40.02	56.40	67.14	57.99	57.05	48.77	57.10

CHEMICAL VARIATIONS IN OTHER CIRCUM-PACIFIC BATHOLITHS

The oxide trends across the Alaska-Aleutian batholith are in general similar to trends for the Sierra Nevada batholith (Bateman and Dodge, 1970), as shown by the least-squares lines on the diagrams of figure 3. The right-hand side of each oxide diagram represents the Pacific margin, the left-hand side the landward margin of the respective batholiths. Any slope shown by least-squares lines for the Sierra Nevada batholith will be steepened on the diagrams (fig. 3) because the section line constructed by Bateman and Dodge is about 173 km long (F. C. W. Dodge, oral commun., 1971), whereas line W–E (fig. 3) is about 114 km long. This steepening effect is significant only on the CaO and K_2O plots, as the rest of the least-squares lines for the Sierra Nevada batholith are either horizontal or have a very shallow dip. The actual slope of the Sierra Nevada CaO and K_2O lines is approximately ½° less steep than shown on the diagrams (fig. 3).

The least-squares lines for all samples on the W–E profiles (fig. 3) show both similarities and differences in chemical composition across the two batholiths. In the Alaska-Aleutian Range batholith, SiO_2 decreases and Al_2O_3 increases toward the Pacific margin, whereas across the Sierra Nevada batholith there are no significant changes in SiO_2 and Al_2O_3. Trends for Fe_2O_3, FeO, MgO, Na_2O, K_2O, H_2O+, and MnO in the two batholiths are quite similar. The slope of the Alaska CaO least-squares lines is steeper than that for the Sierra Nevada batholith, and TiO_2 increases towards the Pacific, whereas it remains constant across the Sierra Nevada batholith. In addition to chemical dissimilarities, the distribution of rock units is somewhat different in the two batholiths. For example, the oldest (Jurassic) rocks in the Alaska-Aleutian Range batholith occupy the oceanic side of the main batholith and Late Cretaceous and Tertiary plutons, the continental side. In the central part of the Sierra Nevada batholith, the oldest rocks occur on the continental side of the batholith, and the youngest rocks, toward the center of the batholith (Bateman and Dodge, 1970; Evernden and Kistler, 1970).

The Alaska-Aleutian Range batholith is similar in age to the Coast Range batholith of British Columbia, where minimum ages for emplacement of plutons across the Coast Range batholith are 90–140 m.y. for western plutons, 65–80 m.y.

Table 1.—*Chemical analyses, norms, and differentiation indices of plutonic rocks of the Alaska-Aleutian Range batholith between lat 60° 30′ and 61° 15′ N.*—Continued

	Jurassic rocks—Continued														
Sample No. . .	65	66	67	68	69	70	71	72	73	74	75	76	77	78	79
Field No.	70AR-139	68AR-261	70AR-142	70AR-143	70AR-145	70AR-184	70AR-157	70AR-156	70AR-155	70AR-154	66AR-1464	70AR-178	70AR-177	70AR-175	70AR-176
Chemical analyses (weight percent)—Continued															
SiO_2	60.8	60.0	57.8	61.2	60.0	57.8	52.7	47.3	68.1	57.8	75.0	63.4	57.2	70.8	70.8
Al_2O_3	17.4	16.7	17.2	16.8	16.3	17.4	18.6	18.3	17.6	18.0	13.6	15.8	17.2	16.5	17.2
Fe_2O_3	2.1	3.0	2.9	2.3	2.8	3.0	3.1	2.9	1.1	2.5	.76	1.8	1.7	.88	.81
FeO	3.4	3.0	4.2	3.4	4.1	4.3	5.4	7.2	1.2	4.7	.76	4.1	6.2	.84	.72
MgO	2.4	3.1	3.2	2.4	3.0	3.4	4.8	7.3	.64	3.2	.40	2.4	4.2	.26	.19
CaO	5.4	5.4	6.5	5.4	6.1	6.8	8.4	11.0	3.8	7.0	1.2	5.5	7.8	3.1	2.6
Na_2O	4.4	3.7	4.0	4.0	3.6	4.0	3.4	2.2	5.4	3.4	3.6	2.6	2.6	4.9	5.8
K_2O	1.6	3.2	1.7	2.2	1.9	1.4	.51	.28	.86	.70	3.4	1.9	.83	1.6	1.0
H_2O+	.76	.59	.98	.87	1.1	.86	1.2	.89	.67	1.4	.49	1.3	.91	.64	.68
H_2O-	.04	.05	.02	.04	.09	.01	.11	.02	.04	.05	.11	.16	.03	.03	.04
TiO_2	.81	.78	.95	.83	1.0	.90	.98	1.1	.31	.72	.26	.62	.64	.24	.24
P_2O_5	.35	.32	.38	.34	.33	.41	.28	.23	.14	.23	.05	.12	.14	.07	.05
MnO	.12	.00	.16	.12	.12	.16	.16	.19	.09	.16	.05	.12	.16	.09	.09
CO_2	.04	<.05	.05	.02	.04	.02	.04	.02	.04	.04	<.05	.04	.06	.04	.02
Total	100	100	100	100	100	100	100	99	100	100	100	100	100	100	100
CIPW norms (weight percent)—Continued															
Q	13.81	11.30	9.88	14.60	14.62	9.97	5.20	—	24.39	14.03	37.99	23.87	13.32	29.20	27.33
or	9.50	18.95	10.04	13.02	11.18	8.24	3.03	1.67	5.08	4.14	20.18	11.26	4.92	9.46	5.90
ab	37.39	31.37	33.84	33.89	30.34	33.70	28.90	18.82	45.72	28.81	30.59	22.07	22.08	41.48	48.98
an	23.10	19.55	23.95	21.41	22.62	25.27	34.13	39.66	17.69	31.83	5.65	25.91	32.93	14.68	12.42
C	—	—	—	—	—	—	—	—	1.30	—	1.94	—	—	1.33	2.01
ne	—	—	—	—	—	—	—	—	—	—	—	—	—	—	—
wo	.52	2.17	2.29	1.28	2.14	2.30	2.35	5.79	—	.50	—	.18	1.92	—	—
en	6.00	7.74	7.97	5.98	7.44	8.43	12.01	14.45	1.60	7.98	1.00	6.00	10.50	.65	.47
fs	3.41	1.75	4.04	3.2	3.77	4.21	6.06	7.44	.95	5.68	.43	5.26	9.26	.59	.42
fo	—	—	—	—	—	—	—	2.75	—	—	—	—	—	—	—
fa	—	—	—	—	—	—	—	1.56	—	—	—	—	—	—	—
mt	3.06	4.36	4.20	3.34	4.04	4.33	4.51	4.25	1.60	3.63	1.11	2.62	2.47	1.28	1.17
hm	—	—	—	—	—	—	—	—	—	—	—	—	—	—	—
il	1.54	1.48	1.80	1.58	1.89	1.70	1.87	2.11	.59	1.37	.50	1.18	1.22	.46	.46
ap	.83	.76	.90	.81	.78	.97	.67	.55	.33	.55	.12	.28	.33	.17	.12
cc	.09	—	.11	.05	.09	.04	.09	.05	.09	.09	—	.09	.14	.09	.04
Differentiation index	60.70	61.62	53.76	61.51	56.14	51.91	37.12	20.49	75.19	46.98	88.76	57.19	40.33	80.13	82.21

for the central plutons, and an average of 47 m.y. for the eastern plutons (Hutchison, 1972). In British Columbia the plutons on the Pacific side have trondhjemitic characterisitics, and the inland plutons have calc-alkaline characteristics (Hutchison, 1972). For the southern part of the batholith, Culbert (1972) has documented an increase in potassium away from the Pacific margin.

The difference in oxide trends of the Alaska and California batholiths does not seem to be related in any obvious way to their present geographic position relative to the Pacific margin. The midline of the Sierra Nevada batholith lies 250–400 km inland from the present Pacific Coast; however, the position of the continental margin has undoubtedly changed since the late Mesozoic. Hamilton (1969, fig. 4), for example, infers that the Mesozoic batholiths lay approximately along the continental-oceanic boundary and that the distance from the edge of the continent to the midline of the batholith was about 150–200 km in Late Cretaceous time. The midline of the Alaska-Aleutian Range batholith is about 250 km from the edge of the present continental shelf, and about 140 km separates the Early Jurassic magmatic arc from its associated trench (Reed and Lanphere, 1973).

DISCUSSION

The relation of magma chemistry to depth to the inclined seismic zones in modern volcanic arcs, together with a similarity of chemical trends across circum-Pacific Mesozoic batholiths, has led to the suggestion that the Mesozoic batholiths were at least partly derived from subducted oceanic plates. Geologic evidence suggests that the elongate belt of Jurassic plutonic rocks represents the root of an early Mesozoic magmatic arc which formed above a descending oceanic plate (Reed and Lanphere, 1973). Although there is a suggestion than K_2O in the Jurassic rocks increases toward the continent, the sample density is not sufficient to document a convincing statistical variation across the belt.

The problem of episodic plutonism in composite batholiths makes it difficult to relate chemical trends across composite batholiths containing rocks of widely differing ages to the process of magma generation along or above subduction zones. For example, it is difficult to reconcile a paleoseismic zone that existed for 140 m.y., as in the Alaska-Aleutian Range batholith, with generation of magma taking place intermittently and at various depths along the zone. When the

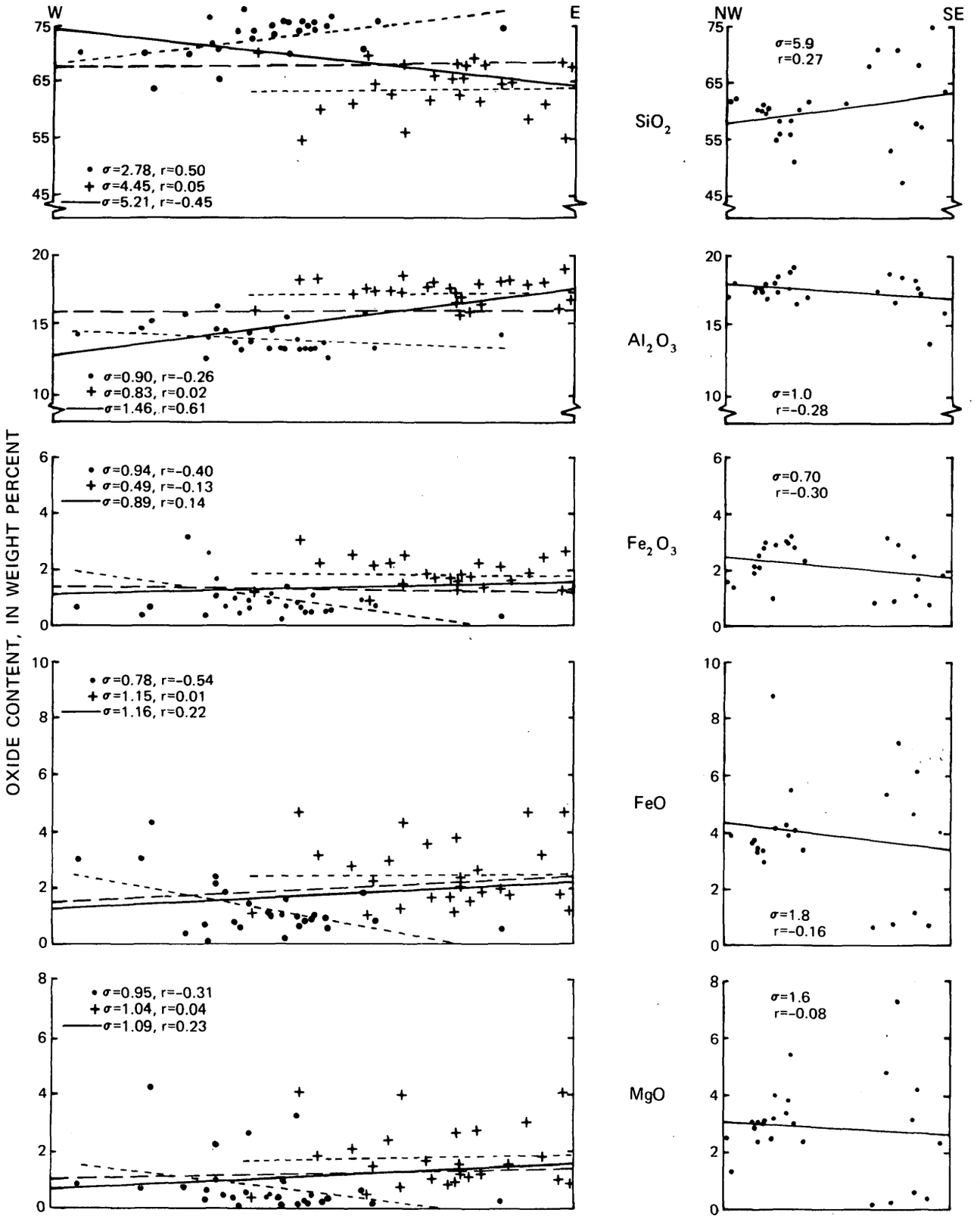

Figure 3.—Oxide contents of Alaska-Aleutian Range rocks projected on lines W–E and NW–SE of figure 2. On the W–E line, the data are separated into two groups: (1) Summit Lake rocks (crosses) and (2) undivided plutonic rocks of Late Cretaceous and early Tertiary age,

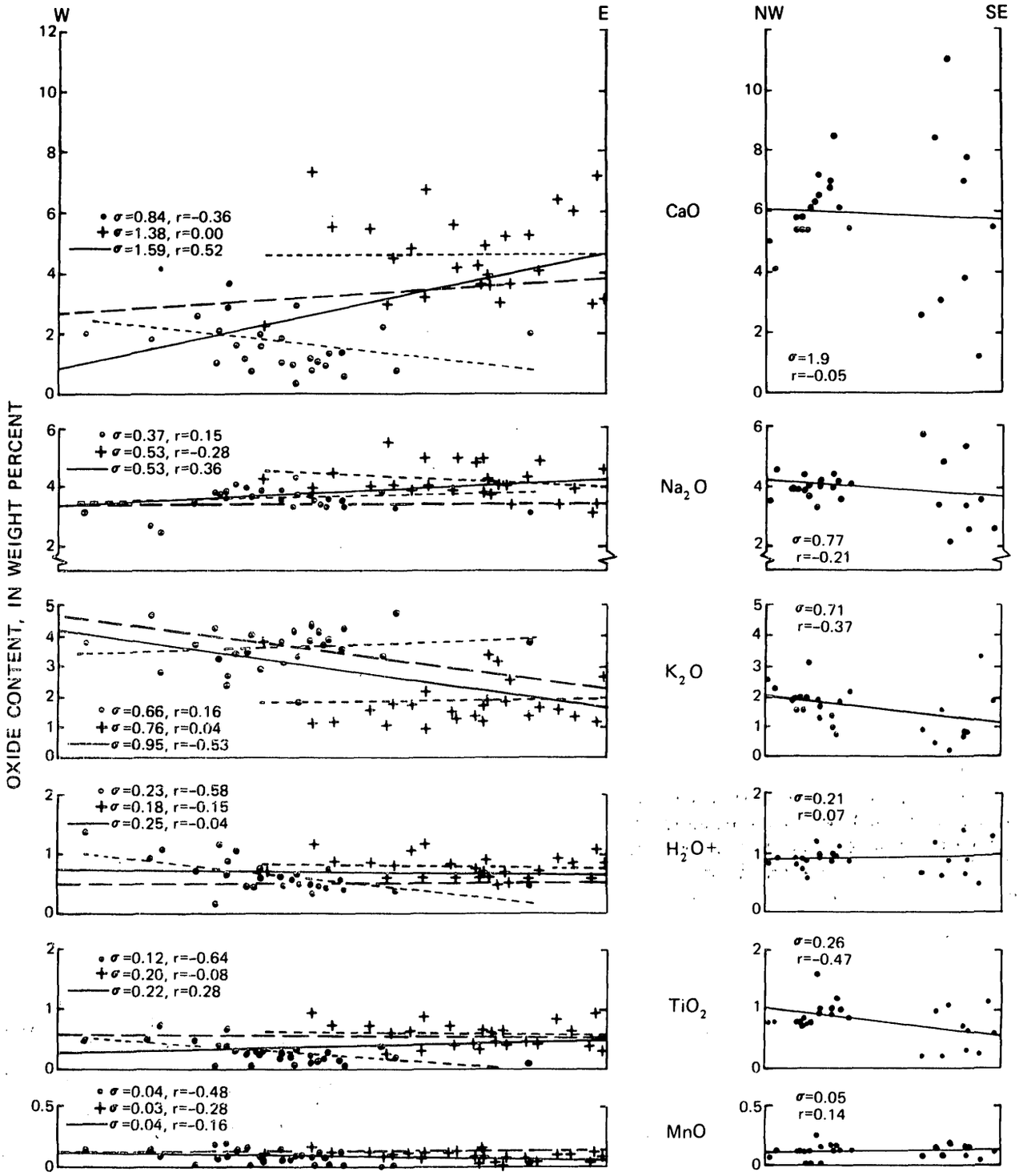

Crystal Creek sequence, quartz monzonite of Tired Pup, and Merrill Pass sequence (dots). Least-squares lines are fitted to each group separately (short-dashed lines) and for both groups as a whole (solid line). These lines represent least-squares approximations to the formula $y=ax+b$, where y is weight percent of a specific oxide and x the distance along line W–E or NW–SE. The long-dashed line is the least-squares approximation given by Bateman and Dodge (1970) for the Sierra Nevada batholith; see text for discussion. σ represents one standard deviation from the least-squares lines and r is the correlation coefficient.

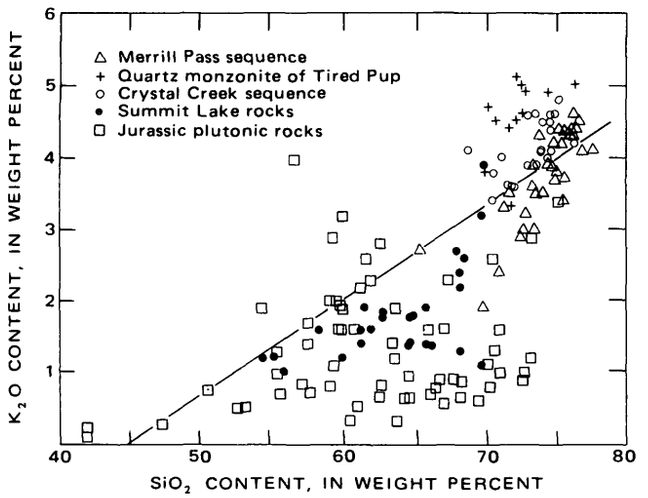

Figure 4.—K_2O content plotted in relation to SiO_2 content for the Merrill Pass sequence, quartz monzonite of Tired Pup, Crystal Creek sequence, Summit Lake rocks, and Jurassic plutonic rocks. See text for discussion.

available analyses are viewed collectively, K_2O on the W–E profile shows a general increase away from the Pacific margin. This is consistent with the hypothesis of magma generation taking place along or above a descending oceanic plate. This simple model, however, is suspect for two reasons. First, if the K_2O trends of the Late Cretaceous and Tertiary plutons in the northern part of the batholith indicate a relation to arc-trench systems, then the arcs are subparallel and only partly coincident with the Jurassic arc system. These younger rocks occur on the contintental side of the earlier Jurassic arc system, and there are no associated "trench" rocks of this age west of the early Mesozoic trench system. Second, the slope of the K_2O trends for each of the two groups of rocks is opposite that of the two groups combined; that is, K_2O for each group appears to increase slightly toward the Pacific margin. Most of the other oxides also have a slope opposite that of the two groups combined. It is difficult to determine the significance of these opposite trends because the correlation coefficients are generally quite low. The number of samples for each group probably is not sufficient to rigorously define any trend. Nonetheless, although the trends must be used with caution, they do appear to be distinct from the overall trends across the batholith.

Finally, an anatectic model for the observed chemical differences in the Late Cretaceous and Tertiary rocks cannot be ruled out. For example, the Summit Lake rocks are chemically similar to, and rose through, the Jurassic plutonic rocks; anatexis of these Jurassic plutonic rocks could have been the source of, or at least influenced, subsequent plutonism in this region. The origin of the younger plutonic rocks in this part of the batholith is therefore still conjectural; it will take additional geologic mapping as well as isotope tracer studies to determine whether these younger rocks evolved through anatexis or differentiation of oceanic material along inclined seismic zones.

ACKNOWLEDGMENTS

T. P. Miller and J. G. Smith reviewed this paper and offered several helpful suggestions. We also benefited from suggestions by P. C. Bateman and F. C. W. Dodge on an earlier version.

REFERENCES CITED

Bateman, P. C., and Dodge, F. C. W., 1970, Variations of major chemical constituents across the central Sierra Nevada batholith: Geol. Soc. America Bull., v. 81, p. 409–420.

Buddington, A. F., 1927, Coast Range intrusives of southeastern Alaska: Jour. Geology, v. 35, p. 224–246.

Culbert, R. R., 1972, Abnormalities in the distribution of K, Rb and Sr in the Coast Mountains batholith, British Columbia: Geochim. et Cosmochim. Acta, v. 36, no. 10, p. 1091–1110.

Dickinson, W. R., 1970, Relations of andesites, granites, and derivative sandstones to arc-trench tectonics: Rev. Geophysics and Space Physics, v. 8, p. 813–860.

Dickinson, W. R., and Hatherton, Trevor, 1967, Andesitic volcanism and seismicity around the Pacific: Science, v. 127, p. 801–803.

Evernden, J. F., and Kistler, R. W., 1970, Chronology of emplacement of Mesozoic batholithic complexes in California and western Nevada: U.S. Geol. Survey Prof. Paper 623, 42 p.

Forbes, R. B., and Lanphere, M. A., 1973, Tectonic significance of mineral ages of blueschists near Seldovia, Alaska: Jour. Geophys. Research, v. 78, no. 8, p. 1383–1386.

Hamilton, Warren, 1969, Mesozoic California and the underflow of Pacific mantle: Geol. Soc. America Bull., v. 80, p. 2409–2430.

Hatherton, Trevor, 1969, The geophysical significance of calc-alkaline andesites in New Zealand: New Zealand Jour. Geology and Geophysics, v. 12, p. 436–459.

Hutchison, W. W., 1972, Chemical variations in major parautochthonous plutons of the Canadian Coast plutonic complex, British Columbia, between 53–55°N: Geol. Soc. America Abs. with Programs, v. 4, no. 3, p. 175–176.

Jakes, P., and White, A. J. R., 1972, Major and trace element abundances in volcanic rocks of orogenic areas: Geol. Soc. America Bull., v. 83, p. 29–40.

Lindgren, Waldemar, 1915, The igneous geology of the Cordilleras and its problems, *in* Problems of American geology: New Haven, Conn., Yale Univ., Silliman Foundation, p. 234–286.

Moore, J. G., 1959, The quartz diorite boundary line in the western United States: Jour. Geology, v. 67, p. 198–210.

Moore, J. G., Grantz, Arthur, and Blake, M. C., Jr., 1963, The quartz diorite line in northwestern North America, *in* Short papers in geology, hydrology, and topography: U.S. Geol. Survey Prof. Paper 450-E, p. E89–E93.

Payne, T. G., 1955, Mesozoic and Cenozoic tectonic elements of Alaska: U.S. Geol. Survey Misc. Geol. Inv. Map I-84, scale 1:5,000,000.

Reed, B. L., and Lanphere, M. A., 1972, Generalized geologic map of the Alaska-Aleutian Range batholith showing potassium-argon ages of the plutonic rocks: U.S. Geol. Survey Misc. Field Studies Map MF-372, scale 1:1,000,000.

—— 1973, The Alaska-Aleutian Range batholith—Geochronology, chemistry, and relation to circum-Pacific plutonism: Geol. Soc. America Bull., v. 84, no. 8 p. 2583–2610.

Roddick, J. A., and Hutchison, W. W., 1972, Plutonic and associated rocks of the Coast Mountains of British Columbia: Internat. Geol. Cong., 24th, Montreal 1972, Guidebook AC04.

Shapiro, Leonard, and Brannock, W. W., 1962, Rapid analysis of silicate, carbonate, and phosphate rocks: U.S. Geol. Survey Bull. 1144-A, 56 p.

Jour. Research U.S. Geol. Survey
Vol. 2, No. 3, May-June 1974, p. 353–355

SPECTROPHOTOMETRIC DETERMINATION OF NIOBIUM IN ROCKS

By L. PAUL GREENLAND and E. Y. CAMPBELL, Washington, D.C.

Abstract.—After acid decomposition and evaporation to volatilize silica, samples containing 0.5–6 μg Nb are fused with pyrosulfate and dissolved in hydrochloric acid–tartaric acid. Niobium is separated by thiocyanate extraction with amyl alcohol and back-extracting from the organic solvent with dilute hydrofluoric acid. Niobium is reacted with 4-(2-pyridylazo)-resorcinol to obtain a colored species. Analytical error, estimated from replicate analyses of eight U.S. Geological Survey standard rocks, ranges from 2.9 to 6.4 percent at the 1–27 μg/g Nb level.

There is a continuing need in the U.S. Geological Survey for rapid and accurate determinations of niobium in rocks and minerals. An analytical method that used the thiocyanate color (Grimaldi, 1960) was used by us until it was replaced by a more rapid isotope dilution–spectrophotometric method (Greenland and Campbell, 1970) utilizing the pyridylazo-resorcinol (PAR) color. Subsequent experience has shown that the PAR method can be simplified further by omitting the radioactive tracer and by using only a single extraction separation without loss of analytical accuracy or precision. A simplified method, which permits twice as many niobium determinations per day, is described below.

REAGENTS

Extraction acid: Dissolve 50 g tartaric acid in 500 ml H_2O, add 330 ml HCl, dilute to 1,000 ml with H_2O.

Thiocyanate solution: Dissolve 29.2 g potassium thiocyanate in 100 ml H_2O.

Stripping solution: Dilute 5 ml HF to 1,000 ml with H_2O.

Complexing solution: Dissolve 37.2 g ethylene diaminotetra-acetic acid (EDTA) and 100 g sodium potassium tartrate in 1,000 ml H_2O.

Reagent solution: Dissolve 1.50 g 4-(2-pyridylazo)-resorcinol in 1,000 ml H_2O.

Sodium acetate: Dissolve 399 g in 1,000 ml H_2O.

Buffer solution: Dissolve 80 g ammonium acetate in 500 ml H_2O, add 3.0 ml acetic acid, and dilute to 1,000 ml with H_2O.

Standard niobium solution: Fuse 0.2 g niobium pentoxide with 3 g potassium pyrosulfate. Dissolve the melt by heating with 30 ml H_2SO_4 and dilute with H_2O to 200 ml in a volumetric flask. This solution contains 1,000 μg/g Nb_2O_5. Prepare dilute standards as needed by dilution with 7 *M* H_2SO_4.

ANALYTICAL PROCEDURE

Weigh 0.25-g samples (2–25 μg/g Nb) into 100-ml platinum dishes. Prepare four standard solutions by pipetting aliquots of the niobium standard solution (or by weighing appropriate amounts of standard rocks) into 100-ml platinum dishes to cover the 0.5–6 μg Nb range. Add 5 ml HNO_3 and 10 ml HF to the dishes and evaporate overnight on a hotplate at 120°C. Fuse the residue in the dish with 2.0 g potassium pyrosulfate and dissolve the fusion cake by heating with 25.0 ml of the extraction acid. Cool the solution, add 1.0 ml thioglycollic acid, and transfer the solution to separatory funnels. Let the solution stand for 15 min. or until the yellow ferric color disappears. Add 15 ml amyl alcohol and 5.0 ml of the thiocyanate solution to the funnels and extract for 2 min; discard the aqueous layer. Wash the organic phase with 5 ml water; then strip niobium from the organic phase with 5.0-ml stripping solution. Wash the aqueous phase three times with 5-ml portions of a 1+1 mixture of amyl alcohol and chloroform, adding 1.0 ml of the thiocyanate solution to the aqueous phase before each of the first two washes. Wash the aqueous phase with 10 ml of ethyl acetate. Transfer the aqueous phase to a 50-ml beaker and add sequentially, while stirring, 2.0 ml of complexing solution, 0.50 ml of reagent solution, and 2.0 ml of sodium acetate. Prepare a reference solution by adding 6.0 ml water, 0.5 ml of complexing solution, 0.5 ml of reagent solution, and 4.5 ml of buffer solution to a 50-ml beaker. The final pH of these solutions should be 6.1±0.2; if it is not, the composition of the buffer solution should be adjusted accordingly. Let the color develop for 40 min, then measure the absorbance in 5-cm cells at 550 nm against the reference solution with a spectrophotometer. Plot absorbance against weight of niobium in the standards and determine the concentration of niobium in the samples by reference to this curve.

DISCUSSION

A thorough study of the Nb-PAR color reaction (Belcher and others, 1963) has shown it to be highly selective in the presence of tartrate and EDTA complexing agents. Greenland and Campbell (1970) ignored the selectivity of the reaction and separated niobium completely for the analysis of rocks. At the other extreme, Meyrowitz (1972) made no separation of

niobium for the analysis of rutile but added iron and titanium to the standard solutions to compensate for their interference. The present procedure separates niobium from the bulk of the sample and relies on the selectivity of the reaction to prevent interference from the remaining contaminants.

Iron is the major interference with the Nb-PAR color in rock analysis. Prevention of the extraction of ferric thiocyanate by reduction to Fe^{+2} with $SnCl_2$ failed because the large amount of tin required interfered with the Nb-PAR color. Although thioglycollic acid is a much less satisfactory reductant, it does prevent the extraction of most of the iron. Most of the iron that does accompany niobium in the extraction remains in the organic phase when niobium is stripped with dilute hydrofluoric acid. Finally, the residual iron is extracted as the thiocyanate with the organic washes.

The preliminary acid decomposition of the sample dissolves most minerals and volatilizes the silica which would otherwise interfere with the extraction of niobium by precipitating. The subsequent fusion dissolves acid-resistant minerals, volatilizes residual fluoride, and ensures a clear solution for the extraction of niobium.

It was originally intended that the recovery of niobium from the separations would be determined by counting ^{94}Nb tracer added to the sample. Analytical experience soon showed, however, that the recovery of niobium could be maintained so constant that the tracer was unnecessary. The average recovery from 79 rocks was 62.2±4.7 percent amounting to a 7.5 percent relative error in the niobium recovery; of this error, 2.3 percent can be attributed to errors resulting from counting statistics, and much of the remainder reflects random day-to-day variations. Therefore, if standards are analyzed concomitantly with samples, the recovery of niobium can be maintained constant at least within ±5 percent.

The loss of 30–40 percent of the original niobium content is about equally distributed between the extraction and stripping of niobium; less than 3 percent is lost in the combined organic washes. Losses are the same from pure niobium solutions as from rock solutions (rhyolite to basalt range, at least) and apparently reflect equilibrium distribution coefficients.

Because this analytical method relies on the constancy of niobium losses in the separations, solution variables affecting the distribution coefficient of niobium (ratio of the concentration of niobium in the organic phase to that in the aqueous phase) must be controlled. Although solution volumes and reagent concentrations are easily maintained constant, it is often necessary to change the sample weight and sometimes the amount of pyrosulfate to adjust the niobium content to the analytical range. Increasing the amount of pyrosulfate in the fusion decreases the distribution coefficient of niobium in the initial extraction but does not affect the back-extraction (table 1). The effect of pyrosulfate on the distribution coefficient is due to sulfate complexing of niobium preventing the formation of the thiocyanate complex. Although the distribution coefficient changes fourfold over the pyrosulfate concentration range studied, this represents a relatively small change in the percentage of niobium extracted which can be adequately controlled by weighing the pyrosulfate to the nearest 0.1 g. The effect of varying sample size on the distribution coefficient (table 2) is so small that no significant error results from varying the sample size in the 0–0.4 g range.

Table 1.—*Effect of pyrosulfate fusion on distribution coefficient of niobium thiocyanate*

Pyrosulfate used in fusion (g)	Distribution coefficient[1]	
	Initial extraction	Hydrofluoric acid stripping
0.75	11.6	0.046
1.5	5.9	.046
2.5	3.7	.042
3.0	2.8	.042

[1] Distribution coefficient is the ratio of niobium concentration in organic phase to that in aqueous phase.

Table 2.—*Effect of sample size on distribution coefficient of niobium thiocyanate*

Sample[1] weight (g)	Distribution coefficient[2]	
	Initial extraction	Hydrofluoric acid stripping
0.050	5.4	0.042
.10	4.6	.046
.20	3.0	.051
.40	3.5	.053

[1] BCR-1 basalt.

[2] Distribution coefficient is the ratio of niobium concentration in organic phase to that in aqueous phase.

Solution volumes throughout the procedure must be controlled because the fraction of Nb extracted with a given distribution coefficient depends on the relative aqueous-organic phase volumes and because the final colored solution is not adjusted to a fixed volume. We have found that graduated cylinders are adequate for volumes of 5 ml and greater and that only normal care is required for the phase separations.

Analytical precision and accuracy of the procedure have been estimated from replicate analyses of the USGS standard rocks (table 3). The individual analyses are duplicate determinations of niobium in three bottles of each of the rocks; the analyses were made in random order over a period of a month and thus reflect the precision to be expected on a routine basis. These analyses have been used elsewhere in an analysis of variance experiment to determine the homogeneity of the standard rocks (Greenland and Campbell, 1974), and the analytical error given in table 3 is derived from the analysis of variance. The analytical error, ranging from 2.9 to 6.4 percent, is satisfactorily low.

Table 3.—*Niobium content (μg/g) of USGS standard rocks*

Sample	Individual analyses	Mean	Error (percent)	Previous analyses 1	Previous analyses 2
QLO-1	11.2, 11.8 11.2, 11.2 11.9, 12.9	11.7	4.1	. . .	. . .
GSP-1	27.8, 29.0 27.9, 29.6 29.1, 28.9	28.7	3.0	29.4	27.5
SDC-1	20.9, 21.6 21.4, 21.0 22.4, 19.4	21.1	6.0	. . .	. . .
BCR-1	16.0, 14.7 15.7, 16.9 15.2, 15.4	15.6	4.7	13.5	23.6
BHVO-1	22.5, 21.0 21.5, 19.8 21.2, 19.9	21.0	5.1	. . .	. . .
G-2	12.8, 13.7 13.9, 14.0 13.0, 13.7	13.4	2.9	13.3	12.6
RGM-1	9.5, 9.5 8.8, 9.5 9.6, 9.5	9.4	3.1	. . .	. . .
AGV-1	15.3, 15.5 16.0, 15.5 14.8, 17.2	15.7	6.4	15.0	16.0

1. Isotope dilution-PAR method of Greenland and Campbell, (1970).
2. Spectrophotometric-thiocyanate method of Grimaldi (1960) as quoted by Flanagan (1969).

This method has been in routine use here for 6 mo and has produced 14 analyses per day. Several hundred of these analyses were repeated days or weeks after the first analysis; the duplicate analyses were usually within 5 percent of the mean, and only rarely did the difference exceed 10 percent. These results, and the data in table 3, show that the method yields reliable results in routine analysis and confirms that the loss of niobium in the separations is reproducible. If necessary, however, greater precision can be obtained by monitoring losses with radioactive niobium tracer and by making the final solution to a fixed volume. These analyses were made with pure niobium solutions as standards, and thus the good agreement of niobium contents determined by this method with previous methods makes it unlikely that systematic errors or interferences are present.

REFERENCES CITED

Belcher, Ronald, Ramakrishna, T. V., and West, T. S., 1963, Absorptiometric determination of niobium with 4-(2-pyridylazo)-resorcinol as reagent: Talanta, v. 10, p. 1013–1022.

Flanagan, F. J., 1969, U.S. Geological Survey standards–2. First compilation of data for the new U.S.G.S. rocks: Geochim. et Cosmochim. Acta, v. 33, no. 1, p. 81–120.

Greenland, L. P., and Campbell, E. Y., 1970, Determination of niobium in rocks by an isotope dilution–spectrophotometric method: Anal. Chim. Acta, v. 49, p. 109–114.

——1974, Homogeneity of Nb content of eight USGS standard rocks, *in* Flanagan, F. J., compiler and ed., Descriptions and analyses of seven new USGS rock standards: U. S. Geol. Survey Prof. Paper 840. (In press.)

Grimaldi, F. S., 1960, Determination of niobium in the parts per million range in rocks: Anal. Chemistry, v. 32, no. 1, p. 119–121.

Meyrowitz, Robert, 1972, Chemical analysis of rutile–direct spectrophotometric determination of titanium, total iron, niobium, phosphorus, and vanadium, *in* Geological Survey research 1972: U.S. Geol. Survey Prof. Paper 800-B, p. B157–B164.

Jour. Research U.S. Geol. Survey
Vol. 2, No. 3, May-June 1974, p. 357–360

SPECTROPHOTOMETRIC DETERMINATION OF SILICA AT HIGH CONCENTRATIONS USING FLUORIDE AS A DEPOLYMERIZER

by LEONARD SHAPIRO, Washington, D.C.

Abstract.—Solutions containing in excess of 200μg/ml of silica form polymers which do not react with molybdate in the spectrophotometric determination of silica. Fluoride ions catalyze the depolymerization of silica so that precise spectrophotometric determinations of silica can be made, even when silica is present predominantly as polymers.

In the analysis of rocks and minerals by the single-solution method of Shapiro (1967), the solutions prepared after a lithium metaborate fusion of 0.0500 g of sample contain 100 μg/ml of sample. The use of a 0.200-g sample to improve sampling of geological materials results in a concentration of 800 μg/ml of sample. This concentration is suitable for all constituents except silica. Spectrophotometric determinations of silica, when made from solutions at this concentration, yield depressed values because of the formation of silica polymers, which do not react to form the silicomolybdate complex. Aoki (1951) suggested that silica dissolved in water forms a true solution only to a specific concentration, above which the remaining silica forms a colloidal solution. Richardson and Waddams (1954) used the silicomolybdate reaction to investigate the polymerization of silica and reported 180 μg/ml as the maximum concentration for stability of ionic species. Goto (1955) reported that ions that promote the polymerization of silica also promote its depolymerization. Thus, hydroxyl ions, hydrofluoric acid, and molybdic acid catalyze both polymerization and depolymerization.

A recommended procedure when analyzing solutions of silica that have polymerized is to digest an aliquot with sodium bicarbonate for 1 h prior to redilution and determination (Rainwater and Thatcher, 1960). Silica is said to be converted to the ionic state very efficiently, but the procedure is time consuming. This paper describes the use of fluoride as a depolymerizer to replace the bicarbonate procedure.

In the procedure of Shapiro (1967) for decomposing samples, a lithium metaborate flux was used which is difficult to remove from the graphite crucible in the presence of high iron or where no sample is present. In this study, it was found that a flux mixture of lithium metaborate and lithium tetraborate, 1:2, decomposed the samples well and provided a readily removable pellet.

REAGENTS AND APPARATUS

Reagents

Flux mixture: Mix thoroughly 1 part lithium metaborate, $LiBO_2$, and 2 parts lithium tetraborate, $Li_2B_4O_7$.

H_2SO_4, 1:1 dilution with water.

HNO_3, 1:1 dilution with water.

NaF, 3 percent solution in water.

Dilute fluoride solution: Dilute 20 ml of the 3 percent NaF solution and 5 ml of 1:1 H_2SO_4 to 1 liter with water.

Ammonium molybdate solution: Dissolve 6.0 g $(NH_4)_6Mo_7O_{24}\cdot 4H_2O$ in 1 liter of water.

Tartaric acid solution: Dissolve 16 g of tartaric acid in 1 liter of water.

Reducing solution: Dissolve 0.28 g of sodium sulphite, 3.6 g of sodium bisulphite, and 0.06 g of 1-amino-2 napthol-4-sulfonic acid in 1 liter of water. Prepare within 48 h of use.

Apparatus

Muffle furnace.

Graphite crucibles 25 mm deep, 20 mm ID.

Spectrophotometer.

Pipet, 0.500-ml, water-repellent-coated or high-precision plunger type with reproducibility 0.5 percent or better.

Pipetting machine (optional): For dispensing 25-ml portions of a reagent rapidly with high precision when many samples are analyzed.

PROCEDURE

Place 1.2 g of the mixed flux on a plastic-coated paper 10X13 cm or larger. Add 200 mg of sample to the flux and mix. Transfer the mixture carefully to a graphite crucible. As a standard, use a material of known silica content containing less than 80 percent silica, such as National Bureau of Standards feldspar 99a. Include one portion of the flux mixture only to serve as a reagent blank.

Fuse in a muffle furnace for 1 h at 1,000°C. Remove from the furnace and allow to cool to room temperature. To each of a series of 250-ml polyethylene bottles add a magnetic stirrer bar, one of the fused pellets, and 50 ml of boiling water. Transfer 5 ml of 1:1 NHO_3 to each while stirring. Stir for about 1 h or until the beads are completely dissolved. Add about 100 ml of water to each bottle; then, one at a time, transfer the contents to a 250-ml volumetric flask using a

funnel to catch the magnetic stirrer. Allow the solutions to drain into the flask from the plastic bottles as much as possible, add water to the mark, mix, and transfer the contents back to the plastic bottles for storage. These solutions contain 800 μg/ml of each sample.

To a series of plastic beakers, transfer 0.500 ml of each of the previously prepared solutions. Use at least three aliquots of the standard solution to provide a dependable average value for this solution. To each beaker add 25 ml of the dilute fluoride solution. Wait 5 min; then add 25 ml of the molybdate solution in the same way and stir. After 10 min add 25 ml of the tartaric acid solution, stir, and then add 25 ml of the reducing solution while stirring. All solutions are added by pipet or pipetting machine.

Allow 1 h for development of color; then read the transmittance with the spectrophotometer set at 640 nm against the blank set at zero with a 2-cm path length cuvette. Calculate results for each sample, using the SiO_2 content of the standard to establish the reference line.

DISCUSSION AND RESULTS

Studies were undertaken to establish some parameters relating levels of fluoride, polymerized silica, and ionic silica in HNO_3 solutions prepared after fusion with a flux of $LiBO_2$ plus $Li_2B_4O_7$. The effect of various concentrations of fluoride was studied at a fixed level of SiO_2, and the results are shown in table 1. The procedure was carried out as described in the preceding section, except that the sodium fluoride was added in increasing amounts to each beaker rather than to the dilute sulfuric acid. The data were obtained using the National Bureau of Standards feldspar 99a which contains 65.2 percent SiO_2 and gives a sample solution of about 520 μg/ml SiO_2. It can be seen from table 1 that without the addition of fluoride the silica result would be about 15 percent low because of polymerization. The addition of 3 to 18 mg of NaF effectively reactivated the silica. When more than 18 mg of NaF is added and, very noticeably, when more than 30 mg is added, the absorbance decreases, presumably because of fluosilicate complexing.

Table 1.—*Relation between NaF content and absorbance at a fixed level (520 μg/ml) of silica*

NaF .... mg ...	0	3.0	7.5	15.0	18.0	22.5	30.0
Absorbance	0.700	0.820	0.825	0.830	0.830	0.810	0.480

To study the extent of polymerization on standing and the influence of added fluoride on silica after various standing periods, a series of sample solutions were prepared containing levels of pure quartz corresponding to 0 to 100 percent SiO_2 in 10 percent steps relative to a 200-mg sample. These solutions, ranging in actual concentration from 0 to 800 μg/ml SiO_2, were allowed to stand for a week, during which aliquots were removed from time to time and silica determined with and without added fluoride. The results are shown in figure 1.

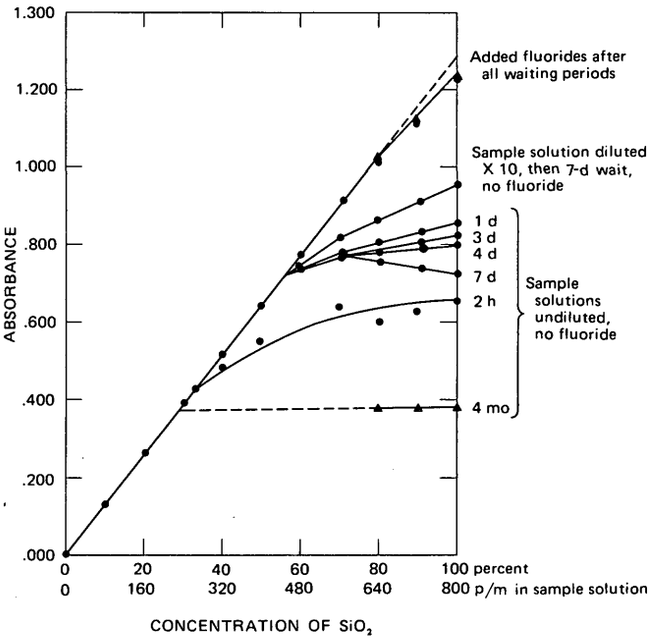

Figure 1.—Absorbance versus concentration of silica with and without fluoride after various waiting periods. Triangles represent samples prepared 4 mo prior to determination of data.

When aliquots were withdrawn within 2 h after dilution and no fluoride was added, the results were linear to about 240 μg/ml. At greater concentrations, the results departed sharply from the line above this and were erratically distributed along a flattened curve. Aliquots taken the next day and run without fluoride gave a linear response to about 450 μg/ml, with higher responses than the initial curve for all concentrations above this. In subsequent days, concentrations above 450 μg/ml showed a gradual decrease, the highest levels dropping more rapidly than the lower ones. Whenever fluoride was added, all points fell along the same line, linear to 640 μg/ml, regardless of the length of time of setting of the sample solutions. Three solutions prepared 4 mo previously, shown by the triangles in the lower right part of the chart all gave nearly the same absorbance, corresponding to about 240 μg/ml before fluoride addition; these solutions gave points on the same line as above when fluoride was added. It is clear from the information and the graph that under the conditions existing when the sample is first put into solution, silica is ionic to about 240 μg/ml but forms polymers above this concentration. After it is diluted and allowed to stand overnight, some depolymerization occurs. On further standing, polymerization begins again and continues. By 4 mo, an equilibrium condition has been established at 240 μg/ml which is the same order as reported in the literature for natural waters.

If complete ionization is achieved at 240 μg/ml, then it should be possible to dilute the original solutions below this

level and to observe the depolymerization. A series of dilutions was made by diluting 10 ml to 100 ml from the silica solutions when they were first prepared; they were allowed to stand for 7 d and then determined with and without fluoride. As can be seen in figure 1, the diluted silica is much less polymerized than the undiluted solution after the same length of time and appears to be heading for further depolymerization if allowed to stay longer. When fluoride was added, once again all points fell on the same straight line.

The straight line obtained using the procedure is linear up to the equivalent of 80 percent SiO_2, or 640 μg/ml. Above this, it deviates by about 2 percent at the 100 percent level. It is possible to use a 0.400-ml pipet in place of a 0.500-ml pipet and to use only the linear part of the curve with a 20 percent reduction in sensitivity. It has been observed that in our laboratory most of the silicate rocks contain less than 80 percent SiO_2, and the choice was made to retain the higher sensitivity obtained from a 0.500-ml aliquot while treating higher level samples separately. Higher standards are run along with these samples to obtain a proper value.

In the procedure, when the sample is first dissolved in nitric acid, the resultant solution is five times more concentrated than it is after dilution. The length of time it can remain in this condition prior to dilution without loss of gelatinous silica was studied to arrive at a safe time for this step. A series of 80 percent and 100 percent SiO_2 solutions was prepared up to the point where the fused melt was dissolved in nitric acid and dilutions made periodically during the same day. One set of solutions was left overnight before dilution. They were then all run with and without fluoride. The longer they stood before dilution, the more polymerization occurred, but in all runs, on addition of fluoride, depolymerization was complete. Therefore, dilution of the initial concentrated solutions can be made safely at any time on the same day the melts are dissolved.

Table 2 presents measurements of precision necessary to estimate the quality that may be expected from the spectrophotometric determinations. The first column represents a series of weighings of aliquots of water delivered by a precision pipet. This step in the procedure can easily introduce significant error if done using improper technique, and therefore the analyst should convince himself that his pipetting is within acceptable limits. Commercially available high-precision piston-type pipets that use plastic conical tips providing extremely low carryover from one sample to another give better precision than do mouth pipets. One of these high-precision pipets, rated to delivery 500 μl, was used in the present study and, as seen from table 2, delivered 0.5007 g with a coefficient of variation of 0.30. As our objective is an error not to exceed 1 percent of the amount present, an error of 0.3 percent of the amount present is well within our limits. In the course of our study we took a series of aliquots from a solution of granite G-1, a diabase W-1, and the National Bureau of Standards feldspar 99a. The results shown in table 2 give values for the coefficient of variation to be close to that given for the precision of the pipet, which shows that no additional significant errors are introduced.

Table 2.—*Precision measurements*

Amount, in grams, delivered by precision pipet	Absorbance		
	G-1	W-1	NBS 99a
0.4984	0.930	0.677	0.840
.5022	.935	.673	.840
.5023	.932	.677	.836
.5005	.932	.675	.840
.5024	.930	.673	.836
.4997	.930	.673	.838
.5016	.930	.673	....
.5021	....	.670	....
.4991	....	....	....
.4991	....	....	....
[1]0.5007	[1]0.931	[1]0.673	[1]0.838
[2].0015	[2].0018	[2].0024	[2].0016
[3].30	[3].19	[3].35	[3].19

[1] Average.
[2] Standard deviation.
[3] Coefficient of variation.

Table 3 presents the results of determinations run on 10 geological materials for which well-established silica values are available. The aliquots were taken on different days. The standard used to establish the reference line was a previously prepared solution of the feldspar 99a from which three aliquots were taken and averaged. The results on these samples show satisfactory agreement with the published values.

Table 3.—*Comparison of values obtained by described procedure with published values*

Sample designation	Values obtained by described procedure		Published values	Source of published values
	Run 1	Run 2		
G-2 granite	69.4	69.0	69.2	Flanagan (1969, p. 109).
GSP-1 granodiosite ...	67.1	67.4	67.3	Do.
AGV-1 andesite	59.3	59.5	59.0	Do.
DTS-1 dunite	40.2	40.6	40.5	Do.
PCC-1 peridotite	41.7	41.9	41.9	Do.
BCR-1 basalt	54.3	54.4	54.5	Do.
G-1 granite	72.4	72.1	72.4	Stevens and others (1969, p. 31).
W-1 diabase	52.6	52.4	52.4	Stevens and others (1960, p. 32).
1A limestone	14.2	14.2	14.1	U.S. National Bureau of Standards certificate.
56b phosphate rock ..	10.2	10.3	10.1	Do.

REFERENCES CITED

Aoki, F., 1951, Properties of silica in water: Chem. Soc. Japan Jour., Pure Chem. Sec. v. 72, p. 17.

Flanagan, F. J., 1969, U.S. Geological Survey Standards—[Pt]2, First compilation of data for new U.S.G.S. rocks: Geochim. et Cosmochim. Acta, v. 33, no. 1, p. 81–120.

Goto, K., 1955, Properties of silica in water: Chem. Soc. Japan Jour., Pure Chem. Sec. v. 76, p. 729.

Rainwater, F. H., and Thatcher, L. L., 1960, Methods for collection and analysis of water samples: U.S. Geol. Survey Water-Supply Paper 1454, 301 p.

Richardson, E., and Waddams, J. A., 1954, Use of the silico-molybdate reaction to investigate the polymerization of low molecular weight silicic acids in dilute solutions: Research, v. 7, p. 542–543.

Shapiro, Leonard, 1967, Rapid analysis of rocks and minerals by a single-solution method, *in* Geological Survey research 1967: U.S. Geol. Survey Prof. Paper 575-B, p. B187–B191.

Stevens, R. E., and others, 1960, Second report on a cooperative investigation of the composition of two silicate rocks: U.S. Geol. Survey Bull. 1113, 126 p.

Jour. Research U.S. Geol. Survey
Vol. 2, No. 3, May-June 1974, p. 361—369

OCCURRENCE OF DISSOLVED ORGANIC CARBON IN SELECTED GROUND-WATER SAMPLES IN THE UNITED STATES

By J. A. LEENHEER, R. L. MALCOLM, P. W. McKINLEY;
and L. A. ECCLES; Denver, Colo.; Garden Grove, Calif.

Abstract.—A study of nonvolatile DOC (dissolved organic carbon) in ground water was conducted to establish base levels of naturally occurring dissolved organic materials. Samples of ground water were obtained at 100 sites in 27 States. Samples were pressure filtered at the time of collection and immediately frozen on dry ice. DOC concentrations were determined by wet oxidation of organic carbon to carbon dioxide which was measured by an infrared analyzer. The DOC concentrations ranged from less than the 0.1 mg/l limit of detection to 15 mg/l. Concentrations of DOC were directly correlated with specific conductance and alkalinity, but did not correlate with pH. The DOC mean concentration was 1.2 mg/l; however, the DOC median value was lower at 0.7 mg/l. Differences in DOC concentration for various types of consolidated rock aquifers were slight; for example, median DOC values for sandstone, limestone, and crystalline rock aquifer types ranged from 0.5 to 0.7 mg/l. No difference was found in the median DOC concentration between shallow (<200 ft; 61 m) and deep (>200 ft) sand and gravel aquifers.

During the past few years, contamination of surface waters by organic materials has attracted increasing concern and attention, and numerous studies have been initiated to document this problem. However, there have been few studies conducted in the United States to ascertain the occurrence of nonvolatile, natural organic materials in ground water.

Nonvolatile organic materials in ground-water supplies of five small towns in Illinois were studied by Robinson, Connor, and Engelbrecht (1967). Organic matter was extracted from the waters by filtration through activated carbon filters, and then retrieved from the filters by successive extractions with various solvents. On each individual extract, chemical oxygen demand (COD) and total carbon analysis were performed. The COD values fell between values reported for short-chain carboxylic acids and pure carbon. DOC concentrations ranged from 1.5 to 7.2 mg/l.

Dissolved, volatile hydrocarbon gasses can given very high levels of DOC in ground water if the samples are collected and retained for analysis under hydrostatic pressure. In a study to determine the amount and type of dissolved hydrocarbon gasses in subsurface waters of the Gulf Coast region of the United States, Buckley, Hocott, and Taggart (1958) found dissolved gas concentrations equivalent to 1,340 mg/l DOC in ground water obtained from depths to 10,000 ft (3,048 m). In most areas, the amount of dissolved hydrocarbon gasses in ground water generally increased with increasing depth because of higher solubility with increasing pressure.

METHODS AND MATERIALS

From December 10, 1970, to January 8, 1971, the authors collected samples from 100 wells and springs in 27 States. Sampling sites in each State were selected by U.S. Geological Survey district personnel. The goal was to obtain uncontaminated ground-water samples from three to four sites in each State in which sampling was done.

To obtain a sample having minimal contamination, flowing wells, springs, and continuously pumped wells were sampled wherever possible. For wells which had to be pumped just for the purpose of sampling, the pumping times ranged from 0.5 to 2 h, depending on the depth of well to assure that several casing volumes of water were flushed through the well before a sample was taken. Two samples of water were collected in gallon glass jugs. Part of the water from one of the jugs was used for field analysis of specific conductance, alkalinity, and pH. The contents of the second sample were poured into a filtration unit. This unit consisted of a 4-liter stainless-steel pressure vessel connected by 0.125-in. stainless-steel tubing to a 47-mm-diameter and 200-ml capacity pressure filtration funnel which contained the membrane filter. The filter selected for use in this study was a 47-mm, 0.45-μm silver-membrane filter. The filtration unit was pressurized to a maximum of 100 lb/in^2 (6.89 bars) by zero-grade carbon-free nitrogen from a Q-size cylinder.

The sampling apparatus was designed to reduce the adsorption or contribution of organic matter by any of the components of the sampling apparatus. A Teflon ring seal in the pressure filtration funnel was the only organic component in the filtering system, and this contributed no detectable organic impurities. Trace quantities of organic carbon in the silver-membrane filter were removed by slow leaching with

100 ml of ground-water sample which was discarded. Approximately 2 liters were then passed through the filter, and the filtrate collected in a 2-liter glass erlenmeyer flask. The filtrate was swirled, and an approximately 150-ml aliquot was poured into a 300-ml glass BOD bottle which previously had been rinsed with a small amount of the filtrate. The water samples were shipped after freezing on dry ice. To prevent the glass bottle from breaking, it was placed on its side and periodically rotated during freezing.

The samples were thawed at room temperature for 12 h prior to analysis. In a few samples, a small amount of a white gelatinous precipitate had formed. In order to include the precipitate in the organic carbon analysis, the samples were subjected to ultrasonic vibration for 30 s at 140 W by an ultrasonic probe. This treatment served to bring precipitated materials back into solution and (or) colloidal suspension.

DOC concentrations of the ground-water samples were determined by wet oxidation of organic carbon to carbon dioxide in a sealed glass ampoule containing 10 ml of sample after removal of inorganic carbon and volatile organic carbon by acidification and oxygen purge. After oxidation with potassium persulfate in a pressure vessel at 175°C and 115 lb/in^2 (7.92 bars), the ampoule was broken in a closed gas-tight system, and the carbon dioxide oxidation product was purged from the sample with nitrogen and carried through the gas cell of an infrared analyzer. The output from the analyzer was displayed on a strip chart recorder, and the peak areas were determined by an electronic digital integrator. DOC concentrations were determined as a function of integrated peak areas. Calibration curves were obtained for standard organic carbon solutions made of potassium hydrogen phthalate and carbon-free water.

RESULTS AND DISCUSSION

The results of the analysis for DOC in ground water collected in the sampling program are given in table 1. The use of the water, type of pump, type of water-bearing material, well depth, geologic age of aquifers, stratigraphic units, date sampled, and field measurements of pH, specific conductance, and alkalinity are also included in table 1 for purposes of information and correlation. The sample locations were selected to be essentially uncontaminated, so that the DOC analysis should indicate the amount of natural organic materials dissolved in the water from various aquifers.

Regression analysis consisted of the linear regression of DOC on well depth and multiple regression of all combinations of DOC on pH, specific conductance, and alkalinity. The multiple regression equation is $Y=a+b_1X_1+b_2X_2+b_3X_3$, where Y is DOC; a is the regression constant; b_1, b_2, and b_3 are the regression coefficients; and X_1, X_2, and X_3 are the independent variables of pH, specific conductance, and alkalinity. For the multiple regression, the step-backward regression-analysis computer program (G. I. Selner, unpub. data, 1974) was slightly modified to show the output from all possible regression combinations rather than from just the most favorable regression combination.

The summary of the regression analysis shown in table 2 indicates trends towards increasing DOC levels and increases in specific conductance and alkalinity. No significant relationship exists between DOC and well depth and between DOC and pH in any of the regression combinations which include pH. The best relationship is obtained in the multiple regression of DOC on specific conductance and alkalinity where about 27 percent of the total sum of squares of the dependent DOC variable is explained.

The lack of significant correlation between pH and DOC may be due to varying pH values in samples in which outgassing of dissolved carbon dioxide has occurred. Carbon dioxide is removed from the sample when measuring alkalinity, and it appears to be the better parameter to use for relating the acid-base characteristics of water to DOC concentrations.

The lack of correlation of DOC with well depth may partly result from the fact that most of the wells sampled were individually screened at several depths in water-bearing zones; thus, well depth is only a very general index of the depth from which the water samples were obtained. However, the very low correlation of DOC with well depth most probably indicates that depth to ground water does not significantly affect DOC for the samples obtained in this study.

The correlation between DOC and specific conductance probably results from a number of factors. Organic materials in the aquifer may slowly degrade to soluble forms when in contact with water to increase the DOC while dissolution of inorganic minerals is causing a simultaneous increase in the specific conductance. Mineralized water may also contain high levels of alkali-metal carbonates which may react with insoluble organic acids to form soluble organic salts. The multiple regression of DOC on specific conductance and alkalinity suggests that both specific conductance and alkalinity affect the levels of DOC found in ground water. Water of high specific conductance frequently has high alkalinity because of dissolved carbonates and bicarbonates.

Table 3 shows distribution of DOC concentrations for several types of aquifers and for wells with oil-lubricated turbine pumps. This table shows sources of DOC in ground water compared by aquifer lithology, aquifer depths in unconsolidated sand and gravel aquifers, and the type of pump lubrication.

The same median DOC value of 0.7 mg/l was found for the sandstone, limestone, and sand and gravel aquifers. These sedimentary aquifer materials, regardless of whether they are consolidated or unconsolidated, may be closely related in the availability of organic materials contributing to DOC, and may contain water of comparable specific conductance and alkalinity which were found to be related to DOC. In contrast, crystalline rock aquifers which frequently contain water with

Table 1.—*Summary of analyses of selected ground water*

Well or spring: Location given as 344444N0863453 indicates lat 34°44'44" N., long 86°34'53" W.
Use of water: D, domestic; I, irrigation; N, industrial; O, observation; P, public supply; R, recreation U, unused.
Type of pump: C, centrifugal; N, none; P, piston; S, submergible; OT, oil-lubricated turbine; WT, water-lubricated turbine. F indicates flowing well.
Water-bearing material: CR, crystalline rock; G, gravel; L, limestone; S, sand; Ss, sandstone.

Well or spring	Owner or tenant	Use of water	Type of pump	Water-bearing material	Well depth below land surface (Meters)	Well depth below land surface (Feet)	Geologic age of aquifers	Stratigraphic units	Date sampled	pH	Specific conductance (μmho)	Alkalinity (mg/l)	DOC (mg/l)
Alabama													
1. 344444N0863453	City of Huntsville.	P	OT	L	31.1	102	.....	.....	12-22-70	6.9	290	164	0.2
2. 321955N0862550	City of Montgomery.	P	OT	S,G	221	726	Late Cretaceous.	Eutaw, Gordo, and Coker Formations.	12-19-70	5.8	341	140	2.4
3. Composite sample from city wells 1, 2, 3, and 4.	City of Tuscaloosa.	P	OT	S,G	24.7 (avg)	81	.....	.....	12-21-70	5.3	111	4	.1
Arizona													
4. 321452N1105438	City of Tucson.	P	OT	S,G	113	370	Pleistocene	Basin fill, upper and lower undifferentiated.	12-21-70	7.8	148	340	<.1
5. 321227N1105748	.....do.....	P	OT	S,G	83.5	274	.....do.....	Upper basin fill.	12-22-70	7.9	855	102	1.2
6. 323608N1144034	Yuma County Water Users Assoc.	I	OT	S,G	73.2	240	.....do.....	Upper sand and gravel.	12-21-70	7.4	274	264	2.2
Arkansas													
7. 343054N0930311	U.S. Natl. Park Service, Hot Springs.	R	N	Ss	.....	.....	Mississippian	Hot Springs Sandstone.	12-8-70	7.6	288	156	.5
8. 344754N0920007	Remington Arms Co. (Lonoke).	N	WT	G	39.3	129	Holocene	Alluvium	12-9-70	6.4	222	82	.1
9. 341141N0920230	General Waterworks (Pine Bluff).	P	OT	S	263	863	Eocene	Sparta Sand	12-9-70	5.4	121	80	.4
California													
10. 335142N1175044	Orange County Water Dept. (Anaheim).	P	OT	.....	89.9	295	.....	.....	12-18-70	7.2	990	152	1.8
11. 334438N1175634	Orange County Water Dist.	O	WT	S,G	274	900	Pliocene	Upper Pico Formation.	12-18-70	8.2	365	210	4.1
12. 371952N1215345	San Jose Waterworks.	P	S	S,G	245.3	805	Pleistocene-Holocene.	Pleistocene-Holocene.	12-16-70	7.8	678	251	.8
13. 372040N1215223	.....do.....	P	S	S,G	255	835	.....do.....	.....do.....	12-16-70	7.9	578	274	.1
14. 371847N1215225	.....do.....	P	S	S,G	222	728	.....do.....	.....do.....	12-16-70	7.5	750	354	<.1
15. 373111N1215032	.....do.....	P	S	S,G	238	780	.....do.....	.....do.....	12-16-70	7.6	760	410	.9
Connecticut													
16. 415451N0723334	Connecticut Water Co. (East Windsor).	P	WT	S,G	15.2	50	Pleistocene	Stratified drift.	12-9-70	7.4	387	84	.3
17. 414924N0721405	Univ. of Connecticut.	P	WT	G	22.2	73	.....do.....	.....do.....	12-9-70	6.5	65	17	.1
18. 414108N0724052	Wethersfield Country Club.	I	S	CR	96.9	318	Late Triassic.	East Berlin Formation.	12-9-70	7.7	1,440	134	.1

Table 1.—*Summary of analyses of selected ground water*—Continued

Well or spring	Owner or tenant	Use of water	Type of pump	Water-bearing material	Well depth below land surface (Meters)	Well depth below land surface (Feet)	Geologic age of aquifers	Stratigraphic units	Date sampled	pH	Specific conductance (μmho)	Alkalinity (mg/l)	DOC (mg/l)
Florida													
19. 294946N0801715	Miami Water Dept.	P	.....	L	32.3	106	Late Miocene to Pleistocene	Biscayne limestone aquifer.	3-19-71	7.2	590	292	15.0
20. 290953N0820313	U.S. Geol. Survey (Ocala).	O	N	L	.....	.....	Tertiary	Floridan aquifer.	3-17-71	8.0	207	88	.1
21. 303037N0871235	City of Pensacola.	P	OT	S,G	.....	.....	do.....	Northwest Florida sand and gravel aquifer.	3-15-71	4.0	370	0	.2
22. 303657N0871543	Monsanto-Chemstrand Corp. (Pensacola).	O	F	L	.....	.....	do.....	Floridan aquifer.	3-16-71	7.3	17,000	331	1.4
23. 264923N0820137 (Hot Mineral Springs, Punta Gordo).	.....	R	F	L	.....	.....	do.....	.....do.....	1-26-71	7.5	56,000	2,680	1.4
24. 291252N0820315 (Silver Springs, Ocala).	.....	R	N	L	.....	.....	.....	.....	12-17-70	7.6	405	208	.3
25. 291252N0820315 (Silver Springs, Ocala).	.....	R	N	L	.....	.....	.....	.....	3-7-71	7.6	410	205	.2
26. 280847N0824003	Eldridge Water Co.	P	OT	L	.....	.....	Tertiary	Floridan aquifer.	1-28-71	7.6	391	248	4.7
27. 302307N0871626 (Warrington).	.....	U	F	S,G	308	1,011	Miocene	Sand and gravel aquifer.	3-16-71	7.9	6,300	310	4.8
Georgia													
28. 334631N0842538	Seydel-Wooley Co. (Atlanta).	N	S	CR	.....	.....	Precambrian-Paleozoic.	Crystalline rocks.	12-18-70	...	475	.....	1.8
29. 320040N0810549	City of Savannah.	P	WT	L	229	750	Tertiary	Principal artesian aquifer.	12-17-70	7.4	232	148	.6
30. 323624N0833652	City of Warner Robbins.	P	OT	S	119	390	Late Cretaceous.	Cusseta Sand.	12-17-70	4.1	16	0	.2
Idaho													
31. 423659N1141421	Henry Jones (Eden).	D	P	CR	91.4	300	Pleistocene and Holocene	Snake River Group.	12-11-70	7.8	660	260	1.0
32. 424542N1145120 (spring).	U.S. Fish and Wildlife Fish Hatchery (Haggerman).	D	N	CR	.....	.....	.....	.....	12-11-70	7.9	329	168	.4
33. 423654N1142752 (spring).	(Twin Falls)	U	N	CR	.....	.....	.....	.....	12-11-70	7.9	635	223	.5
Illinois													
34. 394145N0881754	City of Arcola.	P	S	S	....	.....	.....	.....	1-5-71	7.6	1,045	586	6.9
35. 400705N0881318	City of Champaign.	P	WT	S,G	101	332	.....	.....	1-5-71	7.6	537	408	1.7
36. 394800N0881724	City of Tuscola.	P	WT	L	168	550	.....	.....	1-5-71	7.3	879	285	5.0

Table 1.—*Summary of analyses of selected ground water*—Continued

Well or spring	Owner or tenant	Use of water	Type of pump	Water-bearing material	Well depth below land surface (Meters)	Well depth below land surface (Feet)	Geologic age of aquifers	Stratigraphic units	Date sampled	pH	Specific conductance (μmho)	Alkalinity (mg/l)	DOC (mg/l)
Indiana													
37. City Well 2	City of Lawrence.	P	OT	L	76.2	250			12-23-70	7.7	880	396	.8
38. City well 2	City of West Lafayette.	P	OT	S,G	27.4	90			12-23-70	7.6	495	346	.4
Maine													
39. 442024N0694836	Augusta Water Dist.	P	WT	S,G	27.1	89	Pleistocene	Ice-contact deposits.	12-14-70	8.4	258	134	.4
40. 442017N0694826	do	P	WT	S,G	25.9	85	do	do	12-14-70	7.5			.2
41. 442015N0694825	do	P	WT	S,G			do	do	12-14-70	7.5			.2
42. 464827N0680129	Leo Berube (Caribou).	D	F	S,G	15.5	51	do	Outwash	12-15-70	7.6	350	184	1.3
43. 465407N0680638	Colby Coop Starch Co. (Caribou).	N	F	L	29.9	98	Middle Ordovician to Early Silurian.	Cary Mills Formation.	12-15-70	7.6	353	174	.7
44. 441305N0700015	(Monmouth) (spring).	D	N	S,G			Pleistocene	Ice-contact deposits.	12-14-70	6.8	155	43	.3
45. 463915N0680024	Main Agr. Expt. Sta. (Presque Isle).	D	P	L	24.4	80	Silurian	Sprague ville Formation.	12-15-70	7.3	665	280	1.2
46. 442326N0693513	Virgil Tyler (South China).	D	F	CR	39.6	130	Paleozoic	Bed rock, undifferentiated.	12-14-70	7.8	281	114	1.1
Massachusetts													
47. 420609N0712904	Town of Bellingham.	P	WT	S,G	9.8	32	Pleistocene	Delta deposits	12-10-70	7.4	135	26	.1
48. 421032N0712811	Town of Holliston.	P	C	S,G	25.9	85	do	do	12-11-70	5.8	145	36	.8
49. 421036N0712812	do	P	C	S,G	19.8	65	do	do	12-11-70	6.0	131	26	1.8
50. 420939N0713048	Milford Water Co.	P	C	S,G	10.7	35	do	Outwash deposits	12-11-70	5.5	132	27	1.3
51. 421036N0712108	Town of Millis.	P	OT	S,G	15.2	50	do	Delta deposits	12-11-70	6.5	221	46	1.3
52. 420422N0712114	Town of Wrentham.	P	WT	S,G	18.3	60	do	Ice-contact deposits.	12-11-70	5.5	116	14	.1
Michigan													
53. 421858N0851238	Battle Creek Township.	P	OT	Ss	45.7	150	Osagean (Mississippian)	Lower Marshall Sandstone.	12-29-70	7.6	672	428	.6
54. 431314N0853240	Village of Cedar Springs.	P	OT	S,G	27.4	90	Pleistocene	Sand and gravel	12-29-70	7.5	535	248	.7
55.	Justin Leenheer (Forest Grove).	D	C	S,G	4.6	15	do	do	12-29-70	7.0	362	212	.7
56. 424455N0843444	Lansing Board of Water and Light.	P	WT	Ss	125	410	Morrowan (Pennsylvanian).	Saginaw Formation.	12-29-70	6.8	755	468	3.2
Missouri													
57. 375720N0913257 (Meramec spring).		R	N	L			Early Ordovician (Canadian).	Gasconade Dolomite.	12-7-70	7.2	204	157	.7

Table 1.—*Summary of analyses of selected ground water*—Continued

Well or spring	Owner or tenant	Use of water	Type of pump	Water-bearing material	Well depth below land surface		Geologic age of aquifers	Stratigraphic units	Date sampled	pH	Specific conductance (μmho)	Alkalinity (mg/l)	DOC (mg/l)
					Meters	Feet							
58. 375613N0914610	City of Rolla.	P	WT	L	335	1,100	Late Cambrian	Potosi Dolomite	12-7-70	7.2	575	324	.2
59. 384919N0903148	City of St. Charles.	P	OT	S,G	30.5	100	Holocene	Alluvium	12-7-70	6.2	482	470	1.5
New Hampshire													
60. 424729N0713602 (Witch Spring).		D	N	S			Holocene	Outwash deposits	12-12-70	6.1	320	12	.5
61. 430350N0712630	Manchester Sand and Gravel.	N	WT	S,G	14.6	48	do	do	12-12-70	5.5	278	3	.9
62. 424321N0713140	Peenichuck Waterworks (Nashua).	P	WT	S,G	20.7	68	do	do	12-12-70	6.4	115	36	.2
63. 424327N0713148	Noel Morey (Nashua).	D	S	CR	91.4	300	Paleozoic	Crystalline rocks, undifferentiated.	12-12-70	7.3	110	59	.1
New Jersey													
64. 395546N0750533	Camden Water Dept.	P	OT	S,G	80.8	265			12-22-70	5.6	195		1.3
65. 395920N0750319	do	P	OT	S,G	35.1	115			12-21-70	6.8	425		2.5
66. Company well 6	Texaco Corp. (Eagle Point).	N	OT	S,G	96.9	318			12-22-70	6.6	285		.8
67. 394944N0751734	E. I. Dupont Co.	N	OT	S,G	33.2	109			12-21-70	4.2	460	0	1.5
68. 394408N0751338	South Jersey Water Co. (Mullica Hill).	P	OT	S,G	82.3	270			12-22-70	8.0	950		1.5
69. 394858N0743746	Birches Cranberry Farm (Burlington).	I	F	S,G	27.4	90			12-22-70	3.9	30	0	.4
New Mexico													
70. 350518N1063140	City of Albuquerque.	P	OT	G	334	1096	Miocene	Santa Fe Group, lower part.	11-25-70	7.9	300	144	.1
71. 353719N1084603	City of Gallup.	P	OT	Ss	975	3200	Late Cretaceous.	Gallup Sandstone.	11-27-70	8.6	740	252	.8
New York													
72. 404551N0733419	Westbury Water District.	P	OT	S	79.2	260	Late Cretaceous.	Magothy Formation.	12-7-70	5.8		36	0.1
73. 404219N0731905	Suffolk County Water Authority.	P	WT	S,G	18.3	60	Pleistocene	Upper glacial aquifer.	12-8-70	5.5		22	.9
74. 404539N0731635	do	P	WT	S,G	44.8	147	do	do	12-8-70	6.3		17	1.3
75. Tilson, Delora subdivision well.		P		L					12-18-70	7.6	490		2.5
76. Municipal well.	City of Warwick.	P		S,G					12-18-70	7.5	530		.6
North Carolina													
77. 353253N0763747 (city wells 1, 2, 3, and 4).	Town of Belhaven.	P		L	83.8 (avg)	275	Eocene	Upper Castle Hayne Limestone aquifer.	12-15-70	6.9	1,075	486	2.5

Table 1.—*Summary of analyses of selected ground water*—Continued

Well or spring	Owner or tenant	Use of water	Type of pump	Water-bearing material	Well depth below land surface (Meters)	Well depth below land surface (Feet)	Geologic age of aquifers	Stratigraphic units	Date sampled	pH	Specific conductance (μmho)	Alkalinity (mg/l)	DOC (mg/l)
78. 353544N0784823	City of Fuquay-Varina.	P	WT	CR	107	350	Precambrian	Basement complex.	12-15-70	6.3	197	62	<.1
79. 351557N0773547	City of Kinston.	P	OT	S,G	114	375	Late Cretaceous.	Black Creek Formation.	12-15-70	6.0	229	126	.7
Oregon													
80. 441258N1231238	Junction City	P	WT	S,G	41.1	135	Pleistocene	Alluvium	12-14-70	7.1	410	180	1.0
81. 432627N1241610	Coos Bay-North Bend Water Board.	P	WT	S,G	57.9	190	Pleistocene	Marine deposits	12-15-70	8.1	339	174	3.8
82. 453114N1223112	Richland Water Dist. (Portland).	P	S	S,G	122	400	Pliocene	Troutdale Formation.	12-14-70	7.1	175	108	1.6
83. City well 1	Tigard Water Dist.	P	WT	CR	187	612	.....	.....	12-14-70	7.2	175	159	3.3
Rhode Island													
84. 415434N0712258	Pawtucket Water Co.	P	WT	S,G	17.4	57	Pleistocene	Ice-contact deposits.	12-10-70	6.3	158	28	.2
85. 413809N0712803	Kent County Water Authority.	P	OT	S,G	34.7	114	Pleistocene	Outwash deposits	12-10-70	6.1	158	118	1.9
South Carolina													
86. 340418N0810125	Heater Well Co. (Columbia).	N	WT	CR	76.2	250	Paleozoic	Metamorphic and intrusive rocks.	12-16-70	6.2	114	60	<.1
87. 335605N0802054	City of Sumter.	P	WT	S,G	226	740	Late Cretaceous.	Black Creek and Tuscaloosa Formations.	12-16-70	5.3	43	6	<.1
Tennessee													
88. 354122N0833218	Nath Park Service, Smoky Mts. Natl. Park.	D	S	CR	.....	.....	Precambrian	Great Smoky Group.	12-11-70	5.4	59	28	.2
89. 350935N0900137	Memphis Light, Gas and Water Co.	P	OT	S	179	587	Eocene	500-ft sand of Memphis area.	12-10-70	5.4	166	103	.3
Vermont													
90. 440845N0722853	Rock of Ages Corp. (Barre).	N	WT	CR	183	601	Devonian	Crystalline rocks, undifferentiated.	12-16-70	7.5	336	.....	1.2
91. 441303N0723341	Central Vermont Hospital (Berlin).	D	S	L	64.0	210	Devonian	Crystalline rocks, carbonate.	12-16-70	7.8	.....	.....	.5
92. 435532N0730547	Vermont Fish and Game Dept.	D	WT	S,G	21.3	70	Pleistocene	Stratified deposits, undifferentiated.	12-16-70	7.9	.....	166	.5
93. 443256N0724739	Vermont Forest and Parks Mt. Mansfield.	U	.....	CR	.....	.....	Cambrian	Crystalline rocks, noncarbonate.	12-16-70	6.9	.....	14	.7
Virginia													
94. 364151N0765439	Union Camp Corp. (Franklin).	N	OT	S	264	865	Early Cretaceous.	Lower Cretaceous.	12-14-70	7.1	420	232	.6
95. 375055N0792840 (spring).	(Lexington)	R	.....	L	.....	.....	Early Ordovician.	Beekmantown Group.	12-12-70	7.2	403	242	.4

Table 1.—*Summary of analyses of selected ground water*—Continued

Well or spring	Owner or tenant	Use of water	Type of pump	Water-bearing material	Well depth below land surface Meters	Well depth below land surface Feet	Geologic age of aquifers	Stratigraphic units	Date sampled	pH	Specific conductance (μmho)	Alkalinity (mg/l)	DOC (mg/l)
96. 363350N0761530	U.S. Naval Radio Sta. (Northwest).	D	WT	S	18.3	60	Miocene and Pliocene.	Chesapeake Group.	12-14-70	6.8	420	152	1.2
Washington													
97. 460140N1181234	Baker and Baker Ranch (Walla Walla).	D	F	CR	187	612	.....do.....	Columbia River Group or Basalt.	12-13-70	7.5	128	71	.1
98. 460112N1182140	Larry Preso (Walla Walla).	D	S	G	.....	.....	Cenozoic	Older gravel of Walla Walla.	12-12-70	7.4	189	108	.4
Wyoming													
99. 410747N1045948	City of Cheyenne.	P	WT	G	57.0	187	Miocene	Ogallala Formation.	12-10-70	6.7	290	.....	1.0
100. 412017N1053542	U.S. Bur. of Mines (Laramie).	D	S	Ss	408	1337	Early Permian ...	Upper Casper Formation.	12-10-70	7.5	340	170	.7

Table 2.—*Regression analysis of dependent variable of DOC with independent variables of depth, pH, specific conductance, and alkalinity*

Independent variables	Degrees of freedom	Regression constant (*a*)	Regression coefficients b_1	b_2	b_3	Correlation coefficient (*r*)	Percentage of total sum of squares of dependent variable explained
Well depth	77	0.996	1.97×10^{-4}	.....	.....	0.081	0.66
pH	96	−.471	2.19×10^{-1}	.....	.....	.177	3.15
Specific conductance	89	.741	7.83×10^{-4}	.....	.....	.415	17.24
Alkalinity	85	.362	4.15×10^{-3}	.....	.....	.435	18.95
pH, specific conductance	88	.014	1.07×10^{-1}	7.39×10^{-4}	.....	.424	17.95
pH, alkalinity	85	.898	-8.65×10^{-2}	4.52×10^{-3}	.....	.439	19.28
Specific conductance, alkalinity	80	.260	5.62×10^{-4}	3.19×10^{-3}	.....	.521	27.09
pH, specific conductance, alkalinity	80	.998	-1.19×10^{-1}	5.75×10^{-4}	3.66×10^{-3}	.526	27.70

low specific conductance and alkalinity because of the absence of soluble minerals, and the heat and pressure involved with metamorphic and igneous rock formation may convert organic materials to refractory forms which are less soluble in ground water. This may account for the lower DOC median value between 0.4 and 0.5 mg/l for crystalline rock aquifers.

Another postulation was that shallow sand and gravel aquifers (<200 ft deep) were more likely to be infiltrated with DOC in surface water than deep sand and gravel aquifers (>200 ft deep). However, the median value for both the shallow and deep sand and gravel aquifers was 0.7 mg/l.

The DOC distribution in the right-hand column of table 3 is intended to be a comparison of DOC values of ground-water samples obtained from wells with oil-lubricated turbine pumps versus the remainder of the data which was based on samples obtained from springs, flowing wells, and various types of water-lubricated pumps. Significant oil contamination of ground water is a possibility with oil-lubricated turbine pumps as the small amount of oil which lubricates the bearings in the line shaft is not recirculated and eventually enters the well. Therefore, the wells with oil-lubricated turbine pumps were sampled only after the casing and pump were thoroughly flushed with ground water to minimize the possibility of oil contamination. The DOC distribution for oil-lubricated turbine pumps in table 3 does not show an increase in DOC due to oil contamination, and the median value of 0.7 mg/l DOC is the same as the median value for the remainder of the data.

The availability of organic source materials apparently inflated the DOC levels in certain samples. Site 19 in Miami, Fl. was a shallow aquifer which received its high DOC from infiltration of surface water high in DOC. Sites 34, 36, and 56 in Illinois and Michigan may have elevated DOC levels due to

Table 3.—*Distributions of DOC concentrations*

[M indicates the median for DOC concentrations]

Sandstone	Limestone	Crystalline rock	Shallow sand and gravel (<200 ft deep)		Deep sand and gravel (>200 ft deep)		Wells with oil-lubricated turbine pump	
0.2	0.2	0.1	0.1	.7	0.1	2.4	0.1	1.8
.5	.2	.1	.1	.8	.1	4.1	.1	1.9
.6	.3	.1	.1	.9	.1	6.9	.1	2.2
.7 M	.4	.1	.1	.9	.1		.2	2.4
.8	.4	.1	.1	1.0	.1		.2	2.5
3.2	.5	.2	.1	1.0	.1		.2	
	.6	.4	.2	1.2	.2		.3	
	.7 M	.5 M	.2	1.2	.2		.4	
	.7	.7	.2	1.3	.3		.4	
	.8	1.0	.2	1.3	.4		.6	
	1.2	1.1	.3	1.3	.6		.6	
	1.4	1.2	.3	1.3	.7 M		.7	
	2.5	1.8	.4	1.5	.8		.7 M	
	2.5	3.3	.4	1.5	.8		.8	
	4.7		.4	1.8	.9		.8	
	4.8		.4	1.9	1.3		1.2	
	5.0		.5	2.2	1.5		1.3	
			.5	2.5	1.6		1.5	
			.6	3.8	1.7		1.5	
			.7 M	15.0	1.8		1.5	

the presence of small amounts of gas, oil, and coal found within the aquifer. Therefore, each aquifer has its individual characteristics and should be treated separately.

SUMMARY AND CONCLUSIONS

The concentration of dissolved organic carbon in groundwater samples collected from various parts of the country was generally very low. Although the values ranged from undetectable levels to as much as 15 mg/l, 85 percent of all the values were below 2 mg/l. Furthermore, the median value for all five aquifer types ranged from 0.5 to 0.7 mg/l. Because of the predominance of low values, most, if not all, of the concentrations of DOC measured are believed to be inherent to the ground water of the various aquifers and not the result of outside contamination.

DOC levels were correlated with the alkalinity and specific conductance of the samples. The increase of DOC in mineralized waters may indicate that not only inorganic materials but also organic materials are added in the processes which produce mineralized water.

This study has provided some threshold ranges for nonvolatile DOC in water from essentially unpolluted aquifers. The low DOC values in most ground water enhance the ability to assess trends in the concentrations of organic materials in an aquifer. Organic contamination will often cause an increase in DOC of one order of magnitude, or more, over background DOC levels (Malcolm and Leenheer, 1973). Values greater than the threshold levels of DOC (>5 mg/l DOC) could indicate contaminent and possibly pollutant organic materials moving into the aquifer from sources such as surface-water infiltration and subsurface waste-disposal operations. This study does not advocate DOC as the absolute parameter for the detection of organic contamination in ground water. Certain organic materials such as pesticides can be toxic in concentrations below the detection limits of the organic carbon analysis.

REFERENCES CITED

Buckley, S. E., Hocott, C. R., and Taggart, M. S. Jr., 1958, Distribution of dissolved hydrocarbons in subsurface waters, *in* Habitat of Oil: Tulsa, Okla., Am. Assoc. Petroleum Geologists, p. 850–852.

Malcolm, R. L. and Leenheer, J. A., 1973, The usefulness of organic carbon parameters in water quality investigations: Anaheim, Calif., Inst. Environmental Sci., Proc., no. 19, p. 336–340.

Robinson, L. R., Connor, J. T., and Engelbrecht, R. S., 1967, Organic materials in Illinois groundwaters: Am. Water Works Assoc. Jour., v. 59, p. 227–236.

Shvets, V. M., 1964, Distribution of organic substances in subsurface waters: Nauchno-Issled. Inst. Gidrogeol. i Inzh Geol., no. 9, p. 159–175.

Jour. Research U.S. Geol. Survey
Vol. 2, No. 3, May-June 1974, p. 371—377

THE SOIL CREEP—CURVED TREE FALLACY

By RICHARD L. PHIPPS, Arlington, Va.

Abstract.—No evidence has been found in eastern deciduous forests to substantiate statements that curved tree trunks, downslope tilted tree trunks, and upslope trailing tree root systems are the result of soil creep. Curvature and tilting of trunks are described as geotropic and phototropic responses to physical and physiological conditions unrelated to soil creep. The occurrence of upslope trailing of roots has not been demonstrated.

Soil creep is usually so slow that its detection generally depends on recognition of its results or of related phenomena. Tree deformation (curves or angles of tree trunks as opposed to the classical vertical orientation) has often been cited as the result of soil creep. (Sharpe (1938, p. 24) stated:

> Downslope tilting of trees and a compensating upslope curvature of their trunks is unusually well developed on hillsides of relatively loose material * * *.

Penck (1953, p. 109) presented the accepted argument justifying the correlation as causal:

> The root system of these trees is anchored in the deeper soil horizons which move more slowly, or in the living rock itself, whilst the quicker moving superficial layer presses the upper part of the root system downslope. This rotation couple makes the trees oblique at the base, while the trunks as a whole tend to grow vertically upwards. Thus they show curvature, convex on the downslope side.

Leet and Judson (1958, p. 154) have apparently abandoned upslope curvature of tree trunks as evidence of creep but still adhere to the trailing roots theory:

> Although when viewed from the surface, the tree appears to be growing in a normal way, it is actually creeping very slowly downslope. Since the surface of the soil is moving more rapidly than the soil beneath it, the roots of the tree are unable to keep up with the trunk. Consequently, they spread out like great streamers along the slope.

Parizek and Woodruff (1957) doubt that tree deformation is the result of soil creep (p. 64), stating:

> It would appear that the willing acceptance by many geologists of distorted trees as an evidence of soil creep, without examination of the physiology of the growth, has been, in effect, search *for* rather than examination *of* the evidence.

They contend that tree curvature is the result of a geotropic response of the tree brought about by causes other than soil creep. Primarily on the basis of the arguments of Parizek and Woodruff (1957), Carson and Kirkby (1972) conclude that "Curvature of trees cannot therefore be accepted as evidence of soil movement." However, a number of authors of other recent textbooks, "those formidable fossilizers of misconception" (Tomlinson, 1964), still cite bent trees as evidence of soil creep. Gilluly, Waters, and Woodford (1968, p. 187) use the classic illustration of Sharpe (1938) and state that "on many slopes, rock structures, trees, posts, and even buildings, all show the effects of creep." Small (1970, p. 31) fully accepts tree deformation as evidence of creep:

> The evidence of creep may be seen on almost any moderately steep soil-covered slope * * *. Trees tend to lean over in a downslope direction, owing to the fact that movement in the upper soil layers is greater than at the base * * * (and though) tree roots tend to stabilize the soil * * * the bending of tree trunks shows that creep is not halted altogether * * *.

In an extensive treatise on the use of trees in interpreting geomorphic processes Alestalo (1971), in citing Sharpe (1938), accepts without question the contention that "bending of roots is caused by soil creep, which may also lead to inclination of the stem." Furthermore, Parizek and Woodruff (1957), who argued against tree deformation as evidence of soil creep, have been misinterpreted by Alestalo (1971, p. 71) and cited as authority for the statement that "In soil creep the rate of movement is highest in the surface layer of the ground * * *. Consequently, the roots bend and the trunks tilt downslope."

Acknowledgments.—Sincere appreciation is expressed to Sidney E. White, Department of Geology, the Ohio State University, for having created the stimulus to question tree deformation as an indicator of soil creep. Robert D. Bugenhagen, a visiting high school science student, conducted the preliminary measurement study concerning degree of leaning of beech and white oak. Appreciation is also expressed to Sidney P. Spalding for his continued interest in field-science research and his willingness to permit research within his Patowmack Farms wildlife sanctuary.

TRAILING TREE ROOTS

That tree roots stabilize the soil is very generally accepted and quite well documented in the literature. In typical woodlands, tree roots form a dense subterranean mat with obvious soil stabilization qualities. On the other hand, descriptions of root displacement caused by tree and (or) soil movement are apparently not to be found in the botanical

literature. An extensive study of root distribution of deciduous tree species conducted at Harvard's Black Rock Forest (Stout, 1956) gave no mention of tree movement or root trailing. In that study complete root systems of 25 trees representing 11 species, on 5 different sites ranging from 20 to 45 percent slope, were carefully washed out, mapped, and described. One of the sites was a gravelly kame terrace, which by descriptions in geologic literature (such as Sharpe, 1938, p. 24) should have been an ideal site for evidence of soil creep. However, root distributions here were no different from those at any of the other four sites. In a general description of the distribution of root systems at all sites, Stout stated (1956, p. 16, 17):

> [the root system of a tree] may be more or less symmetrically arranged around the stump, or mostly upslope or downslope from the stump, or to one side or the other * * *. The direction of root growth away from the stump appears quite unpredictable * * *. Frequently roots terminate in a mass of fine rootlets surrounding and lying beneath the base of a neighboring tree.

Several references were made by Stout to directional growth of roots, but no evidence was presented which supported the theory of relative displacement of the already formed root system.

A wide range in the rate of soil creep has been reported. However, something in the order of 5–6 mm per year may be typical, as in the semiarid southwest (Leopold and others, 1966), on lumbered coniferous slopes in southern Alaska (Barr and Swanston, 1970), and in eastern deciduous forests (Everett, 1963). If a tree growing in the soil moves at the same rate as the soil, then the tree moves only about 50–60 cm (about 1½–2 ft) downslope in 100 yr. This amount of movement hardly seems adequate to result in an obvious upslope trailing of roots on a root system which may be 15m or more in diameter. Stout (1956) found the root-crown ratio of trees at Black Rock Forest to be roughly 4.5:1. Thus, he stated (p. 20), "this indicates that the total area of the root systems in a unit area within a closed stand is four and one-half times the area of the ground surface." Such extensive overlap of root systems between trees must result in a very cohesive soil layer. The lack of evidence of root distortion, the rate of soil creep, and the apparent cohesiveness of a forest root zone together suggest that, if soil creep does in fact occur in forested sites, then movement of the entire slope forest, trees and root systems, must be as a unit without distortion of the root systems. Neither field observations nor accounts in the literature can be construed as evidence that roots of trees may be distorted and trail upslope.

CURVED TREE TRUNKS

Curved or tilted tree trunks are the two most common types of tree deformation cited as evidence of soil creep. The conventional concept of tree deformation resulting from soil creep is a curve at the base (convex on the downslope side), above which the trunk is straight and vertical (Sharpe, 1938; Penck, 1953). Partial tipping of the tree is supposed to result from the fact that the upper layers of the soil move faster than the lower layers (fig. 1).

Height growth of trees occurs from the stem tips and is a geotropic response resulting in essentially vertical growth. If a tree is tipped, the tipped trunk will remain tipped, but new growth from the tip will right itself vertically (geotropic response) as the result of growth regulators whose distribution is determined by gravity. As pointed out by Parizek and Woodruff (1957), continuous movement of the tree by the soil would not result in a single curve at the base of the trunk, but in a continuous curve throughout the length of the trunk (fig. 2).

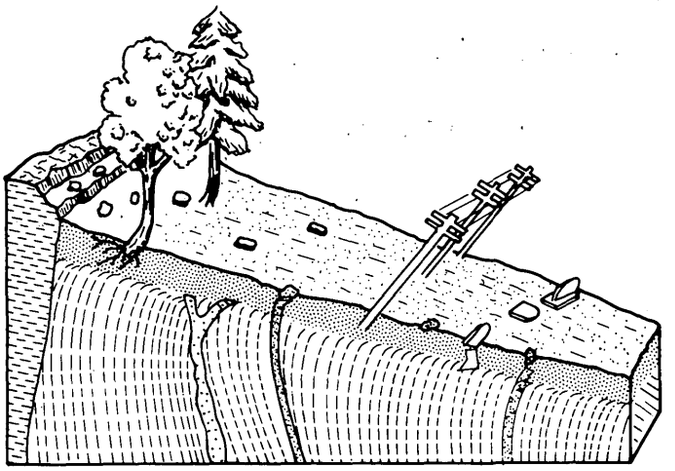

Figure 1.–Conventional surface and subsurface evidence of soil creep. Modified from Sharpe (1938).

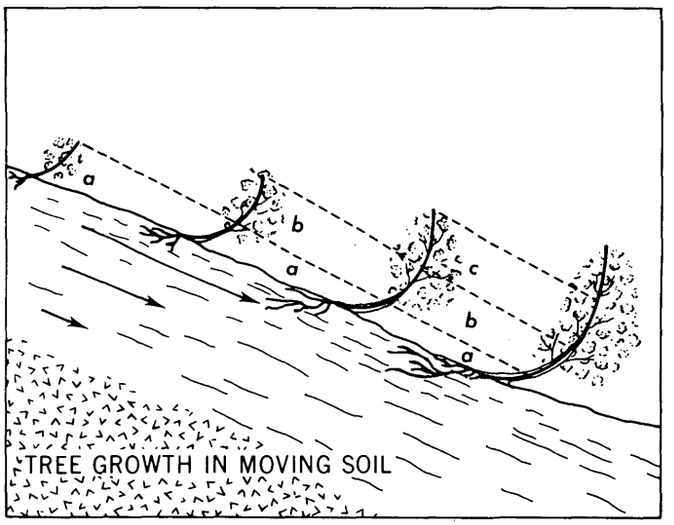

Figure 2.–Sequence indicating continuous curve in tree trunk which would hypothetically result if soil creep (arrows indicate direction of creep) continuously tipped tree. Letters *a*, *b*, and *c* indicate increments of growth in the same hypothetical tree. After Parizek and Woodruff (1957).

The classic tree shape ascribed to soil creep, "oblique at the base, while the trunks as a whole tend to grow vertically upwards," can only result from conditions which were much different when the tree was young and small than when it grew older. A common example is that of a small tree being bent quite suddenly, such as by flood water or by a large falling tree (fig. 3), the small tree becoming permanently tilted, with subsequent near-vertical growth from the tip of the tilted tree. The classic shape cannot result from continuously changing conditions.

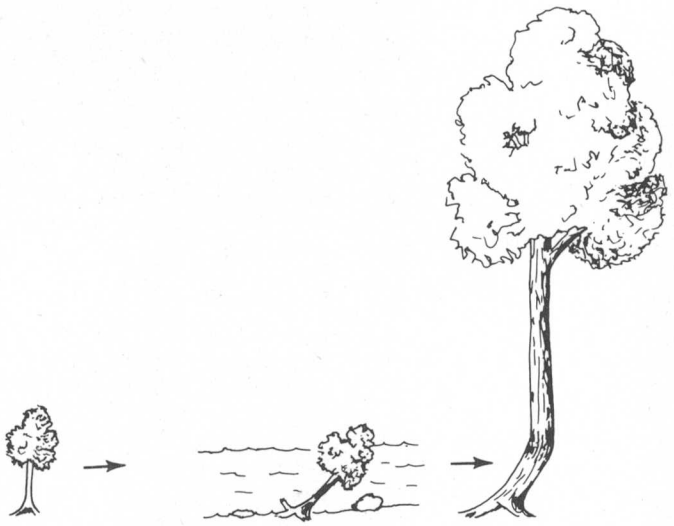

Figure 3.—Time sequence of normal vertical growth, tipping of tree by mechanical force such as flood water, and subsequent vertical growth from tipped trunk.

Stump sprouts, or epicormic shoots, frequently develop from the stumps of recently felled trees. Typical sprouts are curved at the base, curvature of sprouts being radially oriented from the center of the old stump (fig. 4). Surrounding trees on the slope do not necessarily exhibit similar trunk curvature. The first year after cutting, numerous sprouts probably develop. As the small compound crown of sprouts becomes dense, the height growth of the sprouts is away from the lower light intensities at the center of the crowded clump. Growth away from lower toward higher light intensities is described as phototropic growth response and is the result of photosensitive growth regulators moving away from, or being destroyed by, light at high intensities. With time, some of the sprouts die, as light and soil moisture become limiting. After the death of each sprout, light intensities near the remaining sprouts increase, thus resulting in a more vertical orientation of the trunks. If, as is quite probable, all but one of the remaining trunks die, the one that is left may appear very much like the classical tree supposedly representing soil creep.

Tree-trunk curvature as a consequence of phototropic response may, in addition to the stump-sprout example, result from any situation in which the relative light intensities on various sides of a tree change. Inside a mixed-age stand the

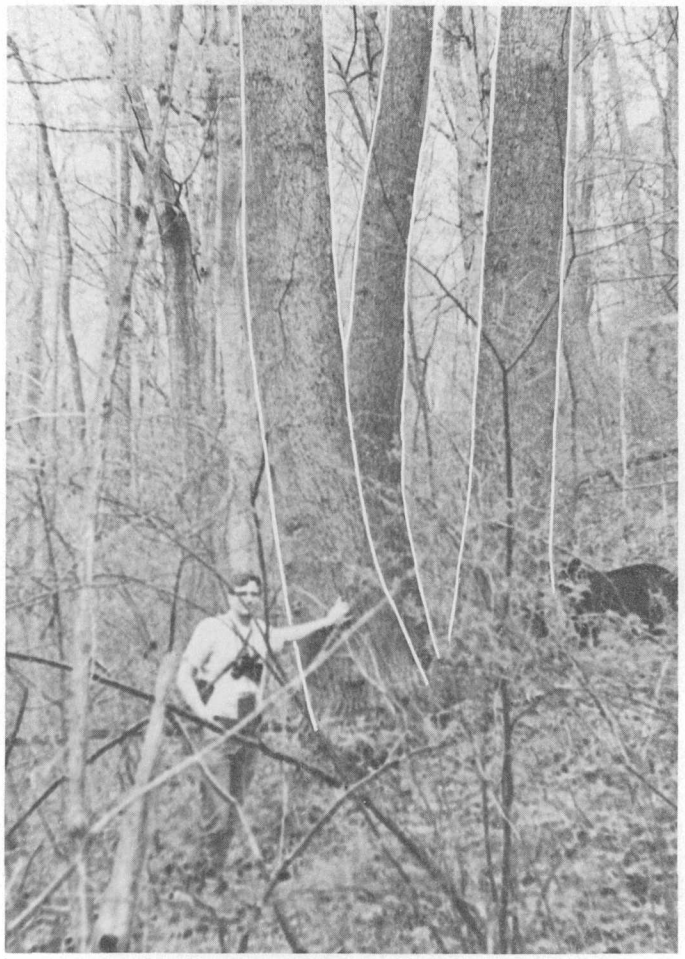

Figure 4.—Tree trunks of yellow poplar (*Liriodendron tulipfera*) which have grown as stump sprouts from a common stump. Curvature near base of sprouts is similar to hypothetical curve of trees used as evidence of soil creep.

light conditions on opposite sides of a tree are subject to numerous changes as the tree progresses from seedling size to canopy size. Perhaps the most common light change results from the changing positions of the crown relative to surrounding trees or objects as the tree grows in height. Sudden dramatic changes in light result from removal of any surrounding trees by natural death or lumbering. It is to be expected, then, that trees with some degree of curvature or a bend anywhere between the base and the crown will be quite common in mixed-aged stands. Illustrated in figure 5 is a white pine (*Pinus strobus*) which for some time was overtopped by a basswood (*Tilia americana*). While in the shade of the basswood, the pine grew at a rather pronounced angle away from the basswood. As it escaped the shade of the basswood, height growth of the pine became more vertical, resulting in a pronounced trunk curvature. Any condition which results in changes in light intensities on opposite sides of a tree crown, such as convergence or divergence of adjacent crowns, will result in trunk curvature.

Figure 5.—Curved trunk of white pine which originally grew in the shade of tree at extreme right. As it escaped shade, growth became more vertical.

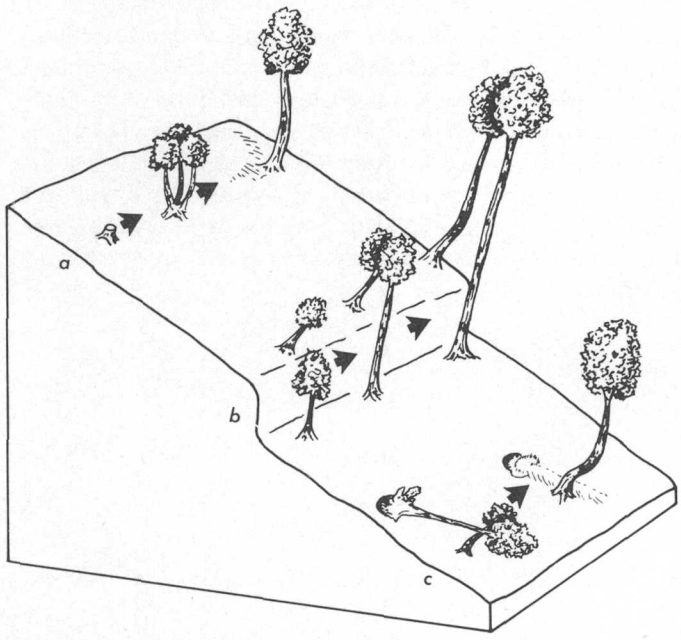

Figure 6.—Sequential development of curved tree trunks from (a) stump sprouts, (b) crown mergers consequent on changes in levels of light intensities, and (c) physical damage to small trees. Arrows indicate sequence in each example.

Another situation resulting in a relative change in light intensities may be seen in the trees growing immediately above a small clifff (*b* in fig. 6). The greater degree of downslope tilt of the lower part of the trunk is the result of the small tree growing away from the crowded conditions above the cliff and toward the higher light intensities above the crowns of the young trees below the cliff. Relative reduction of downslope-light intensity probably resulted when the crown of the tree above the cliff came in contact with the crowns or shade of crowns of trees growing below the cliff. Subsequent growth has been parallel to trunk orientation of downslope trees.

The conditions which result in bent trees by causes other than soil creep may be categorized as those arising from physical causes and those arising from physiological causes. Physical causes include events and conditions which bend, distort, or injure trees and may be brought about by floods, ice or snow storms, falling or fallen trees, snow or earth slides, and any of man's activities which injure or partly topple trees. Growth response to physical movement of the tree is typically geotropic. Physiological causes of distorted tree trunks as discussed include conditions which result in changes of relative light intensities on different sides of the tree. Growth responses to changes in light are described as phototropic. Three types of conditions resulting in curved tree trunks are sequentially illustrated in figure 6. Essentially all forested areas of uneven-aged trees afford ample evidence of individual trees with bent trunks resulting from causes other than soil creep. By contrast, other than the generalizations that curved trees indicate soil creep, there seems to be no evidence in the literature which can be construed to indicate that tree curvature can be or has been demonstrated to be the result of soil creep.

TILTED TREE TRUNKS

Downslope tilting of trees with or without associated curvature of the lower trunk is often cited as evidence of soil creep. During field observations in eastern deciduous forests, no evidence has been found to substantiate this. It has been found that trees are normally tilted downslope, but such tilting can easily be explained as the consequence of phototropic response. Phototropic response can be illustrated on flat, level ground where no soil creep would be expected. Trees along the long-established roads commonly lean away from the lower light intensity of the forest and toward the higher light intensity of the right-of-way (fig. 7). Trees lean away from the darker wooded area toward the open, regardless of whether the resultant lean is upslope or downslope (fig. 8). The lean in this figure is upslope. Trees planted close to buildings lean away from the buildings though soil creep is obviously not the cause (fig. 9).

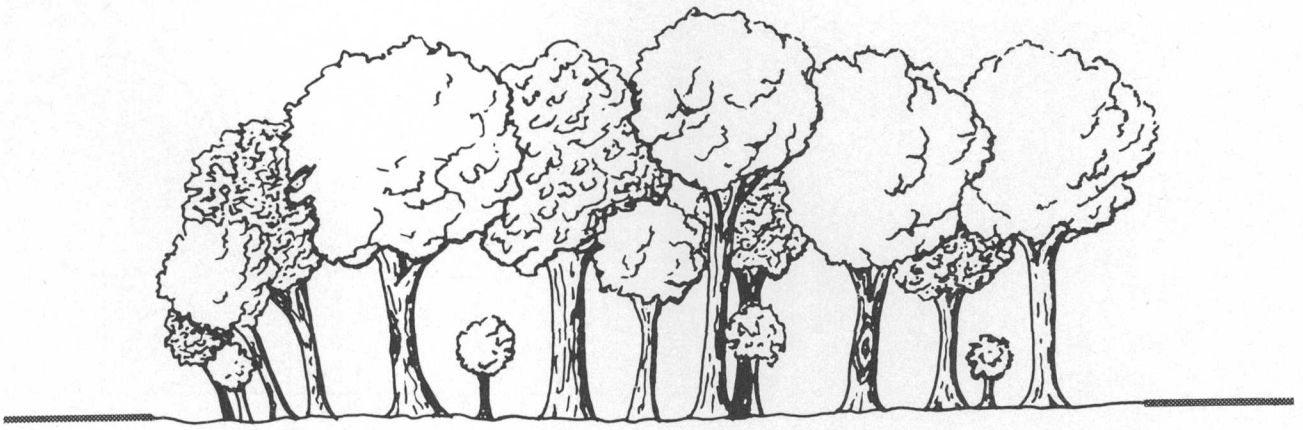

Figure 7.—Hypothetical patch of woods with long established right-of-way on left and recently cut right-of-way on right, showing leaning of trees.

Figure 8.—Trees leaning away from wood grove on left and toward upslope direction on right.

Figure 9.—Trees leaning away from the Department of Interior building are example of phototropic response.

We unconsciously use trees on hillsides to estimate the vertical. As a method of recording degree of leaning on slopes, a carpenter's level is affixed in a level position to the trunk and the tree is photographed (fig. 10). Even while purposely measuring degree of lean in this manner, assistants will frequently aline the camera, not with the carpenter's level, but with the tree trunks.

The cause of phototropism of trees growing on hillsides is that hillside trees receive more direct solar radiation on their downslope side than on their upslope side. If the crown of a deciduous tree is regarded as a sphere, then the canopy of a closed forest may be regarded as a group of closely packed spheres, each sphere having some overlap with each adjacent sphere, and each containing a directly exposed surface on top. Progressing from level ground to increasing slope, the relative position of the exposed surface shifts from directly on top toward the downslope side (fig. 11). As long as the angle of the upper surface of the forest canopy remains constant, so that the proportion of downslope to upslope surface of each crown remains constant, the angle of trunk growth will not change and the trunk will be straight. If the proportion

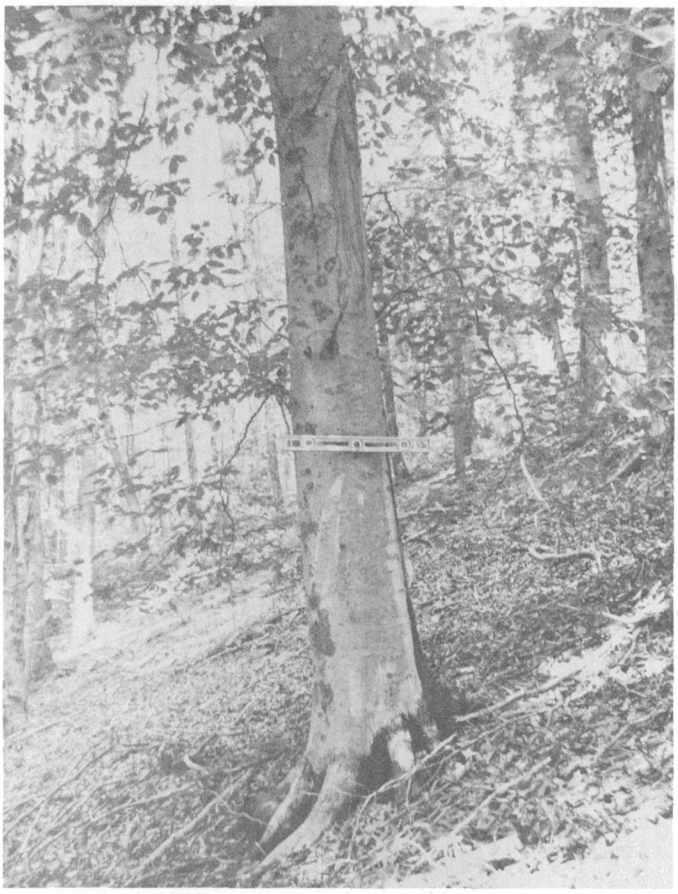

Figure 10.–General leaning of trees on hillslope. Note carpenter's level as reference on tree in foreground.

changes, then subsequent growth direction will also change, resulting in trunk curvature.

The degree of phototropism exhibited by an individual tree to a given set of light conditions seems to be a function of species. In general, shade-tolerant species (those capable of reproducing in shaded conditions) do not exhibit as great a phototropic response as shade-intolerant species (those having higher light-intensity requirements for reproduction). Thus, distorted trunks are more noticeable among shade-intolerant than shade-tolerant species. Also, shade-intolerant species tend to lean downslope to a greater degree than shade-tolerant species. Preliminary studies of trunk leaning of shade-tolerant beech (*Fagus grandifolia*) and relatively intolerant white oak (*Quercus alba*) indicated very little leaning among the beech, with only a suggestion that perhaps a bit more leaning occurred on steeper slopes. White oak, growing on slopes ranging from 10° to 30°, leaned downslope almost 1° from the vertical for each 3° of slope. The relationship between leaning and slope steepness seemed independent of direction of slope exposure.

No evidence has been found to suggest that general tilting of trees on slopes is greater than can be attributed to phototropism. Among tree species of similar degrees of shade

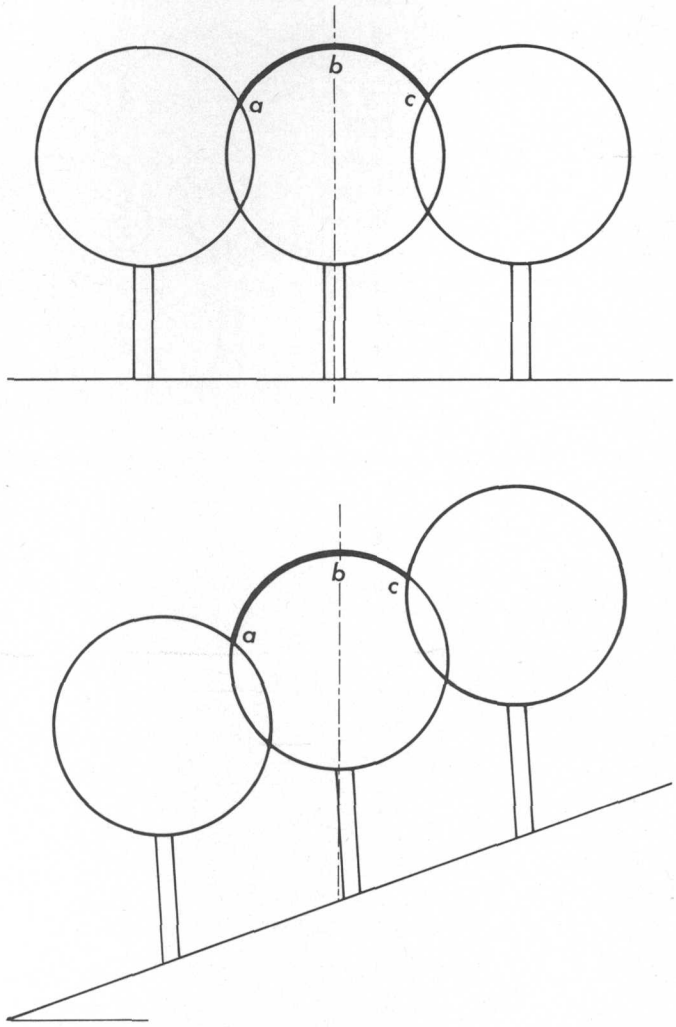

Figure 11.–Top diagram shows trees on level ground. Bottom diagram shows that trees on slope have more crown surface exposed to direct solar radiation on the downslope side (*ab*) than on the upslope side (*bc*).

tolerance, tilting is relatively uniform on a given slope. Changes in angle of tilt occur with changes in slope angle and at the forest margin. For any given tree on a slope, an adjacent-upslope tree obstructs more direct light than an adjacent-downslope tree. Phototropic response of the tree to light imbalance between upslope- and downslope-sides results in terminal growth progressing somewhat downslope from vertical.

SUMMARY

Curved tree trunks, upslope trailing of root systems, and downslope tilting of trees are frequently cited as evidence of soil creep. Studies of tree-root systems have failed to demonstrate that upslope trailing of roots occurs. Root systems of adjacent trees have been found to exhibit considerable overlap, which tends to stabilize the upper soil layer. It is suggested that if soil creep moves roots, then the entire root zone must

move as a unit. Tree-trunk curvature can result from a geotropic response following physical displacement of the tree, but evidence has not yet been found to substantiate soil creep as a mechanism of physical displacement of the tree. The classical trunk shape, oblique at the base above which the trunk is straight, cannot result from soil creep which continuously tips the trunk downslope. Such a shape can result from any mechanical force or phototropism which exerts a much greater force when the tree is small than when it grows larger. Trees on slopes have a tendency to lean downslope as a phototropic response, which is throught by the author to be a function of slope steepness and degree of shade tolerance of the individual tree species. No evidence has been found to substantiate the claim that downslope leaning of trees is the result of soil creep.

REFERENCES CITED

Alestalo, J., 1971, Dendrochronological interpretation of geomorphic processes: Helsinki, Societas Geographica Finniae, 140 p.

Barr, D. J., and Swanston, D. N., 1970, Measurement of creep in a shallow, slide-prone till soil: Am. Jour. Sci, v. 269, p. 467–480.

Carson, M. A., and Kirkby, M. J., 1972, Hillslope form and process: London, Cambridge Univ. Press, 475 p.

Everett, K. R., 1963, Slope movement, Neotoma Valley, southern Ohio: Ohio State Univ. Inst. Polar Studies Rept. 6, 59 p.

Gilluly, J., Waters, A. C., and Woodford, A. O., 1968, Principles of geology: San Francisco, W. H. Freeman and Co., 687 p.

Leet, L. D., and Judson, S. S., Jr., 1958, Physical geology: Englewood Cliffs, N.J., Prentice-Hall, Inc., 502 p.

Leopold, L. B., Emmett, W. W., and Myrick, R. M., 1966, Channel and hillslope processes in a semiarid area, New Mexico: U.S. Geol. Survey Prof. Paper 352-G, p. 193–253.

Parizek, E. J., and Woodruff, J. F., 1957, Mass wasting and deformation of trees: Am. Jour. Sci, v. 255, p. 63–70.

Penck, Walther, 1953, Morphological analysis of landforms, *translated from* German by H. Czech and K. C. Boswell: New York, St. Martin's Press, 429 p.

Sharpe, C. F. S., 1938, Landslides and related phenomena: New York, Columbia Univ. Press, 136 p.

Small, R. J., 1970, The study of landforms: London, Cambridge Univ. Press, 486 p.

Stout, B. B., 1956, Studies of the root systems of deciduous trees: Cambridge, Mass., Harvard Univ., Black Rock Forest Bull., no. 15, 45 p.

Tomlinson, P. B., 1964, The good eye: Carolina Tips, v. 27, p. 13.

Jour. Research U.S. Geol. Survey
Vol. 2, No. 3, May-June 1974, p. 379—384

SOME ASPECTS OF AQUATIC INSECT POPULATIONS OF POOLS AND RIFFLES IN GRAVEL BED STREAMS IN WESTERN UNITED STATES

By BRUCE W. LIUM, Doraville, Ga.

Abstract.—Relationships were studied between aquatic-insect populations on rocks of different sizes and variations of populations between different stream localities. All aquatic insects were counted and identified on streambed gravels and cobbles chosen at random from four rivers on three to four types of locations ranging from riffles to pools. The measurements used span 3 to 4 months in 1 year. Insect density (number of insects per unit of rock area) was determined to be a function of rock size. Highest insect densities occurred on rocks between 45 and 90 mm mean diameter, with larger and smaller rocks having lower insect densities. The insect population differed significantly with location within a stream; that is, from pool to riffle, as well as by stream and season.

An investigation has been made by the author to use aquatic insect counts in such a way that the kinds of organisms found on rocks in streams can be related to environmental factors. In this investigation, the macroscopic insects on rocks taken from the gravel substrate of the streambed were collected, counted, and identified. A sample consisted of 10 rocks chosen at random from the streambed in each of several localities of a stream. The streams were sampled and collections were made at each of 3 to 4 months in a 1-year period. Western mountain streams were selected for the study on the basis of several general similarities: the nature and composition of the channel bed, the gradient, and presence of a typical riffle-pool sequence. The choice was also based on the premise that these streams were pristine in nature and unaffected by pollution. This paper describes the study method and presents data on the number of organisms of different genera and discusses variables representing physical characteristics of the individual localities.

Acknowledgment.—The author is particularly indebted to Luna B. Leopold, who directed the study and aided in analyzing the data and in writing the manuscript. L. D. Jensen, R. L. Vannote, M. G. Wolman, and J. L. Barker gave technical reviews and many helpful suggestions in preparation of the manuscript.

FIELD TECHNIQUES

In each stream studied, a typical riffle-pool sequence area was chosen for sampling. The area to be sampled was divided visually into categories representing essentially similar environments described as fast pool, falls, fast riffle, and slow pool. The words fast and slow refer to mean-stream velocity. The fast pools were either zones where the stream swings round a curve near the concave bank or a long swift reach, where the surface had a slight ripple. The slow pools in the stream were zones near the convex bank or a deep part of no rippling. The fast riffles were zones where streambed cobbles tended to accumulate in groups, and the water was flowing as a rapid. Each of these zones, here called a province, was treated as a homogeneous unit. Within each province, 10 rocks were chosen at random from the streambed, the insects collected for identification, and the size of each rock recorded.

A sampler was used to catch all insects that washed off a rock as it was picked from the streambed (Lium, 1969). The hood of the sampler was placed over a selected rock and was pressed down to the streambed. The sampler had a flexible margin beneath the hood, where it touched the bed, to reduce the likelihood of losing organisms when a rock was picked from the stream. Insects that were dislodged as the rock was picked up were carried by the current into the screen behind the hood. Both the insects on the rock and those caught in the screen were placed in vials containing alcohol and were later identified.

On the assumption that a major factor controlling the occurrence of insects in a stream is the substratum, it was attempted to show some aspects of how different substrata support different numbers and proportions of insects. This led to making counts of insects on rocks of varying size from one province to another within a stream. The size of each rock in all samples were measured across the *b*-axis (Leopold, 1970).

DATA COLLECTED

A sketch map of the studied reach in Pole Creek is presented in figure 1 as a typical example of the types of provinces

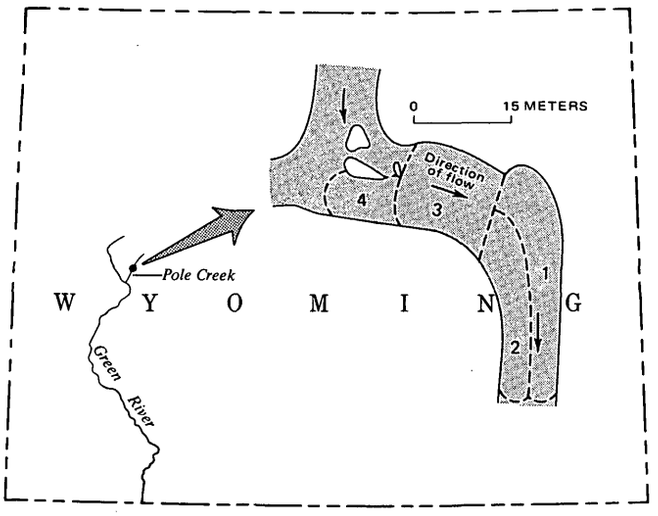

Figure 1.—Provinces in Pole Creek to illustrate typical pool and riffle areas of the streams studied. A quartile distribution of rock particle size is shown for each province. 1, Fast pool: Mean, 118 mm; 75 percent, <145 mm; 25 percent, <94 mm. 2, Slow pool: Mean, 60 mm; 75 percent, <72 mm; 25 percent, <41 mm. 3, Fast riffle: Mean, 61 mm; 75 percent, <74 mm; 25 percent, <44 mm. 4, Fast pool: Mean, 90 mm; 75 percent, <111 mm; 25 percent, <75 mm.

found in the four streams. Pole Creek is near Pinedale, Wyo., and is one of the many headwater streams of the Green River system. Carter Creek is near Dutch John, Utah. At one time it was a tributary of the Green River but now flows into the lower part of the Flaming Gorge Reservoir. The Weber and Provo Rivers are on the western flank of the Uinta Mountains.

During the investigation, 8,643 insects were collected from 420 rocks. The identification was generally to the genus level, but some were identified only as to family and others as to species. Thirty-two different forms were identified. The family and genus and, where identified, the species of the insects observed in each stream are given in table 1.

Table 1.—*Assemblages of insects collected*

Pole Creek:
- Ephemeroptera (mayflies):
  - *Baetis bicaudatus* Dodds
    - *tricaudatus* Dodds
  - *Cinygmula* sp.
  - *Epeorus longimanus* Eaton
  - *Ephemerella doddsi* Needham
    - *flavilinea* McDunnough
    - *inermis* Eaton
  - *Paraleptophlebia* sp.
  - *Tricorythodes* sp.
- Tricoptera (caddisflies):
  - *Brachycentrus* sp.
  - *Glossosoma* sp.
  - *Hesperophylax* sp.
  - Hydroptilidae
  - Limnephilidae
  - *Neothremma* sp.
- Diptera (trueflies):
  - Chironomidae
  - *Simulium* sp.
- Plecoptera (stoneflies):
  - *Alloperla* sp.

Table 1.—*Assemblages of insects collected*—Continued

Weber River:
- Ephemeroptera (mayflies):
  - *Baetis bicaudatus* Dodds
    - *intermedius* Dodds
    - *tricaudatus* Dodds
  - *Cinygmula* sp.
  - *Epeorus longimanus* Eaton
  - *Ephemerella doddsi* Needham
    - *inermis* Eaton
    - *tibialis* McDunnough
  - *Rhithrogena* sp.
- Tricoptera (caddisflies):
  - *Brachycentrus* sp.
  - *Neothremma* sp.
  - *Ryhacophila* sp.
- Diptera (trueflies):
  - Blephariceridae
  - Chironomidae
  - *Simulium* sp.
- Pelcoptera (stoneflies):
  - *Alloperla* sp.
  - *Isogenus* sp.
  - *Isoperla* sp.

Carter Creek:
- Ephemeroptera (mayflies):
  - *Ameletus* sp.
  - *Baetis bicaudatus* Dodds
    - *intermedius* Dodds
    - *tricaudatus* Dodds
  - *Cinygmula* sp.
  - *Epeorus longimanus* Eaton
  - *Ephemerella doddsi* Needham
    - *grandis* McDunnough
    - *inermis* Eaton
    - *tibialis* McDunnough
  - *Paraleptophlebia* sp.
  - *Rhithrogena* sp.
- Tricoptera (caddisflies):
  - *Glossosoma* sp.
  - *Hydropsyche* sp.
  - *Lepidostoma* sp.
  - *Neothremma* sp.
  - *Rhyacophila* sp.
- Diptera (trueflies):
  - Chironomidae
  - *Simulium* sp.
- Plecoptera (stoneflies):
  - *Alloperla* sp.

Provo River:
- Ephemeroptera (mayflies):
  - *Baetis bicaudatus* Dodds
    - *intermedius* Dodds
    - *tricaudatus* Dodds
  - *Cinygmula* sp.
  - *Epeorus longimanus* Eaton
  - *Ephemerella doddsi* Needham
    - *inermia* Eaton
    - *tibialis* McDunnough
  - *Paraleptophlebia* sp.
- Tricoptera (caddisflies):
  - *Brachycentrus* sp.
  - *Glossosoma* sp.
  - *Neothremma* sp.
  - *Rhyacophila* sp.
- Diptera (trueflies):
  - Chironomidae
  - *Simulium* sp.
- Plecoptera (stoneflies):
  - *Alloperla* sp.
  - *Claassenia* sp.
  - *Pteronarcella* sp.

The fauna was generally similar in each of the streams and comprised insects in the orders Ephemeroptera, Tricoptera, Diptera, and Plectoptera. More kinds of Ephemeroptera were

found than representatives from the other orders. The relative abundance of insects in each order for all streams and percentage of insects in each stream are given in table 2.

More mayflies (Ephemeroptera) and caddisflies (Tricoptera) were found in Pole Creek and Carter Creek than in the Weber and Provo Rivers. An abundance of truefiles (Diptera) was found in the Weber and Provo Rivers. Very few stone flies (Plecoptera) were found in any of the streams.

EFFECTS OF ROCK SIZE

The variation of size of rock particles in the Pole Creek provinces is shown in figure 1. In the fast pools, the mean diameter of the rocks found was 118 mm in province 1 and 90 mm in province 4. In provinces 2 (slow pool) and 3 (fast riffle), the mean diameter of the rocks found was 60 mm and 61 mm, respectively. A quartile distribution of the rocks found in all four provinces of Pole Creek is also shown in figure 1. These findings were typical in the provinces of all four streams.

To find how different rock sizes affected the density of organisms, the total insect count per rock was divided by πd (d being the intermediate axis of the rock) to give number of insects per square centimeter rock area.

Density of insects increased with rock size from 22 to 64 mm, then decreased as rock size increased to 256 mm (fig. 2). Maximum density of organisms per square centimeter occurred on rocks in the 45–90 mm size class. The reasons for this are unclear, but increase in density with increasing rock size from 22 to 32 mm suggests that there is proportionately more surface area available for supporting fauna as rock size becomes greater. Decreasing density in larger rocks (128 to 256 mm) suggests that larger rocks have proportionately fewer available preferred microhabitat sites per unit of rock area.

As pointed out by Percival and Whitehead (1929), a main factor affecting the presence of an organism on a particular substrate is the availability of sheltered crevices, and they found fewer animals on loose stones than on embedded ones. It is also possible that loose smaller stones have fewer organisms because these stones are moved and washed downstream more readily than larger stones. Sprules, (1947) further suggests that the space available for colonization is a major factor controlling the abundance of fauna in stony streams. The problem becomes more difficult when consideration is given to silting, which makes small-grade rocks less likely for colonization than larger particles, Lauff and Cummins (1964). Pennak and Gerpen (1947) found the average number of organisms per square meter in a northern Colorado trout stream to be greatest in rocks 2.54–20.32 cm in diameter, with decreased density in larger (>20.32) and smaller (0.64–2.54 cm) rocks.

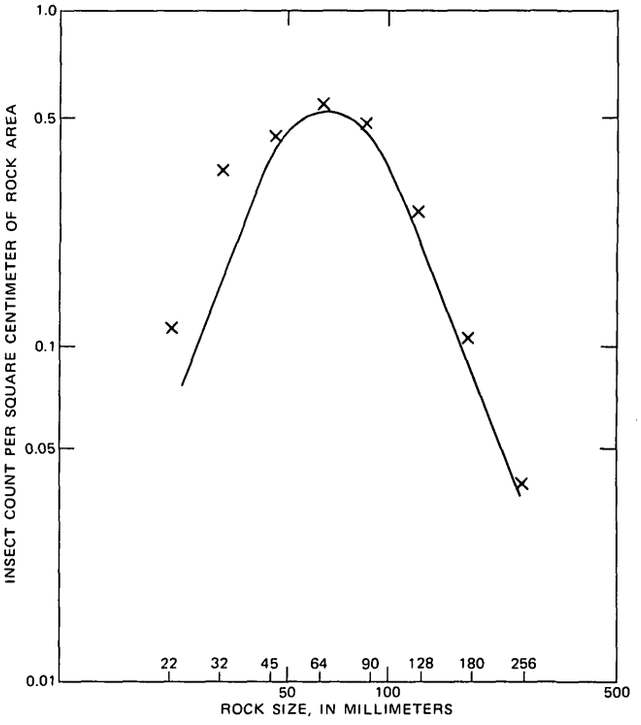

Figure 2.—Relationship of mean density values of insects to rock sizes. Data are from all provinces, seasons, and streams.

DETERMINANTS OF FAUNAL DENSITY

To find if there were differences in insect density of province, stream, and season, an analysis of variance included five

Table 2.—*Total number and percentage of insects in each order for all streams*
[Data include counts from all 10-rock samples]

Stream	Ephemeroptera		Tricoptera		Diptera		Plecoptera		Total insects in each stream
	Number of organisms	Percent	Number of organisms	Percent	Number of organisms	Percent	Number of organisms	Percent	
Pole	444	43.65	532	52.31	38	3.73	3	0.29	1,017
Weber	482	11.79	149	3.64	3,425	83.82	30	.73	4,017
Carter	307	30.03	625	61.15	82	8.02	8	.78	1,022
Provo	105	4.16	148	5.87	2,258	89.67	7	.27	2,518
Totals	1,338	.....	1,454	.....	5,803	.....	48	.....	8,643

separate analyses on total insect count per rock, divided by length squares. One analysis was for three streams, three months, and three provinces. Four analyses were by individual streams to determine month and province effects. In the first analysis, the province was not exactly the same from stream to stream but was always in order of increasing province velocity, possibly showing some stream-province interaction. The four analyses on individual streams allowed much more complete utilization of the data. All these analyses, with the exception of the Weber River, showed the province the variable with the greatest contribution of variance, followed by stream and month, and all significant at the 95-percent-level of confidence. On the Weber River, where the province effect is less than the month effect, note that those provinces used were fast riffle, fast pool, and fast riffle, which indicates little variation should be expected.

This finding indicates that the factors controlling the insect density and the variability between provinces were generally similar in these four streams and that the environmental conditions are generally the same.

DIVERSITY INDEX

Diversity, or the evenness of distribution of insects, gives some indication of the environmental condition of a stream. Diversity was computed separately, by season, for each stream and each province by the Shannon-Wiener approximation:

$$D=-\Sigma\, PI \log_2 PI$$

where PI is the probability of occurrence of the Ith species. The probability (PI) is equal to NI/NS, where NI is the number of individuals in each species and NS is the total number of individuals in all species (Hutchinson, 1967).

When the assemblage consists of a single species, D=0, and no more information can be gained when a random individual is identified, D increases as the number of species increases and is greatest when all species are equally abundant. This approximation is useful as an estimate of diversity for comparison with other environmental variables because it makes no theoretical assumption regarding the nature of the distribution of the organisms. (Hutchinson, 1967).

The mean seasonal diversity of insects for all streams was generally highest in the early summer, as shown in table 3. Diversity declined through midsummer but increased slightly in the fall. It was greatest in Carter Creek, then in Pole Creek, Weber Creek, and Provo River, respectively.

EFFECT OF VELOCITY

In an attempt to show the relationship between insect diversity and stream velocity (cm/s), figure 3 has been constructed using insect diversity versus stream velocity at 1.52 cm above the stream bottom, with the plotted values representing mean values for all provinces within the various streams. A considerable increase in the insect diversity occurred from the slow pools to the other provinces. Within these provinces (falls, fast riffles, and fast pools) the insect diversity was about the same, with only a slight increase (1.8–1.9) from the fast pools to the falls. There was a corresponding change of stream velocity from 24.38 cm/s to 67.05 cm/s.

Table 3.—*Monthly diversity (D) of insects in each stream province*
[Location of Pole Creek provinces is shown in fig. 1]

Stream	Month	Province		D
		Location	Description	
Pole Creek	June	1	Fast pool	2.329
		2	Slow pool	2.496
		3	Fast riffle	2.090
		4	Fast pool	2.374
	July	1	Fast pool	1.470
		2	Slow pool	1.013
		3	Fast riffle	2.477
		4	Fast pool	1.875
	August	1	Fast and slow pool	.502
		2	Fast and slow pool	.502
		3	Fast riffle	dry
		4	Fast pool	.115
	September	1	Fast pool	2.148
		2	Slow pool	.851
		3	Fast riffle	1.758
		4	Fast pool	2.172
Carter Creek	July	1	Slow pool	2.820
		2	Fast riffle	3.171
		3	Falls	2.878
		4	Fast riffle	1.775
	August	1	Slow pool	1.696
		2	Fast riffle	2.221
		3	Falls	1.092
		4	Fast riffle	1.778
	September	1	Slow pool	1.293
		2	Fast riffle	.825
		3	Falls	1.394
		4	Fast riffle	2.107
Provo River	July	1	Fast riffle	.392
		2	Fast pool	2.265
	August	1	Fast riffle	1.045
		2	Fast pool	2.153
		3	Slow pool	.912
	September	1	Fast riffle	2.127
		2	Fast pool	1.915
Weber River	July	1	Fast riffle	2.219
		2	Fast pool	1.127
		3	Fast riffle	1.733
	August	1	Fast riffle	1.577
		2	Fast pool	2.363
		3	Fast riffle	1.065
	September	1	Fast riffle	9.15
		2	Fast pool	2.043
		3	Fast riffle	1.477

ROCK STABILITY

The data from these streams were used to calculate levels of confidence to determine whether or not 10 rocks chosen at random represent a sample large enough to be representative of the insect populations in various stream provinces.

The number of samples required to achieve an error within 10 to 20 percent of the mean of an ecologically homogeneous

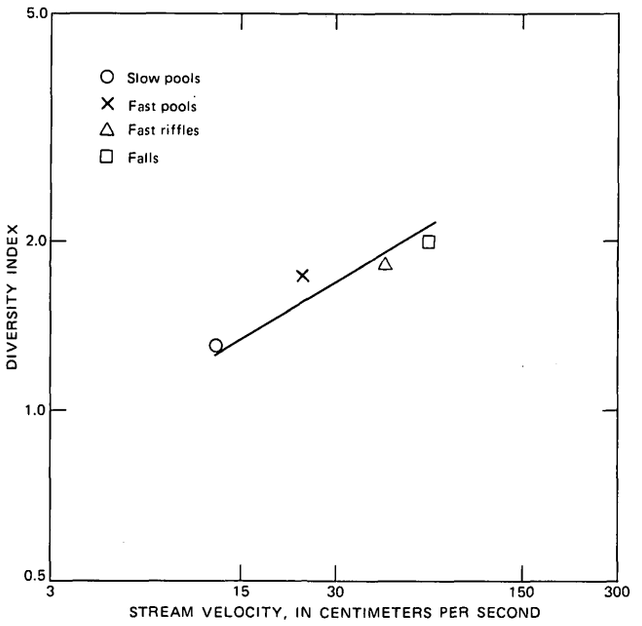

Figure 3.—Relationship, by province, of mean-diversity index of insects to mean velocity of streams. Velocity measured at 1.52 cm above streambed.

habitat can be calculated from the formula given by Southwood (1966). The number of samples required (N) is given by:

$$N=\frac{ts}{D\bar{x}}$$

where $\bar{x}$=mean, s=standard deviation, D=required level of accuracy expressed as a decimal (0.1 or 0.2), and t is from Student's t distribution and has $N-1$ degrees of freedom. At a 0.95 level of confidence and ±10 percent of the true mean, it was found that on the average 200 rocks were needed, using the data from all provinces in all streams. The number of rocks needed at ±20 percent of the true mean was found to be 50, using the same data. Table 4 shows the actual and mean number of rocks necessary to estimate the aquatic insect populations within ±10 and ±20 percent of the true mean at 95 percent level of confidence for each stream. The number of rocks necessary to estimate the aquatic insect population within ±10 percent and ±20 percent of the true mean ranged in value from 53 to 967 and 13 to 241, respectively.

SUMMARY

The results presented show that aquatic insect density on rocks differs most significantly between provinces (stream zones), then by stream and season. Insect density was also shown to be a function of rock size; the greatest density on rocks was in the 45 to 90 mm size. The density and diversity of insects increased with increasing stream velocity in different provinces. Both were greatest in riffles and smallest in fast pools to slow pools. The study indicated the large sample of rocks necessary to obtain a statistically valid sample of the insect population on rocks in streams.

Table 4.—*Number of rocks necessary to estimate the aquatic insect population for each of four streams*

Stream	Estimates within indicated percentage of true mean at 95-percent confidence level for each set of 10-rock samples	
	±10	±20
Pole Creek	53	13
	114	28
	104	26
	137	34
	94	23
	400	100
	216	54
	119	30
	154	38
	104	26
	69	17
	177	44
	216	54
	130	33
Total	2,087	520
Mean	149	37
Carter Creek	100	25
	56	14
	112	28
	88	22
	392	98
	139	35
	199	49
	112	28
	177	44
	92	23
	310	77
	190	48
Total	1,967	491
Mean	164	41
Provo River	182	46
	110	27
	74	19
	967	241
	64	16
	437	109
	177	44
	151	38
Total	2,162	539
Mean	270	67
Weber River	94	24
	234	59
	306	77
	130	33
	368	92
	216	54
	493	123
	71	18
	204	51
	400	100
	182	46
	139	35
	76	19
	96	24
Total	3,009	755
Mean	215	54
Total of means of four streams	798	199
Mean of four streams	199.5	49.7

REFERENCES CITED

Hutchinson, G. E., 1967, A treatise on limnology: New York, John Wiley and Sons, Inc., v. 2, p. 362–365.

Lauff, G. H., and Cummins, K. W., 1964, A model stream for studies in lotic ecology: Ecology, v. 45, p. 188–191.

Leopold, L. B., 1970, An improved method for size and distribution of streambed gravel: Water Resources Research, v. 6, no. 5, p. 1357–1366.

Lium, B. W., 1969, The distribution of aquatic insects in stream and river provinces as determined by chemical, physical, and hydrological factors: Utah Univ., Ph. D. dissert., 84 p.

Pennak, R. W., and Van Gerpen, E. E., 1947, Bottom fauna production and physical nature of the substrate in a northern Colorado trout stream: Ecology, v. 28, p. 42–48.

Percival, E., and Whitehead, H., 1929, A quantative study of some types of stream bed: Jour. Ecology, v. 17, p. 282–314.

Southwood, T. R. E., 1966, Ecological methods, with particular reference to the study of insect populations: London, Methuen, 391 p.

Sprules, W. M., 1947, An ecological investigation of streams insects in Algonquin Park, Ontario: Toronto Univ. Studies, Biol. Ser. 56, p. 1–81.

☆U.S. Government Printing Office: 1974-543-467/5

RECENT PUBLICATIONS OF THE U.S. GEOLOGICAL SURVEY

(The following books may be ordered from the Superintendent of Documents, Government Printing Office, Washington, DC 20402, to whom remittances should be sent by check or money order. Give series number, title, stock number shown in parentheses in this list, and catalog number shown in brackets. Prices of Government publications are subject to change. Increases in costs make it necessary for the Superintendent of Documents to increase the selling prices of many publications offered. As it is not feasible for the Superintendent of Documents to correct the prices manually in all of the publications stocked, the prices charged on your order may differ from the prices printed in the publications and in this list)

Professional Papers

387-B. Recent activity of glaciers of Mount Rainier, Wash., by R. S. Sigafoos and E. L. Hendricks. 1972 (1973). p. B1–B24; plates in separate case. $8.95. (2401-2179) [I 19:16:387-B]

529-M. Atlantic Continental Shelf and Slope of the United States–Texture of surface sediments from New Jersey to southern Florida, by C. D. Hollister. 1973. p. M1–M23; plates in pocket. $2.05. (2401-02432) [I 19:16:529-M]

802-B. Summary of turbulence data from rivers, conveyance channels, and laboratory flumes, by R. S. McQuivey. 1973. p. B1–B66. $1.55. (2401-02429) [I 19:16:802-B]

804. Erosional and depositional aspects of Hurricane Camille in Virginia, 1969, by G. P. Williams and H. P. Guy. 1973. 80 p. $1.80. (2401-02442) [I 19:16:804]

830. Zeolites and associated authigenic silicate minerals in tuffaceous rocks of the Big Sandy Formation, Mohave County, Ariz., by R. A. Sheppard and A. J. Gude 3d. 1973. 36 p. $1.05. (2401-02404) [I 19:16:830]

Bulletins

1370. Biliography of North American geology, 1970. 1973. 1,276 p. $8.70. (2401-02420) [I 19:3:1370]

1372-I. New Cretaceous formations in the western Wyoming thrust belt, by W. W. Rubey. 1973. p. I1-I35. 50¢. (2401-02402) [I 19:3:1372-I]

1394-C. Gastineau Channel Formation, a composite glaciomarine deposit near Juneau, Alaska, by R. D. Miller. 1973. p. C1-C20. 35¢. (2401-02438) [I 19:3:1394-C]

Water-Supply Papers

1591-E. Sediment movement in an area of suburban highway construction, Scott Run basin, Fairfax County, Va., 1961-64, by R. B. Vice, N. P. Guy, and G. E. Ferguson. 1969. p. E1-E41. 70¢. (reprinted 1973.) (2401-0251) [I 19:13:1591-E]

2017. Improvement of trout streams in Wisconsin by augmenting low flows with ground water, by R. P. Novitzki. 1973. 52 p. 65¢. (2401-00305) [I 19:13:2017]

2096. Quality of surface waters of the United States, 1968–Part 7, Lower Mississippi River basin. 1973. 438 p. $2.95. (2401-02441) [I 19:13:2096]

2098. Quality of surface waters of the United States, 1968–Parts 9 and 10, Colorado River basin and the Great Basin. 1973. 296 p. $2.35. (2401-02440) [I 19:13:2098]

2100. Quality of surface waters of the United States, 1968–Parts 12-16, North Pacific slope basins, Alaska, Hawaii, and other Pacific areas. 1973. 464 p. $3.05. (2401-02439) [I 19:13:2100]

Techniques of Water-Resources Investigations

TWI3-A8. Discharge measurements at gaging stations, Chapter A8, by T. J. Buchanan and W. P. Somers. 1969. 65 p. 70¢. (Reprinted 1973.) (2401-0498) [I 19:15/5:Bk. 3/chap. A8.